Molecular Tuneability of Imine-based Covalent Adaptable Networks

Sybren K. Schoustra

Propositions

1. Polyimines are excellent materials for tuneable and recyclable thermosets and elastomers.
   (this thesis)

2. Macroscopic material properties of covalent adaptable networks (CANs) can be predicted and controlled from their molecular composition.
   (this thesis)

3. *If a covalent adaptable network shows vitrimer-like properties, it is a vitrimer, irrespective of whether it displays associative or dissociative bond exchange.*

4. A material can only be considered self-healing when it is able to heal in its solid/elastic phase without requiring manual input.

5. One of the hardest things for scientists is to accept that they will never know everything.

6. Curiosity is one of the most important qualities that defines a good scientist.

7. One can only fully thrive when well rested.

8. Times New Roman is not a suitable font for publishing.

Propositions belonging to the thesis, entitled:

"Molecular Tuneability of Imine-based Covalent Adaptable Networks"

Sybren K. Schoustra

Wageningen, 7 March 2023

Molecular Tuneability of Imine-based Covalent Adaptable Networks

Sybren K. Schoustra

Thesis committee

Promotor

Prof. Dr H. Zuilhof

Professor of Organic Chemistry

Wageningen University & Research

Co-promotor

Dr M.M.J. Smulders

Associate professor at the Laboratory of Organic Chemistry

Wageningen University & Research

Other members

Prof. Dr J. van der Gucht, Wageningen University & Research

Dr J.P.A. Heuts, Eindhoven University of Technology

Prof. Dr K. Loos, University of Groningen

Prof. Dr F. Du Prez, Ghent University, Belgium

Molecular Tuneability of Imine-based Covalent Adaptable Networks

Sybren K. Schoustra

Thesis

submitted in fulfilment of the requirements for the degree of doctor

at Wageningen University

by the authority of the Rector Magnificus,

Prof. Dr A.P.J. Mol

in the presence of the

Thesis Committee appointed by the Academic Board

to be defended in public

on Tuesday 7 March 2023

at 1.30 p.m. in the Omnia Auditorium.

Table of Contents

Chapter 1

General Introduction

Parts of this chapter are included in the following review:

1.1 Polymers and Covalent Adaptable Networks

1.1.1 Classical polymers

Polymers play an important part in our daily lives, and our current society would not have existed without them. They come in many forms, either synthetically or biologically, and have one thing in common: they are made of small repeating units, called monomers, to form a larger structure or chain. As the units are all covalently connected, a polymer is basically a very large molecule, which is commonly referred to as a macromolecule.

Many types of polymers can be found in nature. For example, proteins and DNA are examples of biological polymers that are essential to sustain life. Other well-known biological polymers are, for example, cellulose (gives strength to plants), chitin (protective shell of insects), and (spider) silk.

The term polymer is however more commonly used to refer to synthetic materials (plastics). Since the concept of synthetic polymers was first introduced by Hermann Staudinger in 1920,[1] the field of polymer chemistry and physics has rapidly developed up to the point where we can nowadays no longer live without them. Some of the most notorious examples of early synthetic polymers that are still of high relevance in current days include PVC (1926), polystyrene (1931) and nylon (1935).

Classically, synthetic polymers are commonly distinguished in two different types: thermoplastics and thermosets. These terms quite literally indicate how the material responds to heat. Thermoplastics become soft when heated, meaning that they will melt and are able to flow. Thermosets do not respond when heated: they are set and permanent. The difference for this heat response can be explained when looking at the chemical structure of the two different materials (Figure 1.1). Thermoplastics are long linear chains that have a spaghetti-like appearance. When heated, the polymer chains become malleable and can rearrange. Thermosets, on the other hand, are crosslinked. This means that the polymer chains are all covalently connected into a big network. When heated, they can therefore not rearrange, because they are physically locked from moving. In addition, the crosslinked network structure of a thermoset offers much greater physical strength to the material as the whole bulk is strongly bound together.

The superior strength and heat resistance of thermosets over thermoplastics offers much greater possibilities in terms of applications of the polymer materials. However, because the network structure of a thermoset is permanent, they have one big disadvantage: they cannot be recycled. Thermoplastics on the other hand can be recycled, because they can be

melted and reprocessed into a new material. Their flaw is however that they are not able to compete with the superior strength of thermosets. To make a single material that is both strong and recyclable, there is thus a need for something new and innovative.
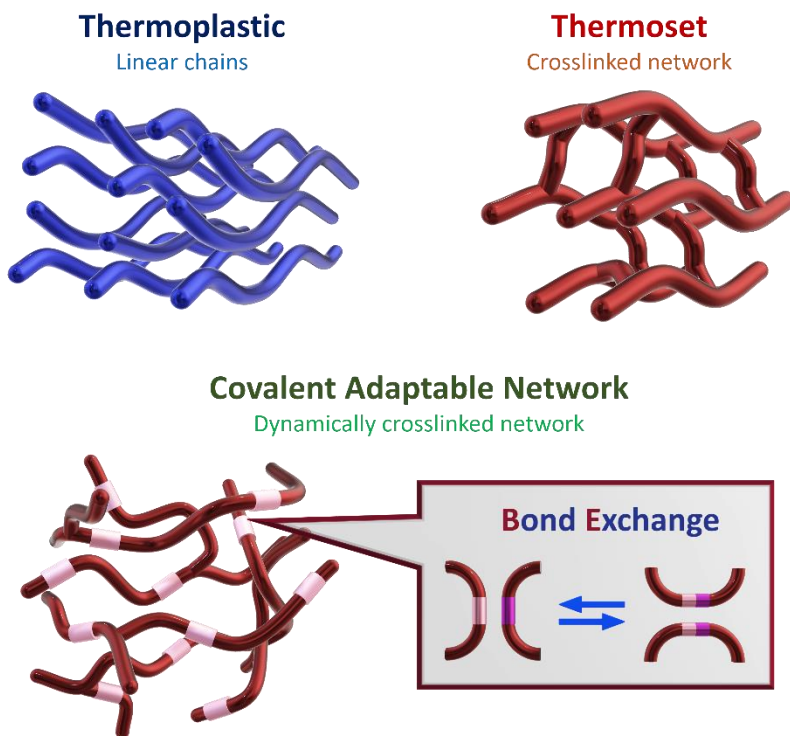
Figure 1.1 Visual representation of a thermoplastic (left) as linear chains, a thermoset (right) as crosslinked network structure, and a CAN (bottom) as a dynamically crosslinked network.

1.1.2   Covalent adaptable networks

The solution to overcome the problem of non-recyclable thermosets was presented by the development of covalent adaptable networks (CANs).[2, 3] Sometimes, they are also referred to as dynamic covalent (polymer) networks (DCNs/DCPNs),[4, 5] however, in this thesis we will use to the term "CAN". CANs are in essence similar to thermosets, as they have the same crosslinked network structure. There is, however, one major difference between CANs and traditional thermosets: CANs have dynamic covalent bonds within their structure (Figure 1.1). A dynamic covalent bond is a covalent bond, which means that it has the same strength as a conventional non-reversible covalent bond. What makes dynamic covalent

bonds unique, however, is their ability to perform bond exchange reactions under equilibrium control.[6] For CANs, this effectively means that within the polymer network rearrangements can occur as a result of such bond exchange reactions (see Figure 1.1). The bond exchange in CANs requires some form of activation (trigger),[7] which is generally achieved by heating. However, other ways of activating bond exchange, such as *via* light or pH, are known as well.[8, 9]

Many different types of dynamic bond exchange reactions are known, and have already been implied in different fields of (bio)chemical research.[6, 10, 11] Bond exchange reactions can be sub-divided in two categories: dissociative bond exchange and associative bond exchange (Figure 1.2).[12] For dissociative bond exchange, chemicals bonds are first broken and later reform into a new bond. This means that in a CAN, the network connectivity (crosslinking) is temporarily lost during bond exchange (Figure 1.2A). For associative bond exchange, a reactive group first attaches to the dynamic covalent bond before it is broken (Figure 1.2B). As such, a polymer network relying on associative bond exchange never loses its connectivity, and the crosslinking density remains constant.
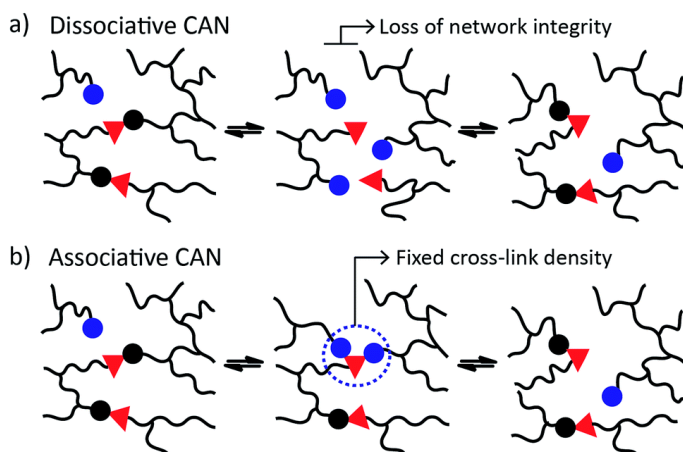
Figure 1.2 Visual representation of a dissociative CANs, loosing network integrity during bond exchange, and an associative CAN, in which the crosslinking density is fixed. Figure reproduced from Du Prez *et al.*, *Chem. Sci.* **2016**.[12]

A breakthrough for CANs occurred around 2012 when Leibler and co-workers documented on the introduction of dynamic covalent transesterification motifs in polymer networks to construct recyclable thermosets,[13-15] and introduced the term *vitrimer* to describe these new polymeric systems.[13] The term vitrimer refers to the Arrhenius-like gradual temperature dependence of the material's viscosity variations when nearing the glass

transition temperature (T_g), which is similar to that of vitreous silica.[15] As such, the materials behave similar to glass in terms of thermal properties. These works have inspired others to develop similar systems using different types of reversible chemistries. Some examples of other very promising approaches include the use of vinylogous urethanes,[16-18] dioxaborolanes,[19-24] disulfides,[25-28] and imines,[29-32] among many more.

1.1.3 Self-healing

CANs are most well known for their unique property to make recyclable thermosets, however, various studies have shown that they have many other desirable properties.[33, 34] As the dynamic covalent bonds are responsive to various stimuli, depending on the exact mode of exchange, they can be utilised to "program" polymers to respond or behave differently in different environments, or in response to certain stimuli. One of such unique features is the self-healing behaviour of CANS.[4] In a CAN, the dynamic covalent bonds are able to reattach severed parts of material through bond exchange. For example, when a material is cut or scratched, the dynamic covalent groups on the edges of one side of the cut can interact and exchange with the dynamic covalent groups on the other side of the cut.[26] As such, they can reattach the two sides back together (Figure 1.3).[25] This self-healing behaviour is what makes CANs very interesting for applications that require long-lasting materials or applications in which frequent (small) damages cause wear of the materials.
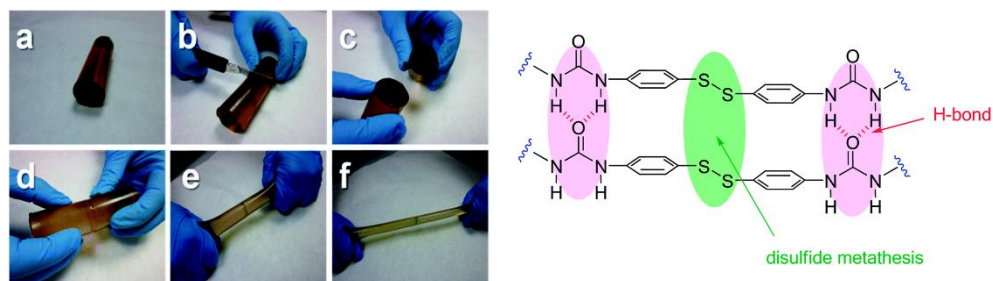
Figure 1.3 Example of a self-healing disulfide-based CAN. Image adapted from Odriozola *et al*. *Mater. Horiz.* **2014**.[25]

1.2 Material properties and analysis of CANs

Many of the material properties of CANs can be analysed an studied, in which the use of rheology plays a central role.[35] Traditionally, rheology is a branch of physics that studies the deformation and flow of materials. Nowadays it is a rather broad field of science that studies

many more characteristics of materials and mixtures.[36] For CANs specifically, rheology is mainly used to derive physical parameters regarding the thermal-mechanical properties of the materials, as well as study the underlying kinetics. In the following paragraphs, several typical types of measurements and analyses for CANs will be discussed, for which rheology is used. In addition, some alternative methods for analysis and additional features of CANs are discussed.

1.2.1   Storage and loss modulus

The storage (G') and loss (G'') modulus are two important physical parameters for viscoelastic materials, such as CANs. A viscoelastic material is a material that shows both solid- and liquid-like behaviour. The solid-like (elastic) component is expressed as the storage modulus (G'), and the liquid-like (viscous) component is expressed as the loss modulus (G''). When the storage modulus is higher than the loss modulus, the material behaves mostly as a solid. *Vice versa*, when the loss modulus is higher than the storage modulus, the material shows mostly characteristics of a liquid.

A typical experiment to analyse these solid and liquid characteristics of CANs is by performance of frequency sweep experiments. A piece of material is then placed between two plates, and the top plate will rotate slightly in an oscillating motion (see Figure 1.4 for a general rheological setup). In a frequency sweep experiment, the frequency of the oscillation is varied and the G' and G'' can be followed as a function of the frequency. From these experiments we can see how materials behave when exposed to either rapid or slow deformations. Very fast deformations (high frequency) usually give a stiff/elastic response (solid-like behaviour), whereas for slow deformation (low frequency) the materials flow more easily (liquid-like behaviour).
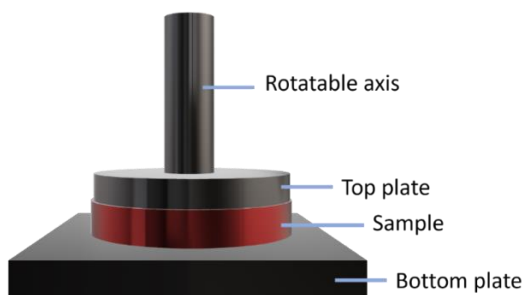

Figure 1.4 General rheology setup for a plate-plate configuration. The parts of the rheometer are shown in black, whereas the sample is shown in red.

When performing frequency sweep experiments for CANs, we can derive another important characteristic: namely whether their crosslinking density remains constant at elevated temperatures. The constant crosslinking density is one of the typical requirements of an associative CAN that define it as being a vitrimer (see Section 1.1.2).[12, 37] For dissociative CANs, crosslinks are broken when heated, which means that the crosslinking density decreases at elevated temperatures.[38, 39] In a frequency sweep experiment, the presence of a constant or dropping crosslinking density can be shown by following the storage modulus as a function of the frequency (see Figure 1.5).[40] When the frequency sweep is performed at different temperatures, a rubbery plateau should be visible for which the *G'* remains constant (typical vitrimer-like behaviour). If the rubbery plateau does not remain constant at elevated temperatures, this is an indication that the crosslinking density decreased (typical for dissociative CANs). Examples have however shown that some dissociative CANs can still show vitrimer-like behaviour, depending on the reaction rate and equilibrium constant of the bond exchange reaction.[41]
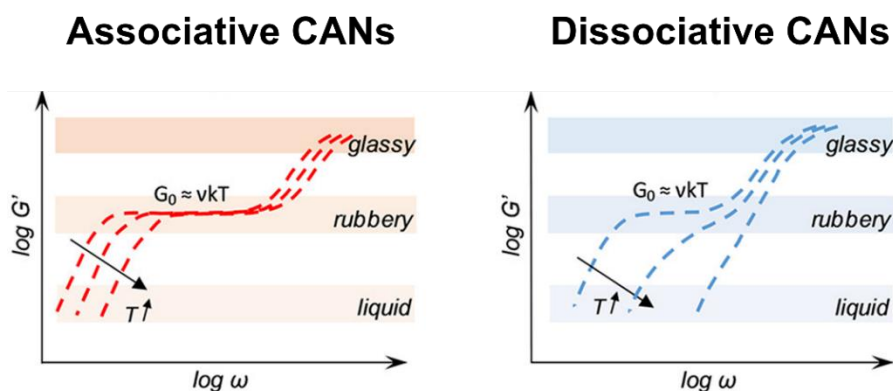
Figure 1.5 Example of a frequency sweep experiments performed at several different temperatures, for which the storage modulus is plotted as a function of the frequency. For associative CANs (left), a constant rubbery plateau is observed. For dissociative CANs (right), the rubbery plateau is typically lost at elevated temperatures. Figure adapted from Montarnal *et al*. *Macromolecules* **2020**.[40]

1.2.2 Temperature dependent measurements and phase transitions

When performing temperature-dependent measurements, information can be derived on the phase transitions of materials. Typically, two phase transitions are of major importance for CANs: the transition from a glassy to rubbery state, and the transition from the rubbery to a viscous state. A third transition temperature –the topology freezing temperature (T_v)–

is also commonly reported. The T_v defines the minimal required temperature for bond exchange reactions to occur.[14] Below T_v the network topology is frozen,[42] and as such, the CAN can be considered as a classical non-dynamic thermoset. The T_v can be derived from extrapolation of stress relaxation data (see Section 1.2.3) or with the use of dilatometry.[12]

The temperature at which the transition from glass to rubber phase occurs is generally referred to as the glass transition temperature (T_g). The point in temperature at which the material transitions from a rubbery to a viscous state is less clearly defined in literature. For dissociative CANs, this point is commonly referred to as the gel point temperature (T_{gel}),[2, 3, 43] as here the dynamic crosslinks dissociate and the network falls apart (*i.e.*, it becomes a gel). Associative CANs can however show a similar transition at which the viscous component (G'') overtakes the elastic component (G'), without observing dissociation of the network. Instead, the rate of bond exchange becomes so high that deformations of the material are being compensated *via* relaxation, faster than the rate of deformation. In other words, the malleability of the material is a function of the reaction rate of the bond exchange.[44] As such, the material can appear liquid-like even though it is still crosslinked. This phase transition is therefore technically not an actual gelation or melting process. To describe this transition point, in this thesis the term crossover temperature (T_{cross}) will be used, as it describes the temperature at which the viscous en elastic moduli cross ($G' = G''$).[45]

To determine the T_g and T_{cross} with the use of rheology, temperature sweep experiments are typically performed. A similar rheological setup as before is used (see Figure 1.4), but now a constant frequency (generally 1 Hz) is applied, while (slowly) heating (or cooling) the material. This time the G' and G'' are plotted as a function of the temperature (An example is shown in Figure 1.6). Commonly, also the damping factor ($\tan(\delta) = G'' / G'$) is plotted in the same figure, which helps in the determination of T_g and T_{cross}. Instead of oscillatory rheology, dynamic mechanical analysis (DMA) can also be performed. The main difference is the physical setup of the machine. With DMA, also a deformation is applied, however, this deformation is axial. This means that the sample is being stretched vertically instead of the rotational movement we discussed before. The data can typically be plotted in a similar fashion as for the rotational rheology to derive information, for example regarding the glass transition temperature.

From the temperature sweep curves, the T_g can be determined at the temperature at which a steep increase in dynamic moduli is observed as a result of the glass transition from rubber to glass when cooling the material (*i.e.*, when going from right to left in the curve shown in Figure 1.6). It can however be more accurately determined from the peak in the $\tan(\delta)$ curve (see the black line in Figure 1.7).[30] In this thesis, such rheological analysis is generally

performed to determine the T_g. In literature, other techniques, such as differential scanning calorimetry (DSC), are also reported to determine the T_g.[46-48] The obtained T_g values from different methods are generally in relatively good agreement, but it is still important to always document which technique is used for proper comparison. For determination of the rubber to viscous phase transition, typically a drop in dynamic moduli is observed when going to higher temperatures. The exact point of this transition (in this thesis referred to as T_{cross}) is determined where G' and G'' cross (*i.e.*, when tan(δ) = 1), as this is the temperature from which the loss modulus overtakes the storage modulus.[49]
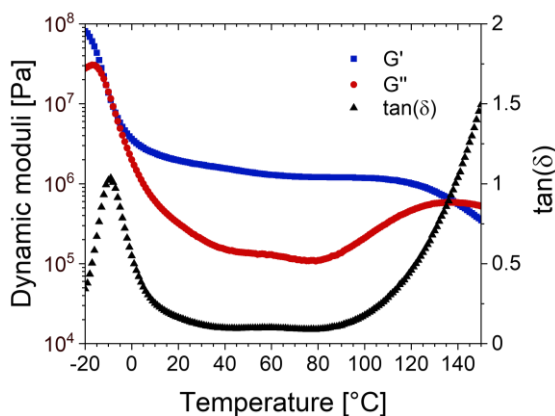

Figure 1.6 Example of a temperature sweep experiment. G' (blue), G'' (red), and tan(δ) (black) are plotted as a function of the temperature. The T_g can be derived from the top of the tan(δ) curve (here at −9 °C), and the T_{cross} can be derived from the point where tan(δ) = 1 (here at 140 °C).

1.2.3 Stress relaxation and kinetic activation energy

As a results of the exchangeable bonds in CANs, they are able to release stress when a deformation is applied to the material.[39] In other words, when a CAN is deformed (a stress is applied) it first resists the deformation, but over time the polymer network will rearrange to compensate for the deformation.[7] This stress relaxation can be studied with rheology as well. Using the previously shown rheology setup (Figure 1.4), a deformation is made by rotation of the axis by a chosen angle that is known to be in the linear response region of the material. The rheometer can then measure the relaxation modulus ($G(t)$) over time, expressing to what degree the material resists the deformation. When a material is able to relax stress, it can be seen by a decrease in the $G(t)$ over time. When $G(t) = 0$, all stress has relaxed and the material no longer expresses any resistance (*i.e.*, a new steady state is reached).[50]

As the stress relaxation is caused by bond exchange reactions, and the kinetics of these bond exchange reactions are temperature-dependent, the stress relaxation of the material is also temperature-dependent.[4] Performing stress relaxation experiments at different temperatures can then give more information on the required energy of rearrangements as a result of the bond exchange. This energy is commonly referred to as the (kinetic) activation energy (E_a). The E_a can be derived from Arrhenius plots that follow from the stress relaxation experiments (Figure 1.7A shows an example of such stress relaxation curves at various temperatures).[51] First, the relaxation time (τ) is determined for each temperature at the point where the normalised relaxation (G/G_0) = 1/e, according to the general Maxwell model for stress relaxation. Then, $\ln(\tau)$ is plotted as a function of $1/T$ (Figure 1.7B). Following the vitrimer terminology,[15] this should give a linear line, indicating that the relaxation follows the Arrhenius law with temperature.[14] The E_a can then be determined as the slope of the fitted line multiplied by the gas constant (R = 8.314). The higher this E_a is, the more energy is required in order to activate efficient bond exchange. High E_a can be favourable if applications require a material that remains tough at (slightly) elevated temperatures, but low E_a materials can be favourable for applications that require fast relaxation or easy reprocessability. An alternative method to calculate E_a describes the use of frequency sweep experiments (see Section 1.2.1), in which the determination of the crossover frequency (when G' = G'') at different temperatures is used.[52] In this thesis, we will however focus on the use of stress relaxation experiments for the calculation of E_a.
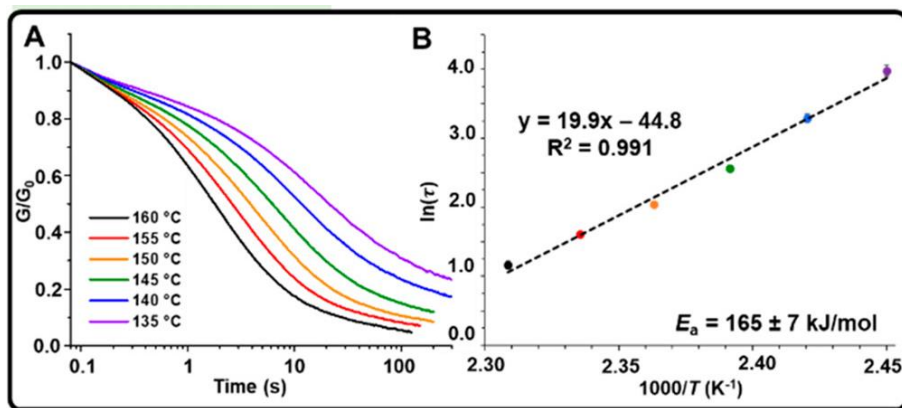

Figure 1.7 A) Normalised stress relaxation curves of a CAN at different temperatures. B) Arrhenius plot that follows from the relaxation times. The fit shows a linear trend, indicating that the material shows Arrhenius-type relaxation. Image adapted from Sumerlin *et al. ACS Appl. Polym. Mater*. **2020**.[51]

1.3   Imines

1.3.1   Mechanisms of imine and exchange

To narrow the focus to one type of dynamic covalent system, in this thesis, we will mainly focus on the applications of reversible imine chemistry. The imine (in some cases also referred to as Schiff base)[53] is a well-known functional group in the field of organic chemistry and biology.[54-57] Imines are generally synthesised *via* a condensation reaction between an aldehyde (or ketone) and an amine (Figure 1.8A). During the reaction, water is released. The imine condensation reaction is reversible, which means that the imine can be hydrolysed back to aldehyde an amine if water remains present. Water can be removed to prevent the reverse reaction. However, the imine can also be designed in such a way that it is stable enough not to fall apart again (*i.e.*, the equilibrium is pushed entirely towards the imine). This can, for example, be achieved *via* aromatic conjugation.[32]
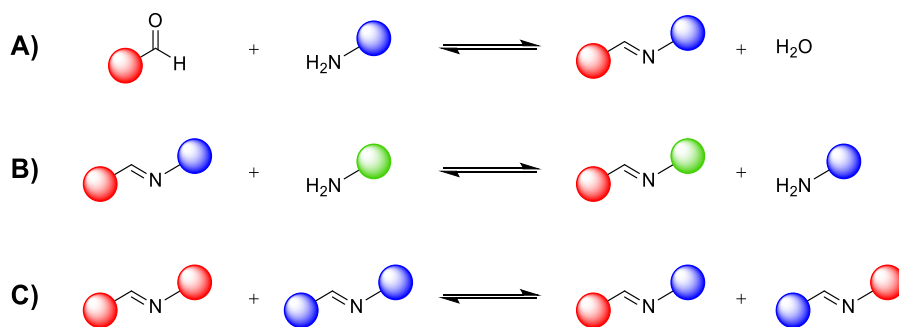
Figure 1.8 Schematic overview for the formation of an imine from an aldehyde and amine.

The reversible reaction of imine condensation and hydrolysis is only one of three possible reversible reactions that imines can undergo. The second is an exchange reaction that occurs when a primary amine reacts with the amine, and is called transimination (Figure 1.8B).[58] This exchange reaction occurs rapidly and spontaneously at room temperature when an excess of amine is added with the aldehyde during the synthesis, or when additional amines are later added to the formed imine.[59, 60]

The third exchange reaction of imines occurs between imines themselves, and is called imine metathesis (Figure 1.8C). Many speculations have been made on the exact mechanism of this exchange,[61-63] but the general concept prescribes that once two imines

come close, they can exchange their end groups. Specifically for aromatically bonded imines, Zhang and co-workers revealed that free radical intermediates were found to be involved in the non-equilibrium stage.[32] Their assumption for the presence of free radicals was raised from the applications of imines as antioxidants and flame retardants,[64] in which the imines often act as radical scavengers. Using electro spin resonance (ESR) spectroscopy, they could conclude that free radicals indeed appear during the imine exchange reaction. It was, however, also noted that the exchange reaction was still able to proceed in the absence of free radicals. A possible elaborated reaction mechanism of the imine metathesis was therefore presented (Figure 1.9). Note that in this study imines were used for which both amine and aldehyde ends were aryl-linked. Therefore, a conjugated imine-aryl system is formed in which π electrons are delocalised across all adjacent aligned p-orbitals. Electronic effects of substituents on the aromatic rings may, therefore, influence the distribution of the electronic clouds in the imine bond, leading to variations in reactivity.[65]
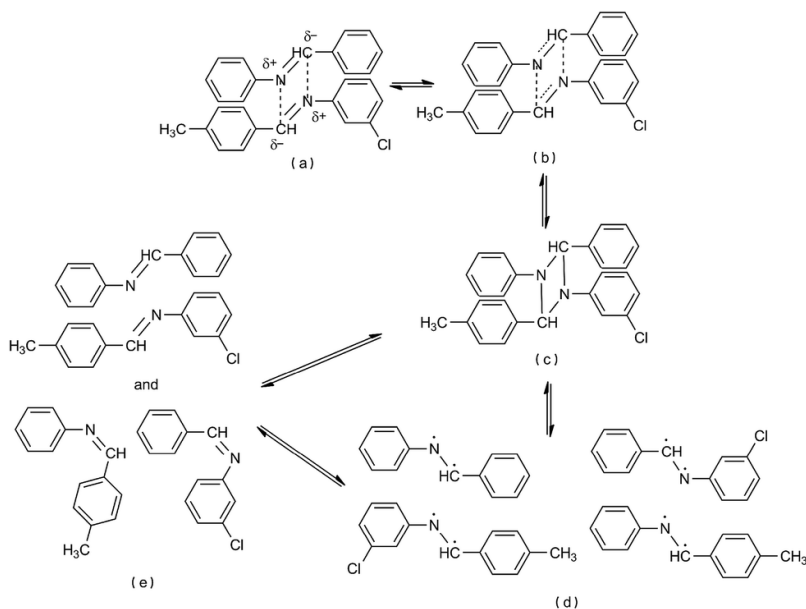

Figure 1.9 Mechanism of the radical mediated imine metathesis of aromatically linked imines, as documented by Zhang *et al.*, *J. Mater. Chem. A* **2015**.[32]

1.3.2   Imine-based CANs

Constructing an imine polymer (generally referred to as a polyimine) requires both amine and aldehyde monomers. When constructing a polymer network, a crosslinker is also

required. This crosslinker usually is a multivalent monomer with three or more functional groups. Most early works on polyimine CANs describe the use both a dialdehyde and diamine, and an additional crosslinker unit, which is typically a triamine.[66, 67] However, other examples have been reported as well.[68-73] Early studies on polyimines commonly showed a network composition in which terephthalaldehyde (**TA**) was used was as dialdehyde monomer, *tris*(2-aminoethyl)amine (**TREN**) was used as a triamine crosslinker, and a variable linear diamine was added to fine-tune the network composition (a classical example by Taynton *et al*. is shown in Figure 1.10). Zhang, Taynton, and co-workers have constructed several of such polyimine materials on this basis,[29, 30, 44, 74] and others have followed from their designs.[31, 75-80] Along the way, many adjustments have been made to these designs, covering a wide range of different materials with their own unique properties. Other studies also include the synthesis of polyimines from a trifunctional aldehyde (*e.g.*, triformylbenzene) and a (long, aliphatic) diamine.[62, 81]
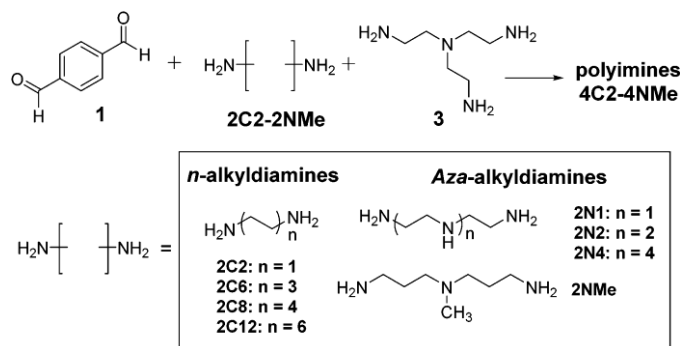
Figure 1.10 Synthetic overview for the preparation of polyimine CANs using terephthalaldehyde (**1**), a variable diamine (**2**), and TREN (**3**) as the crosslinker, as documented by Taynton *et al*., *Polym. Chem.* **2016**.[30]

A different technique to construct polyimine networks is by first synthesising (non-dynamic) polymer chains, and later crosslinking them with dynamic covalent imine bonds.[32, 82-85] For example, He *et al*. started from linear polyolefins that were functionalised with aldehyde groups in the chain, to which a triamine crosslinker was added to construct a dynamic covalent network (Figure 1.11).[83] The other way around, linear chains with amine functionalities can also be dynamically crosslinked by addition of aldehydes.[45, 86, 87] Alternatively, it is also possible to first synthesise linear imine chains, which can be later crosslinked *via* another reaction type. This was for example done by Mo *et al*., who first synthesised linear polyimines and crosslinked them in a second step by addition of epoxy resin.[88]

Figure 1.11 Synthesis of a polyimine network by dynamic crosslinking of functionalised linear polymers, as documented by He *et al*., *Polymer* **2021**.[83]

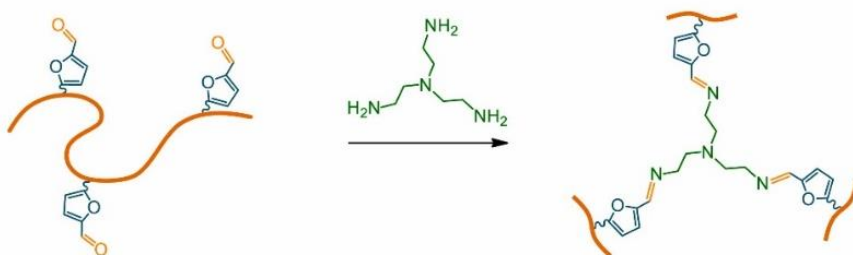It has also been shown that imine and epoxy reactions are combined in one step, or following directly after each other to synthesise the polymer network.[89-97] In a similar fashion, this has also been studied for the synthesis of imine-incorporated polyurethanes.[98, 99] These examples show that the incorporation of dynamic covalent imine bonds in existing materials can be performed to make recyclable thermosets close to the original design of established materials in industry.

1.4   Tuneability and Control of Material Properties

Designing materials for different applications and purposes requires adequate tuneability of material properties.[100, 101] For example, some applications require very stiff materials, whereas others require elasticity. For classical polymers (either thermoplastics or thermosets), their material properties rely on many different factors, such as the chemical composition of the polymer, addition of (functional) side chains / branching, or the crosslinking density. For CANs such factors apply as well. However, the dynamic covalent bonds in CANs also affect the material properties by a large part, as the molecular exchange dynamics can be directly linked to various macroscopic material properties.[9, 102-104]

In this thesis, the main focus will be on how to tune –and ultimately control– the material properties of imine-based CANs from a molecular perspective. In the research chapters that follow later, several strategies will be discussed that were applied to gain insights in the dynamics of the imine exchange, and how they correlate to the macroscopic material properties of the polymers. Other very promising techniques to tune material properties of

CANs have been documented in literature as well,[9, 104-109] and many have served as a source of inspiration for the work discussed in this thesis. Some important examples of (molecular-level) strategies for controlling material properties of CANs will be discussed below.

1.4.1   Crosslinking density

Just as for conventional thermosets, the crosslinking density is an important characteristic parameter to tune material properties of CANs. When a material has a high crosslinking density, the chains are highly interconnected and flexibility is low. As a result, the material is generally stiffer and more brittle. A lower crosslinking density results in more flexibility of polymer chains and generally gives rise to more elastic materials. Very low crosslinking densities can however significantly reduce the strength of the material.[88]
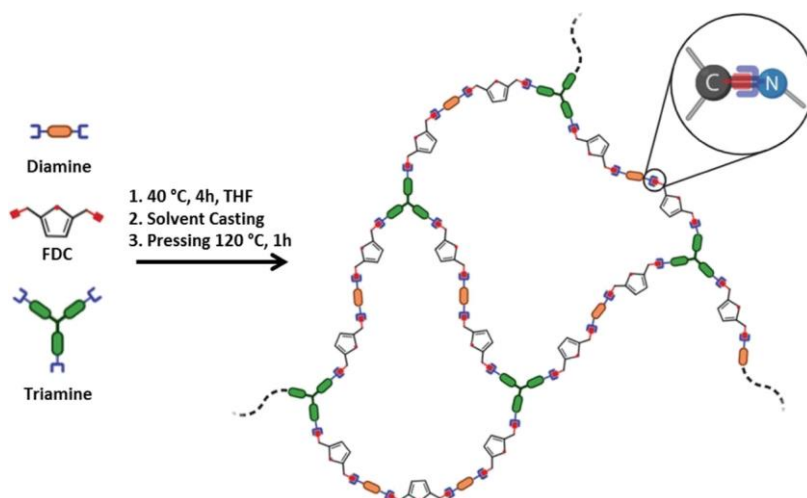
Figure 1.12 General overview for the synthesis of polyimine networks, as documented by Avérous *et al*. By varying the length of the diamine monomer, or by changing the triamine:diamine ratio, the crosslinking density could be adjusted, resulting in tuneable material properties. Image adapted from Avérous *et al*., *Macromolecules* **2020**.[110]

Investigations with regards to the crosslinking density in polyimine CANs were nicely described in recent work by Avérous and co-workers.[110] They synthesised polyimines from 2,5-furandicarboxaldehyde (FDC) and a combination of di- and trifunctional polyetheramines (Figure 1.12). The crosslinking density could be controlled in two ways: by the length of the diamine monomer chains, and by the ratio between di- and triamine monomers. First, by increasing the length of the diamine monomer, the space between crosslinks became greater, leading to a lower crosslinking density. Increasing the

diamine:triamine ratio in favour of the diamine had a similar effect. Only the triamine monomer facilitated crosslinking, whereas the diamines formed linear chains. When less triamine monomers were present, the total amount of crosslinks therefore also decreased. The work by Avérous and co-workers shows that tuneability of crosslinking density *via* either of the two strategies resulted in characteristic materials with unique properties. They were able to show that decreasing the crosslinking density reduced the glass transition temperature, relaxation time and kinetic activation energy of the materials. Thermographic analysis (TGA), however, showed that all materials had a similar decomposition temperature, suggesting that the thermal decomposition mechanism is independent from the composition of the network.

Recent work by Osswald and co-workers showed that the crosslinking density may also affect the crystallinity of the poly(ethylene) networks, crosslinked with dynamic covalent disulfide bonds.[111] They observed that a higher degree of crosslinked inhibited the growth of crystalline structures, leading to a decrease in yield strength and creep resistance. This observation was important to note, as generally a higher crosslinking density would result in increased toughness of the materials. Maintaining the crystalline structure was thus considered more important than an increased crosslinking density when high material strength is desired.

1.4.2   Concentration of dynamic covalent bonds

As mentioned in the previous section, longer monomers decrease crosslinking density, however, the concentration of dynamic covalent bonds also decreases (*i.e.*, lower ratio of dynamic : static bonds), which lowers overall bond exchange. Simply changing to a longer monomer to decrease crosslinking density is therefore not always feasible, as this could result in loss of bond exchange potential. As such, it can be more feasible to add an increased amount of short difunctional monomers (effectively lowering the concentration of trifunctional monomers) rather than extend the length of the existing monomers.

Investigations on the concentration of dynamic covalent bonds in poly(alkylurea-*co*-urethane) CANs were performed by Rowan and-coworkers.[112] They synthesised networks bearing both dynamic covalent alkylurea bonds and non-dynamic urethane bonds. By varying the ratio between dynamic and non-dynamic bonds, they were able to show that a minimum of 50% of dynamic covalent alkylurea was required in order to facilitate efficient reprocessability. When the concentration of dynamic covalent bonds became too low, the material thus lost its potential for efficient recycling due to the lack of bond exchange reactions in the material.

1.4.3   Chemical nature of the polymer network

Apart from varying the crosslinking density, other alterations to the polymer network can be made.[47, 113] For example, work by Taynton *et al*. compared the use of hydrophobic aliphatic chains *versus* hydrophilic and hydrogen-bonding amine-containing chains in polyimine CANs.[30] Their results showed that the hydrophilic hydrogen-bonding chains greatly induced the moisture sensitivity of the materials, as well as alter the thermal and mechanical properties. Another example by Liu *et al*. elaborates on the introduction of aliphatic side chains in epoxy-based CANs, relying on transesterification exchange.[114] The addition of such flexible side chains can promote segmental movement, and as such enhance the probability of dynamic covalent groups to find each other and perform bond exchange reactions. In addition, the introduction of the pendant aliphatic chains could be utilised to tune either flexibility or crystallinity as a result of the chain length dependant crystallisation of the side chains.

1.4.4   Kinetic control of bond exchange *via* steric effects

The material properties of CANs can for a large part be related to the dynamic of the bond exchange reaction. As such, control over the kinetics of the bond exchange can serve as a tuneable handle for moderating the material properties.

An elegant way of tuning the dynamicity of dynamic covalent bonds in poly(alkylurea-urethane) CANs was described by Zhang and Rowan, who investigated the role of steric bulk as a part of the hindered alkyl area moiety (Figure 1.13).[115] Their results showed that increased steric bulk increased the temperature sensitivity of the materials, resulting in an acceleration in network relaxation when increasing the temperature. This trend was then also observed in the topology freezing transition temperature (T_v) and kinetic activation energy (E_a), suggesting that the steric bulkiness can be used as a tuneable, molecular handle to control material properties.
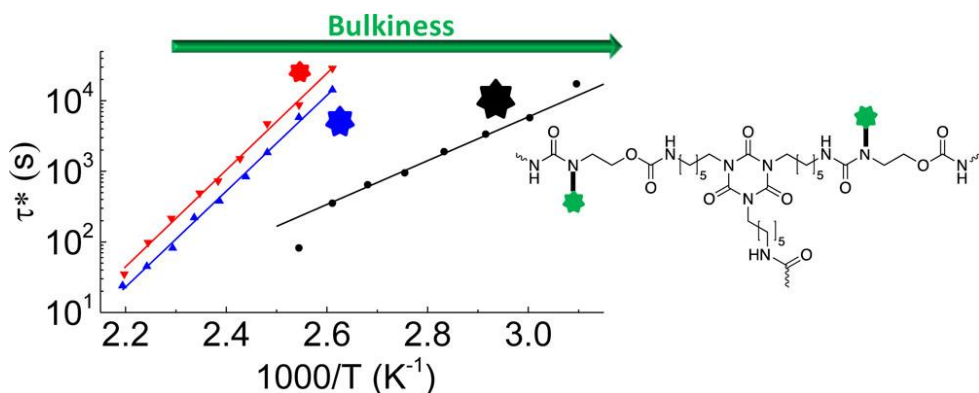
Figure 1.13 Increasing or decreasing the steric bulk on hindered alkylureas enables tuneability of material properties of the CAN. The red star represents an ethyl group, the blue star an *iso*-propyl group, and black a *tert*-butyl group. Image adapted from Rowan *et al*. *Macromolecules* **2017**.[115]

1.4.5   Kinetic control of bond exchange *via* electronic effects

Another efficient way to control the kinetics of bond exchange reactions is *via* electronic effects. More specifically, pushing or pulling of electrons away from the dynamic bond can either activate or deactivate the dynamic covalent bond. Such effects can either affect the thermodynamics (*e.g.*, to prevent dissociation as a result of an equilibrium shift) and/or the kinetics (*e.g.* lower energy barrier to accelerate bond exchange reactions).

As a recent example, Ladmiral and co-workers introduced strongly electron-withdrawing fluorinated groups adjacent to ester groups, activating the esters to perform transesterification reactions without the requirement of a catalyst.[116] Further tuneability *via* electronic effects was discussed by Du Prez and co-workers, who studied the development of thiol-yne-based CANs with tuneable exchange rates relying on electronic effects near the thioacetal crosslinks (Figure 1.14).[117] Exchange rates could be varied over several orders of magnitude based on the steric and electronic nature of the alkyne crosslinker. They observed that electron-withdrawing groups caused faster bond exchange, while electron-donating groups slowed down the bond exchange. In the polymer materials, these translated to either faster or slower relaxation, respectively. Kalow and co-workers also developed a similar study for PDMS CANs relying on dynamic thiol-ene exchange.[118] The stress relaxation of the polymers correlated nicely to differences in the $\Delta G^{\ddagger}$ of the exchange reaction, as a result of electronic effects present in the dynamic crosslinkers. These works thus described nicely how to tune and predict macroscopic material properties *via* control on the molecular level.
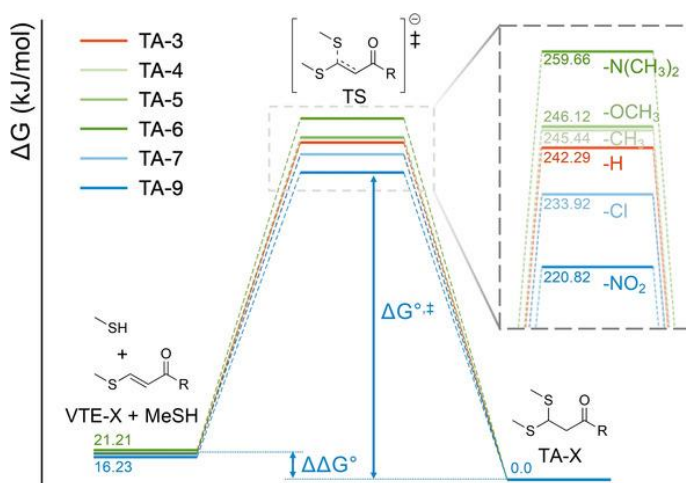
Figure 1.14 DFT results for the differences in Δ*G* of the reversible thiol-Michael bond exchange reaction with different electronic substituents, as documented by Du Prez *et al. Angew. Chem. Int. Ed.* **2020**.[117]

1.4.6   Combining different dynamic chemistries

Rather than sticking to one type of dynamic covalent bond, two or more types of dynamic covalent bonds can be incorporated within the same material (given that the two chemistries are compatible and do not interfere).[119-122] Each dynamic bond would have its own characteristic properties, and as such, the material would have a multi-stimuli response.[123, 124] Additionally, increasing the dynamic covalent bond multiplicity could cause synergistic effects between the different exchange mechanisms.[125, 126] An example of such synergism from the combination of dissociative Diels-Alders and associative imine exchange was documented by Ma *et al.*[123] Although imines are generally known to perform bond exchange at relatively low temperatures, the crosslinked network structure in a CAN may still supress diffusion of reactive imine groups through the bulk.[127] However, the addition of Diels-Alders groups enables (partial) dissociation of the network structure upon heating of the material, and thereby freeing the imines. As a result, the imine exchange becomes more prominent, resulting in a significant acceleration of rearrangements and realising rapid reprocessability.[123] It is also possible to combine the use of dynamic covalent bonds with other dynamic non-covalent supramolecule bonds/interactions, such as hydrogen bonding or metal-coordination.[128-132] Such supramolecular bonds or interactions generally require less energy to activate or break, facilitating a lower barrier for rapid bond exchange.[7, 9, 102]
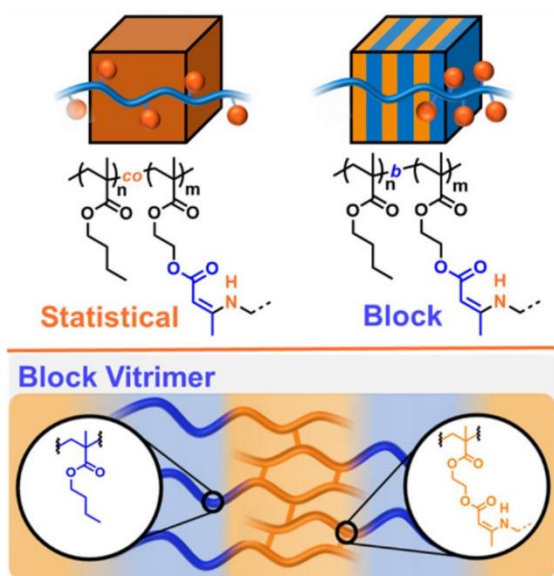
1.4.7   Phase separation

Phase separation in a widely known tool in materials science for structuring and imparting functionalities within polymeric materials.[133, 134]   Phase separation relies on the spontaneous process of polymer chains to segregate from a mixture into separated areas (domains) with higher local concentrations of specific functionalities with clear borders between the different domains.[135] In polymers, phase separation is often applied to enhance mechanical strength, to facilitate order on a wide range of different length scales, or to add localised functionalities to the material.[136]

Several studies to induce phase separation in CANs to enhance their material properties have been reported as well.[137-139] For example, Sumerlin and co-workers described the synthesis of block copolymer vitrimers to induce phase separation (Figure 1.15).[140] They prepared block copolymers with one block containing dynamic covalent vinylogous urethane crosslinks, and one block without these dynamic groups. They compared the block copolymer with a statistical polymer with the same groups, but then randomly distributed, and concluded that the block copolymer exhibited significantly higher strength as a result of the self-assembly into phase-separated domains. Other works on the use of block copolymers for construction of phase-separated CANs showed similar outcomes in which the phase separation caused enhanced material performance,[141-143] concluding that this is an efficient technique for improvement and control of material properties.

Another technique to induce phase separation in CANs is by grafting dynamic covalent groups onto polymer chains that have incompatible chemical properties. As an example, in work by Ricarte and co-workers, dynamic dioxaborolane functional groups were (randomly) grafted onto polyethylene (PE) chains, and they observed graft-poor and graft-rich parts in the polymers. As the borolane units are technically incompatible to the PE chains, they cluster together and the polymers segregate into domains with graft-poor (high PE content) and graft-rich (high borolane content) parts.[144] This way, local areas with either higher or lower dynamicity were formed. Later works on such materials also studied how the grafting and phase separation decelerated the dynamics of the individual polymer chains,[145] or how the degree of grafting affected the nano- and macrostructure,[146] dictating the thermal mechanical properties of the materials.

A) Polymer Structure

B) AFM images
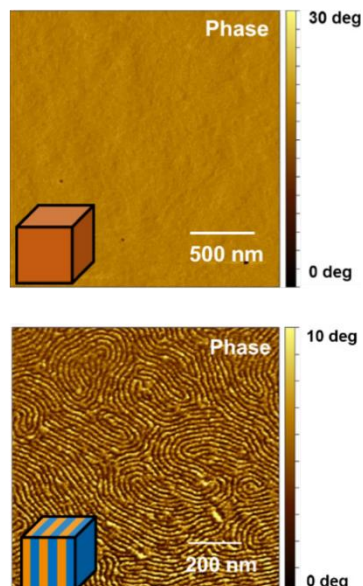
Figure 1.15 A) Depiction of a statistical and block-copolymer vitrimer, and general phase-separated structure of the block-copolymers. B) AFM images of the materials. Figure adapted from Sumerlin *et al.*, *J. Am. Chem. Soc.* **2020**.[140]

1.5 Thesis outline

In **Chapter 2** it is presented how material properties of polyimine CANs can be tuned *via* electronic effects, as expressed by the Hammett equation. From a selection of different dianiline monomers, distinct correlations were observed between the Hammett parameter, operating at the molecular level, to various thermal-mechanical properties of the materials on the macroscopic level.

In **Chapter 3**, a further investigation is discussed on how phase separation in polyimine materials was triggered as a result of inter-chain aromatic interactions between the dianiline moieties, and how phase separation can be used to alter and improve material properties. Additionally, Raman imaging is introduced as an efficient tool to visualise phase separation in CANs.

In **Chapter 4**, the effects of network polarity in imine-based CANs are investigated. It is shown how alterations in the network structure not only affect the dynamicity of the network itself, but also significantly influence the bond exchange kinetics of the dynamic covalent imine groups.

In **Chapter 5**, the use of metal-coordination to imines is discussed as an efficient tool to arrest the highly dynamic imine groups, in order to prevent creep and enhance material properties. In addition, it is reported how different metal ions or anions could be used to tune and control the material properties.

In **Chapter 6**, internal hydrogen bonding to the imines is discussed as a means to suppress the high dynamicity of the imines, to prevent high bond exchange rates that cause creep of the material. It is demonstrated that the additional stability as a result of the internal hydrogen bonding leads to materials with enhanced material properties and significantly higher creep resistance.

In **Chapter 7**, a study is presented how (imine-based) CANs respond to solvents. It is discussed how CANs can be designed with high solvent resistance for applications that require robust materials, but also how CANs can be designed that are soluble in good solvents in order to facilitate chemical recycling or enable post-synthetic functionalisation.

In **Chapter 8**, all results from the previously discussed chapters will be discussed in a broader context. They will be related back to the initial research question on how molecular level control can be utilised as a tool to tune macroscopic material properties of CANs. Additionally, an outlook is provided on the future of CANs and their potential applications.

References

1. H. Staudinger, *Berichte der deutschen chemischen Gesellschaft (A and B Series)*, 1920, **53**, 1073-1085.
2. C. J. Kloxin and C. N. Bowman, *Chem. Soc. Rev.*, 2013, **42**, 7161-7173.
3. C. J. Kloxin, T. F. Scott, B. J. Adzima and C. N. Bowman, *Macromolecules*, 2010, **43**, 2643-2653.
4. N. Zheng, Y. Xu, Q. Zhao and T. Xie, *Chem. Rev.*, 2021, **121**, 1716-1745.
5. W. Zou, J. Dong, Y. Luo, Q. Zhao and T. Xie, *Adv. Mater.*, 2017, **29**, 1606100.
6. S. J. Rowan, S. J. Cantrill, G. R. L. Cousins, J. K. M. Sanders and J. F. Stoddart, *Angew. Chem. Int. Ed.*, 2002, **41**, 898-952.
7. M. J. Webber and M. W. Tibbitt, *Nat. Rev. Mater.*, 2022, **7**, 541-556.
8. X.-L. Zhao, P.-X. Tian, Y.-D. Li and J.-B. Zeng, *Green Chem.*, 2022, **24**, 4363-4387.

9. S. V. Wanasinghe, O. J. Dodo and D. Konkolewicz, *Angew. Chem. Int. Ed.*, 2022, **n/a**, e202206938.
10. A. Herrmann, *Chem. Soc. Rev.*, 2014, **43**, 1899-1933.
11. P. T. Corbett, J. Leclaire, L. Vial, K. R. West, J.-L. Wietor, J. K. M. Sanders and S. Otto, *Chem. Rev.*, 2006, **106**, 3652-3711.
12. W. Denissen, J. M. Winne and F. E. Du Prez, *Chem. Sci.*, 2016, **7**, 30-38.
13. M. Capelot, D. Montarnal, F. Tournilhac and L. Leibler, *J. Am. Chem. Soc.*, 2012, **134**, 7664-7667.
14. M. Capelot, M. M. Unterlass, F. Tournilhac and L. Leibler, *ACS Macro Lett.*, 2012, **1**, 789-792.
15. D. Montarnal, M. Capelot, F. Tournilhac and L. Leibler, *Science*, 2011, **334**, 965-968.
16. W. Denissen, G. Rivero, R. Nicolaÿ, L. Leibler, J. M. Winne and F. E. Du Prez, *Adv. Funct. Mater.*, 2015, **25**, 2451-2457.
17. W. Denissen, M. Droesbeke, R. Nicolaÿ, L. Leibler, J. M. Winne and F. E. Du Prez, *Nat. Commun.*, 2017, **8**, 14857.
18. S. Engelen, A. A. Wróblewska, K. De Bruycker, R. Aksakal, V. Ladmiral, S. Caillol and F. E. Du Prez, *Polym. Chem.*, 2022, **13**, 2665-2673.
19. M. Röttger, T. Domenech, R. van der Weegen, A. Breuillac, R. Nicolaÿ and L. Leibler, *Science*, 2017, **356**, 62-65.
20. O. R. Cromwell, J. Chung and Z. Guan, *J. Am. Chem. Soc.*, 2015, **137**, 6492-6495.
21. J. J. Cash, T. Kubo, A. P. Bapat and B. S. Sumerlin, *Macromolecules*, 2015, **48**, 2098-2106.
22. X. Zhang, S. Wang, Z. Jiang, Y. Li and X. Jing, *J. Am. Chem. Soc.*, 2020, **142**, 21852-21860.
23. J. Ma, Y. Yang, C. Valenzuela, X. Zhang, L. Wang and W. Feng, *Angew. Chem. Int. Ed.*, 2022, **n/a**, e202116219.
24. L. Porath, J. Huang, N. Ramlawi, M. Derkaloustian, R. H. Ewoldt and C. M. Evans, *Macromolecules*, 2022, **55**, 4450-4458.
25. A. Rekondo, R. Martin, A. Ruiz De Luzuriaga, G. Cabañero, H. J. Grande and I. Odriozola, *Mater. Horiz.*, 2014, **1**, 237-240.
26. I. Azcune and I. Odriozola, *Eur. Polym. J.*, 2016, **84**, 147-160.
27. A. Ruiz de Luzuriaga, R. Martin, N. Markaide, A. Rekondo, G. Cabañero, J. Rodríguez and I. Odriozola, *Mater. Horiz.*, 2016, **3**, 241-247.
28. A. Ruiz de Luzuriaga, J. M. Matxain, F. Ruipérez, R. Martin, J. M. Asua, G. Cabañero and I. Odriozola, *J. Mater. Chem. C*, 2016, **4**, 6220-6223.
29. P. Taynton, K. Yu, R. K. Shoemaker, Y. Jin, H. J. Qi and W. Zhang, *Adv. Mater.*, 2014, **26**, 3938-3942.
30. P. Taynton, C. Zhu, S. Loob, R. Shoemaker, J. Pritchard, Y. Jin and W. Zhang, *Polym. Chem.*, 2016, **7**, 7052-7056.
31. X. Lei, Y. Jin, H. Sun and W. Zhang, *J. Mater. Chem. A*, 2017, **5**, 21140-21145.
32. Z. Q. Lei, P. Xie, M. Z. Rong and M. Q. Zhang, *J. Mater. Chem. A*, 2015, **3**, 19662-19668.
33. Y. Wu, Y. Wei and Y. Ji, *Polym. Chem.*, 2020, **11**, 5297-5320.

34. M. Podgórski, B. D. Fairbanks, B. E. Kirkpatrick, M. McBride, A. Martinez, A. Dobson, N. J. Bongiardina and C. N. Bowman, *Adv. Mater.*, 2020, **32**, 1906876.
35. F. Meng, M. O. Saed and E. M. Terentjev, *Nat. Commun.*, 2022, **13**, 5753.
36. T. Mezger, *The Rheology Handbook*, Vincentz Network, Hannover, Germany, 2020.
37. N. J. Van Zee and R. Nicolaÿ, *Prog. Polym. Sci.*, 2020, **104**, 101233.
38. G. M. Scheutz, J. J. Lessard, M. B. Sims and B. S. Sumerlin, *J. Am. Chem. Soc.*, 2019, **141**, 16181-16196.
39. J. M. Winne, L. Leibler and F. E. Du Prez, *Polym. Chem.*, 2019, **10**, 6091-6108.
40. A. Jourdain, R. Asbai, O. Anaya, M. M. Chehimi, E. Drockenmuller and D. Montarnal, *Macromolecules*, 2020, **53**, 1884-1900.
41. B. R. Elling and W. R. Dichtel, *ACS Cent. Sci.*, 2020, **6**, 1488-1496.
42. Y. Jin, Z. Lei, P. Taynton, S. Huang and W. Zhang, *Matter*, 2019, **1**, 1456-1493.
43. W. Liu, S. Yang, L. Huang, J. Xu and N. Zhao, *Chem. Commun.*, 2022, **58**, 12399-12417.
44. P. Taynton, H. Ni, C. Zhu, K. Yu, S. Loob, Y. Jin, H. J. Qi and W. Zhang, *Adv. Mater.*, 2016, **28**, 2904-2909.
45. H. Zhang, D. Wang, W. Liu, P. Li, J. Liu, C. Liu, J. Zhang, N. Zhao and J. Xu, *J. Polym. Sci., Part A: Polym. Chem.*, 2017, **55**, 2011-2018.
46. A. M. Hubbard, Y. Ren, D. Konkolewicz, A. Sarvestani, C. R. Picu, G. S. Kedziora, A. Roy, V. Varshney and D. Nepal, *ACS Appl. Polym. Mater.*, 2021, **3**, 1756-1766.
47. Y. Spiesschaert, C. Taplan, L. Stricker, M. Guerre, J. M. Winne and F. E. Du Prez, *Polym. Chem.*, 2020, **11**, 5377-5385.
48. J. Zheng, Z. M. Png, S. H. Ng, G. X. Tham, E. Ye, S. S. Goh, X. J. Loh and Z. Li, *Mater. Today*, 2021, **51**, 586-625.
49. B. J. Adzima, H. A. Aguirre, C. J. Kloxin, T. F. Scott and C. N. Bowman, *Macromolecules*, 2008, **41**, 9112-9117.
50. B. Krishnakumar, R. V. S. P. Sanka, W. H. Binder, V. Parthasarthy, S. Rana and N. Karak, *Chem. Eng. J.*, 2020, **385**, 123820.
51. J. J. Lessard, G. M. Scheutz, R. W. Hughes and B. S. Sumerlin, *ACS Appl. Polym. Mater.*, 2020, **2**, 3044-3048.
52. L. E. Porath and C. M. Evans, *Macromolecules*, 2021, **54**, 4782-4791.
53. E. H. Cordes and W. P. Jencks, *J. Am. Chem. Soc.*, 1962, **84**, 832-837.
54. C. D. Meyer, C. S. Joiner and J. F. Stoddart, *Chem. Soc. Rev.*, 2007, **36**, 1705-1723.
55. R. W. Layer, *Chem. Rev.*, 1963, **63**, 489-510.
56. M. E. Belowich and J. F. Stoddart, *Chem. Soc. Rev.*, 2012, **41**, 2003-2024.
57. L. H. Choudhury and T. Parvin, *Tetrahedron*, 2011, **67**, 8213-8228.
58. M. Ciaccia, S. Pilati, R. Cacciapaglia, L. Mandolini and S. Di Stefano, *Org. Biomol. Chem.*, 2014, **12**, 3282-3287.
59. M. Ciaccia, R. Cacciapaglia, P. Mencarelli, L. Mandolini and S. Di Stefano, *Chem. Sci.*, 2013, **4**, 2253-2261.
60. P. Kovaříček and J.-M. Lehn, *J. Am. Chem. Soc.*, 2012, **134**, 9446-9455.
61. M. Ciaccia and S. Di Stefano, *Org. Biomol. Chem.*, 2015, **13**, 646-654.
62. A. Chao, I. Negulescu and D. Zhang, *Macromolecules*, 2016, **49**, 6277-6284.

63.   M. C. Burland, T. Y. Meyer and M.-H. Baik, *J. Org. Chem.*, 2004, **69**, 6173-6184.
64.   Y. Liu, Y. Zhang, Z. Cao and Z. Fang, *Ind. Eng. Chem. Res.*, 2012, **51**, 11059-11065.
65.   S. K. Schoustra, J. A. Dijksman, H. Zuilhof and M. M. J. Smulders, *Chem. Sci.*, 2021, **12**, 293-302.
66.   H. Geng, Y. Wang, Q. Yu, S. Gu, Y. Zhou, W. Xu, X. Zhang and D. Ye, *ACS Sustainable Chem. Eng.*, 2018, **6**, 15463-15470.
67.   Y. Wang, A. Xu, L. Zhang, Z. chen, R. Qin, Y. Liu, X. Jiang, D. Ye and Z. Liu, *Macromol. Mater. Eng.*, 2022, 2100893.
68.   S. Wang, S. Ma, Q. Li, W. Yuan, B. Wang and J. Zhu, *Macromolecules*, 2018, **51**, 8001-8012.
69.   D.-P. Wang, Z.-H. Zhao, C.-H. Li and J.-L. Zuo, *Mater. Chem. Front.*, 2019, **3**, 1411-1421.
70.   Y. Tao, L. Fang, J. Zhou, C. Wang, J. Sun and Q. Fang, *ACS Appl. Polym. Mater.*, 2020, **2**, 295-303.
71.   T. Liu, J. Peng, J. Liu, X. Hao, C. Guo, R. Ou, Z. Liu and Q. Wang, *Compos. B. Eng.*, 2021, **224**, 109188.
72.   X. Yang, Y. Ke, Q. Chen, L. Shen, J. Xue, R. L. Quirino, Z. Yan, Y. Luo and C. Zhang, *J. Clean. Prod.*, 2022, **333**, 130043.
73.   H. Zhang, Z. Su and X. Wang, *ACS Sustainable Chem. Eng.*, 2022, **10**, 8650-8657.
74.   J. M. Whiteley, P. Taynton, W. Zhang and S.-H. Lee, *Adv. Mater.*, 2015, **27**, 6922-6927.
75.   H. Li, J. Bai, Z. Shi and J. Yin, *Polymer*, 2016, **85**, 106-113.
76.   C. Zhu, C. Xi, W. Doro, T. Wang, X. Zhang, Y. Jin and W. Zhang, *RSC Adv.*, 2017, **7**, 48303-48307.
77.   H. Zheng, Q. Liu, X. Lei, Y. Chen, B. Zhang and Q. Zhang, *J. Polym. Sci., Part A: Polym. Chem.*, 2018, **56**, 2531-2538.
78.   H. Zheng, Q. Liu, X. Lei, Y. Chen, B. Zhang and Q. Zhang, *J. Mater. Sci.*, 2019, **54**, 2690-2698.
79.   Z. Feng, B. Yu, J. Hu, H. Zuo, J. Li, H. Sun, N. Ning, M. Tian and L. Zhang, *Ind. Eng. Chem. Res.*, 2019, **58**, 1212-1221.
80.   Y. Shen, N. Xu, Y. A. Adraro, B. Wang, Y. Liu, W. Yuan, X. Xu, Y. Huang and Z. Hu, *ACS Sustainable Chem. Eng.*, 2020, **8**, 1943-1953.
81.   B. Zhang, P. Zhang, H. Zhang, C. Yan, Z. Zheng, B. Wu and Y. Yu, *Macromol. Rapid Commun.*, 2017, **38**, 1700110.
82.   R. L. Snyder, C. A. L. Lidston, G. X. De Hoe, M. J. S. Parvulescu, M. A. Hillmyer and G. W. Coates, *Polym. Chem.*, 2020, **11**, 5346-5355.
83.   Z. He, H. Niu, L. Liu, S. Xie, Z. Hua and Y. Li, *Polymer*, 2021, **229**, 124015.
84.   Y. Wang, Y. Xiong, C. Hu, J. Yang and Y. Huang, *Eur. Polym. J.*, 2021, **160**, 110780.
85.   Y. Yang, Z. Xia, L. Huang, R. Wu, Z. Niu, W. Fan, Q. Dai, J. He and C. Bai, *ACS Appl. Mater. Interfaces*, 2022, **14**, 47025-47035.
86.   M. Kathan, C. Jurissek, P. Kovaříček and S. Hecht, *J. Polym. Sci., Part A: Polym. Chem.*, 2019, **57**, 2378-2382.

87.   P. Wang, L. Yang, B. Dai, Z. Yang, S. Guo, G. Gao, L. Xu, M. Sun, K. Yao and J. Zhu, *Eur. Polym. J.*, 2020, **123**, 109382.
88.   R. Mo, J. Hu, H. Huang, X. Sheng and X. Zhang, *J. Mater. Chem. A*, 2019, **7**, 3031-3038.
89.   X. Liu, L. Liang, M. Lu, X. Song, H. Liu and G. Chen, *Polymer*, 2020, **210**, 123030.
90.   Q. Yu, X. Peng, Y. Wang, H. Geng, A. Xu, X. Zhang, W. Xu and D. Ye, *Eur. Polym. J.*, 2019, **117**, 55-63.
91.   X. Xu, S. Ma, J. Wu, J. Yang, B. Wang, S. Wang, Q. Li, J. Feng, S. You and J. Zhu, *J. Mater. Chem. A*, 2019, **7**, 15420-15431.
92.   H. Memon, H. Liu, M. A. Rashid, L. Chen, Q. Jiang, L. Zhang, Y. Wei, W. Liu and Y. Qiu, *Macromolecules*, 2020, **53**, 621-630.
93.   H. Memon, Y. Wei, L. Zhang, Q. Jiang and W. Liu, *Compos. Sci. Technol.*, 2020, **199**, 108314.
94.   R. Mo, L. Song, J. Hu, X. Sheng and X. Zhang, *Polym. Chem.*, 2020, **11**, 974-981.
95.   X. Liu, E. Zhang, Z. Feng, J. Liu, B. Chen and L. Liang, *J. Mater. Sci.*, 2021, **56**, 15733-15751.
96.   Y.-Y. Liu, G.-L. Liu, Y.-D. Li, Y. Weng and J.-B. Zeng, *ACS Sustainable Chem. Eng.*, 2021, **9**, 4638-4647.
97.   H. Memon, Y. Wei and C. Zhu, *Mater. Today Commun.*, 2021, **29**, 102814.
98.   D.-M. Xie, D.-X. Lu, X.-L. Zhao, Y.-D. Li and J.-B. Zeng, *Ind. Crops Prod.*, 2021, **174**, 114198.
99.   Y. Sun, X. Tian, H. Xie, B. Shi, J. Zhong, X. Liu and Y. Yang, *Polymer*, 2022, **258**, 125313.
100.   W. Alabiso and S. Schlögl, *Polymers*, 2020, **12**, 1660.
101.   L. Porath, B. Soman, B. B. Jing and C. M. Evans, *ACS Macro Lett.*, 2022, **11**, 475-483.
102.   N. De Alwis Watuthanthrige, P. Chakma and D. Konkolewicz, *Trends Chem.*, 2021, **3**, 231-247.
103.   B. Marco-Dufort, R. Iten and M. W. Tibbitt, *J. Am. Chem. Soc.*, 2020, **142**, 15371-15385.
104.   F. Van Lijsebetten, J. O. Holloway, J. M. Winne and F. E. Du Prez, *Chem. Soc. Rev.*, 2020, **49**, 8425-8438.
105.   M. Guerre, C. Taplan, J. M. Winne and F. E. Du Prez, *Chem. Sci.*, 2020, **11**, 4855-4870.
106.   Z. P. Zhang, M. Z. Rong and M. Q. Zhang, *Prog. Polym. Sci.*, 2018, **80**, 39-93.
107.   A. Hernández, H. A. Houck, F. Elizalde, M. Guerre, H. Sardon and F. E. Du Prez, *Eur. Polym. J.*, 2022, **168**, 111100.
108.   M. Delahaye, J. M. Winne and F. E. Du Prez, *J. Am. Chem. Soc.*, 2019, **141**, 15277-15287.
109.   F. Van Lijsebetten, K. De Bruycker, J. M. Winne and F. E. Du Prez, *ACS Macro Lett.*, 2022, **11**, 919-924.
110.   R. Hajj, A. Duval, S. Dhers and L. Avérous, *Macromolecules*, 2020, **53**, 3796-3805.
111.   M. C. Montoya-Ospina, H. Verhoogt, M. Ordner, X. Tan and T. A. Osswald, *Polym. Eng. Sci.*, 2022, **1**, DOI: 10.1002/pen.26178.

112. L. Chen, L. Zhang, P. J. Griffin and S. J. Rowan, *Macromol. Chem. Phys.*, 2019, **221**, 1900440.
113. J. J. Lessard, K. A. Stewart and B. S. Sumerlin, *Macromolecules*, 2022, **55**, 10052-10061.
114. Y. Liu, Z. Yu, X. Xu, B. Wang, H. Feng, P. Li, J. Zhu and S. Ma, *Macromol. Rapid Commun.*, 2022, **n/a**, 2200379.
115. L. Zhang and S. J. Rowan, *Macromolecules*, 2017, **50**, 5051-5060.
116. F. Cuminet, D. Berne, S. Lemouzy, É. Dantras, C. Joly-Duhamel, S. Caillol, É. Leclerc and V. Ladmiral, *Polym. Chem.*, 2022, **13**, 2651-2658.
117. N. Van Herck, D. Maes, K. Unal, M. Guerre, J. M. Winne and F. E. Du Prez, *Angew. Chem. Int. Ed.*, 2020, **59**, 3609-3617.
118. B. M. El-Zaatari, J. S. A. Ishibashi and J. A. Kalow, *Polym. Chem.*, 2020, **11**, 5339-5345.
119. X. Xu, S. Ma, H. Feng, J. Qiu, S. Wang, Z. Yu and J. Zhu, *Polym. Chem.*, 2021, **12**, 5217-5228.
120. C. Lv, J. Wang, Z. Li, K. Zhao and J. Zheng, *Compos. B. Eng.*, 2019, **177**, 107270.
121. Y. Lei, A. Zhang and Y. Lin, *Polym. Chem.*, 2021, **12**, 4052-4062.
122. H. Liang, S. Zhang, Y. Liu, Y. Yang, Y. Zhang, Y. Wu, H. Xu, Y. Wei and Y. Ji, *Adv. Mater.*, **n/a**, 2202462.
123. X. Xu, S. Ma, S. Wang, B. Wang, H. Feng, P. Li, Y. Liu, Z. Yu and J. Zhu, *Macromol. Rapid Commun.*, 2022, **n/a**, 2100777.
124. Z. Liu, Y. Ma, Z. Zhang, Z. Shi and J. Gao, *Langmuir*, 2022, **38**, 4812-4819.
125. S. Yu, G. Zhang, S. Wu, Z. Tang, B. Guo and L. Zhang, *J. Mater. Chem. A*, 2020, **8**, 20503-20512.
126. D. Berne, B. Quienne, S. Caillol, E. Leclerc and V. Ladmiral, *J. Mater. Chem. A*, 2022, DOI: 10.1039/D2TA05067F.
127. S. K. Schoustra, T. Groeneveld and M. M. J. Smulders, *Polym. Chem.*, 2021, **12**, 1635-1642.
128. H. Zhang, D. Wang, N. Wu, C. Li, C. Zhu, N. Zhao and J. Xu, *ACS Appl. Mater. Interfaces*, 2020, **12**, 9833-9841.
129. S. Wang, S. Ma, Q. Li, X. Xu, B. Wang, K. Huang, Y. liu and J. Zhu, *Macromolecules*, 2020, **53**, 2919-2931.
130. P. Zhao, L. Wang, L. Xie, W. Wang, L. Wang, C. Zhang, L. Li and S. Feng, *Macromol. Rapid Commun.*, 2021, **42**, 2100519.
131. L. Bai, X. Yan, B. Feng and J. Zheng, *Compos. B. Eng.*, 2021, **223**, 109123.
132. L. Hammer, N. J. Van Zee and R. Nicolaÿ, *Polymers*, 2021, **13**, 396.
133. Y. Liu, *J. Appl. Polym. Sci.*, 2013, **127**, 3279-3292.
134. Y. S. Lipatov, *J. Macromol. Sci. B*, 2006, **45**, 871-888.
135. W. Hu, in *Polymer Physics: A Molecular Approach*, ed. W. Hu, Springer Vienna, Vienna, 2013, DOI: 10.1007/978-3-7091-0670-9_9, pp. 167-185.
136. C. Fernández-Rico, T. Sai, A. Sicher, R. W. Style and E. R. Dufresne, *JACS Au*, 2022, **2**, 66-73.

137. X. Chen, L. Li, T. Wei and J. M. Torkelson, *Macromol. Chem. Phys.*, 2019, **220**, 1900083.
138. X. Chen, L. Li and J. M. Torkelson, *Polymer*, 2019, **178**, 121604.
139. K. M. Herbert, P. T. Getty, N. D. Dolinski, J. E. Hertzog, D. de Jong, J. H. Lettow, J. Romulus, J. W. Onorato, E. M. Foster and S. J. Rowan, *Chem. Sci.*, 2020, **11**, 5028-5036.
140. J. J. Lessard, G. M. Scheutz, S. H. Sung, K. A. Lantz, T. H. Epps and B. S. Sumerlin, *J. Am. Chem. Soc.*, 2020, **142**, 283-289.
141. J. S. A. Ishibashi, I. C. Pierce, A. B. Chang, A. Zografos, B. M. El-Zaatari, Y. Fang, S. J. Weigand, F. S. Bates and J. A. Kalow, *Macromolecules*, 2021, **54**, 3972-3986.
142. R. W. Clarke, M. L. McGraw, B. S. Newell and E. Y. X. Chen, *Cell Rep. Phys. Sci.*, 2021, **2**, 100483.
143. S. Weerathaworn and V. Abetz, *Macromol. Chem. Phys.*, 2022, **n/a**, 2200248.
144. R. G. Ricarte, F. Tournilhac and L. Leibler, *Macromolecules*, 2019, **52**, 432-443.
145. R. G. Ricarte, F. Tournilhac, M. Cloître and L. Leibler, *Macromolecules*, 2020, **53**, 1852-1866.
146. M. Maaz, A. Riba-Bremerch, C. Guibert, N. J. Van Zee and R. Nicolaÿ, *Macromolecules*, 2021, **54**, 2213-2225.

Chapter 2

Molecular Control over Vitrimer-like Mechanics – Tuneable Dynamic Motifs based on the Hammett Equation in Polyimine Materials
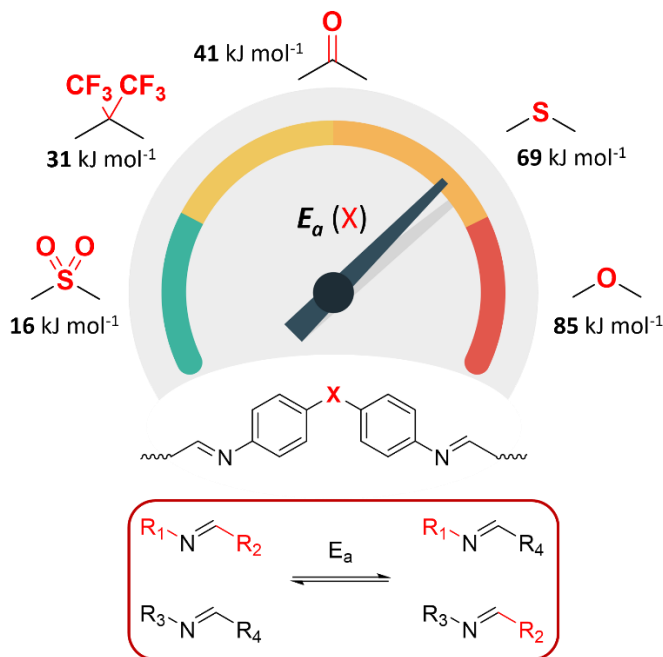
Abstract

In this chapter, we demonstrate that fine-grained, quantitative control over macroscopic dynamic material properties can be achieved using the Hammett equation in tuneable dynamic covalent polyimine materials. *Via* this established physical-organic principle, operating on the molecular level, one can fine-tune and control the dynamic material properties on the macroscopic level, by systematic variation of dynamic covalent bond dynamics through selection of the appropriate substituent of the aromatic imine building blocks. Five tuneable, crosslinked polyimine network materials, derived from dianiline monomers with varying Hammett parameter (σ) were studied by rheology, revealing a distinct correlation between the σ value and a range of corresponding dynamic material properties. Firstly, the linear correlation of the kinetic activation energy (E_a) for the imine exchange to the σ value, enabled us to tune the E_a from 16 to 85 kJ·mol^{-1}. Furthermore, the creep resistance, crossover temperature from rubbery to viscous phase (T_{cross}) and the topology freezing transition temperature (T_v), all showed a strong, often linear, dependence on the σ value of the dianiline monomer. These combined results demonstrate for the first time how dynamic material properties can be directly tuned and designed in a quantitative –and therefore predictable– manner through correlations based on the Hammett equation. Moreover, the polyimine materials were found to be strong elastic rubbers ($G' > 1$ MPa at room temperature) that were stable up to 300 °C, as confirmed by TGA. Lastly, the dynamic nature of the imine bond enabled not only recycling, but also intrinsic self-healing of the materials over multiple cycles without loss in material properties and without the need for additives, such as solvent, catalysts or addition of external chemicals.

2.1   Introduction

Dynamic covalent bonds, which combine chemical strength with reversible formation under conditions of equilibrium control,[1] have gained a tremendous interest in several sub-disciplines of chemistry, such as in self-assembly of macromolecular architectures, reversible formation of molecular cages and containers, and in the design of molecular motors.[1-6] In recent years, dynamic covalent chemistry has also become an important tool for the development of new 'smart' polymer materials that are, for example, renewable, self-healing, reprocessable or shape transformable.[7-13] When dynamic covalent bonds are included into crosslinked polymeric materials, covalent adaptable networks (CANs) can be synthesised.[14, 15] These CANs are thermosets, as they are covalently crosslinked polymer networks. However, in contrast to non-reversible classical thermosets, CANs can be recycled and reprocessed due to bond exchange reactions of the dynamic covalent bonds. Several bond exchange reactions in polymers have been investigated, like transesterifications,[16, 17] reversible Diels-Alder reactions,[18-21] disulphide exchange,[22-25] boronic ester exchange,[26-29] urea exchange,[30, 31] amide-imide exchange,[32, 33] vinylogous urethane exchange ,[34-36] and imine exchange.[37-41]

While the choice of type of bond exchange reaction can affect the dynamic material properties, other, more fine-grained approaches are still needed to allow careful, bottom-up design of dynamic polymer materials. In this regard it should be noted that the dynamics of the reversible covalent bonds within CANs are a key factor in the function of a dynamic polymeric material.[42] Control over the material properties at the macroscopic level can thus be traced back to controlling the behaviour of the dynamic covalent bond at the molecular level.[7, 14, 31, 43, 44] In other research domains, such as liquid-crystalline materials,[45, 46] supramolecular chemistry,[47] organic photovoltaic devices,[48, 49] colloidal systems,[50] and metamaterials,[51-53] this hierarchical translation of (molecular) structure to macroscopic material properties has already proven essential in offering bottom-up material design. However, for CANs this approach is still underexplored. Therefore, a core topic of interest for the tuneability of CANs and their corresponding designability, is to find a delicate handle on how small changes in the molecular structure of the polymer can be translated to changes in –and ultimately control over– macroscopic physical properties of the material.[42] A number of promising initial efforts has already been made to tune the material properties of CANs and broaden their range of applications. Examples include the effect of sterics and degree of crosslinking for poly(alkylurea-urethane) networks,[31] choice of electronically activated crosslinkers for thiol-yne[54] and thiol-ene[55] networks, or the effect of telechelic neighbouring groups in boronic ester transesterifications.[26] These studies show a promising

guide for molecular tuneability of CANs, however a systematic, more quantitative approach, that even allows for correlation of a given dynamic material property to a molecular descriptor, has yet to be designed. Herein, we show that the established physical-organic molecule-based concept defined by the Hammett equation[56-59] can be exploited to achieve quantitatively predictable and subtle chemical control over macroscopic mechanical material properties. Our results indicate that introduction of the Hammett equation in polyimines offers a powerful toolbox for making cheap, tuneable, and recyclable materials suitable for a wide range of applications.

Imines –sometimes referred to as Schiff bases[60]– are commonly synthesised *via* a condensation reaction of an aldehyde and amine. This reaction is also reversible, and is very dependent on the stability of the imine bond.[4] When water is removed, or when the imine bond is sufficiently stable, this reverse reaction can be prevented. Imines show two more reversible exchange reactions: transimination, which requires free amine groups, and imine metathesis, which occurs between two imines.[5] Once these exchangeable imine bonds are included into a polymer matrix, a dynamic polyimine CAN is constructed.[37, 61] Polyimine CANs have gained a tremendous interest in research and industry due to the potential to synthesise strong yet recyclable materials.[37, 62, 63] They are also favourable materials, as a broad variety of monomers is commercially available, as well as for the potential to obtain these from bio-based sources.[64, 65] Polyimine materials have been studied for a broad variety of applications, like fire-resistance,[66, 67] 3D printing,[68] sensing,[69, 70] CO_2 capture,[71-73] antibacterial coatings,[74] and in the production of electronic skins.[75]

Some attempts in tuning the material properties of polyimines have been documented, for example by tuning the degree of crosslinking,[76, 77] composition of the polymer chains,[41, 63, 78, 79] solvent,[39, 80] or metal-coordination.[40, 69, 81] These attempts have produced a number of interesting results, but focussed more on the composition of the polymer matrix rather than on the dynamics of the imine bond itself. Therefore, we propose to tune the intrinsic dynamics of the dynamic covalent bonds in polyimines *via* the electronic effect of substituted aromatic imines, derived from anilines. The reactivity of these imines depends on the nature of the substituent on the aromatic ring, as can be described by the Hammett equation.[56, 57] Kovaříček and Lehn demonstrated a similar Hammett equation-based concept by studying the imine exchange in small molecules, finding differences in exchange rates varying by more than three orders of magnitude for different substituents.[82] Similarly, Schultz and Nitschke relied on the Hammett equation to control imine exchange reactions in multistep transformation in Cu(I):imine complexes.[83] An extension of such control over dynamic covalent bond exchange, based on the Hammett equation, to imine-derived

polymers can therefore offer a (systematically) controllable molecular handle for material tuneability on the macroscopic level.

To demonstrate the extensive control over material properties offered by substituent effect in CANs, we composed a set of tuneable dianiline monomers (**XDA**s), where the effective (*i.e.*, tuneable) substituents are the bridging atoms between the two aniline moieties (Figure 2.1). These tuneable dianiline monomers are ideal building blocks for polymeric materials, given their wide commercial availability, and the option to focus exclusively on electronic effects, rather than to the combination of electronic and steric effects. To complete the network formation of our tuneable polyimine **P-XDA** materials, terephthalaldehyde (**TA**), tris(2-aminoethyl)amine (**TREN**) and 4,7,10-trioxa-1,13-tridecanediamine (**TOTDDA**) are included.
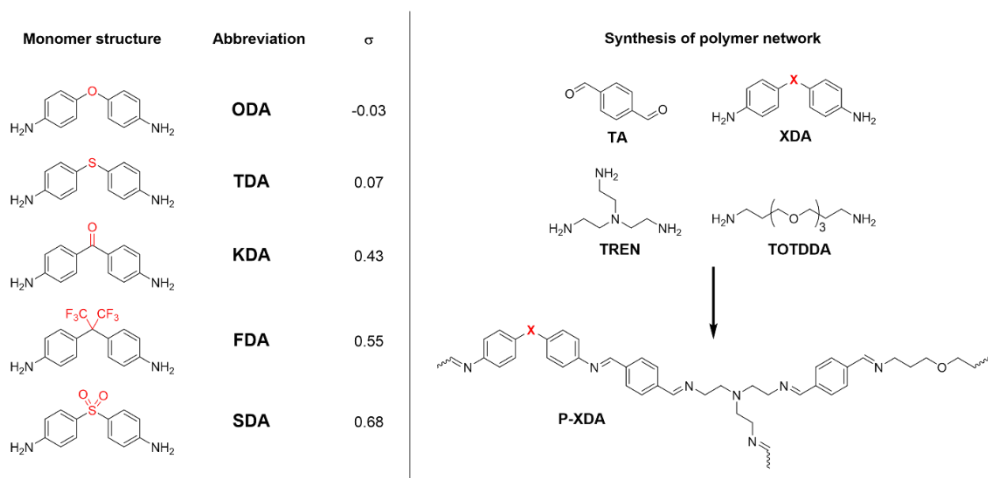

Figure 2.1 (Left) Overview of tuneable dianiline monomers and (Right) construction of the polyimine network. Dianiline monomers will be referred to by their abbreviation (**XDA**) and the corresponding polymers will be referred by the same abbreviation, but preceded by the letter 'P' (**P-XDA**). The Hammett parameter (σ) for each of the **XDA** monomers was taken from structurally highly related reference compounds (See Section 2.5.8 in the Supporting Information).[53, 54]

For this study, five dianiline monomers were selected from a list of commercially available dianilines, based on a wide range of electron-donating or -withdrawing effects that the bridging moieties provide. These effects are expressed by their corresponding Hammett parameter (σ), where a higher σ value relates to a more electron-withdrawing effect (σ values are listed in Figure 2.1). As the imine bonds are stabilised by resonance *via* the

aromatic rings, we hypothesised that more electron-donating substituents (lower σ) result in a more stable and electron rich imine bonds, and therefore, create tougher materials when incorporated into a polyimine network.

We quantitatively verify these hypotheses here by showing a direct correlation between the Hammett parameter and a range of material properties of direct relevance, such as glass transition temperature, topology freezing temperature, relaxation behaviour and kinetic activation energy. The correlation of the Hammett parameter to various material properties thus shows to be a delicate, yet directly applicable handle to tune the dynamic behaviour of polyimine CANs. Furthermore, material recycling over multiple cycles was achieved without loss in material properties, and without the need of a catalyst or other reagents. Also, autonomous self-healing behaviour was observed as cut samples were able to heal back together and retain their material properties.

2.2   Results and Discussion

2.2.1   Small-molecule exchange studies

As a proof of concept, small-molecule studies were initially carried out for all tuneable dianilines before their inclusion into polymer networks. The correlation between the σ value of the substituent on the aniline ring and the equilibrium constant (K) of the exchange reaction (Figure 2.2) was first investigated using ^{1}H NMR spectroscopy. A reference imine (**AN-I**) from benzaldehyde and aniline was synthesised and dissolved in CDCl$_3$. To this solution, 0.5 equivalents of the tuneable dianiline (**XDA**) was added to obtain a 1:1 amine:imine ratio.
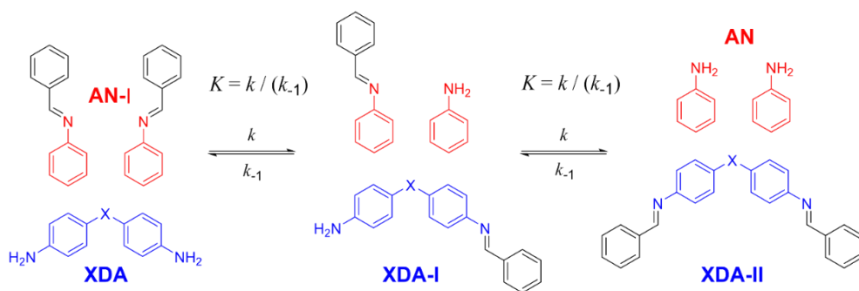

Figure 2.2 Exchange reaction of aromatic imine with tuneable dianiline monomers. For the equilibrium studies (to determine K), 0.5 equivalents of **XDA**, with respect to **AN-I** was added to obtain a 1:1 imine:amine ratio. For the kinetic studies (to determine k), 5 equivalents of **XDA** were added to obtain a 1:10 imine:amine ratio.

Once equilibrium had been reached, the overall equilibrium constant (K) was calculated *via* integration of the relevant ^{1}H NMR signals of the presented compounds (see Section 2.5.2 in the Supporting Information), assuming the two consecutive exchange reactions to occur independently from each other.[83] To obtain a Hammett plot, the obtained K values for all dianilines were plotted on a logarithmic scale as a function of σ (Figure 2.3, red squares).[58, 59] A trendline was then fitted through the individual data points, showing a linear correlation in which a lower σ resulted in a higher log K value. As a lower σ translates to a more electron-donating effect, this effectively means that more strongly electron-donating substituents push the equilibrium reaction (Figure 2.2) towards the right (formation of **XDA-II**). The Hammett reaction constant (ρ), which representing the sensitivity of the reaction towards the substituent effect, was determined from the slope of the fit to be -3.1 ± 0.3.[84] Such a value is typical for reactions in which aromatic ring-conjugated electrons are involved in forming a new bond.[84]
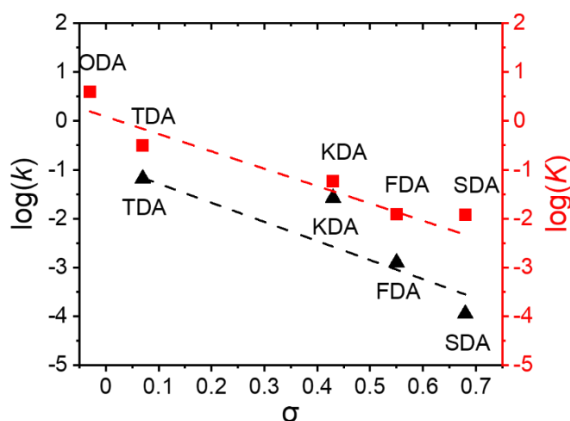

Figure 2.3 Hammett plots of imine exchange reactions for studied tuneable dianilines, showing the equilibrium constant (K, red squares) and the rate constant (k, black triangles) as a function of σ. The correlations are visualised by fitting a linear trendline. For the kinetic studies, the solvent was changed from CDCl$_3$ to acetone-d$_6$ as a consequence of poorer solubility of the dianilines due to the higher required concentration. For the same reason, ODA was excluded from this experiment.

Reaction rate constants (k) were also obtained for the dianiline monomers to investigate their dependence on the Hammett parameter. For this experiment, the same exchange reaction (Figure 2.2) was carried out. However, the reference imine (**AN-I**) was reacted with 5 equivalents of dianiline (meaning 10 equivalents of amine groups) to obtain a *pseudo* first-order reaction. The conversion of the **AN-I** into **XDA-II** was followed over time by ^{1}H NMR,

typically from the imine proton signal (see Section 2.5.2 in the Supporting Information). From this data, the first-order rate constant (k) was determined for all tuneable dianilines, and subsequently plotted as a function of σ (Figure 2.3, black triangles). Despite some deviations for individual data points from the overall trendline, which we attribute to solubility issues, a clear dependence of the rate constant on the Hammett parameter was observed. It should be noted that the observed poor solubility will not be present once the monomers are included into a (solvent-free) bulk polymer matrix.

From the kinetic data it was observed that when σ increased, the reaction rates of the exchange reaction decreased significantly. For example, the conversion of the reaction with **TDA** after 5 hours was already at 91%, whereas the conversion of **SDA** was only at 2% at that time, leading to a k for **TDA** ($6.6 \cdot 10^{-2}$ min^{-1}) to be about 600 times higher than that for **SDA** ($1.1 \cdot 10^{-4}$ min^{-1}). These large differences in imine exchange rates, in addition to the observed changes in exchange equilibrium and stability of the imine bond, already demonstrate the potential for a Hammett exchange-based control over dynamic material properties once these imines are integrated in polymer networks.

2.2.2 Design of the polymer network

To synthesise the tuneable polyimine materials, each of the tuneable dianilines (**XDA**s) was reacted with terephthalaldehyde (**TA**), tris(2-aminoethyl)amine (**TREN**) and 4,7,10-trioxa-1,13-tridecanediamine (**TOTDDA**) (see Figure 2.1 in the Introduction for the synthetic overview, and Section 2.5.3 in the Supporting Information for further experimental details). **TREN** was used as the crosslinking agent, while **TOTDDA** was added to increase flexibility of the polymer chains. The latter is important because without this "flexibility agent" the polymer chains become very rigid due to the short chains lengths and high aromatic content,[62, 66, 85] even to the extent that it would disturb the chains to freely move, which would decrease the occurrence of the bond exchange reaction. Three initial variations of the composition of the polyimine network were prepared in which the dianiline contents were 10%, 20% and 30% of the total amine content. Using rheology, a temperature sweep experiment was performed on the three samples to evaluate the viscous and elastic contribution to the material properties. To quantify this, we plotted the tan(δ) as a function of the temperature (see Section 2.5.9 in the Supporting Information). The 20% dianiline material resulted in the most desirable material for our tuneability studies, as the 30% variant was already very rigid and lacked a clear temperature dependence of G' and G'' in the given temperature range, whereas the 10% material showed a fast drop in viscosity already at relatively low temperatures, and thus limiting the tuneable range of the materials. The crosslinker (**TREN**) concentration was set at 5.0% (Note that **TREN** has 3 amine groups, meaning an effective amine concentration of 7.5 mol%, in relation to the

bisaldehyde **TA** monomer). **TOTDDA** was added as the remaining component to reach 100% of amines. **TA** was added in a 1:1 amine:aldehyde ratio to fully react all amines to imines. This was done to stimulate the imine metathesis exchange mechanism,[86] and minimise occurrence of transimination reactions. Furthermore, due to the aromatic conjugation of the imines, they were stable enough to minimise retro-imination (hydrolysis).[5, 38] Therefore, we assumed that imine metathesis would be the main mechanism of exchange. This hypothesis is further supported by exchange studies on aromatic imine model compounds that have reported a non-catalysed, associative metathesis-based exchange for aromatic imines at room temperature,[38] although we cannot fully rule out absence of the other exchange pathways (*i.e.*, transimination or retro-imination, for example due to trace amounts of amine and water.

The associative exchange mechanism is generally considered necessary for vitrimer-like materials to maintain a constant crosslinking density,[87] with the small proviso that for some previously reported materials it was observed that the rubbery plateau can be lost and flow can be observed.[88] To verify that a constant crosslinking degree was maintained in our **P-XDA** materials, frequency sweep rheological experiment were performed at four different temperatures (25, 50, 75 and 100 °C) (see Section 2.5.4 in the Supporting Information). At all given temperatures the *G*′ reached a plateau of similar value, indicating that the crosslinking degree in the network remained constant. This is in favour of an associative exchange mechanism, as a dissociative mechanism would typically result in a decrease in the crosslinking density.[89] Some dissociative CANs have, however, been shown to display very similar vitrimer-like behaviour as common associative CANs,[90-92] which has raised the question whether the term vitrimer should be used selectively for associative CANs.[93]

2.2.3   Stress relaxation and kinetic activation energy

Crosslinked polymers were synthesised for all five tuneable **XDA**s, and moulded into films with a 0.40 mm thickness and 10 mm diameter. To study the mechanical properties of the polymers, firstly a rheology experiment was conducted in which a constant angular strain (1%) was applied to the films, and the relaxation modulus ($G(t)$) was followed over time. Normalisation of the data (G/G_0) was performed to obtain the stress relaxation curves. Stress relaxation curves were obtained for every sample at temperatures from 10–50 °C, with 5 °C increments. The data for **P-TDA** are shown in Figure 2.4A as a representative example; the results for the other samples can be found in the Supporting Information (see Section 2.5.10). The relaxation time (τ) was taken as the point where G/G_0 reached $1/e$ (≈ 0.37), according to the Maxwell model for stress relaxation ($G/G_0 = \exp[-t/\tau]$).[94]

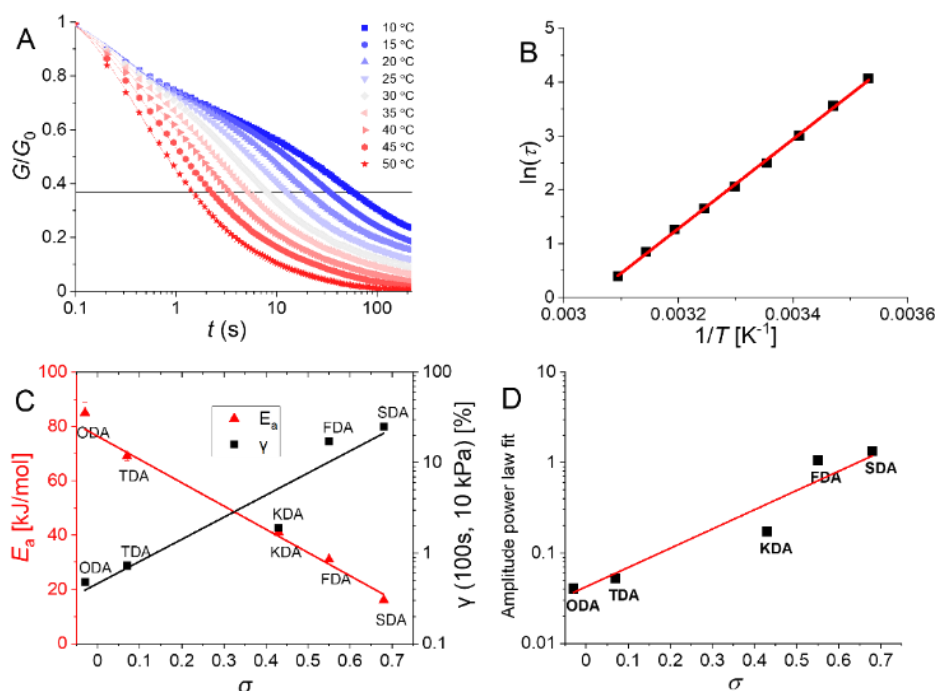**Figure 1.4** A) Normalised stress relaxation curves of **P-TDA** at different temperatures. B) Arrhenius plot of **P-TDA**, based on the data shown in (A). C) Plot of E_a (red triangles) and γ (black squares) as a function of σ. D) Amplitude of the fitted power law creep versus σ. In (C) and (D) a linear trendline was fitted as guide to the eye.

By plotting $\ln(\tau)$ versus the reciprocal temperature ($1/T$) an Arrhenius plot was constructed (Figure 2.4B). As the slope of the Arrhenius plot equals E_a/R, the kinetic activation energy (E_a) could be calculated for each of the **P-XDA** materials. Subsequently, plotting E_a versus the corresponding σ values of the dianiline monomers resulted in a rather striking linear relation (Figure 2.4C, red triangles), with the activation energy between the lowest and highest studied Hammett parameter differing by more than a factor 5. The distinct trend that can be seen is that by increasing the electron-donating effect of the aniline substituent, the E_a increases as well, whereas more electron-withdrawing substituents decrease the E_a. This corresponds to our observation that electron-donating effects stabilise the imine bond, and therefore, increase the energy required for the exchange reaction. As the E_a follows a linear trend with the Hammett parameter, to first approximation, a desired kinetic activation energy can be directly translated into the corresponding required σ value.

Next, a creep test was carried out in which the polymer films were exposed to a constant stress of 10 kPa, and the strain (γ) was measured over time. By comparing the strain of the materials at a fixed point in time (here: 100 s) we observed an increase in the amount of strain when σ increases as well (Figure 2.4C, black squares). We found that all materials display creep reminiscent of Andrade creep,[95, 96] but with a different sublinear power law time dependence, in which strain grows with a diffusive exponent of 0.5–0.6. Deviations from the Andrade creep exponent have been observed in other glassy materials.[97] Importantly, here the creep amplitude correlated directly with the Hammett parameter (Figure 2.4D), and is most likely sensitive to the applied stress and temperature,[98] just like other creep phenomena,[99] offering a wide range of tuneability. Consequently, we observed that also the extent of creep becomes tuneable as a dynamic mechanical material property by selection of the appropriate Hammett parameter (*i.e.*, choice of dianiline monomer).

2.2.4   Thermal properties

The thermal stability of the **P-XDA** materials was tested using thermographic analysis (TGA). A sample of each **P-XDA** material was gradually heated from 30 to 900 °C with a temperature ramp of 1 °C min^{-1} (see Supporting Information, Section 2.5). The temperature at which 5% weight loss of the materials was observed ($T_{d5\%}$), was determined. The results showed that all materials had a similar $T_{d5\%}$ of 298 ± 6 °C. This indicates that independently of the choice of dianiline monomer, the materials remained fully intact up to ~300 °C.

The crossover temperature (T_{cross}), form which the material transitions from a rubbery to a viscous phase, and rubbery domain of the materials were determined using rheology *via* temperature sweep experiments. Storage (G') and loss (G'') moduli were measured as a function of the temperature, and tan(δ) was calculated as G''/G' (see Section 2.5 for further details). The materials with the most electron-donating substituents (**P-ODA** and **P-TDA**) displayed a peak in tan(δ), from which T_{cross} was derived.[41] For the materials with more electron-withdrawing groups (**P-KDA**, **P-FDA** and **P-SDA**), a point in temperature was reached at which the G' rapidly dropped to 0. For these materials, T_{cross} was determined at which tan(δ) = 1.[14] From the determined T_{cross} values (Figure 2.5A), a trend was observed in which T_{cross} decreased when the electron-withdrawing effect of the substituents increased (increase in σ). This was in line with the results obtained from the small-molecule studies, for which the electron-withdrawing substituents resulted in a less stable imine bond, requiring less energy for bond exchange.
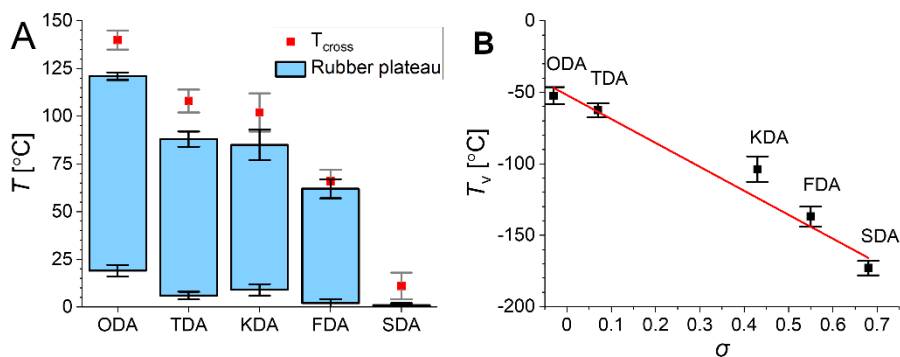
Figure 2.5 A) Rubbery plateaus and T_{cross} for the **P-XDA** materials, as determined by rheology measurements. B) Plot of T_v as function of the σ value for the corresponding substituents of the dianiline monomer (a linear line was fitted to the data points as a guide to the eye).

The rubbery domain of the materials was determined from the plateau region in G' before it reached the T_{cross} (Figure 2.5A).[14] From the determined temperature region of the rubbery plateau we can conclude that –apart from the most electron-withdrawing **P-SDA**– the materials displayed rubbery behaviour in an ambient atmosphere at room temperature. Secondly, the lower temperature of the rubbery state remained similar for all materials roughly in the range of 0–20 °C, whereas the upper temperature decreased when the electron-withdrawing effect of the substituents increases.

Another important parameter for vitrimer(-like) materials is the topology freezing transition temperature (T_v). As previously defined,[100] the T_v is the temperature at which the network topology of the material is considered frozen due the absence of required bond exchange reactions. For vitrimer-like materials this frozen state is considered at the point at which the viscosity (η) reaches 10^{12} Pa·s. In order to determine the T_v for our **P-XDA** materials the data from the stress relaxation and temperature response were combined. Firstly, the stress relaxation time (τ_v) at T_v was determined using Equation 1:

$$\tau_v = \frac{3 * \eta}{G'} \qquad\qquad \text{(Equation 1)}$$

In which $\eta = 10^{12}$ Pa·s, and G' represents the storage modulus of the rubbery plateau, obtained from the temperature sweeps.[31]

Next, the fitted Arrhenius curves from the stress relaxation experiment (see Section 2.5.10 in the Supporting Information) were extrapolated to the point for which $\tau = \tau_v$, allowing the corresponding temperature T_v to be determined. Note that the T_v is a hypothetical

parameter that is derived from extrapolation, and should be treated as a parameter belonging to the specific exchange reaction present within the material.[42] Once the T_v for every material was determined, these values were plotted as a function of σ to reveal a distinct linear trend between the two parameters, with T_v decreasing for increasing σ values (Figure 2.5B). We also observed that the T_v values for all materials were relatively far below their T_{cross} values, which indicates that the bond exchange reaction can occur at very low temperatures, and independent of the composition of the polymer network.[100]

2.2.5   Solvent resistance

The solvent resistance of **P-ODA**, **P-TDA** and **P-KDA** materials was tested by submerging the polymers in a given solvent for 5 days at room temperature (see Section 2.5.6 in the Supporting Information). Afterwards, the solid was separated from the liquid, and the remaining mass of the solid was determined after drying. The remaining fractions for each material and solvent are pictured in Figure 2.6.
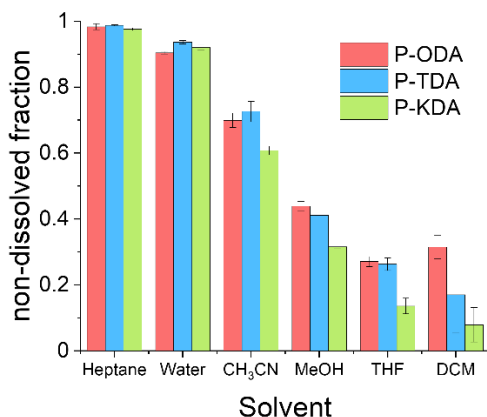

Figure 2.6 Overview of non-soluble fractions for **P-ODA**, **P-TDA** and **P-KDA** polymers after immersion in the corresponding solvent for 5 days at room temperature.

The results showed that the materials have a strong resistance against water and heptane (>0.90 non-dissolved fraction), and only partially to acetonitrile (0.61–0.73 non-dissolved fractions), methanol (0.32–0.44 non-dissolved fractions), THF (0.14–0.27 non-dissolved fractions), and dichloromethane (0.08–0.32 non-dissolved fractions). From the obtained results we could not infer the presence of a σ-dependent solvent resistance of the materials, although indications can be observed for methanol, THF and dichloromethane. While partial dissolution of the polymer was observed for some solvents, ^{1}H NMR analysis of the soluble

material revealed the absence of any aldehyde species. This suggests that a dissociative retro-imination process (*i.e.*, imine hydrolysis) is not the main driving force for the polymer dissolution. Instead, we suggest that the partial network dissolution could have been caused by formation of loops that separate one portion of the network from another, as proposed by Elling and Dichtel in their discussion of the –still not fully understood– solubility of vitrimer(-like) materials.[85]

The poor solubility results indicate that reprocessing *via* redissolving the materials is not suitable, but their relatively good resistance against several common solvents enables applications where the material is exposed to small amounts of solvent or for short time intervals, for example in washing steps or in condensed environments. Reprocessing of the materials remained still possible by other means, such as heating (see next section). In **Chapter 7** of this thesis, we will also further address the solubility of (imine-based) CANs.

2.2.6 Recycling and Self-healing

To test the applicability of this type of tuneable polyimine networks as strong, yet recyclable materials, **P-TDA** and **P-ODA** were evaluated because of their higher relative strength compared to the other three materials. Both **P-TDA** and **P-ODA** were recycled up to three times to establish whether material properties could be recovered. For each cycle the material was cut into small pieces and then hot-pressed (100 °C, 1 MPa, 15 min) into new bars (see Section 2.5.6 in the Supporting Information for full experimental details). Dynamic mechanical analysis (DMA) was used to stretch the materials with a constant stretching speed of 10% per minute, and the stress was measured as a function of the strain until the sample broke. For each cycle, four samples were measured and the average values for yield point (%), yield stress (MPa), elongation at break (%) and Young's modulus (MPa) were determined. The data were normalised for better comparison, and are presented in Figure 2.7. Despite some small deviations in the obtained data, most likely as a result of natural variability, no systematic decrease in any of the material properties was observed over multiple recycles. Therefore, we concluded that recyclability of the materials over multiple cycles is possible without loss in material properties.
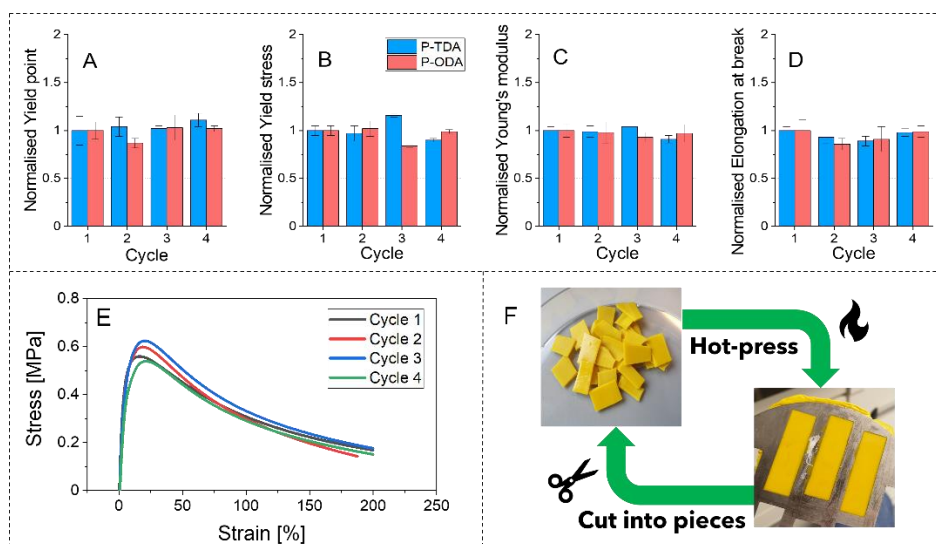
Figure 2.7 Recycling test of **P-TDA** (blue, left bars) and **P-ODA** (red, right bars), showing normalised data over multiple cycles for A) Yield point, B) Yield stress, C) Young's modulus, and D) Elongation at break. Cycle 1 corresponds to the pristine material and cycles 2–4 represent each of the following recycling steps. E) Stress-strain curves of representative samples of **P-TDA** from each recycling step. F) Pictures of cut material and new recycled bars (here in their mould, directly after hot-pressing).

The degree of autonomous self-healing of the **P-TDA** material was also investigated. For this experiment, similar bars as for the recycling experiments were prepared. They were cut in half, and the two halves were placed back into the mould with the cut edges touching. The samples were left in the mould (in a horizontal position), but this time without applying external pressure (see Section 2.5.6 for experimental details). The experiment was carried out at 25, 50 and 75 °C. After the samples were cooled back down to room temperature, DMA was used to determine the material properties of the healed materials (Figure 2.8).

For all of the healed materials, the yield point (blue, left column), yield stress (green, middle column) and Young's modulus (red, right column) were comparable to the pristine material. Furthermore, by stretching the materials, the location at which the break or flow appeared was different from where the material was initially cut. The samples heated at 50 °C and 75 °C were fully healed after 2 hours, while the healing at 25 °C was eventually achieved after 24 hours due to the slower bond exchange at lower temperatures. It is worthwhile to stress again that no external chemicals, solvents or catalysts were required, and as such, these materials are capable of autonomous self-healing.
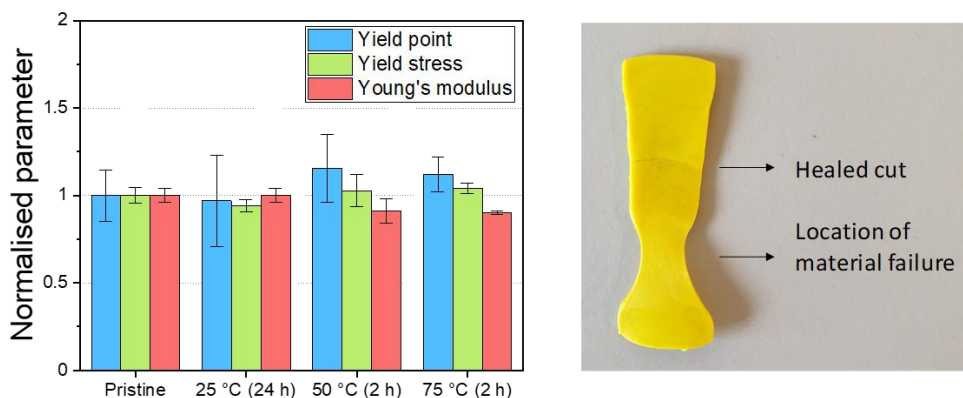
Figure 2.8 (Left) Material properties of self-healed **P-TDA** materials at 25, 50 and 75 °C, compared to the pristine material. The materials healed at 25 °C required 24 hours to heal, whereas the samples at 50 °C and 75 °C required only 2 hours; data were normalised to the pristine material. (Right) **P-TDA** material that was cut, healed, and then stretched. The location of material failure, as a result of an applied strain, is different from the location of the healed cut.

2.3   Conclusion

We developed a precise way to tune the dynamic-mechanical and thermal properties of polyimine CANs *via* electronic effects of dianiline monomers based on the Hammett equation. This allowed for the first time a direct and quantitative correlation of a simple, molecule-based physical parameter to macroscopic material properties. The relaxation time (τ), kinetic activation energy (E_a), creep (γ), crossover temperature (T_{cross}), and topology freezing temperature (T_v) could all be tuned *via* the Hammett parameter (σ). This opens the potential for simply picking the desired macroscopic properties for a CAN material, and then obtaining that property *via* the selection of the required dianiline monomer using only the σ value of the substituent from a large list of available substituents. We also hypothesise that such a Hammett-based guiding principle effect can be extended to other polymer networks, irrespectively of whether their bond exchange reactions occur *via* an associative or a dissociative mechanism. Furthermore, our tuneable polyimine materials show potential to be used for applications in daily life as common rubbers due their stable rubbery state, which could be tuned to over 100 °C based on the choice of dianiline monomer. TGA also showed that all materials were stable from degradation up to 300 °C. Additionally, recycling and intrinsic self-healing without loss of material properties were realised without addition of an external chemical, solvent or catalyst.

2.4   Acknowledgement

2.5   Supporting information

An overview of the most important supporting information is given below, while full details can be accessed from: http://dx.doi.org/10.1039/D0SC05458E

2.5.1   Materials and Methods

NMR spectra were recorded on a Bruker Avance III 400 MHz instrument and analysed with MestreNova software. Chemical shifts are reported in parts per million (ppm), calibrated on the residual peak of the solvent, whose values are referred to tetramethylsilane (TMS, δ_{TMS} = 0 ppm), as the internal standard.

FT-IR analyses were performed on a Bruker Tensor 27 spectrometer with platinum ATR accessory.

Rheological measurements were conducted on an MCR 301 or MCR 501 Anton Paar rheometer in combination with a temperature-controlled plate-plate configuration and temperature controller hood for additional thermal homogeneity.

Dynamic mechanical analysis (DMA) was performed on a Q800 TA Instruments machine with film tension clamp.

2.5.2   Small-molecule exchange studies

Small-molecule exchange studies were performed to gain insight into the kinetics and thermodynamics of the imine exchange reaction (see Figure 2.2 in the Results and Discussion). Two different experiments were performed: 1) to derive equilibrium constants (*K*), and 2) to derive reaction rate constants (*k*) for each of the tuneable dianiline structures (**XDAs**). The combined *K* and *k* values are presented in Table 2.1, and the experimental details are given in the following paragraphs.

Table 2.1 Overview of equilibrium constants (K) and reaction rate constants (k). For the reaction rate experiment, the solvent was changed from CDCl$_3$ to acetone-d$_6$ as a consequence of poorer solubility of the dianilines due to the higher required concentration. For the same reason of poor solubility, **ODA** was excluded from the kinetic experiment.

XDA	K	k [min^{-1}]
ODA	$3.92 \pm 0.05 \cdot 10^{0}$	–
TDA	$3.14 \pm 0.04 \cdot 10^{-1}$	$6.61 \pm 0.15 \cdot 10^{-2}$
KDA	$5.75 \pm 0.13 \cdot 10^{-2}$	$2.63 \pm 0.12 \cdot 10^{-2}$
FDA	$1.23 \pm 0.03 \cdot 10^{-2}$	$1.26 \pm 0.09 \cdot 10^{-3}$
SDA	$1.20 \pm 0.03 \cdot 10^{-2}$	$1.12 \pm 0.10 \cdot 10^{-4}$

Determination of equilibrium constants (K)

Benzaldehyde (0.04 mmol, 4.1 µL) and aniline (0.04 mmol, 3.7 µL) were dissolved in CDCl$_3$ to form the reference imine (**AN-I**). Then the tuneable dianiline (**XDA**) (0.02 mmol, corresponding to approx. 4 mg, depending on the dianiline) was added. The mixture was left at room temperature for several days until exchange equilibrium was reached, as concluded from ^{1}H NMR. Once equilibrium had reached, the ratio of formed imines was determined *via* integration of the appropriate NMR signals. In most cases this was done by integrating the imine peaks, unless these overlapped. When an overlapping imine signal was present, integration of a different (non-overlapping) signal was performed. The following equation was used to derive the overall equilibrium constant (K):

$$K = \frac{[aniline\ amine][XDA\ imine]}{[XDA\ amine][aniline\ imine]}$$
(Equation S1)

Note that both amine groups of the dianiline each count for one reactive species. Therefore, the initial amine groups of the aniline and dianiline are equivalent. Thus, we can also state that [aniline amine] = [**XDA** imine] and [**XDA** amine] = [aniline imine]. The equation then becomes:

$$K = \frac{[XDA\ imine]^2}{[aniline\ imine]^2} = \left(\frac{[XDA\ imine]}{[aniline\ imine]}\right)^2$$
(Equation S2)

The concentration of both imines can be determined from simple integration of their corresponding ^{1}H NMR signal integrals. Log(K) could then be plotted for all dianilines as function of σ to obtain a Hammett plot (see Figure 2.3 in the Results and Discussion), assuming that K is the same for both reaction steps. All determined K values are also presented in Table 2.1.

Determination of reaction rate constants (k)

N-benzylideneaniline **AN-1** (1.81 mg, 0.01 mmol) was dissolved in acetone-d_6. Then, the tuneable dianiline (0.05 mmol, approximately 10 mg, depending on the nature of the dianiline) was added to the mixture. ^{1}H NMR was used to check the conversion of the exchange reaction over time by simple integration (see Figures 2.9–2.12, signals used for integration are highlighted). The conversion into the product was plotted as a function of the time, and curves were fitted according to a first-order reaction rate law:

$$y = A * (1 - e^{-k*t})$$ (Equation S3)

The reaction rate constant (k) was derived from the fitted curves (Figure 2.13), and subsequently, the obtained k values were plotted as a function of the Hammett parameter (σ) of the tuneable dianilines (see Figure 2.3 in the Results and Discussion). All determined k values are also presented in Table 2.1. To allow for the possibility for an incomplete conversion (which is inherently possible for a dynamic covalent bond formation reaction), the value of A was included as a fit parameter to find the value to which the conversion converged (*i.e.*, the maximum value for A was 100).
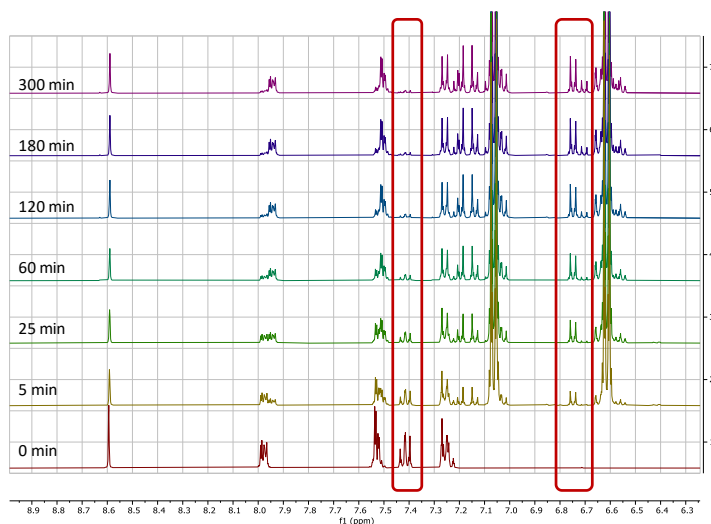

Figure 2.9 ^{1}H NMR spectra at indicated time points for the imine exchange reaction with **TDA**. The signals of the starting imine material (highlighted peak at 7.41 ppm) decreased over time, whereas the signal for the **TDA** imine (highlighted at 6.75 ppm for mono substituted and 6.70 ppm for disubstituted) increased.
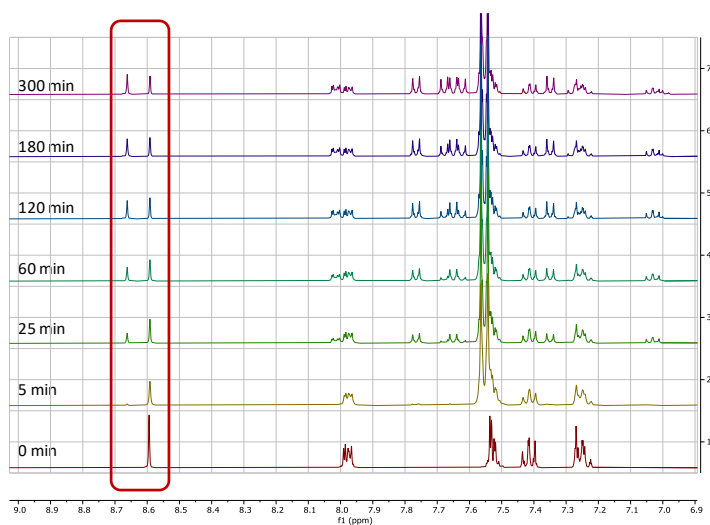
Figure 2.10 ^{1}H NMR spectra at indicated time points for the imine exchange reaction with **KDA**. The signals of the starting imine material (highlighted peak at 8.59 ppm) decreased over time, whereas the signal for the **KDA** imine (highlighted at 8.66 ppm) increased.
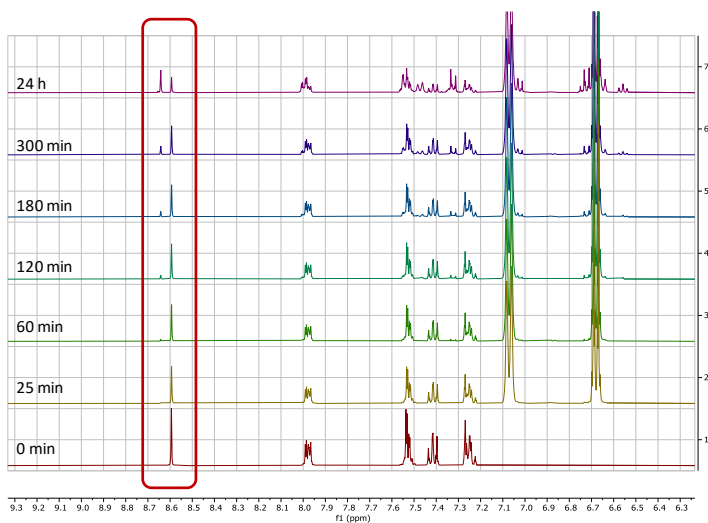

Figure 2.11 ^{1}H NMR spectra at indicated time points for the imine exchange reaction with **FDA**. The signals of the starting imine material (highlighted peak at 8.59 ppm) decreased over time, whereas the signal for the **FDA** imine (highlighted at 8.64 ppm) increased.

Figure 2.12 ^{1}H NMR spectra at indicated time points for the imine exchange reaction with **SDA**. The signals of the starting imine material (highlighted peak at 8.59 ppm) decreased over time, whereas the signal for the **SDA** imine (highlighted at 8.57 ppm) increased.
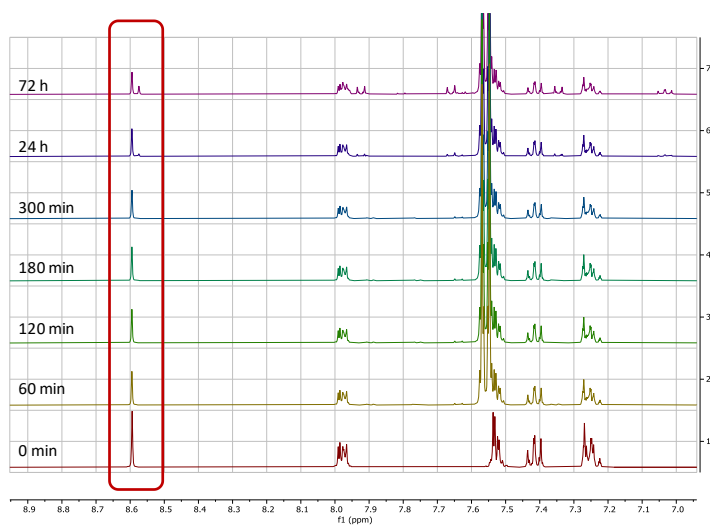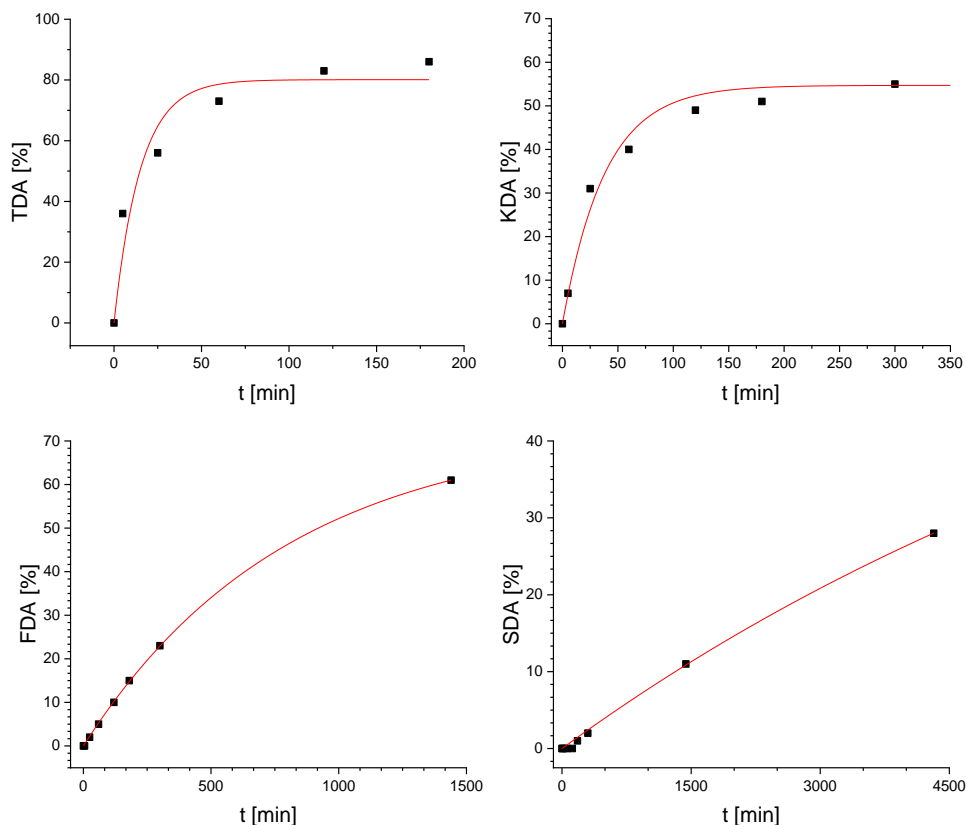
Figure 2.13 Overview of the kinetic data and best-fitted curves for estimation of the reaction rate constants. The results of the fitting have been included in Table S1.

2.5.3   General synthesis of polyimine networks

The tuneable dianiline (0.80 mmol, corresponding to approx. 180 mg, depending on the nature of the tuneable dianiline), **TREN** (0.20 mmol, 30 µL) and **TOTDDA** (2.90 mmol, 0.64 mL) were mixed together in THF (5.0 mL). Terephthalaldehyde **TA** (4.00 mmol, 537 mg) was then added to the mixture at room temperature, and the mixture was briefly shaken until a homogeneous solution was obtained. The solution was poured into a petri dish and was left for overnight to slowly evaporate the solvent. The samples were further dried in a vacuum oven at 50 °C for 3 more nights. Subsequently, the materials were cooled to room temperature and FT-IR spectroscopy was used to check the conversion from aldehyde (signal at ~1700 cm^{-1}) to imine (~1640 cm^{-1}).

2.5.4   Rheology experiments

For rheological analysis, discs with a 10 mm diameter and a 0.4 mm thickness were prepared by hot-pressing the synthesised **P-XDA** polymer materials at a maximum temperature of 75 °C and maximal force of 40 N.

Four types of rheology experiments were performed: stress relaxation, a creep experiment, frequency sweeps at several temperatures, and a temperature sweep.

In the stress relaxation tests, the discs were subjected to a constant strain of 1% and the relaxation modulus (G) was followed over time. The experiment was carried out for all materials at temperatures from 10–50 °C, with increments of 5 °C. After every measurement, the stress was brought back to 0 and the samples were given 10 minutes to reach the new temperature. The normalised relaxation modulus (G/G_0) was plotted against the time to obtain the relaxation curves. The relaxation time (τ), where $G/G_0 = 1/e$ according to the Maxwell model for stress relaxation ($G/G_0 = \exp(-t/\tau)$), was then interpolated for every temperature curve to construct an Arrhenius plot. This plot was derived by plotting $\ln(\tau)$ against the reciprocal temperature ($1/T$). The kinetic activation energy (E_a) was calculated from the slope of the fitted line multiplied by the gas constant ($R = 8.3145$ J K^{-1} mol^{-1}). The E_a values were derived for all materials and were then plotted as a function of their corresponding Hammett parameter (σ).

The creep test was performed by exposing each polymer disc to a constant stress of 10 kPa and following the strain (γ) over time, which was subsequently plotted for every material. The temperature was held constant at 20 °C. A constant point in time of 100 s was taken to derive the total amount of strain in the given time frame. The total strain at 100 s was then plotted against the Hammett parameter (σ) of the corresponding material.

Frequency sweeps were carried out on the polymer discs at angular frequency (ω) range of 0.1–100 Hz, and an applied strain of 0.1%. The measurement was performed at 25, 50, 75 and 100 °C. The storage (G') and loss (G'') modulus were consequently plotted as a function of the frequency at all given temperatures for all **P-XDA** materials.

Temperature sweeps were performed on the polymer discs on temperature range from 0–150 °C with a constant angular frequency of 1 Hz and strain of 0.1%. Storage (G') and loss (G'') moduli were measured as a function of the temperature. Tan(δ) was calculated as G''/G' and was also plotted as a function of the temperature. The materials with the most electron-donating substituents (**P-ODA** and **P-TDA**) displayed a peak in tan(δ), and therefore T_{cross} was determined from the top of this peak.[S41] For the materials with more electron-withdrawing groups (**P-KDA**, **P-FDA** and **P-SDA**), a point in temperature was reached at

which the G' rapidly drops to 0. For these materials T_{cross} was determined at the point where tan(δ) = 1.S[14] The rubbery domain of the materials was taken as the temperature range over which a constant plateau value was observed in the G' curve.

2.5.5   Thermal stability tests

Thermal stability was tested using thermographic analysis (TGA). Small pieces (10 mg) of the **P-XDA** materials were loaded and heated on a temperature ramp of 30–900 °C with a heating speed of 1 °C per minute. The total remaining weight percentage was followed as a function of the temperature.

2.5.6   Solvent resistance / solubility tests

A small piece of the **P-XDA** material (20 mg) was cut off and placed in a vial containing 2 mL of a specific solvent (water, THF, acetonitrile, DCM, methanol or heptane). The vials were capped and left for 5 days at room temperature. The non-dissolved solid was removed from the vial and dried to air for overnight, followed by drying *in vacuo* at 50 °C for another day. The dried solids were weighed and the non-soluble fraction was determined as the weight after the experiment divided by the weight of the initial sample. For the NMR experiment, approx. 4 mg of **P-ODA** was added to an NMR tube and then dissolved in the specific (deuterated) solvent. After leaving the sample for 72 hours at room temperature, the ^{1}H NMR spectrum of the soluble fraction was recorded.

2.5.7   Recycling and self-healing

The pristine material for the recycling test was prepared by hot-pressing (100 °C, 1 MPa, 15 min) the raw **P-XDA** materials into bars with a dimension of 1.5 × 1.0 × 0.1 cm (length × width × thickness). Afterwards, the samples were left for 1 day at ambient atmosphere before being measured. DMA was then used to stretch the materials at a constant stretching speed of 10% per min until the sample reached its maximal elongation and either snapped or flowed. Four samples were measured and the average values for yield point (%), yield stress (MPa), elongation at break (%) and Young's modulus (MPa) were reported. For the following recycling steps, the materials were cut into small pieces (approximately 0.2 cm^2) and again hot-pressed in a similar fashion as before (Figure 2.14). The recycled samples were again measured in sets of four as described. A total of 4 cycles were performed (1 of the pristine material and 3 recycling steps).
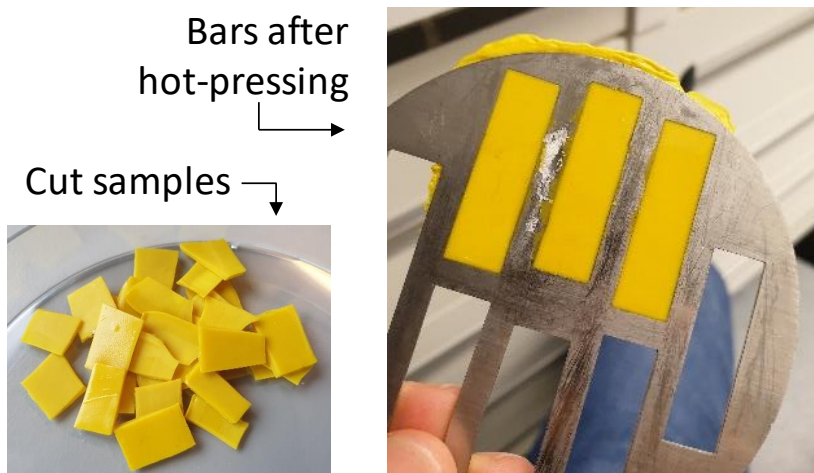
Figure 2.14 Photos of the cut **P-TDA** material and of the bars (still in the mould) after hot-pressing.

For the self-healing experiment, bars of the same dimension were prepared, which were then cut in half. The two halves were placed back into the mould so that the cut edges would touch each other. The experiment was carried out at 25, 50 and 75 °C without applying external pressure. Full self-healing of the material was achieved within 2 hours at 50 and 75 °C, and 25 hours at 25 °C. The healed samples (Figure 2.15) were then tested for their material properties using the same DMA procedure as the recycling experiment.
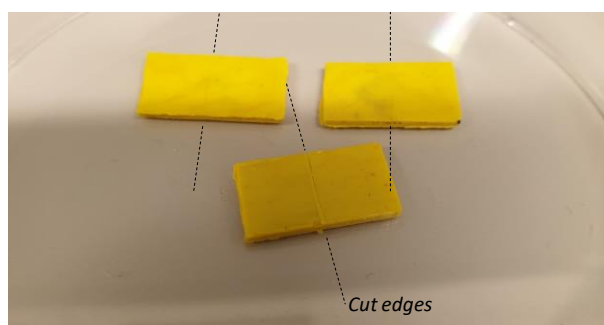

Figure 2.15 Photo of healed **P-TDA** samples. Dotted lines represent the edges where the material was cut in half.

2.5.8 Hammett parameters

Figure 2.16 gives an overview of the five tuneable dianilines (**XDAs**) used in this study, and their corresponding Hammett parameter (σ). The σ values were chosen from their most structurally similar compound used in Hammett studies,[58, 59] which are shown as well. For all cases the σ value for the para-substituent (σ_p) was used.
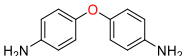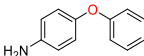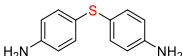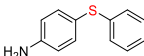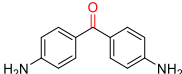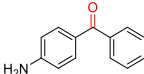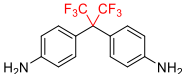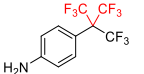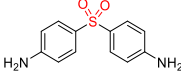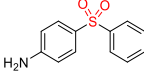

XDA monomer	Monomer structure	σ_p	Derived from:
ODA		-0.03	
TDA		0.07	
KDA		0.43	
FDA		0.55	
SDA		0.68	

Figure 2.16 Overview of **XDA** monomers, their corresponding Hammett parameter (σ) values, and the structures of which the σ values were derived from.[58, 59]

2.5.9 Determination of ideal monomer ratios

To determine the ideal contents of dianiline and **TOTDDA** in the polymer system, three samples with different dianiline contents (Table 2.2) were prepared following the standardised synthetic procedure. As this was an indicative experiment, only **TDA** was used in this test. The crosslinker (**TREN**) content was first tested at 5 mol%, and was concluded to be a satisfactory amount. Using rheology, a temperature sweep experiment was performed on a temperature range of 20–150 °C for each of the three materials. A constant strain of 0.1% and angular frequency of 1 Hz was applied. The tan(δ) was plotted as a function of the temperature to obtain the curves presented in Figure 2.17. As seen in the figure, a dianiline content of 30% resulted in the material to be relatively unsusceptible for changes in temperature below 150 °C. On the other hand, a dianiline content of 10% resulted in the material to initiate fast liquification already before 100 °C, as tan(δ) = 1 was

observed at 75 °C and increased rapidly thereafter. The material incorporating 20% of dianiline showed ideal behaviour as the material displayed a distinct temperature dependency, but also the effect was delicate enough in order for the dianiline to serve as a tuneable handle.
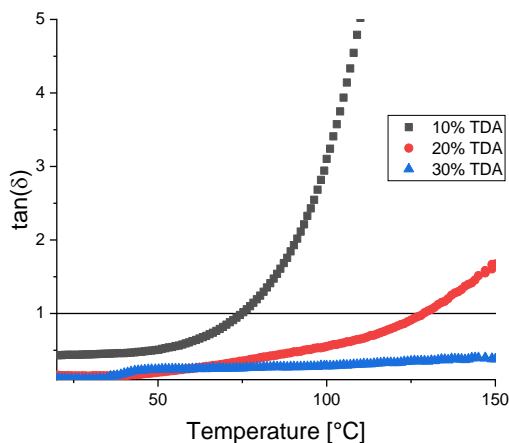
Figure 2.17 Tan(δ) curves for polyimine materials with 10% (black squares), 20% (red spheres) and 30% (blue triangles) of **TDA** dianiline content. Tan(δ) = 1 for 10% dianiline at 75 °C, and increasing rapidly after. Tan(δ) = 1 for 20% dianiline at 129 °C. Tan(δ) for 30% dianiline remains below 1 for the entire duration of the experiment (up to 150 °C).

Table 2.2 List of tested dianiline ratios in **P-TDA** materials. Note that **TREN** has 3 amine groups, whereas **TDA** and **TOTDDA** have 2 amine groups. Therefore the 5% of **TREN** nets to 7.5% of amine relative to the aldehyde content, adding the total to 100%. To form the polymer network an equimolar amount (100%) of terephthalaldehyde was added to provide full conversion of amines to imines.

Entry	TDA [%]	TOTDDA [%]	TREN [%]
1	10	87.5	5.0
2	20	77.5	5.0
3	30	65.5	5.0

2.5.10 Stress relaxation curves and Arrhenius plots
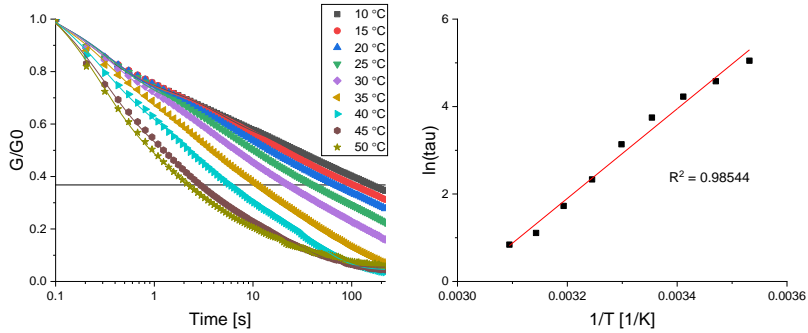
Figure 2.18 Stress relaxation curves (left) and Arrhenius plot (right) of **P-ODA**.
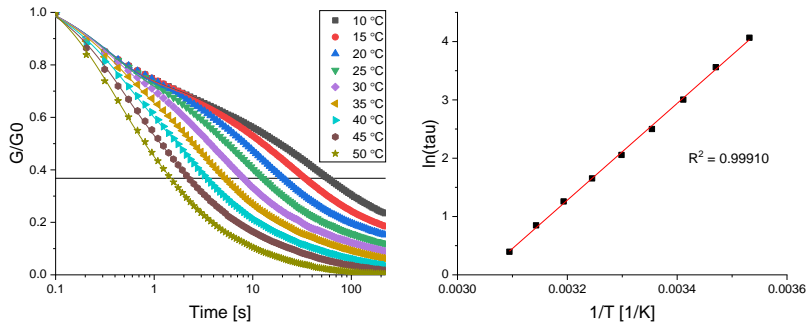
Figure 2.19 Stress relaxation curves (left) and Arrhenius plot (right) of **P-TDA**.
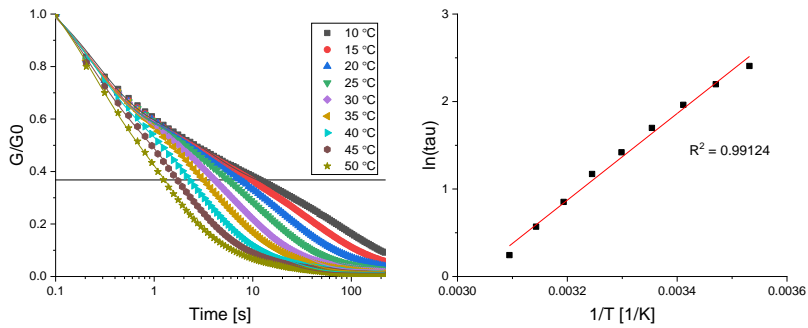
Figure 2.20 Stress relaxation curves (left) and Arrhenius plot (right) of **P-KDA**.
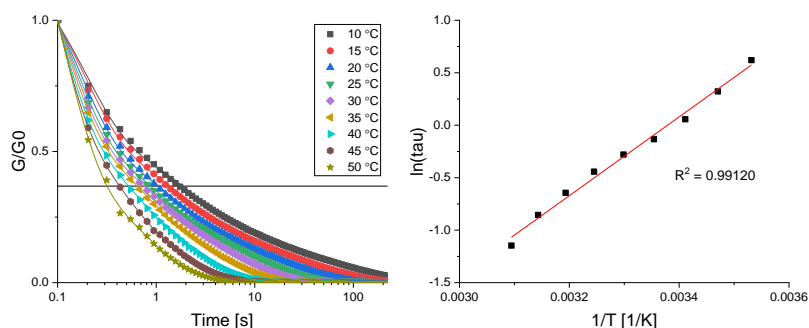
Figure 2.21 Stress relaxation curves (left) and Arrhenius plot (right) of **P-FDA**.
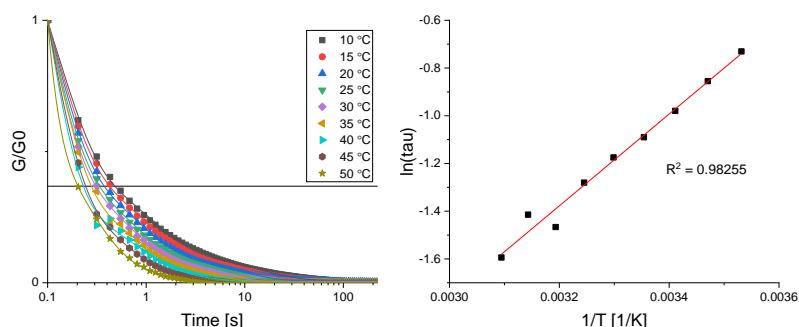
Figure 2.22 Stress relaxation curves (left) and Arrhenius plot (right) of **P-SDA**.

References

1. S. J. Rowan, S. J. Cantrill, G. R. L. Cousins, J. K. M. Sanders and J. F. Stoddart, *Angew. Chem. Int. Ed.*, 2002, **41**, 898-952.

2. P. T. Corbett, J. Leclaire, L. Vial, K. R. West, J.-L. Wietor, J. K. M. Sanders and S. Otto, *Chem. Rev.*, 2006, **106**, 3652-3711.

3. N. M. Rue, J. Sun and R. Warmuth, *Isr. J. Chem.*, 2011, **51**, 743-768.

4. M. E. Belowich and J. F. Stoddart, *Chem. Soc. Rev.*, 2012, **41**, 2003-2024.

5. C. D. Meyer, C. S. Joiner and J. F. Stoddart, *Chem. Soc. Rev.*, 2007, **36**, 1705-1723.

6. R. Tian, X. Fan, S. Liu, F. Li, F. Yang, Y. Li, Q. Luo, C. Hou, J. Xu and J. Liu, *Macromol. Rapid Commun.*, 2020, **41**, 1900586.

7. J. M. Winne, L. Leibler and F. E. Du Prez, *Polym. Chem.*, 2019, **10**, 6091-6108.

8. G. M. Scheutz, J. J. Lessard, M. B. Sims and B. S. Sumerlin, *J. Am. Chem. Soc.*, 2019, **141**, 16181-16196.

9.   Y. Jin, Z. Lei, P. Taynton, S. Huang and W. Zhang, *Matter*, 2019, **1**, 1456-1493.
10.   W. Zou, J. Dong, Y. Luo, Q. Zhao and T. Xie, *Adv. Mater.*, 2017, **29**, 1606100.
11.   C. J. Kloxin, T. F. Scott, B. J. Adzima and C. N. Bowman, *Macromolecules*, 2010, **43**, 2643-2653.
12.   F. García and M. M. J. Smulders, *J. Polym. Sci., Part A: Polym. Chem.*, 2016, **54**, 3551-3577.
13.   N. J. Van Zee and R. Nicolaÿ, *Prog. Polym. Sci.*, 2020, **104**, 101233.
14.   C. J. Kloxin and C. N. Bowman, *Chem. Soc. Rev.*, 2013, **42**, 7161-7173.
15.   M. Podgórski, B. D. Fairbanks, B. E. Kirkpatrick, M. McBride, A. Martinez, A. Dobson, N. J. Bongiardina and C. N. Bowman, *Adv. Mater.*, 2020, **32**, 1906876.
16.   D. Montarnal, M. Capelot, F. Tournilhac and L. Leibler, *Science*, 2011, **334**, 965-968.
17.   M. Capelot, D. Montarnal, F. Tournilhac and L. Leibler, *J. Am. Chem. Soc.*, 2012, **134**, 7664-7667.
18.   N. Bai, K. Saito and G. P. Simon, *Polym. Chem.*, 2013, **4**, 724-730.
19.   M. Fan, J. Liu, X. Li, J. Zhang and J. Cheng, *Ind. Eng. Chem. Res.*, 2014, **53**, 16156-16163.
20.   Y. Min, S. Huang, Y. Wang, Z. Zhang, B. Du, X. Zhang and Z. Fan, *Macromolecules*, 2015, **48**, 316-322.
21.   Q.-T. Li, M.-J. Jiang, G. Wu, L. Chen, S.-C. Chen, Y.-X. Cao and Y.-Z. Wang, *ACS Appl. Mater. Interfaces*, 2017, **9**, 20797-20807.
22.   M. Pepels, I. Filot, B. Klumperman and H. Goossens, *Polym. Chem.*, 2013, **4**, 4955-4965.
23.   J. Canadell, H. Goossens and B. Klumperman, *Macromolecules*, 2011, **44**, 2536-2541.
24.   Z. Q. Lei, H. P. Xiang, Y. J. Yuan, M. Z. Rong and M. Q. Zhang, *Chem. Mater.*, 2014, **26**, 2038-2046.
25.   L. Imbernon, E. K. Oikonomou, S. Norvez and L. Leibler, *Polym. Chem.*, 2015, **6**, 4271-4278.
26.   O. R. Cromwell, J. Chung and Z. Guan, *J. Am. Chem. Soc.*, 2015, **137**, 6492-6495.
27.   J. J. Cash, T. Kubo, A. P. Bapat and B. S. Sumerlin, *Macromolecules*, 2015, **48**, 2098-2106.
28.   A. Breuillac, A. Kassalias and R. Nicolaÿ, *Macromolecules*, 2019, **52**, 7102-7113.
29.   M. Röttger, T. Domenech, R. van der Weegen, A. Breuillac, R. Nicolaÿ and L. Leibler, *Science*, 2017, **356**, 62-65.
30.   Z. Wang, S. Gangarapu, J. Escorihuela, G. Fei, H. Zuilhof and H. Xia, *J. Mater. Chem. A*, 2019, **7**, 15933-15943.
31.   L. Zhang and S. J. Rowan, *Macromolecules*, 2017, **50**, 5051-5060.
32.   Y. Chen, H. Zhang, S. Majumdar, R. A. T. M. van Benthem, J. P. A. Heuts and R. P. Sijbesma, *Macromolecules*, 2021, **54**, 9703-9711.
33.   F. Van Lijsebetten, Y. Spiesschaert, J. M. Winne and F. E. Du Prez, *J. Am. Chem. Soc.*, 2021, **143**, 15834-15844.
34.   W. Denissen, M. Droesbeke, R. Nicolaÿ, L. Leibler, J. M. Winne and F. E. Du Prez, *Nat. Commun.*, 2017, **8**, 14857.

35.	W. Denissen, G. Rivero, R. Nicolaÿ, L. Leibler, J. M. Winne and F. E. Du Prez, *Adv. Funct. Mater.*, 2015, **25**, 2451-2457.
36.	S. Engelen, A. A. Wróblewska, K. De Bruycker, R. Aksakal, V. Ladmiral, S. Caillol and F. E. Du Prez, *Polym. Chem.*, 2022, **13**, 2665-2673.
37.	P. Taynton, K. Yu, R. K. Shoemaker, Y. Jin, H. J. Qi and W. Zhang, *Adv. Mater.*, 2014, **26**, 3938-3942.
38.	Z. Q. Lei, P. Xie, M. Z. Rong and M. Q. Zhang, *J. Mater. Chem. A*, 2015, **3**, 19662-19668.
39.	A. Chao, I. Negulescu and D. Zhang, *Macromolecules*, 2016, **49**, 6277-6284.
40.	F. García, J. Pelss, H. Zuilhof and M. M. J. Smulders, *Chem. Commun.*, 2016, **52**, 9059-9062.
41.	P. Taynton, C. Zhu, S. Loob, R. Shoemaker, J. Pritchard, Y. Jin and W. Zhang, *Polym. Chem.*, 2016, **7**, 7052-7056.
42.	M. Guerre, C. Taplan, J. M. Winne and F. E. Du Prez, *Chem. Sci.*, 2020, **11**, 4855-4870.
43.	R. J. Wojtecki, M. A. Meador and S. J. Rowan, *Nat. Mater.*, 2011, **10**, 14-27.
44.	P. Chakma and D. Konkolewicz, *Angew. Chem. Int. Ed.*, 2019, **58**, 9682-9695.
45.	Y.-J. Choi, Y. Lee, G. Bang, J. Jeong, N. Kim, J.-H. Lee and K.-U. Jeong, *Adv. Funct. Mater.*, 2019, **29**, 1905214.
46.	L. T. Roling, J. Scaranto, J. A. Herron, H. Yu, S. Choi, N. L. Abbott and M. Mavrikakis, *Nat. Commun.*, 2016, **7**, 13338.
47.	T. Shiraki, M. Morikawa and N. Kimizuka, *Angew. Chem. Int. Ed.*, 2008, **47**, 106-108.
48.	M. D. Perez, C. Borek, S. R. Forrest and M. E. Thompson, *J. Am. Chem. Soc.*, 2009, **131**, 9281-9286.
49.	V. V. Brus, J. Lee, B. R. Luginbuhl, S.-J. Ko, G. C. Bazan and T.-Q. Nguyen, *Adv. Mater.*, 2019, **31**, 1900904.
50.	M. Gerth and I. K. Voets, *Chem. Commun.*, 2017, **53**, 4414-4428.
51.	X. W. Sha, E. N. Economou, D. A. Papaconstantopoulos, M. R. Pederson, M. J. Mehl and M. Kafesaki, *Phys. Rev. B*, 2012, **86**, 115404.
52.	X. Yu, J. Zhou, H. Liang, Z. Jiang and L. Wu, *Prog. Mater. Sci.*, 2018, **94**, 114-173.
53.	K. Bertoldi, V. Vitelli, J. Christensen and M. van Hecke, *Nat. Rev. Mater.*, 2017, **2**, 17066.
54.	N. Van Herck, D. Maes, K. Unal, M. Guerre, J. M. Winne and F. E. Du Prez, *Angew. Chem. Int. Ed.*, 2020, **59**, 3609-3617.
55.	B. M. El-Zaatari, J. S. A. Ishibashi and J. A. Kalow, *Polym. Chem.*, 2020, **11**, 5339-5345.
56.	L. P. Hammett, *J. Am. Chem. Soc.*, 1937, **59**, 96-103.
57.	L. P. Hammett, *Chem. Rev.*, 1935, **17**, 125-136.
58.	C. Hansch, A. Leo and R. W. Taft, *Chem. Rev.*, 1991, **91**, 165-195.
59.	C. Hansch, A. Leo, S. H. Unger, K. H. Kim, D. Nikaitani and E. J. Lien, *J. Med. Chem.*, 1973, **16**, 1207-1216.
60.	H. Schiff, *Liebigs Ann.*, 1864, **131**, 118-119.

61. C. Luo, Z. Lei, Y. Mao, X. Shi, W. Zhang and K. Yu, *Macromolecules*, 2018, **51**, 9825-9838.
62. H. Zheng, Q. Liu, X. Lei, Y. Chen, B. Zhang and Q. Zhang, *J. Mater. Sci.*, 2019, **54**, 2690-2698.
63. H. Li, J. Bai, Z. Shi and J. Yin, *Polymer*, 2016, **85**, 106-113.
64. S. Dhers, G. Vantomme and L. Avérous, *Green Chem.*, 2019, **21**, 1596-1601.
65. H. Geng, Y. Wang, Q. Yu, S. Gu, Y. Zhou, W. Xu, X. Zhang and D. Ye, *ACS Sustainable Chem. Eng.*, 2018, **6**, 15463-15470.
66. S. Wang, S. Ma, Q. Li, W. Yuan, B. Wang and J. Zhu, *Macromolecules*, 2018, **51**, 8001-8012.
67. Y. Liu, Y. Zhang, Z. Cao and Z. Fang, *Ind. Eng. Chem. Res.*, 2012, **51**, 11059-11065.
68. X. He, Z. P. Lei, W. Zhang and K. Yu, *3d Print. Addit. Manuf.*, 2019, **6**, 31-39.
69. J. Pignanelli, B. Billet, M. Straeten, M. Prado, K. Schlingman, M. J. Ahamed and S. Rondeau-Gagné, *Soft Matter*, 2019, **15**, 7654-7662.
70. M. Kathan, C. Jurissek, P. Kovaříček and S. Hecht, *J. Polym. Sci., Part A: Polym. Chem.*, 2019, **57**, 2378-2382.
71. J. Leclaire, G. Husson, N. Devaux, V. Delorme, L. Charles, F. Ziarelli, P. Desbois, A. Chaumonnot, M. Jacquin, F. Fotiadu and G. Buono, *J. Am. Chem. Soc.*, 2010, **132**, 3582-3593.
72. J. Wang, I. Senkovska, M. Oschatz, M. R. Lohe, L. Borchardt, A. Heerwig, Q. Liu and S. Kaskel, *J. Mater. Chem. A*, 2013, **1**, 10951-10961.
73. C. Xu, Z. Bacsik and N. Hedin, *J. Mater. Chem. A*, 2015, **3**, 16229-16234.
74. X. Xu, S. Ma, J. Wu, J. Yang, B. Wang, S. Wang, Q. Li, J. Feng, S. You and J. Zhu, *J. Mater. Chem. A*, 2019, **7**, 15420-15431.
75. Z. Zou, C. Zhu, Y. Li, X. Lei, W. Zhang and J. Xiao, *Sci. Adv.*, 2018, **4**, eaaq0508.
76. Y. Liu, Z. Tang, J. Chen, J. Xiong, D. Wang, S. Wang, S. Wu and B. Guo, *Polym. Chem.*, 2020, **11**, 1348-1355.
77. R. Hajj, A. Duval, S. Dhers and L. Avérous, *Macromolecules*, 2020, **53**, 3796-3805.
78. R. Mo, J. Hu, H. Huang, X. Sheng and X. Zhang, *J. Mater. Chem. A*, 2019, **7**, 3031-3038.
79. P. Taynton, H. Ni, C. Zhu, K. Yu, S. Loob, Y. Jin, H. J. Qi and W. Zhang, *Adv. Mater.*, 2016, **28**, 2904-2909.
80. C. Zhu, C. Xi, W. Doro, T. Wang, X. Zhang, Y. Jin and W. Zhang, *RSC Adv.*, 2017, **7**, 48303-48307.
81. S. Wang, S. Ma, Q. Li, X. Xu, B. Wang, K. Huang, Y. liu and J. Zhu, *Macromolecules*, 2020, **53**, 2919-2931.
82. P. Kovaříček and J.-M. Lehn, *J. Am. Chem. Soc.*, 2012, **134**, 9446-9455.
83. D. Schultz and J. R. Nitschke, *J. Am. Chem. Soc.*, 2006, **128**, 9887-9892.
84. J. Clayden, N. Greeves and S. G. Warren, *Organic chemistry*, Oxford University Press, Oxford ; New YorK, 2nd edn., 2012.
85. H. Zheng, Q. Liu, X. Lei, Y. Chen, B. Zhang and Q. Zhang, *J. Polym. Sci., Part A: Polym. Chem.*, 2018, **56**, 2531-2538.

86. M. Ciaccia, R. Cacciapaglia, P. Mencarelli, L. Mandolini and S. Di Stefano, *Chem. Sci.*, 2013, **4**, 2253-2261.
87. W. Denissen, J. M. Winne and F. E. Du Prez, *Chem. Sci.*, 2016, **7**, 30-38.
88. W. Denissen, I. De Baere, W. Van Paepegem, L. Leibler, J. Winne and F. E. Du Prez, *Macromolecules*, 2018, **51**, 2054-2064.
89. A. Jourdain, R. Asbai, O. Anaya, M. M. Chehimi, E. Drockenmuller and D. Montarnal, *Macromolecules*, 2020, **53**, 1884-1900.
90. M. M. Obadia, A. Jourdain, P. Cassagnau, D. Montarnal and E. Drockenmuller, *Adv. Funct. Mater.*, 2017, **27**, 1703258.
91. P. Chakma, Z. A. Digby, M. P. Shulman, L. R. Kuhn, C. N. Morley, J. L. Sparks and D. Konkolewicz, *ACS Macro Lett.*, 2019, **8**, 95-100.
92. P. Chakma, C. N. Morley, J. L. Sparks and D. Konkolewicz, *Macromolecules*, 2020, **53**, 1233-1244.
93. B. R. Elling and W. R. Dichtel, *ACS Cent. Sci.*, 2020, **6**, 1488-1496.
94. P. W. Atkins and J. De Paula, *Physical chemistry*, W.H. Freeman and Company, New York, Ninth Edition. edn., 2010.
95. E. N. D. C. Andrade and F. T. Trouton, *Proc. R. Soc. A*, 1910, **84**, 1-12.
96. E. N. D. C. Andrade and A. W. Porter, *Proc. R. Soc. A*, 1914, **90**, 329-342.
97. M. Siebenbürger, M. Ballauff and T. Voigtmann, *Phys. Rev. Lett.*, 2012, **108**, 255701.
98. J. M. Hutchinson, *Prog. Polym. Sci.*, 1995, **20**, 703-760.
99. M. E. Kassner and M. T. Pérez-Prado, *Prog. Mater. Sci.*, 2000, **45**, 1-102.
100. M. Capelot, M. M. Unterlass, F. Tournilhac and L. Leibler, *ACS Macro Lett.*, 2012, **1**, 789-792.

Chapter 3

Raman Spectroscopy Reveals Phase Separation in Imine-based Covalent Adaptable Networks
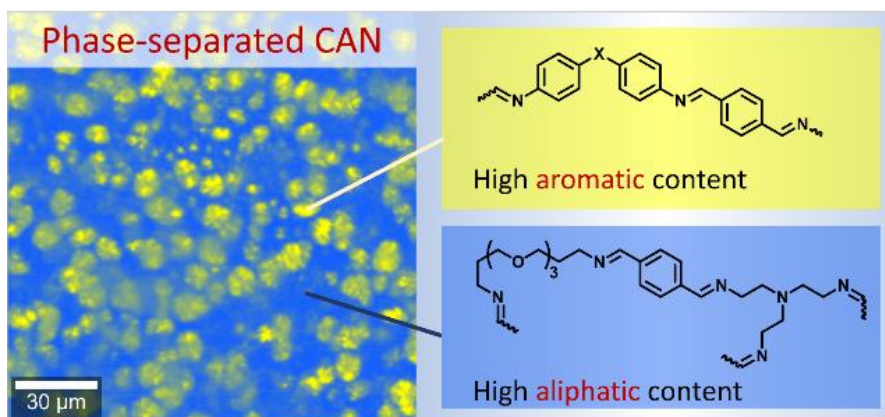
This work was published as:

S. K. Schoustra, M. H. P. de Heer Kloots, J. Posthuma, D. van Doorn, J. A. Dijksman, M. M. J. Smulders, *Macromolecules*, 2022, **55**, 10341-10355.

*This work was featured on a cover in Macromolecules, Issue 23 (13 December 2022)

Abstract

The introduction of dynamic covalent bonds into crosslinked polymer networks enables the development of strong and tough materials that can still be recycled or repurposed in a sustainable manner. To achieve the full potential of these covalent adaptable networks (CANs), it is essential to understand –and control– the underlying chemistry and physics. In particular, understanding the structure of the network architecture that is assembled dynamically in a CAN is crucial, as exchange processes within this network will affect the dynamic-mechanical material properties. In this context, the introduction of phase separation in different network hierarchies has been proposed as a useful handle to control or improve the material properties of CANs. Here we report how Raman confocal microscopy can be used to visualise phase separation in imine-based CANs on the scale of several micrometres. Independently, AFM also confirmed phase separation. Remarkably, the materials were found to undergo phase separation despite being built up from miscible monomers, which arguably should yield homogeneous materials. We found that the phase separation did not only affect the appearance of the material, but also had a noticeable effect on the thermal mechanical properties of the material: CANs (of equal aliphatic/aromatic monomer composition) that displayed phase separation had a higher crossover temperature (at which the material transitions from a rubbery to a viscous state), and an increased elastic modulus (G'). By modifying the CAN architecture, we were able to either suppress or induce phase separation, and it is proposed that the phase separation is driven by favourable $\pi-\pi$ interactions between the aromatic components. Our work further shows the potential of phase separation in CANs, including in networks built from miscible components, and provides a handle to control the dynamic material properties. Moreover, our work underlines the suitability of Raman imaging as a method to visualise phase separation in CANs.

3.1 Introduction

Thermosets have a permanent crosslinked polymer network structure that gives them high material strength and resistance against many environments, which makes them suitable for many industrial applications. However, due to this permanent network structure, thermosets cannot be easily recycled or repurposed once they have been produced. Therefore, the use of current thermosetting materials is not sustainable. To overcome this problem, dynamic covalent bonds can be introduced within the polymeric structure to construct covalent adaptable networks (CANs) that enable reprocessability and recyclability.[1, 2] These dynamic covalent bonds can be just as strong as their non-reversible covalent counterparts, and as such do not decrease the strength of the material. What makes dynamic covalent bonds so interesting, is that they can perform bond exchange reactions.[3, 4] This bond exchange requires some sort of activation, which is generally achieved with heat, but other triggers (*e.g.,* light or pH) are known as well.[5] In some cases a catalyst may be required, that can either be external or internal.[6-9] The ability to exchange covalent bonds in the polymeric network of thermosets enables the material to flow, and as such facilitates (re)processability.

The potential of CANs to replace or improve classical thermosets has inspired many researchers to develop and study the underlying chemistry and physics.[10-14] Many of these studies involved application of different dynamic chemistries, each with its characteristic properties based on the nature of the bond exchange reaction.[15-19] Examples of different dynamic chemistries include transesterification reactions,[20-22] disulphide exchange,[23-27] Diels-Alder reactions,[28-30] (vinylogous) urethane exchange,[31-36] dioxaborolane metathesis,[37-40] and imine exchange.[41-46] In addition to the various types of bond exchange chemistries, further tunability of the bond exchange has been investigated. These include, for example, steric or electronic effects (see also **Chapter 2**) with regards to the reactive groups,[47-50] neighbouring group participation,[6, 21, 39, 51] or effects from the accompanying polymer matrix.[52-55]

An ongoing challenge for CANs is to strike a balance between allowing the material to be processed at elevated temperature (*i.e.*, the processing temperature), while at the operating temperature (typically room temperature) the material is robust, displaying no creep.[56, 57] A variety of approaches has been explored to achieve this combination: *e.g.*, by combining different types of dynamic covalent bonds (each with their own temperature-dependent exchange profile),[58-64] adding non-dynamic crosslinks,[56, 65] or relying on a dynamic covalent bond motif with a dual-temperature response.[66]

Chapter 3

Apart from these more chemistry-based approaches, recently also more physical approaches relying on aggregation and phase separation have been proposed.[67-74] For linear polymers the effects of phase separation have already been thoroughly studied over several decades,[75-79] and results have revealed an distinct enhancement in material properties: *e.g.*, Matyjaszewski *et al.* reported on phase separation in PBA-*b*-PS copolymers,[80] and revealed that non-phase-separated materials showed a rapid decrease in storage modulus (G') when heated and started flowing around 120 °C, while phase-separated materials exhibited an extended rubbery plateau with a G' of ~30 MPa and started to flow around 180 °C. In an analogous fashion, several promising approaches to induce phase separation into CANs for enhanced material properties have been developed. For example, grafting of dynamic covalent motifs onto incompatible polymer backbones has been found to result in phase separation.[81-83] In addition, potential polarity effects and hydrogen bonding by the polymer backbones have been suggested as a cause for phase separation.[29, 84, 85] Phase separation was also observed for block copolymers that incorporated co-existing dynamic and non-dynamic blocks,[54, 86] or in polymer networks with blended rigid and soft polymers.[87] A general response of these phase-separated CANs was that the material properties of the bulk materials could be significantly enhanced, which can be expressed in, for example, a higher Young's modulus,[29] or better creep resistance.[54] As such, a better understanding of the process and effects of phase separation in CANs can be key to a new handle in the design of robust –yet dynamic– materials.

In the above examples the polymers were designed such that a phase separation was intentionally induced, for example by selecting incompatible structures or by mixing amorphous and crystalline components. In contrast, the polyimine CANs reported herein were found to display phase separation despite being built up from miscible monomers, which arguably should yield homogeneous materials. We were able to visualise this phase separation of different dynamic domains in the range of several micrometres with Raman confocal spectroscopy. While regularly used for conventional polymers to study for example the polymer structure,[88] polymerisation kinetics,[89] or crystallinity,[90] the use of Raman spectroscopy in CANs has largely been overlooked, with the few reported examples of usage being limited to verification of formed bonds or structures.[91, 92] To the best of our knowledge, we are the first to apply Raman imaging to construct 2D images to reveal chemically different, phase-separated domains within the CAN bulk. We were able to construct these images owing to characteristic and unique bond energies of chemically distinctive imines and aromatic moieties. The fact that Raman could distinguish between the very slight differences in molecular composition makes it a very powerful tool to construct images based solely on these small molecular differences (*e.g.*, between different aromatic or imine signals).[93, 94] The method is also largely insensitive to the physical

appearance of the material. For example, factors such as surface roughness or other inhomogeneities have little impact on the construction and quality of the Raman images. This chemically selective, yet robust, method is also what makes it different from other conventional techniques to study phase separation, such as atomic force microscopy (AFM), scanning electron microscopy (SEM), or X-Ray diffraction (XRD). The further ease of the Raman setup and the relatively short time it takes to construct the Raman images (generally within several minutes, depending on size and resolution of the image), add to the value of choosing Raman over other methods.[95] In addition, the minimal sample preparation for Raman spectroscopy is a major advantage.[94] Samples as thin as a monolayer can be analysed, whereas there is (technically) no upper limit in sample thickness. Raman scattering can, however, only be excited as far in the sample as the light can penetrate.[96] Raman imaging is able to provide detailed images on the micrometre scale, which is a typical length scale for this method, and still above the diffraction limit of the resolution. Limitations occur below 100 nm. It should also be noted that while Raman imaging proved especially useful in the analysis of the different aromatic and imine structures in this work, in other systems overlap of distinctive signals might potentially cause problems to distinguish specific groups.

The Raman imaging served as the key methodology for the visualisation of phase separation in our polyimine CANs. First, we applied Raman imaging on earlier reported **P-XDA** polyimines (Figure 3.1, see also **Chapter 2** of this thesis),[47] revealing phase separation into different domains that were unknown to exist before. Second, by systematically exploring different compositions of the polymers, we found that the occurrence of the phase separation was directly related to the structure and concentration of the dianiline (**XDA**) monomer. The driving force for phase separation was found to be related to interactions between the aromatic components in the polymer network. Last, we also observed several noticeable changes in physical properties of the materials as a consequence of the phase separation. The phase separation generally resulted in mechanically more robust materials. First, the temperature at which the material transits from rubbery to viscous phase was greatly enhanced, and second, the elastic modulus of the materials was found to increase when phase separation was observed. We also observed that phase-separated materials appeared turbid, whereas non-phase-separated materials appeared transparent.
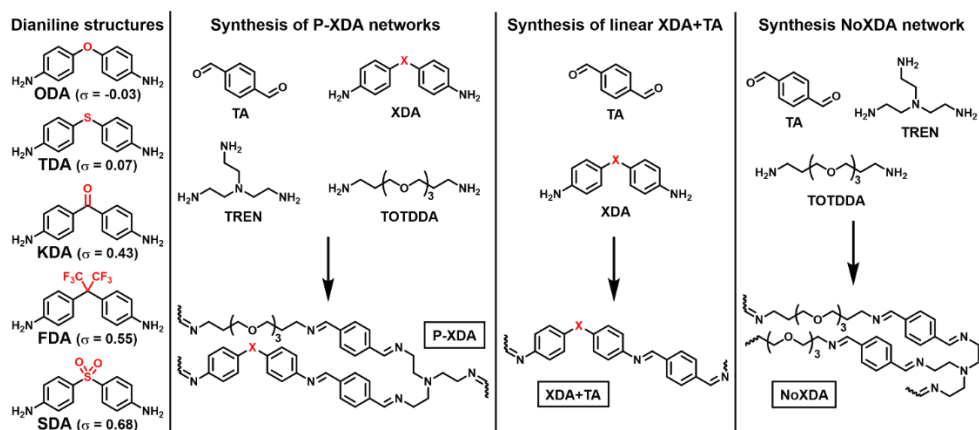
Figure 3.1 Overview of building blocks for the synthesis of polyimines. The **P-XDA** polymer networks contain dialdehyde **TA**, crosslinker **TREN**, flexible linker **TOTDDA**, and either one of the five **XDA** dianilines shown on the left. Linear **XDA+TA** polymers do not contain **TOTDDA** or **TREN**. The **NoXDA** network does not contain any dianilines. The Hammett parameter (σ) of each **XDA** monomer expresses the electron-withdrawing effect of the bridging substituent (highlighted in red).

3.2 Results and Discussion

3.2.1 Raman spectroscopy

For the analysis with Raman spectroscopy five different **P-XDA** polyimines were synthesised following our previously published protocol,[47] with dianiline contents of 20% (see Figure 3.1, and **Chapter 2** for the additional experimental details). The polymers were prepared by dissolving the amines (**XDA**, **TOTDDA** and **TREN**) in THF, to which then the terephthalaldehyde (**TA**) was added. The mixture was shaken briefly and then poured into a petri dish. After solvent evaporation (first to air, later in a vacuum oven at 50 °C), the polymer films were obtained. These were subsequently analysed by Raman spectroscopy (full experimental details are given in Section 3.5).

In addition to the five **P-XDA** polymers, to elucidate the spectral features, several additional polymers were synthesised that contained selective parts of the full polymer composition. These consisted of polymers from only dianiline and terephthalaldehyde (**XDA+TA**) and a polymer with all components except the dianiline (**NoXDA**) (see Figure 3.1). The Raman spectra of all **P-XDA** materials were compared to the spectra of the corresponding **XDA+TA** and **NoXDA** materials (see Figure 3.2 for **P-TDA**, and Section 3.5.2 for all other materials).
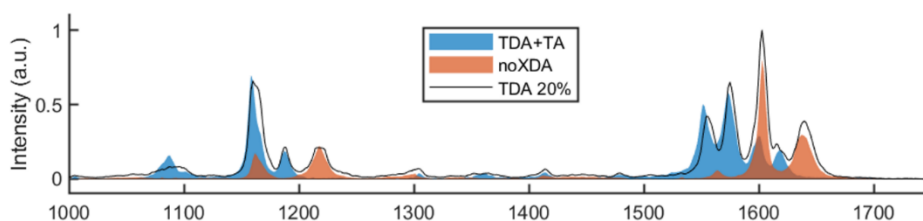
Figure 3.2 Overlapping Raman spectra of a **TDA+TA** polymer (blue) and a polymer matrix of **TOTDDA**, **TREN**, and **TA** (**NoXDA**, orange). Combining the two individual spectra matches that of the **P-XDA 20** material (black line).

The Raman spectra showed three common regions in which Raman signals were observed: 0–200 cm^{-1}, 1100–1250 cm^{-1}, and 1500–1700 cm^{-1} (see Section 3.5.2 for all spectra). The signals in the region of 0–200 cm^{-1} could be ascribed mostly to the aliphatic parts of the material, and were found to be rather uninformative with respect to material composition. The other two regions contained the most characteristic data regarding the distinct aromatic moieties and imines. These include both common signals for all samples, and sample-specific signals. Each individual signal of the **P-XDA** materials was then assigned to the corresponding bond vibration in the material, based on data from the synthesised analogues (**XDA+TA** and **NoXDA**) and data of analogous structures reported in literature.[97-102] An overview of the assigned Raman signals is presented in Table 3.1 and a further elaboration is given in Section 3.5.2.

Table 3.1 Assignment of Raman signals to corresponding parts in the polyimine materials. All signals were assigned by comparison to synthesised analogues of **TA+XDA** and **NoXDA**, and to reported spectra of analogous materials.

Wavenumber (cm^{-1})	Vibration	Monomer(s)	Reference(s)
1140–1160[a]	Phenyl C–H bend	**XDA**	Badawi (2013),[99] Nandi (2017),[100] John (2018),[101] Ullah (2019)[102]
1163[b]	Phenyl C–H bend	**TA**	Nandi (2017),[100] John (2018)[101]
1184–1190[a]	Imine C–N stretch	**XDA**	Nandi (2017)[100]
1218[b]	Imine C–N stretch	**TOTDDA, TREN**	Nandi (2017)[100]
1557–1560[a]	Phenyl C=C stretch	**XDA**	John (2018)[101]
1563[a]	Phenyl C=C stretch	**TA**	John (2018)[101]
1584–1585[a]	Phenyl C=C stretch	**XDA**	Lee (2003),[97] Ullah (2019)[102]
1602[b]	Phenyl C=C stretch	**TA**	Lee (2003),[97] Ullah (2019)[102]
1619–1624[a]	Imine C=N stretch	**XDA, TA**	Nandi (2017),[100] John (2018)[101]
1638[b]	Imine C=N stretch	**TOTDDA, TREN, TA**	Lee (2003),[97] Knöpke (2010),[98] Nandi (2017),[100] John (2018)[101]

[a] Indication that the signal is sample specific. [b] Indication that the signal is coherent for all materials.

3.2.2   Raman imaging of **P-TDA**

When scanning the surface of the **P-XDA** materials using the Raman confocal microscope, we recorded a 2D spectroscopic map and found two distinctly different spectra. These spectra resembled either that of the **XDA+TA** or the **NoXDA** material. This suggested two domains in the material; one containing mostly the aliphatic components (spectrum corresponding to **NoXDA**, in which only aliphatic imines, formed by reaction between **TOTDDA**, **TREN** and **TA**, are present), and one containing mostly aromatic components (spectrum corresponding to **XDA+TA**, in which only aromatic imines, formed by reaction between **XDA** and **TA**, are present). To distinguish between the two types of spectra, we let the accompanying WITec software determine for every pixel to which of the two reference spectra the recorded spectrum best fitted to, and the pixel was coloured accordingly. For all further analyses we assigned a yellow colour to a best fit of **XDA+TA**, and a blue colour to a best fit of **NoXDA**.

The first material for which such a Raman image was constructed was **P-TDA** (Figure 3.3, left). The image revealed a clear phase separation between yellow and blue domains, in which the yellow-coloured domains (**TDA+TA** phase), which had a size of approximately 10–20 µm, separated from the blue coloured matrix (**NoXDA** phase). To verify whether the phase separation remained stable over time, a new Raman image was constructed after two months (Figure 3.3, middle). This image showed a similar phase-separated profile, and thus confirmed stability of the phase separation over time. Next, a sheet of **P-TDA** material was cut into smaller pieces and hot-pressed (100 °C for 30 min) into a new recycled polymer film. The Raman image of this recycled film also gave the same result (Figure 3.3, right). These results thus suggest that the phase separation is thermodynamically favourable as it persists over time and after thermal reprocessing.
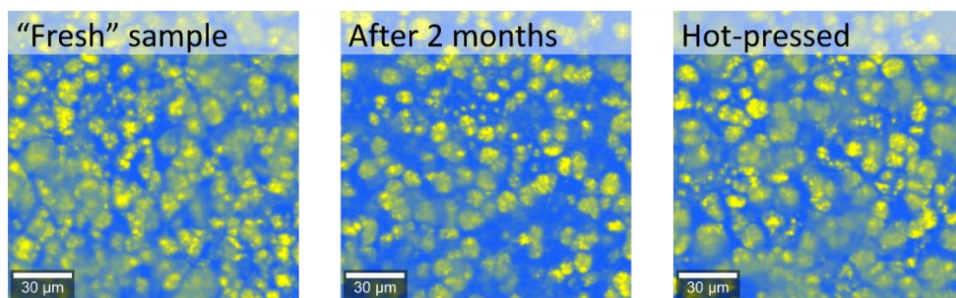

Figure 3.3 Raman images of **P-TDA 20** samples; directly after the synthesis (left) after 2 months (middle) and after hot-pressing (right). The yellow crystal-like domains indicate the regions where **TDA+TA** is predominantly present, and the blue regions represent a matrix of **TOTDDA+TREN+TA** (**NoXDA**) around the separated domains.

To further investigate the occurrence of phase separation, samples of **P-TDA** were prepared with lower concentrations of the dianiline monomer (*i.e.*, lower relative amount of aromatic *versus* aliphatic segments). Both Brightfield and Raman images were recorded for each of the samples (Figure 3.4).
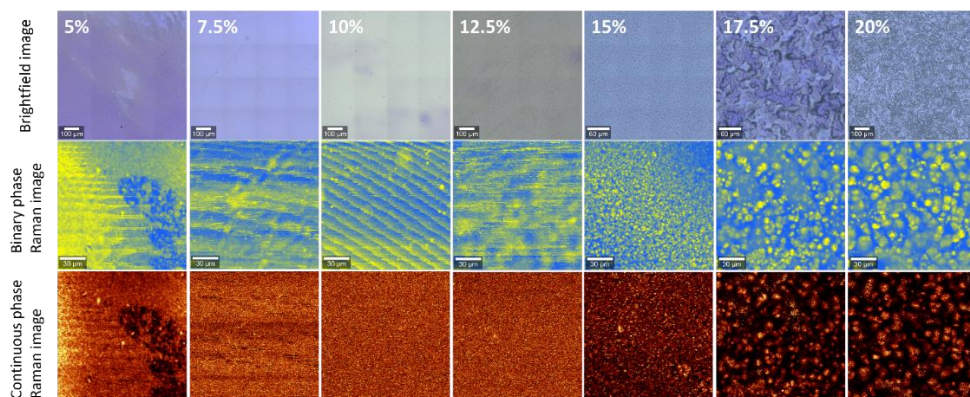

Figure 3.4 Brightfield and Raman images of **P-TDA** materials with varying dianiline concentrations from 5% to 20% (left to right, respectively). For the Raman images, a division was made between images constructed by applying either a binary fitting scale (middle row) or a continuous scale (bottom row).

The Brightfield images suggested a certain surface pattern for the **P-TDA** samples with 17.5% and 20% dianiline content, but conclusive evidence for phase separation was only seen from the Raman images. These images showed that above 17.5% **TDA** phase separation could be clearly observed. At 15% the phase separation was still observed, although the domains appeared smaller in size. Below 12.5% **TDA** no clear phase separation was observed anymore, but rather uninformative images were obtained from the binary fit. These indistinct images are the result of the forced extraction of two components. When the sample is homogeneous (no phase separation), the forced division into two different domains by the software can then show false patterns. This artefact can be clearly seen in the 10% **TDA** sample.

Although the initial binary fit can serve as a fast check to spot phase separation, the method would benefit from extension to a continuous scale fit. Such a continuous scale could also give more information on the exact composition of the phases. In other words: a continuous scale to characterise the relevant features in the Raman spectra no longer provides an all-or-nothing determination of two phases, but can also show how strict the border between the phases is. To construct continuous phase images, we introduced a 256-step scale based

on peak area ratios in the Raman spectra, which was performed for each individual pixel (see Section 3.5.4 for additional experimental details). The continuous-scale Raman images could generally nicely filter noise and artefacts (especially when there was no phase separation), although the choice for a binary fit could in most cases more clearly (and faster) show the contrast between phases when phase separation was observed. For the best representation of results, we therefore generally included both binary and continuous-scale Raman images.

From the processed continuous Raman images (see Figure 3.4, bottom row), we could then conclude that phase separation did not occur for any of the samples with a **TDA** concentration of 12.5% and lower. At 15% **TDA** we observed the first hints of phase separation, which became clearer when further increasing the concentration of **TDA**. These results thus suggest existence of a critical concentration of 15% **TDA**, above which phase separation occurs. Below this threshold concentration the dianiline parts can still blend in with the rest of the matrix; above the threshold they separate into isolated domains. Despite the crystal-like appearance of the phase-separated **TDA**-rich domains, DSC of 10% and 20% **TDA** materials did not reveal any thermal transition that could be assigned to the melting transition of the phase-separated domains or the accompanying matrix (see Supporting Information, Section 3.5).

As an additional analytical method to confirm phase separation, atomic force microscopy (AFM) was applied. First, a height (Figure 3.5A) and phase (Figure 3.5B) image of **P-TDA 20** were constructed. The AFM images showed a similar phase separation in sphere-like hard domains, entrapped in a soft matrix. The size of the phase-separated domains appeared smaller than was observed with Raman. This was attributed to the fact that AFM only scanned the surface of the film, and as such only observed the top of the spherical hard phases. In contrast, with Raman, the entire upper layer of the film (up to several micrometres) can be visualised. Next, AFM images were constructed of **P-TDA 5** (Figures 3.5C and 3.5D, for height and phase, respectively), which revealed the absence of phase-separated domains at low **TDA** concentrations, in line with the Raman images.
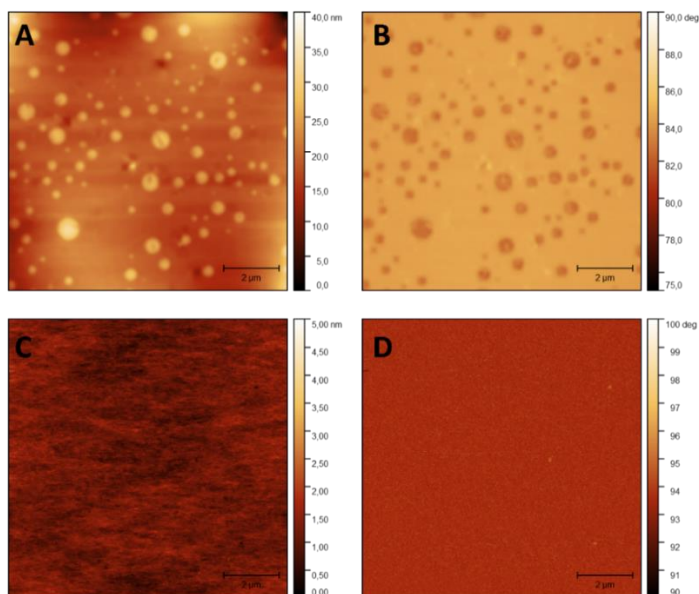
Figure 3.5 AFM images **of P-TDA** materials. A) height profile of **P-TDA 20**, B) phase profile of **P-TDA 20**, C) height profile of **P-TDA 5**, D) phase profile of **P-TDA 5**. The AFM images show a clear phase separation for **P-TDA 20**, whereas for P-TDA 5 no phase separation is observed, confirming the results from the Raman images. Note the difference height scales in panel A and C.

To further study the size and shapes of the phase-separated domains, Raman scans of **P-TDA 15** and **P-TDA 20** were constructed slightly deeper below the surface up until roughly 10 µm (see Supporting Information, Section 3.5). In these images, the phase-separated domains gradually increase in size by several µm (ultimately doubling in size) when moving deeper into the sample. In order to study the dimensions and distribution of the domains in greater detail, 3D multiphoton fluorescence lifetime microscopy was used. A 3D image of **P-TDA 20** was constructed by recording the fluorescence that specifically arose from the distinctive aromatic moieties in the system (Figure 3.6). The image showed phase-separated domains with an approximately spherical shape on a similar scale as was observed by Raman. A cross-section image (Figure 3.6B) indicated that the phase-separated domains appeared smaller and more densely packed near the surface of the film compared to the phase-separated domains deeper in the sample, in line with the observation by AFM of smaller domains at the surface (Figure 3.5). This suggests different dynamic behaviour between the CAN surface and bulk, as has been proposed in recent work by Liu and Wang.[103]
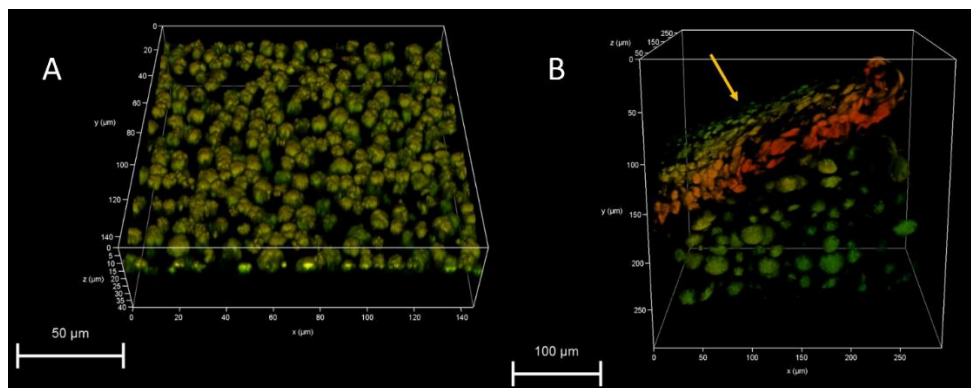
Figure 3.6 A) 3D multiphoton fluorescence lifetime image of the surface of **P-TDA 20**, and B) cross section image of the **P-TDA 20** sample (the yellow arrow indicates the surface of the sample). The coloured parts show the phase-separated domains of **TDA+TA**; the red colour indicates nearby phases, and the greener colours indicate phases further away.

We considered that solvation and drying effects during the formation of the polymer films might affect the phase-separating process.[104-107] In an attempt to study the formation of polymer clusters in solution, dynamic light scattering (DLS) was applied. Solutions were prepared by mixing the monomers for several phase-separating and non-phase separating materials, and with DLS we checked for the formation and size of formed particles in solution over time. Unfortunately, these results could not reveal any underlying dynamics regarding the formation of particles that could be linked to phase separation.

Next, in addition to the standard preparation of the polymer films in THF,[47] **P-TDA 20** films were prepared in different solvents; being either 2-methyltetrahydrofuran (2-MeTHF), methanol, ethyl acetate or toluene. Brightfield and Raman images were constructed of the polymer films (see the Supporting Information, Section 3.5), which all showed a similar phase separation as was seen before. We also prepared several thinner films of **P-TDA 20** to check for potential effects of film thickness on the size and distribution of the microdomains (see the Supporting Information, Section 3.5), but could not identify any observable differences either. The consistency of the combined results underlines the robustness of the preparation for the polyimine materials, as it appears that neither the scale nor the solvent in the material synthesis seemed to affect the occurrence of the phase separation. In favour of this result, in future work we could thus easily adjust the scale of the preparation or switch to greener solvents, such as 2-MeTHF, without observable negative consequences for the prepared polymer material.

3.2.3 Phase separation for other dianilines

After studying the phase separation for the **TDA**-based polymers, the other four dianilines from our earlier work (described **in Chapter 2** of this thesis)[47] were used to prepare their corresponding CANs (see Figure 3.1), and Raman images were again recorded. First, **ODA** was investigated as this was structurally the most similar dianiline to **TDA**. The Raman images of **P-ODA** revealed a clear phase separation, although some differences compared to **P-TDA** were noted. First, the phase separation occurred already at a dianiline concentration of 7.5% for **P-ODA** (Figure 3.7A), compared to 15% for **P-TDA** (Figure 3.4). Second, the shape of the phase-separated domains was slightly different: for **P-ODA** they appeared needle-like, whereas for **P-TDA** they appeared sphere-like. In terms of their chemical structure, **TDA** and **ODA** are rather similar (Figure 3.1). However, the Hammett parameter (σ) for **ODA** is higher than that of **TDA**. This translates to a higher electron-donating effect from the **ODA** towards the imines, which in turn affects the kinetics of the bond exchange.[47] From this perspective, the internal kinetics of the bond exchange might play a role in the character of the phase separation.
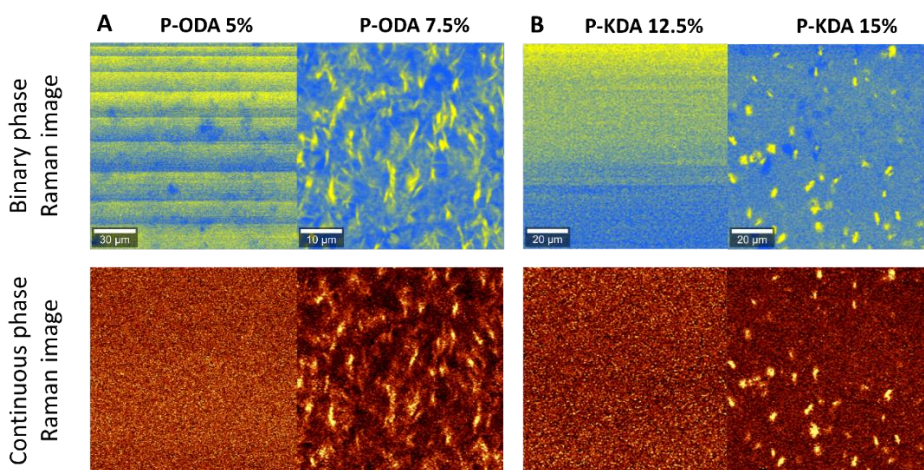
Figure 3.7 Raman images of A) **P-ODA** and B) **P-KDA** samples. The images show that for **P-ODA** phase separation occurs above a dianiline content of 7.5%, while for **P-KDA** a dianiline content of 15% is required at minimum. Binary and continuous colour coding of the phases are included.

Next, the more electron-withdrawing **KDA** monomer was investigated. The Raman images of **P-KDA** indicated a similar phase separation as was seen for **P-TDA**, with the threshold for the phase separation at 15% dianiline content (Figure 3.7B), although the phase-separated

domains appeared slightly smaller in size. Surprisingly, materials of the two most electron-withdrawing dianilines (**FDA** and **SDA**) did not show any observable phase separation, even when increasing the dianiline content to as high as 50% (see the Supporting Information, Section 3.5). We considered two possible hypotheses for these observations. First, because of the strong electron-withdrawing nature of the substituents, the stability of the imines is decreased in case of **FDA** and **SDA**.[108, 109] As such the susceptibility towards exchange reactions increases.[47] This increased reactivity results in more efficient bond exchange with the imines from the aliphatic matrix,[110] and could prevent separation into different phases. Alternatively, the steric bulk of the **FDA** and **SDA** monomers is (slightly) higher compared to the other three (**ODA, TDA** and **KDA**) monomers. This increased steric bulk of the variable bridging moiety in the **XDA** monomer may prevent efficient stacking of the two aromatic rings of the **XDA** monomer, and therefore hamper the phase separation process.
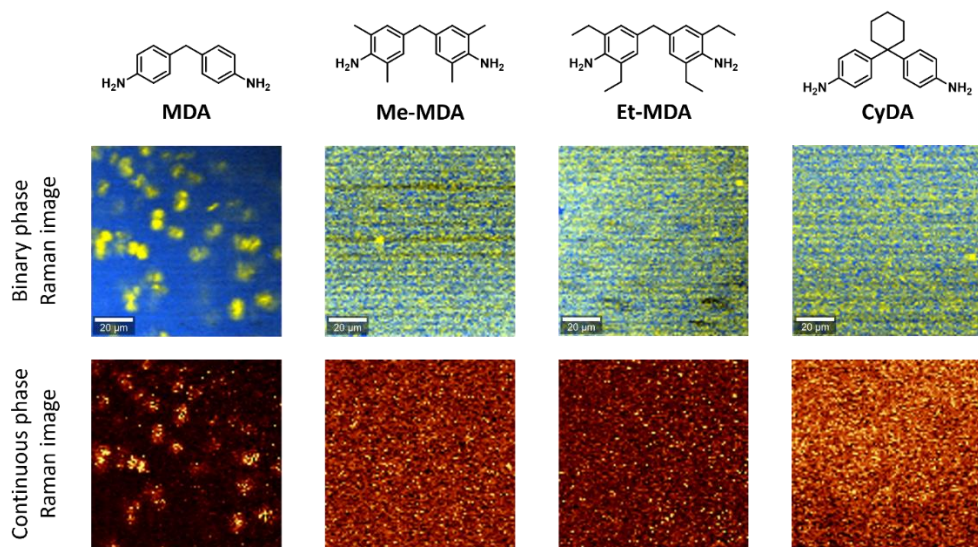
Figure 3.8 Structure and Raman images of dianilines with different steric substituents. The Raman images show that phase separation was clearly observed for the non-hindered **P-MDA**, but not for the sterically hindered analogous materials. For all materials the dianiline content was 20%. Binary and continuous colour coding of the phases are included.

To further the study steric effects, several additional (commercially available) dianilines were selected to synthesise additional materials (Figure 3.8). First, a sterically non-hindered 4,4'-methylenedianiline (**MDA**) was selected to serve as a reference. If the phase separation would be caused by electronic effects, based on the Hammett parameter for this

monomer,[111-113] it is expected to show a similar phase separation as **P-TDA** and **P-ODA**. This was also confirmed from the Raman image (Figure 3.8). Then, several additional polymers were prepared from dianilines with a similar electronic effect but increased steric bulk. We first selected dianilines with alkyl groups (methyl or ethyl, for **Me-MDA** and **Et-MDA**, respectively) on both *ortho* positions next to the amine group on the aromatic ring. In addition, we selected a dianiline monomer with a bulky cyclohexyl substituent on the bridging sp[3] carbon (**CyDA**). Raman images from the sterically materials (Figure 3.8) concluded that none of them showed phase separation, strongly suggesting that steric effects in relation to π–π stacking indeed affect the occurrence of phase separation. These observations were also in line with results from ureidopyrimidone (UPy)-based supramolecular polymers, for which a disappearance in microphase separation was noticed with increasing steric hindrance on the pyrimidone moieties.[114, 115] It was demonstrated that the branching effect of substituents suppresses aggregation, as larger steric groups hinder efficient π–π stacking and prevent phase separation. Similarly, the branched dianilines in our study could suppress aggregation of **XDA+TA** domains and prevent phase separation.
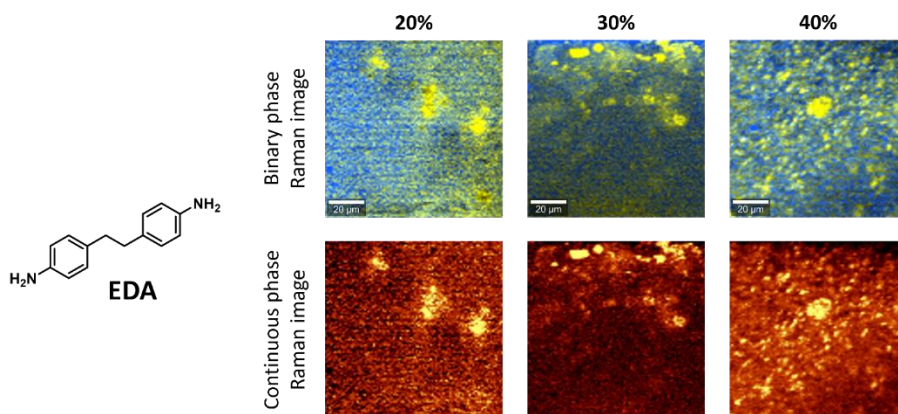
Figure 3.9 Raman images of **P-EDA** materials with 20, 30 and 40% dianiline content. Phase separation was observed for all samples, although less clearly than was seen for **P-MDA**. Binary and continuous colour coding of the phases are included.

A final dianiline monomer was selected that contained a longer ethylene moiety as bridge (**EDA**) (Figure 3.9). The Hammett parameters for methyl (σ = −0.17) and ethyl (σ = −0.15) substituents are similar,[111] however, the rotational freedom of the ethylene is higher due to the longer chain length. The increased flexibility could as a result affect the stacking of the aromatic moieties. The Raman image of **P-EDA** (Figure 3.9) did indicate phase

separation, although less clearly than was seen for **P-MDA**. Phase-separated domains were observed, but the matrix around them did not appear to be entirely free of **EDA** signal, which suggests mixing of **EDA** with the rest of the matrix. Increasing the dianiline content to 30% and 40% yielded similar Raman images to the results at 20%. The lesser degree of phase separation for **P-EDA** compared to **P-MDA** may be explained by the difference in the rigidity of the two monomers. The two dianilines are more rigid than the aliphatic amines in the polymer matrix. As such, the phase separation leads to a division in "hard" aromatic segments and "soft" aliphatic segments.[116, 117] However, when switching from **MDA** to **EDA**, the dianiline parts become less rigid due to the added length and flexibility of the monomer, which results in a smaller driving force for phase separation. Summarising, our studies indicate that the phase separation is –at least in part– driven by aromatic interactions between dianiline monomers, and can be disrupted by steric effects, induced by substituents on –or close to– the aromatic rings, that hamper these aromatic interactions.

3.2.4 Consequences of phase separation on the material properties

Having observed the phase separation in our polyimine materials, we investigated its effects on the polymer's material properties. For this we first made use of our set of **P-TDA** materials with dianiline content from 5 to 20%. First, a simple visual inspection of the samples revealed that they all had a bright yellow-to-orange colour that is characteristic to (poly)imines.[47, 52, 118, 119] However, the samples above the threshold dianiline concentration (>15% **TDA**) for phase separation appeared turbid, whereas the samples below the threshold (<12.5% **TDA**) appeared transparent (Figure 3.10).

Figure 3.10 Difference in transparency between **P-TDA** samples. On the left a transparent sample (**P-TDA 10**), and on the right a turbid sample (**P-TDA 20**). All samples with a dianiline content of 15% **TDA** or higher appeared turbid, and samples with a dianiline content of 12.5% **TDA** or lower appeared transparent. Pictures were made directly after synthesis (including drying), with the samples still in the petri dish they were synthesised in. Thickness of the films is around 0.5 mm.

Looking at the samples from the **P-MDA** and related sterically bulked materials, a similar observation was made in which **P-MDA** and **P-EDA** appeared turbid, while the sterically hindered analogous materials (**P-MeMDA**, **P-EtMDA** and **P-CyDA**) were transparent. The transparency of the materials gives a good initial indication of the microstructure of the polymer network as transparency is commonly linked to amorphous structures.[73] It is also possible that turbid samples contain (semi-)crystalline scattering domains in their network structure of the order of the wavelength of visible light.

All 5–20% **P-TDA** samples were then individually analysed with a rheology setup by performing a temperature sweep experiment and a creep test (see Section 3.5 for full experimental details). From the temperature sweeps the crossover point between G' and G'' (*i.e.*, at which $\tan(\delta) = 1$) was determined, representing the temperature above which the material transitions from a viscoelastic solid to a viscoelastic liquid (*i.e.*, the material starts to flow).[120, 121] For CANs, the description of this point is not as trivial as for traditional thermoplastics. This is because (associative) CANs do not fully melt, as the crosslinking density remains constant at elevated temperatures.[47] Instead, the malleability of the material is a function of the reaction rate of the bond exchange.[122] When at a certain point, the viscous component (G'') becomes more prominent than the elastic modulus (G'), this simply translates to the material showing a higher tendency to permanent deformation as a result of stress relaxation *via* bond exchange, rather than an elastic response, when a strain is applied. In this work, we will refer to this point where G'' exceeds G' (*i.e.*, $\tan(\delta) = 1$) as the crossover temperature (T_{cross}).[121]

Around the threshold for phase separation (here from 10–15% **TDA**) the T_{cross} remained constant around 60 °C (Figure 3.11A). Above 15% the T_{cross} quickly rose to much higher temperatures, while below 10% the T_{cross} slightly dropped. Especially the steep rise in T_{cross} after overcoming the threshold for phase separation gives a clear indication of the effect of phase separation on the material properties. The most likely explanation for this strong increase in T_{cross} is that the phase separation causes the formation of local hard domains with increased rigidity that could hamper strand diffusion and overall network deformation,[54] leading to an increased apparent (non-covalent) crosslinking density.[123] Potentially, hydrophobic interactions and π–π stacking of the aromatic moieties in the phase-separated domains increases the required energy to mobilise the polymer chains.[124] As such, a higher temperature is needed to induce mobility, which is expressed in the increased T_{cross}. Furthermore, the reduced chain mobility hinders the occurrence of bond exchange reactions, leading to reduced dynamicity and chain rearrangements.[52, 125]
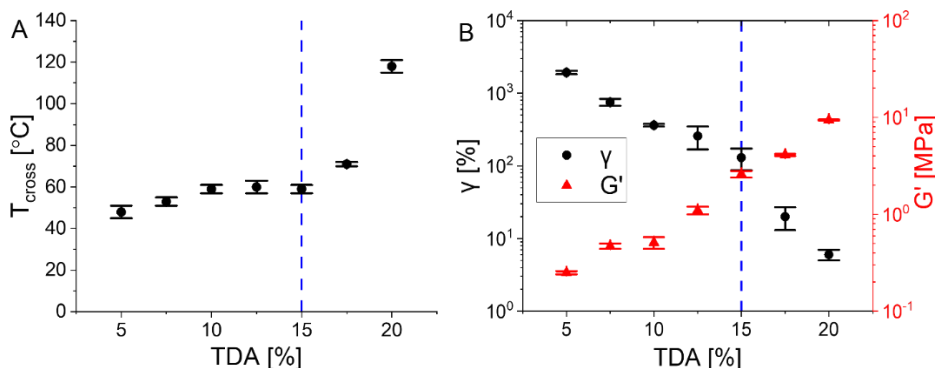
Figure 3.11 A) Plot of T_{cross} as a function of the **TDA** content from 5 to 20%. B) Plot of the creep after 1000s at a 10 kPa stress (black spheres) and elastic modulus (G', red triangles) at room temperature, as a function of the **TDA** concentration. The dotted blue line indicates the threshold value for phase separation at 15% **TDA**.

Other commonly reported results of phase separation in polymers are enhanced creep resistance and dynamic moduli.[86, 126] The results of the creep tests of the **P-TDA** samples (Figure 3.11B, black data points) showed a significant resistance to creep when the **TDA** concentration increased, although it was difficult to identify a clear transition at the onset of phase separation. An increase in **TDA** content also means that the relative concentration of **TOTDDA** decreases, which results in a higher crosslinking density and lower overall strand flexibility. This implies that the resistance to creep is expected to increase upon higher **TDA** concentrations. The same applies to the elastic modulus (G') of the materials (Figure 3.11B, red data points). One might argue that the elastic modulus rises faster after the threshold for phase separation, although the so far obtained data were not yet sufficient to substantiate if the observed changes were selectively caused by phase separation, or if the small differences in ratio between the monomers could have an effect here as well. To further claim the direct effect of the phase separation, and rule out other effects such as the concentration of respective monomers, additional experiments were performed in which we compared the differently substituted **P-MDA** materials (see Figure 3.8 in Section 3.2.3).

The same rheological tests as before were performed on **P-MDA**, **P-MeMDA** and **P-EtMDA** materials with a constant composition of 20% of the respective dianiline. By using this set of materials, we could rule out the effects related to difference in aromatic/aliphatic content as was seen for the **P-TDA** materials with different dianiline contents. From temperature sweep experiments a similar effect on the T_{cross} was first noticed. For the non-

sterically hindered and phase-separated **P-MDA** a T_{cross} of 61 ± 2 °C was found, but for the sterically hindered and non-phase-separated **P-MeMDA** and **P-EtMDA** this value markedly dropped to roughly 30 °C (Figure 3.12A). This time, also a noticeable effect of the phase separation on the elastic modulus (G') was observed. The non-phase-separated **P-MeMDA** and **P-EtMDA** had similar G' values of 0.26 ± 0.04 MPa and 0.29 ± 0.06 MPa, respectively. However, the phase-separated **P-MDA** showed a roughly five-fold increase in G' to 1.31 ± 0.14 MPa (Figure 3.12B). This increase in G' is most likely a direct consequence of the phase separation, since the concentration of the aromatic dianilines in all materials was the same, and as such the average crosslinking density and chain rigidity in the material can be considered identical.
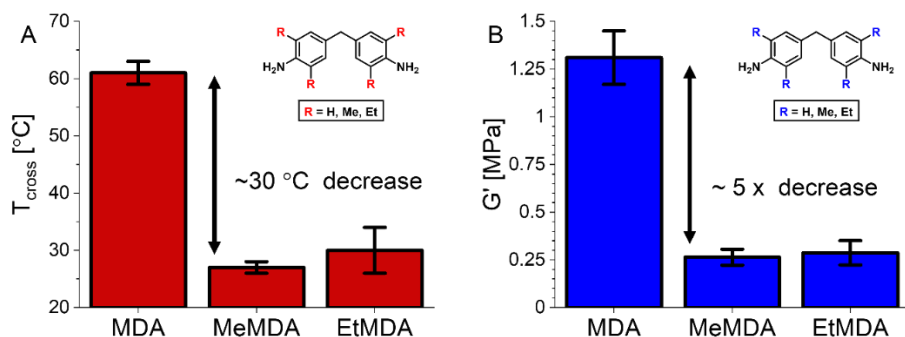

Figure 3.12 A) T_{cross} values for phase-separated **P-MDA** and sterically bulked non-phase-separated **P-MeMDA** and **P-EtMDA**. It can be seen that the T_{cross} drops by as much as ~30 °C when the phase-separated profile is lost. B) G' values for phase-separated **P-MDA** and sterically bulked non-phase-separated **P-MeMDA** and **P-EtMDA**. It can be seen that the G' decreases by a factor ~5 when the phase-separated profile is lost.

By combining all above discussed results we can thus claim that the phase separation had several consequences to the material properties of the polyimine CANs. First, the transparency is affected as phase-separated materials become turbid, whereas non-phase-separated materials are transparent. Second, and more relevantly, the dynamic mechanical properties of the materials are affected, as a significantly higher temperature was required to transition the materials from a rubbery to viscous state (expressed in T_{cross}) once phase separation occurred. Also, the elastic modulus of the materials increased markedly for the phase-separated materials with similar composition with respect to the aliphatic/aromatic content.

3.2.5   Reversing the phase separation

As we concluded before, the phase separation of **P-XDA** materials was dependent on the concentration of the **XDA** dianiline inside the covalent adaptable network. Relying on the intrinsically dynamic nature of this network, we envisioned that we could reverse phase separation of phase-separated polyimines by addition of the other monomers, and thereby decrease the overall **XDA** dianiline content. For this experiment we started with a phase-separated **P-TDA 20** film, with the goal to "dilute" this material to a non-phase-separated **P-TDA 10** film. To do so, we precisely weighed a piece of **P-TDA 20** material. We then added the appropriate amount of **TA**, **TOTDDA** and **TREN** monomers in order to decrease the total **TDA** content from 20% to 10% (see Section 3.5). The **P-TDA** film was then swollen in chloroform. To this sample, first a solution of **TOTDDA** and **TREN** in chloroform was added and the mixture was shaken thoroughly. Then a solution of **TA** in chloroform was added, and the mixture was shaken again. The mixture was left for overnight before the content of the vial was poured into a petri dish. The petri dish was left open to air for 24 hours so that most solvent was able to evaporate to air and a new polymer film was obtained. The newly obtained film was further dried in a vacuum oven at 50 °C for another 24 hours. Then, the new "transformed" **P-TDA 10** film was measured, and we found that the phase separation had indeed disappeared as Raman imaging no longer indicated phase-separated domains and the polymer was transformed from a turbid to a transparent film (Figure 3.13). This shows that the phase separation is a dynamic and reversible process, which is essential for the development and analysis of future CANs. It also further shows that the phase separation is a thermodynamically driven process that can be controlled and reversed.
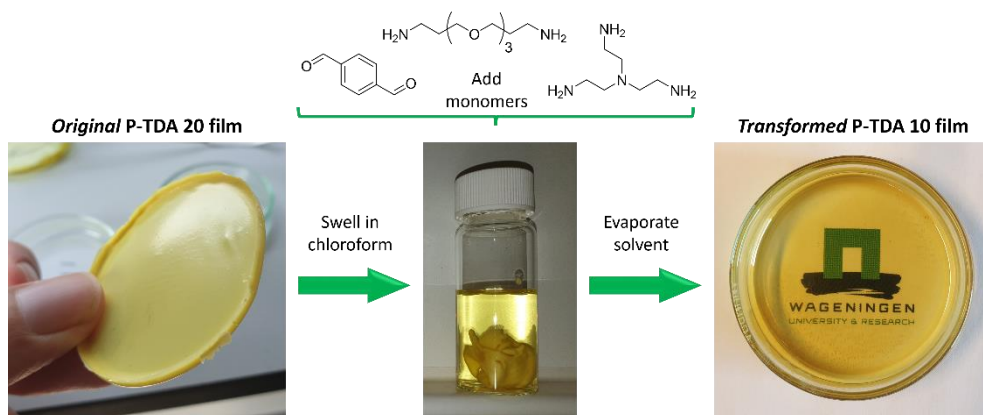

Figure 3.13 Reverse-phase-separation experiment to transform phase-separated **P-TDA 20** (left) into non-phase-separated **P-TDA 10** (right), by addition of fresh monomers (**TA**, **TREN** and **TOTDDA**).

3.3   Conclusion

In this work we introduced Raman confocal spectroscopy to construct 2D images of polyimine CANs based on their chemical composition, leading to the discovery of a phase separation in mainly aromatic *versus* aliphatic domains. The occurrence of this phase separation was dependent on the chemical nature of dianiline monomers, and only occurred above a threshold concentration of the dianilines. Employing the intrinsic dynamic nature of the imine network, after phase separation, by reducing the dianiline concentration *via* swelling in solvent and addition of other monomers, the phase separation could be reversed. Without phase separation the polyimine materials appeared transparent, while phase-separated materials appeared turbid. Also, a significant increase in T_{cross} was observed once the threshold concentration of dianilines for phase separation was crossed. Sterically demanding groups could be introduced on the dianiline monomer structure to prevent phase separation, and loss of the phase-separated profile caused both the T_{cross} and G' to noticeably decrease. Overall, in line with the strengthening effect of phase separation, we demonstrate that this physical-chemical strategy can be used (and visualised by Raman imaging) to toughen polyimine CANs.

Knowledge of the occurrence and the effects of phase separation is of major importance when designing dynamic polymer materials such as polyimines. We foresee that further work on the origin of phase separation in dynamic polymer materials could offer a new handle for physical-chemical tunability of material properties *via* a bottom-up approach, moving away from more chemical approaches (operating at the nanometre scale) to the micrometre scale at which phase separation occurs. Furthermore, our work shows that Raman imaging can be applied as a powerful tool to study phase separation in CANs. As such, we would like to stimulate its further application in the field of dynamic polymer materials.

3.4   Acknowledgement

3.5   Supporting Information

An overview of the most important Supporting Information is given in the following sections. The full Electronic Supporting Information can be accessed from: https://doi.org/10.1021/acs.macromol.2c01595.

3.5.1   Experimental setup

Raman spectroscopy
Raman spectra were recorded using a WITec Alpha 300R Raman microscope. A 784.8 nm near-infrared laser with Topica XTRA diode was used on conjuncture with the Raman microscope (*Note*: for the linear **TDA+TA** samples the 785 nm laser was used on low intensity, as the samples quickly burned when too high intensity was used). The spectrometer was a UHT300S spectrometer by WITec with a grating of 600 g/mm. The microscope was controlled using a WITec Control FIVE suite, which was also used for initial data processing of the Brightfield and Raman data. Further data processing was performed using the joining WITec Project FIVE software. For Brightfield imaging, Zeiss EC Epiplan-Neofluar objectives were used with a magnification of either 20×, 50× or 100×, and a numerical aperture of 0.5, 0.8 and 0.9, respectively. Raman images were constructed over an area of either 50×50, 100×100, or 150×150 µm, with resolutions of 100x100 pixels. Scale bars are always presented in the bottom left corner of the shown image. Calibrations and signal intensity checks were performed using a crystalline silicon substrate, for which the Raman signal was set at 520 cm^{-1} as reference value.[127]

All polymer samples were analysed by placing the film directly under the microscope. It was then closed from the surrounding environment by placing of a costume-made black screen around it. The screen served two purposes: to block incoming light that could potentially interfere at the detector, and to protect the user from potential reflecting laser light.

Rheology

Rheology measurements were performed on an Anton Paar MCR501 rheometer, equipped with a temperature-controlled plate-plate geometry and a temperature control hood for additional thermal homogeneity (see also Section 2.5 in **Chapter 2**). All rheological measurements were performed on polymer discs with a diameter of 10 mm and a thickness (gap size) of 0.5 mm. Due to thermal expansion the gap size may slightly drift over higher temperature domains. If needed, a normal force control of 1 N could be applied when thermal expansion or shrinking occurred that would deteriorate contact between the sample and geometry.

Temperature sweep experiments were performed with increments of 1 °C every 20 seconds, while the samples oscillated with a frequency of 1 Hz and a strain of 0.1%. Storage-(G'') and loss (G') were then plotted as a function of the temperature. The $\tan(\delta)$ was calculated as G''/G', and was also plotted as a function of the conjunct temperature.

Creep tests were performed by applying a constant stress of 10 kPa to the samples, following the deformation (%) over time up to a total of 1000 s. All creep tests were performed at 20 °C and ambient atmosphere.

Atomic force microscopy

Atomic force microscopy (AFM) was performed using an Asylum MFP-3D Origin AFM (Oxford Instruments, United Kingdom). The instrument was operated in tapping mode and equipped with a silicon cantilever (AC240TS-R3, k = 1.3 N m^{-1}) with a nominal tip radius of ≈ 7 nm. The acquired images were processed using Gwyddion 2.53 software.

3D multiphoton fluorescence lifetime microscopy

Multiphoton laser scanning microscopy images were recorded on a Leica SP8 DIVE multiphoton microscope equipped with a Coherent (inc) Chameleon Vision II Ti:Sapphire laser. A 40×/1.1 HC PL IRAPO objective was used for both images. Fluorescence was induced by simultaneous excitation of the sample by two photons (excitation wavelength 720 nm). Emission was recorded between 530–570 nm. The size of each image was 145×145 μm, with a pixel size of 133×133 nm. For a 3D reconstruction, a total of 128 images were recorded in a depth of 80 mm. For optimal results, oil was added between sample and cover glass to alleviate the refraction index mismatch slightly.

3.5.2   Assignment of Raman signals

Raman spectra of 20% **P-XDA** samples

The initial full Raman spectra of all five **P-XDA** (20%) materials are shown in Figure 3.14. Three main regions in the spectra are noted: at 0–200 cm^{-1}, 1100–1250 cm^{-1} and 1500–1700 cm^{-1}. The signals in the region of 0–200 cm^{-1} were assigned to the aliphatic parts of the material caused by the presence of **TOTDDA** and **TREN**, and were found to be of minor interest compared to the other two regions that included information on the aromatic parts and imine groups. Therefore, the following Raman spectra will be shown only from 1000–1750 cm^{-1}.
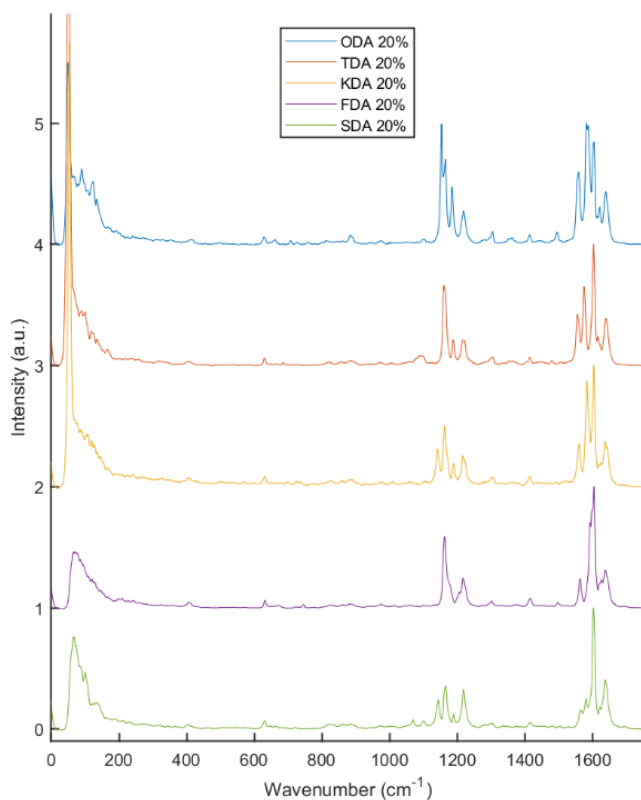
Figure 3.14 Full Raman spectra of 20% **P-XDA** materials. From top to bottom: **P-ODA** (blue), **P-TDA** (red), **P-KDA** (yellow), **P-FDA** (purple), **P-SDA** (green). All spectra showed main signal regions at 0–200 cm^{-1}, 1100–1250 cm^{-1} and 1500–1700 cm^{-1}.

Raman spectra of **NoXDA** and **XDA+TA** analogue samples

To accurately assign all Raman signals, analogue materials were synthesized in addition to the **P-XDA** (20%) samples. These included a **NoXDA** sample, which contained all monomers except the **XDA**, and linear **XDA+TA** samples, which contained only the **XDA** and **TA** monomers. Overlaying the Raman spectra of **NoXDA** and **XDA+TA** resulted in a good resemblance of the full **P-XDA** spectra (Figure 3.15), and facilitated spectrum assignment. Together with literature data on other analogue materials (see Table 3.1 in Section 3.2.1), each signal was allocated to a part in the material. The full assignment of signals is discussed in more detail in the following paragraphs.
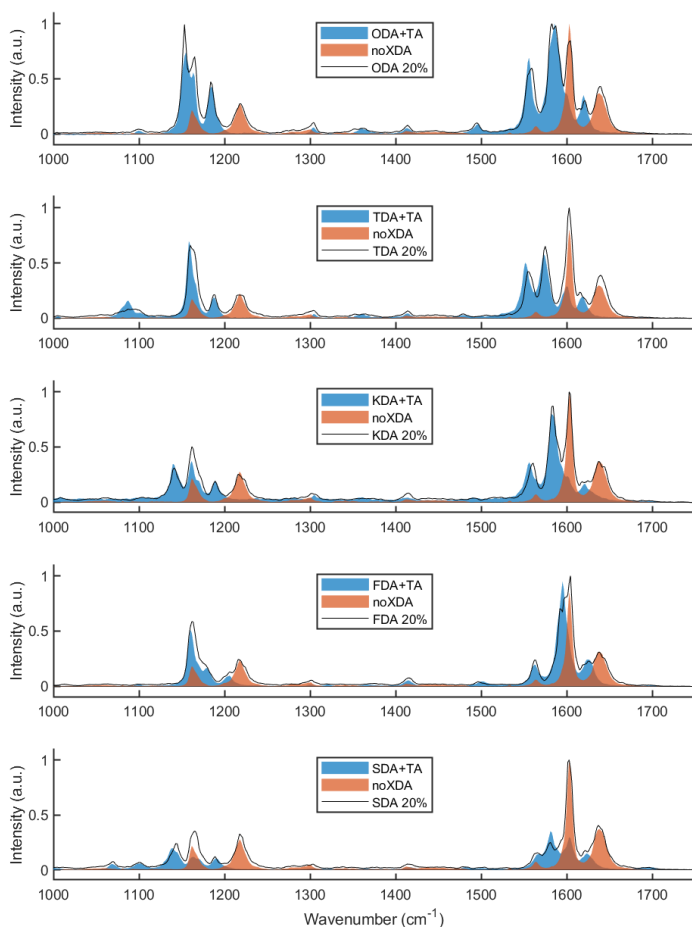
Figure 3.15 Overlayed Raman spectra of **XDA+TA** (blue) and **NoXDA** (orange) analogues to show the resemblance to the full **P-XDA** spectrum (grey line).

Common signals from 1100–1250 cm⁻¹

Two common peaks in this region were found for all samples at approximately 1165–1170 cm⁻¹ and 1215–1225 cm⁻¹. Since these signals were common to all samples, they were expected to be caused by the parts of **TOTDDA**, **TREN**, and **TA**. This was confirmed from the from the Raman spectrum of **NoXDA** (Figure 3.16), containing each of the three mentioned monomers. From documented literature on similar geometries the signal at 1163 cm⁻¹ could be assigned to phenyl C–H bend vibrations of the **TA** parts, and the signal at 1218 cm⁻¹ could be assigned to imine C–N stretch vibrations from the **TOTDDA** and **TREN** parts.[100, 101]
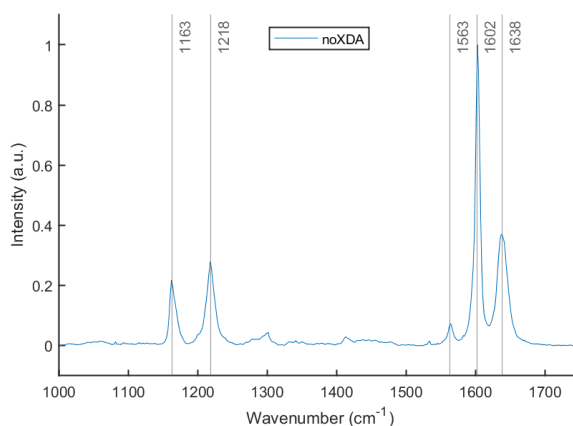
Figure 3.16 Raman spectrum of NoXDA from 1000-1750 cm⁻¹.

Common signals from 1500–1700 cm⁻¹

In this region, signals for aromatic rings, imines and aldehydes are commonly found.[97] In the polyimine samples, there are two clear peaks common to all samples; a strong signal at 1602 cm⁻¹ and a medium signal at 1638 cm⁻¹. Additionally, a small signal at 1563 cm⁻¹ could be observed for **NoXDA**, which generally overlapped with a much stronger signal from the **XDA** containing samples. From reported literature, the signals at 1563 and 1602 cm⁻¹ could be assigned to aromatic C=C stretch vibration, and the signal at 1638 cm⁻¹ to imine C=N stretch vibrations.[97, 98, 100, 101]

Sample specific signals from 1100–1250 cm⁻¹

For each sample, at around 1190 cm⁻¹, there is a signal which corresponds to the C–N signal close to the dianiline monomer. This conclusion is based on research by Nandi *et al.*,[100] where a similar C–N bond between an imine group and an aromatic ring caused a signal with a wavenumber of 1190 cm⁻¹.

Next, a sample-specific signal in the region 1140–1160 cm^{-1} is observed. For **P-ODA**, **P-TDA** and **P-FDA** this signal appears at 1153 cm^{-1}, 1158 cm^{-1} and 1160 cm^{-1}, respectively, while for **P-KDA** and **P-SDA** the signal appears at approximately 1140 cm^{-1}. In this region, the C–H bending vibration for aromatic moieties are generally observed.[99-102] As such, these signals were assigned to the phenyl C–H bend vibrations of the tuneable **XDA** monomer parts.

Sample specific signals from 1500–1700 cm^{-1}

In this region, the expected signals consist of (I) the C=C stretch vibrations for the dianiline phenyls, (II) the **TA** signal noted before and (III) the imine signal for the imine between dianiline and **TA**.

The **TA** signal was once again found around 1602 cm^{-1}, and assigned accordingly. Furthermore, a signal at around 1620 cm^{-1} is observed. This signal is assigned to the imine between the **XDA** and **TA** monomer, specifically to the C=N stretching vibration. For compounds with similar geometries (two phenyl rings with an imine in between),[100, 101] the imine signal was also observed around 1620 cm^{-1}. Moreover, it is relatively close to the previously established imine signal for the imines between an aliphatic chain and **TA**, but shifted to slightly lower wavenumbers. Due to conjugation to the aromatic system, and thus being slightly more stable, this is an expected position for the imine signal. Additionally, for each sample, there are two signals in the region from 1550 cm^{-1} to 1600 cm^{-1}. These signals are likely caused by the **XDA** parts, at least one being caused by the C=C stretch vibrations of the phenyls in the **XDA**. Research by Ullah *et al.*[102] reviewed the Raman spectra of unreacted **SDA**, both using Density Functional Theory (DFT) calculations and by experimental results. They found two signals, at 1584 cm^{-1} and 1602 cm^{-1} which both corresponded to the C=C stretch in the phenyls. It is thus not unlikely that a similar split into two signals is possible for the rest of the dianiline monomers.

3.5.3 Raman imaging analysis for fitting with a binary scale

As mentioned in the Results and Discussion (Section 3.2.2), phase separation for **P-TDA** materials was observed when the dianiline content was at least 15% of the total amount of amines. This was confirmed by Raman imaging of several samples with varying dianiline content. The samples with a dianiline content of 12.5% and below did not show a clear phase separation, but their binary Raman images still showed an apparent division of blue and yellow. This was the result of the (built-in) fitting procedure within the WITec software that for each pixel enforced an assignment to either blue or yellow, in accordance with which reference spectrum the measured spectrum fitted best (*i.e.*, yellow for a best fit to

TDA+TA, and a blue colour to a best fit to **NoXDA**). However, by comparing the spectra of a yellow and blue domain, it is possible to check if the two regions indeed show different Raman spectra. As an example, Raman images of **P-TDA 10** are presented in Figure 3.17. First, a Raman image was constructed from a best fit between reference spectra of **TDA+TA** and **NoXDA** (Figure 3.17A). Then, for both Raman images the spectra of randomly chosen blue and yellow pixels were selected and inspected (Figure 3.17B). The Raman spectra of the selected yellow and blue pixels appeared highly similar, suggesting that no phase separation was present, and an artificial contrast was observed as a result of the forced binary fit. This inspection was performed for all other Raman images as well. As such, we could always determine retroactively if an observed phase separation profile was justified. For comparison, the Raman image and spectra of blue and yellow colour attribution of phase-separated **P-TDA 20** are shown in Figure 3.18. Here, it can be seen that the individual Raman spectra for yellow and blue pixels indeed resemble those of the reference **TDA+TA** and **NoXDA** spectra. As such, we can claim that the observed phase-separated profile is real.
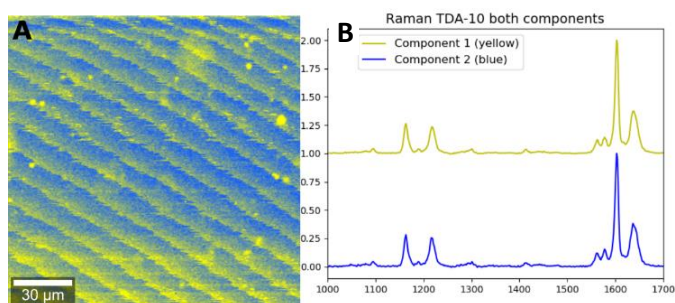
Figure 3.17 A) Raman image of **P-TDA 10**, and B) Raman spectra of a random yellow and blue pixel. The Raman spectra indicate that there is no clear difference between yellow and blue pixels in the Raman image, meaning that no phase separation was present.

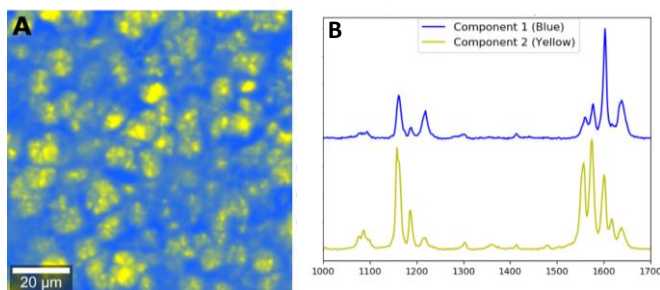**Figure 3.18** A) Raman image of **P-TDA 20**, and B) Raman spectra for a random blue and yellow pixel. The Raman spectra show proper identification of different spectra that resemble either that of reference **TDA+TA** (yellow) or **NoXDA** (blue). As such, the observed phase-separated profile is real.

3.5.4   Continuous colouring scale of Raman images

To overcome problems regarding the (automated) binary pixel assignment (in either yellow or blue), we could also manually fit and analyse the data on a continuous scale. A 256-point scale (yellow-red-black) was applied for each pixel in the Raman image based on the ratios of peak areas between the different signals. Relying on peak area ratio rendered our analyses insensitive to variations in laser intensity. Images can now be constructed that reveal more about the actual content of either the aromatic (**TDA+TA**) and aliphatic (**NoXDA**) parts, rather than an 'all-or-nothing' binary fit. This method also proved efficient to remove artefacts in the Raman images. As an example, in Figure 3.19 three binary-scale Raman images are presented of A) a phase-separated material, B) a non-phase-separated material giving rise to a noisy Raman image, C) a non-phase-separated material with artefacts (diagonal lines appear over the image). In Figure 3.20, the same images are presented on a continuous scale. Here, we clearly see that the observed phase separation in panel A can be confirmed, and that the phases consist of high amounts of the individual components. We also see that the noisy non-phase-separated material (in panel B) indeed shows no phase separation, as the continuous scale shows a mostly well-blended image. Last, we see that the artefacts in panel C are now fully removed to show a non-phase-separated image. The continuous scale fitting can thus serve as a more reliable check to confirm whether phase separation was indeed observed or not, or to filter artefacts. For routine checks, we do however still use the binary fitting as a quick method to see if phase separation is present, as it generally shows a better contrast between the borders of the domains, and saves time due to its simple setup. The continuous scale fit can later serve as either a check to confirm what was seen before, or to clear up artefacts or otherwise unclear images. As such, in the Results and Discussion (Section 3.2) we provided both binary and continuous-scale images.
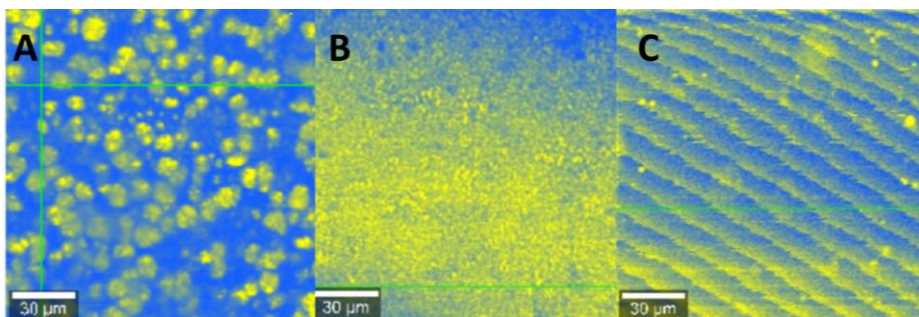

Figure 3.19 Binary scale Raman images of A) a phase-separated material, B) a non-phase-separated material giving rise to a noisy image, C) a non-phase-separated material with artefacts as diagonal lines over the image.
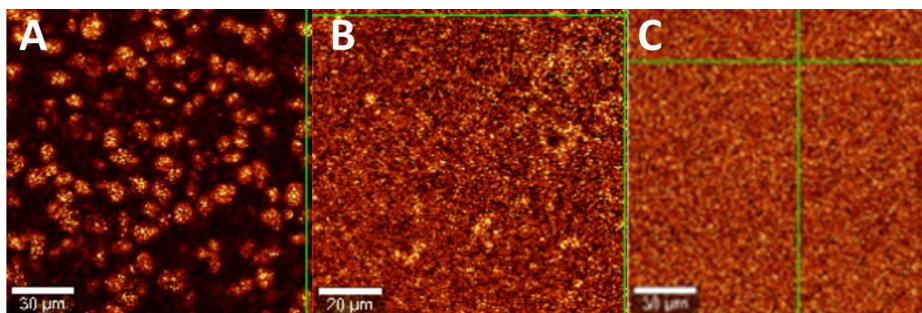
Figure 3.20 Continues scale Raman images of the same materials presented in Figure 3.19. Here we see that the phase-separation can be confirmed for A, that B did indeed not phase-separate, and that the artefacts in C can be removed to show that indeed no phase separation occurred

References

1.   C. J. Kloxin and C. N. Bowman, *Chem. Soc. Rev.*, 2013, **42**, 7161-7173.
2.   C. J. Kloxin, T. F. Scott, B. J. Adzima and C. N. Bowman, *Macromolecules*, 2010, **43**, 2643-2653.
3.   S. J. Rowan, S. J. Cantrill, G. R. L. Cousins, J. K. M. Sanders and J. F. Stoddart, *Angew. Chem. Int. Ed.*, 2002, **41**, 898-952.
4.   P. T. Corbett, J. Leclaire, L. Vial, K. R. West, J.-L. Wietor, J. K. M. Sanders and S. Otto, *Chem. Rev.*, 2006, **106**, 3652-3711.
5.   Q. Chen, X. Yu, Z. Pei, Y. Yang, Y. Wei and Y. Ji, *Chem. Sci.*, 2017, **8**, 724-733.
6.   F. Cuminet, S. Caillol, É. Dantras, É. Leclerc and V. Ladmiral, *Macromolecules*, 2021, **54**, 3927-3961.
7.   H. Zhang, S. Majumdar, R. A. T. M. van Benthem, R. P. Sijbesma and J. P. A. Heuts, *ACS Macro Lett.*, 2020, **9**, 272-277.
8.   F. Van Lijsebetten, J. O. Holloway, J. M. Winne and F. E. Du Prez, *Chem. Soc. Rev.*, 2020, **49**, 8425-8438.
9.   F. I. Altuna, C. E. Hoppe and R. J. J. Williams, *Eur. Polym. J.*, 2019, **113**, 297-304.
10.   J. M. Winne, L. Leibler and F. E. Du Prez, *Polym. Chem.*, 2019, **10**, 6091-6108.
11.   B. R. Elling and W. R. Dichtel, *ACS Cent. Sci.*, 2020, **6**, 1488-1496.
12.   M. Guerre, C. Taplan, J. M. Winne and F. E. Du Prez, *Chem. Sci.*, 2020, **11**, 4855-4870.
13.   M. Podgórski, B. D. Fairbanks, B. E. Kirkpatrick, M. McBride, A. Martinez, A. Dobson, N. J. Bongiardina and C. N. Bowman, *Adv. Mater.*, 2020, **32**, 1906876.
14.   Y. Wu, Y. Wei and Y. Ji, *Polym. Chem.*, 2020, **11**, 5297-5320.

15. F. García and M. M. J. Smulders, *J. Polym. Sci., Part A: Polym. Chem.*, 2016, **54**, 3551-3577.
16. G. M. Scheutz, J. J. Lessard, M. B. Sims and B. S. Sumerlin, *J. Am. Chem. Soc.*, 2019, **141**, 16181-16196.
17. W. Denissen, J. M. Winne and F. E. Du Prez, *Chem. Sci.*, 2016, **7**, 30-38.
18. W. Zou, J. Dong, Y. Luo, Q. Zhao and T. Xie, *Adv. Mater.*, 2017, **29**, 1606100.
19. Z. P. Zhang, M. Z. Rong and M. Q. Zhang, *Prog. Polym. Sci.*, 2018, **80**, 39-93.
20. M. Capelot, D. Montarnal, F. Tournilhac and L. Leibler, *J. Am. Chem. Soc.*, 2012, **134**, 7664-7667.
21. M. Delahaye, J. M. Winne and F. E. Du Prez, *J. Am. Chem. Soc.*, 2019, **141**, 15277-15287.
22. M. Capelot, M. M. Unterlass, F. Tournilhac and L. Leibler, *ACS Macro Lett.*, 2012, **1**, 789-792.
23. J. Canadell, H. Goossens and B. Klumperman, *Macromolecules*, 2011, **44**, 2536-2541.
24. D. J. Fortman, R. L. Snyder, D. T. Sheppard and W. R. Dichtel, *ACS Macro Lett.*, 2018, **7**, 1226-1231.
25. M. Pepels, I. Filot, B. Klumperman and H. Goossens, *Polym. Chem.*, 2013, **4**, 4955-4965.
26. M. A. Bin Rusayyis and J. M. Torkelson, *Polym. Chem.*, 2021, **12**, 2760-2771.
27. I. Azcune and I. Odriozola, *Eur. Polym. J.*, 2016, **84**, 147-160.
28. A. Peterson, M. Roy, J. Fagerlund, G. Lo Re and C. Müller, *Mater. Adv.*, 2021, **2**, 5171-5180.
29. L. M. Polgar, E. Hagting, P. Raffa, M. Mauri, R. Simonutti, F. Picchioni and M. van Duin, *Macromolecules*, 2017, **50**, 8955-8964.
30. L. M. Polgar, M. van Duin, A. A. Broekhuis and F. Picchioni, *Macromolecules*, 2015, **48**, 7096-7105.
31. W. Denissen, M. Droesbeke, R. Nicolaÿ, L. Leibler, J. M. Winne and F. E. Du Prez, *Nat. Commun.*, 2017, **8**, 14857.
32. W. Denissen, G. Rivero, R. Nicolaÿ, L. Leibler, J. M. Winne and F. E. Du Prez, *Adv. Funct. Mater.*, 2015, **25**, 2451-2457.
33. J. Tellers, R. Pinalli, M. Soliman, J. Vachon and E. Dalcanale, *Polym. Chem.*, 2019, **10**, 5534-5542.
34. Y. Zhu, F. Gao, J. Zhong, L. Shen and Y. Lin, *Eur. Polym. J.*, 2020, **135**, 109865.
35. J. J. Lessard, G. M. Scheutz, R. W. Hughes and B. S. Sumerlin, *ACS Appl. Polym. Mater.*, 2020, **2**, 3044-3048.
36. Y. Spiesschaert, J. Danneels, N. Van Herck, M. Guerre, G. Acke, J. Winne and F. Du Prez, *Macromolecules*, 2021, **54**, 7931-7942.
37. S. Wu, H. Yang, S. Huang and Q. Chen, *Macromolecules*, 2020, **53**, 1180-1190.
38. J. J. Cash, T. Kubo, A. P. Bapat and B. S. Sumerlin, *Macromolecules*, 2015, **48**, 2098-2106.
39. O. R. Cromwell, J. Chung and Z. Guan, *J. Am. Chem. Soc.*, 2015, **137**, 6492-6495.

40. M. Röttger, T. Domenech, R. van der Weegen, A. Breuillac, R. Nicolaÿ and L. Leibler, *Science*, 2017, **356**, 62-65.
41. P. Taynton, K. Yu, R. K. Shoemaker, Y. Jin, H. J. Qi and W. Zhang, *Adv. Mater.*, 2014, **26**, 3938-3942.
42. P. Taynton, C. Zhu, S. Loob, R. Shoemaker, J. Pritchard, Y. Jin and W. Zhang, *Polym. Chem.*, 2016, **7**, 7052-7056.
43. R. Hajj, A. Duval, S. Dhers and L. Avérous, *Macromolecules*, 2020, **53**, 3796-3805.
44. S. Dhers, G. Vantomme and L. Avérous, *Green Chem.*, 2019, **21**, 1596-1601.
45. P. Wang, L. Yang, B. Dai, Z. Yang, S. Guo, G. Gao, L. Xu, M. Sun, K. Yao and J. Zhu, *Eur. Polym. J.*, 2020, **123**, 109382.
46. Q. Yu, X. Peng, Y. Wang, H. Geng, A. Xu, X. Zhang, W. Xu and D. Ye, *Eur. Polym. J.*, 2019, **117**, 55-63.
47. S. K. Schoustra, J. A. Dijksman, H. Zuilhof and M. M. J. Smulders, *Chem. Sci.*, 2021, **12**, 293-302.
48. L. Zhang and S. J. Rowan, *Macromolecules*, 2017, **50**, 5051-5060.
49. N. Van Herck, D. Maes, K. Unal, M. Guerre, J. M. Winne and F. E. Du Prez, *Angew. Chem. Int. Ed.*, 2020, **59**, 3609-3617.
50. B. M. El-Zaatari, J. S. A. Ishibashi and J. A. Kalow, *Polym. Chem.*, 2020, **11**, 5339-5345.
51. Y. Chen, H. Zhang, S. Majumdar, R. A. T. M. van Benthem, J. P. A. Heuts and R. P. Sijbesma, *Macromolecules*, 2021, **54**, 9703-9711.
52. S. K. Schoustra, T. Groeneveld and M. M. J. Smulders, *Polym. Chem.*, 2021, **12**, 1635-1642.
53. F. Chen, Q. Cheng, F. Gao, J. Zhong, L. Shen, C. Lin and Y. Lin, *Eur. Polym. J.*, 2021, **147**, 110304.
54. J. J. Lessard, G. M. Scheutz, S. H. Sung, K. A. Lantz, T. H. Epps and B. S. Sumerlin, *J. Am. Chem. Soc.*, 2020, **142**, 283-289.
55. Y. Spiesschaert, C. Taplan, L. Stricker, M. Guerre, J. M. Winne and F. E. Du Prez, *Polym. Chem.*, 2020, **11**, 5377-5385.
56. L. Li, X. Chen, K. Jin and J. M. Torkelson, *Macromolecules*, 2018, **51**, 5537-5546.
57. F. Van Lijsebetten, T. Debsharma, J. M. Winne and F. E. Du Prez, *Angew. Chem. Int. Ed.*, 2022, **n/a**, e202210405.
58. M. Chen, L. Zhou, Y. Wu, X. Zhao and Y. Zhang, *ACS Macro Lett.*, 2019, **8**, 255-260.
59. X. Xu, S. Ma, H. Feng, J. Qiu, S. Wang, Z. Yu and J. Zhu, *Polym. Chem.*, 2021, **12**, 5217-5228.
60. Y. Lei, A. Zhang and Y. Lin, *Polym. Chem.*, 2021, **12**, 4052-4062.
61. S. Yu, G. Zhang, S. Wu, Z. Tang, B. Guo and L. Zhang, *J. Mater. Chem. A*, 2020, **8**, 20503-20512.
62. R. Tian, X. Fan, S. Liu, F. Li, F. Yang, Y. Li, Q. Luo, C. Hou, J. Xu and J. Liu, *Macromol. Rapid Commun.*, 2020, **41**, 1900586.
63. B. Zhang, N. De Alwis Watuthanthrige, S. V. Wanasinghe, S. Averick and D. Konkolewicz, *Adv. Funct. Mater.*, 2021, 2108431.
64. J. O. Holloway, C. Taplan and F. E. Du Prez, *Polym. Chem.*, 2022, **13**, 2008-2018.

65. A. Breuillac, A. Kassalias and R. Nicolaÿ, *Macromolecules*, 2019, **52**, 7102-7113.
66. M. Guerre, C. Taplan, R. Nicolaÿ, J. M. Winne and F. E. Du Prez, *J. Am. Chem. Soc.*, 2018, **140**, 13272-13284.
67. Y. Zhou, J. G. P. Goossens, R. P. Sijbesma and J. P. A. Heuts, *Macromolecules*, 2017, **50**, 6742-6751.
68. Z. Song, Z. Wang and S. Cai, *Mech. Mater.*, 2021, **153**, 103687.
69. H. Han and X. Xu, *J. Appl. Polym. Sci.*, 2018, **135**, 46307.
70. J. S. A. Ishibashi, I. C. Pierce, A. B. Chang, A. Zografos, B. M. El-Zaatari, Y. Fang, S. J. Weigand, F. S. Bates and J. A. Kalow, *Macromolecules*, 2021, **54**, 3972-3986.
71. K. Tangthana-umrung, Q. A. Poutrel and M. Gresil, *Macromolecules*, 2021, **54**, 8393-8406.
72. X. Chen, R. Wang, C. Cui, L. An, Q. Zhang, Y. Cheng and Y. Zhang, *Chem. Eng. J.*, 2022, **428**, 131212.
73. J. Xie, L. Fan, D. Yao, F. Su, Z. Mu and Y. Zheng, *Mater. Today Chem.*, 2022, **23**, 100708.
74. Y. Oba, T. Kimura, M. Hayashi and K. Yamamoto, *Macromolecules*, 2022, **55**, 1771-1782.
75. D. P. Foster, D. Jasnow and A. C. Balazs, *Macromolecules*, 1995, **28**, 3450-3462.
76. T. Pan, K. Huang, A. C. Balazs, M. S. Kunz, A. M. Mayes and T. P. Russell, *Macromolecules*, 1993, **26**, 2860-2865.
77. G. Fleury and F. S. Bates, *Macromolecules*, 2009, **42**, 3598-3610.
78. J. P. Bishop and R. A. Register, *Macromolecules*, 2010, **43**, 4954-4960.
79. H. Schmalz, A. Böker, R. Lange, G. Krausch and V. Abetz, *Macromolecules*, 2001, **34**, 8720-8729.
80. T. Pakula, K. Koynov, H. Boerner, J. Huang, H.-i. Lee, J. Pietrasik, B. Sumerlin and K. Matyjaszewski, *Polymer*, 2011, **52**, 2576-2583.
81. R. G. Ricarte, F. Tournilhac, M. Cloître and L. Leibler, *Macromolecules*, 2020, **53**, 1852-1866.
82. M. Maaz, A. Riba-Bremerch, C. Guibert, N. J. Van Zee and R. Nicolaÿ, *Macromolecules*, 2021, **54**, 2213-2225.
83. L.-M. Peng, Z. Xu, W.-Y. Wang, X. Zhao, R.-Y. Bao, L. Bai, K. Ke, Z.-Y. Liu, M.-B. Yang and W. Yang, *ACS Appl. Energy Mater.*, 2021, **4**, 11173-11182.
84. X. Chen, L. Li, T. Wei and J. M. Torkelson, *Macromol. Chem. Phys.*, 2019, **220**, 1900083.
85. X. Chen, L. Li and J. M. Torkelson, *Polymer*, 2019, **178**, 121604.
86. R. W. Clarke, M. L. McGraw, B. S. Newell and E. Y. X. Chen, *Cell Rep. Phys. Sci.*, 2021, **2**, 100483.
87. J. L. Swartz, D. T. Sheppard, G. Haugstad and W. R. Dichtel, *Macromolecules*, 2021, **54**, 11126-11133.
88. H. G. M. Edwards, A. F. Johnson and I. R. Lewis, *J. Raman Spectrosc.*, 1993, **24**, 475-483.
89. A. Brookes, J. M. Dyke, P. J. Hendra and A. Strawn, *Spectrochim. Acta A Mol. Biomol. Spectrosc.*, 1997, **53**, 2303-2311.

90.   S. L. Hsu and S. Krimm, *J. Appl. Phys.*, 1976, **47**, 4265-4270.
91.   K. M. Herbert, P. T. Getty, N. D. Dolinski, J. E. Hertzog, D. de Jong, J. H. Lettow, J. Romulus, J. W. Onorato, E. M. Foster and S. J. Rowan, *Chem. Sci.*, 2020, **11**, 5028-5036.
92.   J. Caprasse, R. Riva, J.-M. Thomassin and C. Jérôme, *Mater. Adv.*, 2021, **2**, 7077-7087.
93.   S. Mukherjee and A. Gowen, *Anal. Chim. Acta*, 2015, **895**, 12-34.
94.   M. D. Schaeberle, C. G. Karakatsanis, C. J. Lau and P. J. Treado, *Anal. Chem.*, 1995, **67**, 4316-4321.
95.   J. L. Koenig and J. P. Bobiak, *Macromol. Mater. Eng.*, 2007, **292**, 801-816.
96.   C. P. Tarnowski and M. D. Morris, in *Encyclopedia of Materials: Science and Technology*, eds. K. H. J. Buschow, R. W. Cahn, M. C. Flemings, B. Ilschner, E. J. Kramer, S. Mahajan and P. Veyssière, Elsevier, Oxford, 2001, DOI: https://doi.org/10.1016/B0-08-043152-6/01436-4, pp. 7976-7983.
97.   M. Lee, J.-P. Lee, H. Rhee, J. Choo, Y. Gyu Chai and E. Kyu Lee, *J. Raman Spectrosc.*, 2003, **34**, 737-742.
98.   L. R. Knöpke, N. Nemati, A. Köckritz, A. Brückner and U. Bentrup, *ChemCatChem*, 2010, **2**, 273-280.
99.   H. M. Badawi, *Spectrochim. Acta A Mol. Biomol. Spectrosc.*, 2013, **109**, 213-220.
100. R. Nandi, H. K. Singh, S. K. Singh, D. S. S. Rao, S. K. Prasad, B. Singh and R. K. Singh, *Liq. Cryst.*, 2017, **44**, 1185-1193.
101. N. L. John, L. K. Joy, M. S. Kumar, S. S. Shaiju, A. Subashini and D. Sajan, *Mol. Simul.*, 2018, **44**, 40-54.
102. R. Ullah and X. Wang, *J. Mol. Struct.*, 2019, **1175**, 927-934.
103. C. Liu and D. Wang, *Macromolecules*, 2022, **55**, 1260-1266.
104. J. Gao, L. Duan, G. Yang, Q. Zhang, M. Yang and Q. Fu, *Appl. Surf. Sci.*, 2012, **261**, 528-535.
105. A. Gupper and S. G. Kazarian, *Macromolecules*, 2005, **38**, 2327-2332.
106. A. Chao, I. Negulescu and D. Zhang, *Macromolecules*, 2016, **49**, 6277-6284.
107. C. Zhu, C. Xi, W. Doro, T. Wang, X. Zhang, Y. Jin and W. Zhang, *RSC Adv.*, 2017, **7**, 48303-48307.
108. D. Schultz and J. R. Nitschke, *J. Am. Chem. Soc.*, 2006, **128**, 9887-9892.
109. Y. Zhou, L. Li, H. Ye, L. Zhang and L. You, *J. Am. Chem. Soc.*, 2016, **138**, 381-389.
110. M. Ciaccia, S. Pilati, R. Cacciapaglia, L. Mandolini and S. Di Stefano, *Org. Biomol. Chem.*, 2014, **12**, 3282-3287.
111. C. Hansch, A. Leo and R. W. Taft, *Chem. Rev.*, 1991, **91**, 165-195.
112. C. Hansch, A. Leo, S. H. Unger, K. H. Kim, D. Nikaitani and E. J. Lien, *J. Med. Chem.*, 1973, **16**, 1207-1216.
113. L. P. Hammett, *J. Am. Chem. Soc.*, 1937, **59**, 96-103.
114. L. Kan, P. Zhang, H. Jiang, S. Zhang, Z. Liu, X. Zhang, N. Ma, D. Qiu and H. Wei, *RSC Adv.*, 2019, **9**, 8905-8911.
115. W. P. J. Appel, G. Portale, E. Wisse, P. Y. W. Dankers and E. W. Meijer, *Macromolecules*, 2011, **44**, 6776-6784.

116. Y. Tian, Q. Wang, Y. Hu, H. Sun, Z. Cui, L. Kou, J. Cheng and J. Zhang, *Polymer*, 2019, **178**, 121592.
117. X. Yan, B. Zhao, J. Liu, X. Zhang and G. He, *J. Membr. Sci.*, 2018, **564**, 436-443.
118. H. Zheng, Q. Liu, X. Lei, Y. Chen, B. Zhang and Q. Zhang, *J. Mater. Sci.*, 2019, **54**, 2690-2698.
119. Z. Feng, B. Yu, J. Hu, H. Zuo, J. Li, H. Sun, N. Ning, M. Tian and L. Zhang, *Ind. Eng. Chem. Res.*, 2019, **58**, 1212-1221.
120. Z. Q. Lei, P. Xie, M. Z. Rong and M. Q. Zhang, *J. Mater. Chem. A*, 2015, **3**, 19662-19668.
121. H. Zhang, D. Wang, W. Liu, P. Li, J. Liu, C. Liu, J. Zhang, N. Zhao and J. Xu, *J. Polym. Sci., Part A: Polym. Chem.*, 2017, **55**, 2011-2018.
122. P. Taynton, H. Ni, C. Zhu, K. Yu, S. Loob, Y. Jin, H. J. Qi and W. Zhang, *Adv. Mater.*, 2016, **28**, 2904-2909.
123. V. Montano, M. Senardi, S. van der Zwaag and S. J. Garcia, *Phys. Chem. Chem. Phys.*, 2020, **22**, 21750-21760.
124. D. Wang, J. Xu, J. Chen, P. Hu, Y. Wang, W. Jiang and J. Fu, *Adv. Funct. Mater.*, 2020, **30**, 1907109.
125. S.-M. Kim, H. Jeon, S.-H. Shin, S.-A. Park, J. Jegal, S. Y. Hwang, D. X. Oh and J. Park, *Adv. Mater.*, 2018, **30**, 1705145.
126. H. Xia, M. Song, Z. Zhang and M. Richardson, *J. Appl. Polym. Sci.*, 2007, **103**, 2992-3002.
127. C. Smit, R. A. C. M. M. v. Swaaij, H. Donker, A. M. H. N. Petit, W. M. M. Kessels and M. C. M. v. d. Sanden, *J. Appl. Phys.*, 2003, **94**, 3582-3588.

Chapter 4

The Effect of Polarity on the Molecular Exchange
Dynamics in Imine-based Covalent Adaptable Networks

This work was published as:

Sybren K. Schoustra, Timo Groeneveld, Maarten M. J. Smulders, *Polym. Chem.*, 2021, **12**, 1635-1642.

* This work was featured on the front cover of Polymer Chemistry, Issue 11 (21 March 2021).

Abstract

Covalent adaptable networks (CANs) are a rising type of polymeric materials that consist of covalently crosslinked polymer chains, but with the inclusion of dynamic covalent bonds, and that can perform bond exchange reactions under equilibrium control. The dynamic behaviour of these exchange reactions within a polymer matrix has been established to be a key parameter in the control of the material properties. Therefore, in order to fully control the macroscopic material properties of CANs, understanding the underlying molecular exchange processes of these dynamic covalent bonds is essential. In this Chapter a study is presented on the effect of polarity in polyimine-based CANs. Here, not only the network response itself was considered, but also the –so far often overlooked– effect on the exchange dynamics. By combining results from small-molecule kinetic studies and material analysis it was possible to show a distinct correlation between the presence of polar domains in the molecular structure and the thermal and dynamic mechanical properties of the materials. More importantly, the presence of polar domains also greatly affected the exchange kinetics of the dynamic imine bonds. On the molecular level, it was showed that the imine exchange could be greatly enhanced (up to 20 times) when polar groups were present near the reactive imine species. As a result, in the polymer materials, a tuneable range of phase transition temperatures from the glass to rubber state and the rubber to viscous state over roughly 100 °C was established as a result of either presence or absence of polar groups in the polymer matrix. Furthermore, detailed analysis in the stress relaxation behaviour of the polyimine materials revealed three relaxation processes, which were attributed to the relaxation in network topology, to the imine exchange on a local level, and to the imine exchange as a result of diffusion through the polymer network. From this analysis is was possible to illustrate the effect of polarity on the polymer network to each of the three relaxation mechanisms.

4.1   Introduction

Covalent adaptable networks (CANs) are a relatively new type of polymers that exhibit the strength of thermosets *via* a crosslinked network structure, but are still able to be recycled, reshaped, and even self-healed, as a results of dynamic covalent bonds within their molecular structure.[1-5] These dynamic covalent bonds can perform bond exchange reactions under equilibrium control[6, 7] while built into a polymer matrix.[8-10] By stimulating the exchange reactions of the dynamic covalent bonds, for example by introduction of heat or light, a molecular flow is introduced in the material.[11] Several types of bond exchange reactions have been studied over the last decade, such as transesterifications,[1, 12] boronic ester exchange,[13-16] 1,2,3-triazolium exchange,[17, 18] diketoenamine exchange,[19, 20] (alkyl)urea exchange,[21-23] (vinylogous) urethane exchange,[24-28] thiol-ene/yne exchange,[29, 30] amide-imide exchange,[31, 32] and imine exchange.[33-36] Individually, each type of bond exchange reaction possesses different dynamics according to the mechanism of the exchange reaction.[37] Therefore, CANs can be synthesised with selective properties based on the type of bond exchange reaction. However, not only the type of bond exchange reaction is determinative for the dynamic(-mechanical) response of the material, but also the composition of the polymer matrix plays a definitive role,[38] which includes for example the crosslinking density[39] or steric effects.[22] For many polymeric materials, the effect of such network characteristics has been evaluated for their influence on the material properties at the macroscopic level.[21, 24, 40] However, as the dynamic-mechanical properties of these materials are directly influenced by the underlying molecular exchange reaction,[22, 41, 42] further understanding of the specific effects of polymer composition on the molecular bond exchange of dynamic covalent bonds in CANs is still essential.[38, 43]

Tailoring the flexibility of polymer chains is a classic example of a commonly applied parameter to tune material properties, and a conventional approach for enhancing this flexibility is by incorporating ethylene oxide (EO) moieties in the polymer,[44] as the energy barrier for rotation of the C–O bond in ethers is considerably lower than C–C bond rotation in alkanes. For this reason, ethylene oxides and similar ether moieties are frequently found in CANs.[38, 45-49] One factor that is however mainly overlooked when it comes to these ether moieties is the concomitant induced polar effect on the polymer network (dynamics), which was previously reported for materials that rely on ion transport.[50, 51] For example, in the study by Zhao and co-workers, the differences between polar EO linkers and apolar alkyl linkers were noticeable as a significant decrease in the glass transition temperature (T_g), as well as an increased conductivity for the polar EO-containing materials.[51] Furthermore, in a recent study by Polgar and co-workers on Diels-Alder-based CANs, polarity-induced

effects as a result of introduced acetate groups were shown to affect cluster formation within the material.[52] Also in recent work on vitrimer-like anilinium salt CANs, solvation effects as a result of polar groups have been proposed.[53] These works thus suggest that such polarity differences in CANs can have greater consequences to the behaviour on both macroscopic and molecular level than is typically assumed. Additionally, such polar effects could play a distinct role in the kinetics of the bond exchange reactions in CANs, which is a key parameter to their dynamic features.[22]
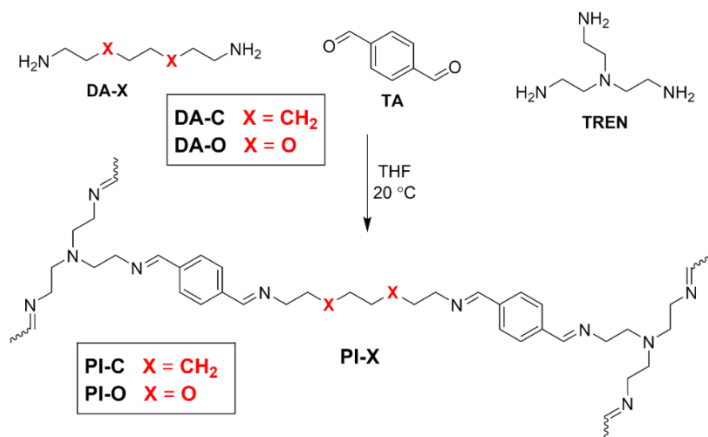

Figure 4.1 Reaction scheme for the formation of dynamic polyimine CANs from terephthalaldehyde (**TA**), tris(2-aminoethyl)amine (**TREN**) and a tuneable diamine (**DA-X**) with built-in domains being either polar (X = O) or apolar (X = CH$_2$) of nature.

To investigate the role of polarity-induced effects by EO moieties, CANs consisting of dynamic imine bonds were used in this chapter (see Figure 4.1). In **Chapter 2** it was shown that the dynamic mechanical properties of such polyimines materials were very dependent on the molecular composition of the material, and thus offer broad tuneability. Furthermore, imines are favourable materials as they can be readily synthesised from a condensation reaction between an aldehyde and amine at room temperature, without a catalyst, and with water as the only side product.[54, 55] While earlier work on polyimine CANs already described the effect of solvent polarity,[56, 57] and moisture sensitivity,[58] the quantification of polar effects in the polymer matrix itself on the imine exchange has not been addressed in great detail yet. Therefore, in this study we synthesised different polyimine materials with varying polar/apolar moieties (also in different components) of the polymer network. With a combination of kinetic studies using small-molecule analogues by NMR analysis, and temperature-dependent rheology experiments on the network

polymers, is was possible to dissect the effect of the polarity in the material on both the macroscopic level, and that of the molecular bond exchange. Furthermore, a better understanding in the relaxation behaviour of CANs was obtained, as is was observed that the stress relaxation proceeded in three individual phases.

4.2   Results and Discussion

4.2.1   Small-molecule bond exchange studies

For the initial kinetic evaluation of the bond exchange reaction, two same-sized diamine monomers (**DA-X**) were selected (Scheme 2). The first consisted of a fully carbon octane chain (**DA-C**), and the second included two oxygen atoms on the 3' and 6' position of the chain (**DA-O**) to represent the EO moiety. Once the amines have reacted with an appropriate aldehyde, imines are formed. These imines can then perform bond exchange reactions *via* either a transimination reaction with a primary amine, or *via* imine metathesis with another imine.[55] In this section, the study of the kinetics of both these exchange reactions will be divided in four parts: 1) transimination for which the tuneable monomer acts as the nucleophile, 2) transimination for which the tuneable monomer acts as the electrophile, 3) metathesis for which the tuneable monomer acts as the nucleophile, and 4) metathesis for which the tuneable monomer acts as the electrophile (Figure 4.2). The material that is added in excess acts as the attacking moiety. The excess is required to obtain a *pseudo*-first-order reaction towards formation of the new imine, as a 1:1 ratio would result in an equilibrium between starting compound and product. In the transamination reactions (Figure 4.2A and 4.2B) the primary amine acts as the nucleophile, which will attack on the carbon atom of the imine bond.[59] For the imine metathesis reactions (Figure 4.2C and 4.2D) the material that is added in excess is considered as the attacking party (nucleophile), as the exchange reaction of the starting material with the excess material will be the most prominent until new equilibrium is reached.

A) Transimination for which the tuneable monomer (**DA-X**) acts as nucleophile.
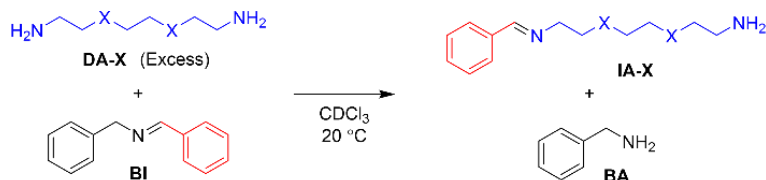
B) Transimination for which the tuneable monomer (**DI-X**) acts as electrophile.
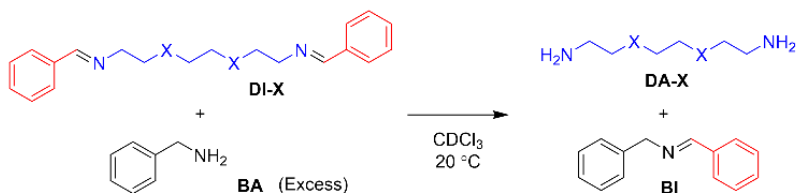
C) Imine metathesis for which the tuneable monomer (**DI-X**) acts as nucleophile.
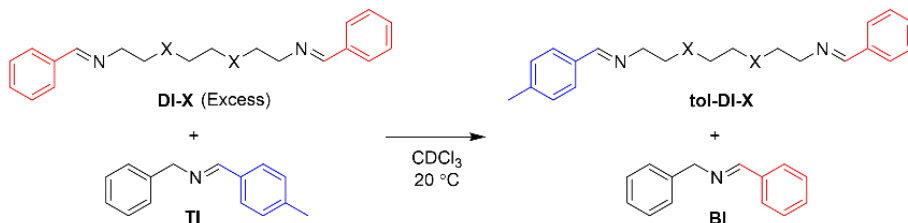
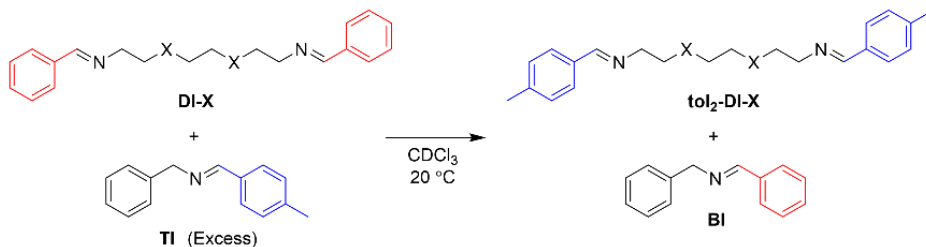D) Imine metathesis for which the tuneable monomer (**DI-X**) acts as electrophile.

Figure 4.2 Overview of imine exchange reactions. A) Transimination with **DA-X** as nucleophile, B) transimination with **DI-X** as electrophile, C) imine metathesis with **DI-X** as nucleophile, and D) imine metathesis with **DI-X** as electrophile.

For the first transimination reaction, in which **DA-X** is the nucleophile (Figure 4.2A), a benzyl imine (**BI**) was synthesised and dissolved in CDCl$_3$. An excess of **DA-X** was then added to push the reaction towards formation of the imine on the tuneable diamine chain (**IA-X**) and freeing the benzylamine (**BA**) from the starting benzyl imine (**BI**) in a *pseudo*-first-order fashion. The conversion over time was followed using ^{1}H NMR by integration of the imine signals of **BI** and **IA-X**. The data (Figure 4.3A) were fitted using the equation for first order reaction kinetics to obtain the reaction rate constant (*k*) for the exchange reaction. The determined *k* values for all exchange reactions have been combined in Table 4.1.
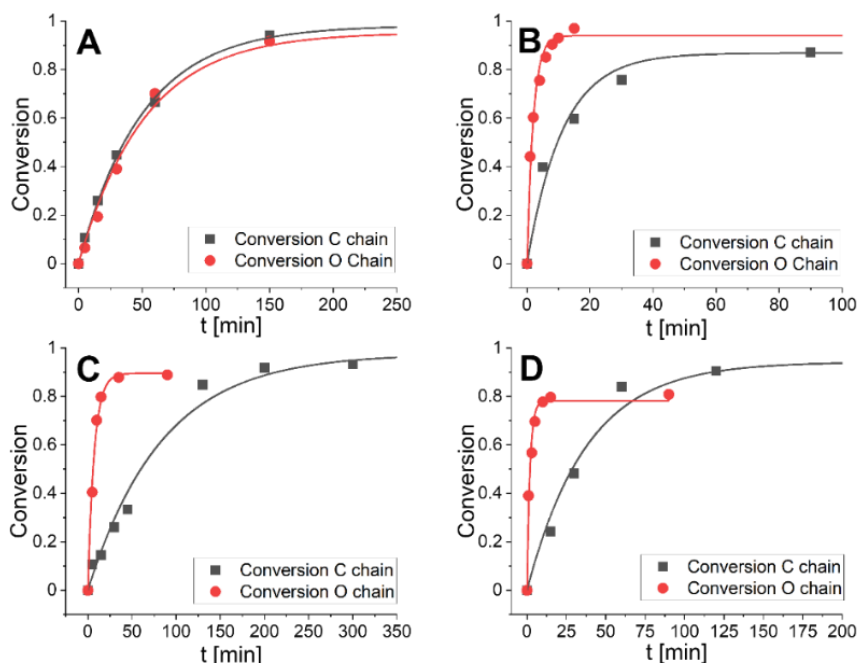
Figure 4.3 Conversion over time for A) transimination with **DA-X** as nucleophile, B) transimination with **DI-X** as electrophile, C) imine metathesis with **DI-X** as nucleophile, and D) imine metathesis with **DI-X** as electrophile. Data points were fitted according to first-order kinetic model. Note the different time scale on the *x*-axis for each plot.

For the second transimination reaction, in which **DI-X** is the electrophile (Figure 4.2B), imines **DI-C** and **DI-O** were first synthesised. The imines were then dissolved in CDCl$_3$ and an excess of benzylamine (**BA**) was added to push the reaction towards the formation of the benzyl imine (**BI**) and transformation of the imines of the tuneable chains back to amine

monomer (**DA-X**). The conversion over time (Figure 4.3B) was followed using ^{1}H NMR by integration of the imine signals of **DI-X** and **BI**. Reaction rate constants (k) were obtained using the same procedure as before and are also presented in Table 4.1.

For the first metathesis reaction, in which **DI-X** acts as nucleophile (Figure 4.2C), a toluene imine (**TI**) was first synthesised and dissolved in CDCl$_3$. An excess of the tuneable imine chain (**DI-X**) derived from benzaldehyde was then added to push the reaction towards the formation of the benzyl imine (**BI**). The conversion over time (Figure 4.3C) was followed over time, and k (Table 4.1) was determined following the same procedure as before.

For the second metathesis reaction, in which **DI-X** acts as electrophile (Figure 4.2D), **DI-X** was reacted with an excess of **TI** to push the reaction towards the formation of the bis-toluene imine chain (**tol$_2$-DI-X**). The conversion over time (Figure 4.3D) was followed over time and k (Table 4.1) was determined following the same procedure as before.

Table 4.1 First-order rate constants (k) for the imine exchange reactions, in 10^3 s^{-1}.

X	Transimination (Nucleophilic)	Transimination (Electrophilic)	Metathesis (Nucleophilic)	Metathesis (Electrophilic)
CH$_2$	**0.33** ± 0.01	**1.68** ± 0.33	**0.20** ± 0.02	**0.44** ± 0.07
O	**0.32** ± 0.03	**8.88** ± 0.92	**2.30** ± 0.17	**8.69** ± 1.20

From the combined data (in Table 4.1) we observed that for the transimination reaction in which the **DA-X** acts as a nucleophile, that the k values were similar for the apolar and polar compound, which thus implies that the presence of the more polar EO moiety in the molecule has no observable effect on the reaction rate. However, for the transimination in which **DI-X** acts as electrophile, we observed that the ether-containing molecule yielded a five-fold higher reaction rate. These results together suggest that the reactivity of the amine is not affected by the presence or absence of the polar EO moiety in the material, but the reactivity of the imine is affected: the presence of the ether moiety enhances the reaction rate fivefold compared to the alkyl chain. The observation that imines are more affected by the polar effect than the amines might be explained by their prominent charge separation *via* the (conjugated) C=N double bond. The transimination reaction can also be catalysed by trace amount of acid (which could even be water) *via* protonation of the imine nitrogen before formation of the aminal intermediate, and therefore result in faster exchange.[59] As this charged species would be stabilised better in polar media, in addition to the availability of oxygen lone pairs to transfer the H$^+$, this could explain the enhanced reaction rate for the

EO-containing material. This acid-catalysed reaction would also only affect the reactivity of the imine, which could explain why no difference in k was observed for different amines. For the metathesis reactions we observed that the reaction rate increased significantly (more than 10-fold) for the polar, EO-containing linker for both the nucleophilic and the electrophilic reaction. Furthermore, we observed that the electrophilic effect (~20-fold rate enhancement) was slightly more prominent than the nucleophilic effect (~10-fold rate enhancement), which suggests that the imines of the more polar EO containing molecules are somewhat more prone to being attacked relative to performing the attack. Just as for the transimination reaction, trace amounts of acid could catalyse the metathesis, and the same effects regarding polarity in the molecules could be proposed. Additionally, trace amounts of (unreacted) primary amine could enhance the reaction rates *via* a series of fast, uncatalysed transimination reactions producing metathetic products.[60, 61]

In conclusion, from the small-molecule kinetic studies we could clearly observe that imines of the more polar, EO-containing molecules showed significantly higher imine exchange rates, compared to the apolar, alkyl-linked molecules. This prompted us to investigate whether these differences in molecular exchange kinetics would also manifest themselves when these exchangeable imine groups are incorporated into a polymer matrix, by revealing different dynamic and/or thermal material properties dependent on the nature (*i.e.*, polarity) of the used linker.

4.2.2 Thermal properties of polyimine networks

Initially the thermal properties of the polyimine materials were studied. To this end, the polymers were synthesised using the **DA-X** monomer, in combination with terephthalaldehyde (**TA**) and tris(2-aminoethyl)amine (**TREN**) (Scheme 1). The synthesis was performed in THF at room temperature, followed by drying *in vacuo* at 50 °C, according to the reported polymerisation procedure for polyimine materials in **Chapter 2**. Two polyimine materials were synthesised: **PI-C**, containing the alkyl-linked diamine monomer **DA-C**, and **PI-O**, containing the EO-linked diamine monomer **DA-O** (see Figure 4.1 in the Introduction). Before the materials were analysed with the use of rheology, they were hot-pressed into flat discs with a 10 mm diameter and 0.4 mm thickness. As the monomer ratios were constant, and the molecular lengths of **DA-C** and **DA-O** are similar, the crosslinking density was assumed to be identical for both **PI-X** materials.

Using rheology, a temperature sweep experiment was performed in which the storage (G') and loss (G'') modulus were measured as a function of the temperature (Full experimental details are provided in the Supporting Information, Section 4.5.2). From the G' and G'' curves (Figure 4.4), typically two phase transitions of the materials were observed: from the

glassy to the rubber state and from the rubbery to the viscous state. The glass-to-rubber phase transition can typically be observed as a steep decrease in the G' when the glass-like material is heated,[22] and is generally referred to as the glass transition temperature (T_g). The phase transition from rubber to a viscous state (*i.e.*, from a viscoelastic solid to a viscoelastic liquid) can be noticed from a second steep drop in G' at increasing temperature, or can sometimes be better visualised at the crossover point of G' and G'' (*i.e.*, where tan(δ) = 1).[9] We will therefore refer to this point as the crossover temperature (T_{cross}).[62]
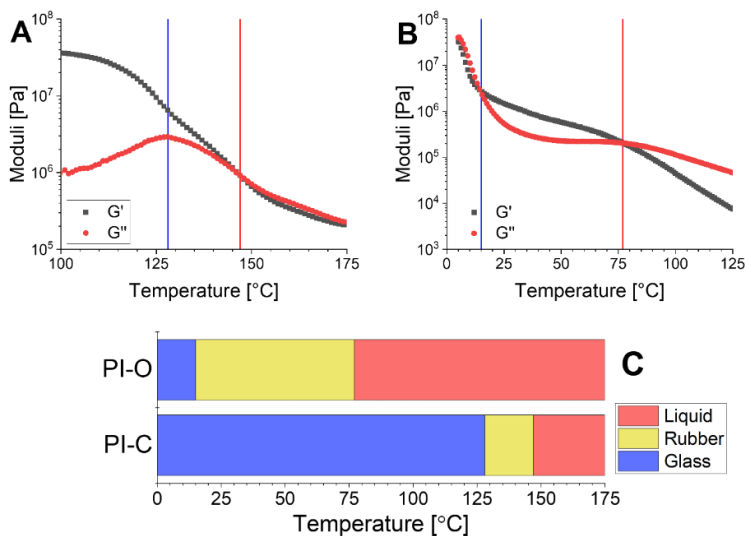
Figure 4.4 Representative temperature sweep curves of A) **PI-C** and B) **PI-O**, where the vertical blue line indicates the glass-rubber transition (T_g) and the vertical red line indicates rubber-viscous transition (T_{cross}). C) Visual representation of the glass, rubber and liquid phases of **PI-O** (top) and **PI-C** (bottom) as a function of the temperature.

From the temperature sweep curves of **PI-O** and **PI-C**, we observed that both phase transitions for **PI-O** occurred at significantly lower temperature than **PI-C**. The decreasing phase transition temperatures for the polar materials are in agreement with the results from the kinetic experiments. As was discussed before, the more polar EO-containing molecules showed faster bond exchange, which translates to more dynamic materials. As a result, the phase transition temperatures decrease. Furthermore, the rubbery domain of the **PI-C** materials is relatively small (temperature range of 19 °C) compared to **PI-O** (temperature range of 62 °C). This could be attributed to a lack of chain mobility in the polymer network of **PI-C** due to poor chain diffusion.

Apart from the polar effect in the diamine monomer, we also considered the effect of more polar EO-containing chains in the aldehyde monomer. Therefore, we synthesised two dialdehyde monomers (**AL-X**) that differ in their linker, similar to those of the previously used diamines, where one monomer included a C_8 alkyl chain, and the other includes the EO moiety (Figure 4.5).
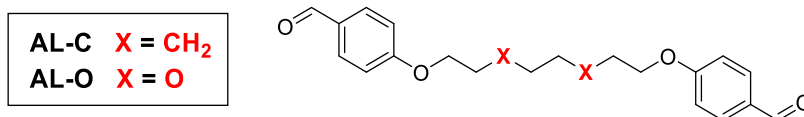

Figure 4.5 Molecular structure of the tuneable dialdehyde monomer (**AL-X**), for which X is either CH_2 (**AL-C**, apolar chain) or O (**AL-O**, polar chain).

With two different aldehyde (**AL-X**) and two diamine (**DA-X**) monomers we could synthesise four different polyimines (crosslinked with **TREN** *via* the same procedure as before): both diamine and dialdehyde are polar (*i.e.*, EO-containing linker, **PI-OO**), both diamine an dialdehyde are apolar (*i.e.*, alkyl linker, **PI-CC**), the diamine is polar and the dialdehyde is apolar (**PI-OC**), the diamine is apolar and the dialdehyde is polar (**PI-CO**).

A temperature sweep experiment was performed on the four polyimine samples using the same rheology setup as before to determine the phase transition temperatures (Figure 4.6). From the results we can draw a clear conclusion that the increasing polarity lowers both phase transition temperatures. In the extreme case where both the aldehyde and amine chains are polar (**PI-OO**) the phase transition of glass to rubber was observed at a temperature as low as 1 °C and the phase transition from rubber to liquid at 37 °C. If we compare this to the other extreme where both monomers were apolar (**PI-CC**), we observed a phase transition from glass to rubber at 119 °C, and a phase transition from rubber to liquid above 150 °C. This means that the phase transition temperatures were increased by more than 100 °C by simply replacing the polar linkers for apolar ones (that vary only in two of the eight atoms that make up the linker). When only one of the monomers –either de dialdehyde or diamine– was polar, we observed that the phase transition temperatures was found in between the two extremes. Comparing the **PI-OC** and **PI-CO** individually shows that the phase transition from glass to rubber is similar (57 °C for **PI-OC** and 59 °C for **PI-CO**), but the phase transition from rubber to viscous phase occurred at slightly higher temperatures for **PI-OC** (83 °C) compared to **PI-CO** (68 °C). This means that the presence of polar domains in either the diamine or dialdehyde monomer decreases the phase transition temperatures of the polyimine materials, with the addition that the presence of EO moieties in the

dialdehyde monomer is slightly more effective in lowering the rubber-to-glass phase transition, and therefore shortening the rubber phase of the material. This slight difference between the effect of polar groups in either the aldehyde or amine monomer could possibly be explained by other, secondary interactions within the network, for example, in relation to the aromatic moieties being present next to the EO moiety.
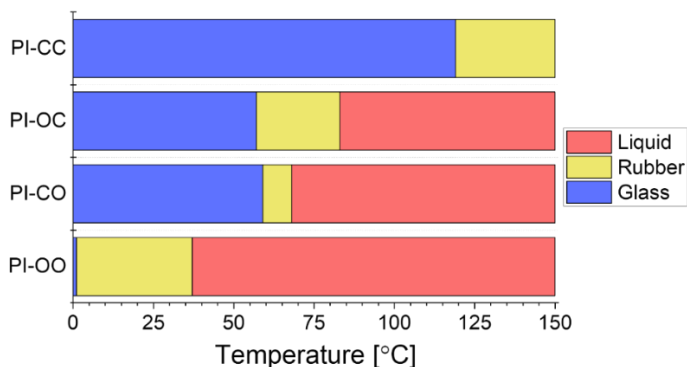

Figure 4.6 Visual representation of the glass (blue), rubber (yellow) and liquid/viscous (red) phases of the **PI-XX** materials as a function of the temperature.

4.2.3 Stress relaxation of polyimine networks

Next to the thermal properties, the stress relaxation behaviour of **PI-C** and **PI-O** was also investigated (see Section 4.5.3 in the Supporting Information for full experimental details). In this relaxation process, we observed multiple relaxation phases, as can be seen in the normalised stress relaxation plots (Figure 4.7). Please note that for **PI-C** and **PI-O** different temperatures needed to be selected in order to study the relaxation behaviour. The relaxation curves could not be accurately fitted to a one-component Maxwell model that is commonly used for the determination of relaxation times (τ) in CANs.[63] However, the data could be fitted with a three-component function (see Section 4.5.3 in the Supporting Information), revealing that three individual modes of relaxation (with corresponding relaxation times) occur within the material: a fast, intermediate and slow process. The relaxation curves for **PI-O** and **PI-C** were measured at several temperatures within their rubber state and at every given temperature the three relaxation times were determined (Table 4.2 for **PI-O** and Table 4.3 for **PI-C**). All relaxation curves are included in Section 4.5.3 in the Supporting Information.
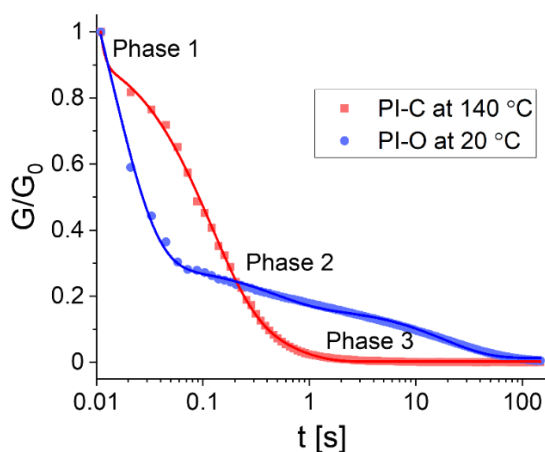
Figure 4.7 Normalised 3-step relaxation curves for **PI-C** at 140 °C (blue) and **PI-O** at 20 °C (red).

From the relaxation times of **PI-O** (Table 4.2) we observed a clear temperature dependency for each of the three relaxation processes: τ_1 changed by a factor ~3.5 over a temperature range of 35 °C, τ_2 by a factor ~8, and τ_3 by a factor ~40. When we compared these observations to the relaxation times of **PI-C** (Table 4.3), we found distinct differences. Firstly, we observed that both τ_1 and τ_3 seem to be largely independent of the temperature for **PI-C**. However, τ_2 was dependent on the temperature, as the relaxation time changed by a factor ~2 over a temperature range of 35 °C.

Table 4.2 Relaxation times (τ) for the three relaxation processes of **PI-O** at several temperatures within the rubbery domain of the material.

T (°C)	τ_1 (ms)	τ_2 (ms)	τ_3 (ms)
20	13.7	4.4×10^2	18.4×10^3
25	13.2	3.3×10^2	9.6×10^3
30	12.1	2.3×10^2	5.1×10^3
35	9.0	1.4×10^2	2.8×10^3
40	7.3	1.0×10^2	1.6×10^3
45	5.5	0.74×10^2	1.0×10^3
50	5.0	0.63×10^2	0.67×10^3
55	4.1	0.56×10^2	0.46×10^3

Table 4.3 Relaxation times (τ) for the three relaxation processes of **PI-C** at several temperatures within the rubbery domain of the material.

T (°C)	τ_1 (ms)	τ_2 (ms)	τ_3 (ms)
140	≤ 1	1.12×10^2	49×10^3
145	≤ 1	0.94×10^2	37×10^3
150	≤ 1	0.83×10^2	32×10^3
155	≤ 1	0.77×10^2	36×10^3
160	≤ 1	0.70×10^2	38×10^3
165	≤ 1	0.65×10^2	48×10^3
170	≤ 1	0.59×10^2	47×10^3
175	≤ 1	0.56×10^2	48×10^3

Based on the observed three-step relaxation process and determined τ values as a function of the temperature, we propose three modes of relaxation to each of the relaxation phases, with corresponding τ. The initial response (τ_1) of the material when it is exposed to a stress was attributed to chain rearrangements in the material.[64, 65] This process is generally very fast, but quickly reaches it maximum potential due to the crosslinked structure of the polymer network.[8, 66] Therefore, in order to fully relax the materials, additional relaxation through bond exchange is required.[67] We do however see that this additional relaxation through bond exchange proceeds on two different timescales (τ_2 and τ_3). This separation in two timescales could be attributed to imine exchange on a local level (τ_2), meaning exchange between imines groups that are in close proximity, and secondly by imine exchange through diffusion (τ_3). The latter occurs on a slower timeframe, as this mechanism requires the imine groups to diffuse through the network as well as find partnering imine groups to perform the bond exchange. The concept of diffusion and flow in the materials could be provided by reptation theory,[68, 69] which applies to random Brownian movement of polymer strains in entangled macromolecular structures,[70] and could be extrapolated to dynamic polymer networks as well.[71] More flexible chains would show an enhanced reptation process (better "slithering" of chains),[71] which in turn promotes the availability of imines as they move better through the medium.

Regarding the mentioned three relaxation mechanisms, we can then further discuss the observations on the stress relaxation behaviour between the polar **PI-O** and apolar **PI-C** material. As can be seen in Table 2, each of the relaxation phases for **PI-O** was significantly influenced by the temperature, whereas for **PI-C** (Table 4.3) only τ_2 showed a clear temperature response. The temperature response of the imine exchange is expected, although the absence of a clear temperature response for the imine exchange through

diffusion (τ_3) is peculiar. An explanation for this absence might be found in earlier work on cluster formation of exchanging polar groups in apolar polymer networks.[52] The diffusion of imine groups in the apolar **PI-C** material might be limited as the polar imine groups tend to cluster together. This would mean that the local imine exchange becomes the main exchange pathway as the imine groups are already in close reach to each other, and the diffusion of imine groups through the polymer matrix is limited. The observation that τ_2 showed stronger temperature response for the polar **PI-O** material (factor ~8 over 35 °C range) over the apolar **PI-C** material (factor ~2 over 35 °C range) suggests that the increasing polarity in the polymer network also enhances the thermal response if the imine exchange. As τ_1 was found to be independent of the temperature for the apolar **PI-C**, this suggests that the glass transition of the material is mainly caused by the imine exchange, whereas for the polar **PI-O** material the flexibility within the material might also contribute to the softening of the material. Lastly, this could also add to the observation that the τ_3 in **PI-O** showed a significant temperature response (factor ~40 over 35 °C) as both the imine exchange and network flexibility are enhanced by increasing the temperature.

Overall, we can conclude that τ_1 can be linked to reptation and is affected by the flexibility of the polymer chains.[71] Additionally, the ease of reptation alters the diffusion and availability of exchanging imine groups, affecting τ_3. Cluster formation of exchanging groups as a result of polarity in the polymer network might cause additional alterations to τ_3, as well as to τ_2.[52] The temperature dependency of the imine exchange further applies to both τ_2 and τ_3. Lastly, our supporting kinetic data from the NMR experiments showed a clear correlation between the rate of imine exchange and presence of polar EO groups, which applies again to both τ_2 and τ_3.

Determination of the relaxation behaviour of the **PI-XX** materials was harder to achieve as the materials were generally very brittle, with the exception of **PI-OO**, and would break easily at the required applied stress. Measurements in the liquid phase of the materials were also unsuccessful as relaxation times were too short (<1 ms) to properly analyse. Therefore, no in-depth stress relaxation analysis could be performed on these materials. Only for the **PI-OO** material (Table 4) we were able to analyse the relaxation behaviour, for which we observed a relatively similar trend in the three relaxation phases as the **PI-O** material (Table 2). This resemblance may result from the fact that both materials contain the polar EO linkers. Note however that the two materials have different crosslinking densities and polarity effects, as the **PI-O** material contains the small **TA** dialdehyde monomer, and **PI-OO** contains the longer **AL-O** dialdehyde monomer that also contains an additional polar EO linker.

Table 1 Relaxation times (τ) for the three relaxation processes of PI-OO at several temperatures within the rubbery domain of the material.

T (°C)	τ_1 (ms)	τ_2 (ms)	τ_3 (ms)
15	11.0	3.7×10^2	12.2×10^3
20	10.0	2.7×10^2	7.3×10^3
25	8.0	1.7×10^2	4.0×10^3
30	5.7	1.1×10^2	2.2×10^3
35	4.1	0.76×10^2	1.3×10^3
40	2.7	0.58×10^2	8.6×10^2
45	2.3	0.52×10^2	6.4×10^2
50	1.4	0.50×10^2	4.8×10^2

4.3   Conclusion

Ethylene oxide and similar ether groups are commonly applied in (dynamic) polymer materials to increase flexibility of the material. What should however not be overlooked in the case of CANs, is the polarity-induced effect of these ethylene oxide groups on the kinetics of the dynamic covalent bond exchange, which in turn results in alteration of the dynamic-mechanical properties of the material. In this study, we showed that the dynamic exchange behaviour in polyimine CANs could be related to polarity effects in the polymer matrix. Kinetic studies on small molecules revealed that the reaction rates of imine exchange could be enhanced by introduction of more polar ethylene oxide groups when compared to apolar purely aliphatic carbon chains in the monomer. Additionally, from rheology studies on the crosslinked polymer materials we concluded that the addition of the more polar ethylene oxide groups resulted in a higher dynamic response in the materials, which was reflected in a decrease in the phase transitions from glass to rubber (T_g), and from rubber to viscous state (T_{cross}). Furthermore, extensive investigations into the stress relaxation behaviour of the materials revealed a gradual three-phase relaxation process. These were appointed to relaxation by chain redistribution within the polymer network, relaxation *via* imine exchange on local level, and imine exchange after diffusion through the network. This division in three relaxation processes within one material offers a better physical-chemical understanding of the dynamic behaviour of CANs and how molecular interactions within the polymer matrix relate to macroscopic properties of the material. These results firstly reveal the subtle, sometimes unexpected, effect that small changes in molecular structure can have on material properties, as reflected here in the

particular changes in the multi-step relaxion processes. Moreover, we envision that this multi-step relaxation could also be applied to other CANs to achieve a more precise insight in, and ultimately control over, the molecular dynamics of the material.

4.4 Acknowledgements

Timo Groeneveld, dr. Joshua Dijksman and prof. Han Zuilhof ar acknowledged for their help and involvement.

4.5 Supporting Information

An overview of the most important supporting information to this chapter is given below. The full electronic supporting information (ESI), corresponding to the published article, is available online at: http://dx.doi.org/10.1039/D0PY01555E.

4.5.1 Small-molecule kinetic studies

Transimination with (**DA-X**) as nucleophile
(E)-*N*-benzyl-1-phenylmethanimine (**BI**) (0.010 mmol, 1.9 μL) was dissolved in 0.50 mL CDCl$_3$. Then the dianiline (**DA-X**) (0.10 mmol, 14.4 mg for **DA-C** or 14.6 mg for **DA-I**) was added to the solution at room temperature. The mixture was briefly shaken and the conversion of **BI** to **IA-X** (see Figure 4.2A in the Results and Discussion, Section 4.2.1) was followed over time using ^{1}H NMR by integration of the imine signals of the corresponding materials. The imine signal of **BI-I** was typically observed around 8.40 ppm, the imine signal of **IA-C** was typically observed at 8.25 ppm, and the imine signal of **IA-O** was typically observed around 8.29 ppm.

Transimination with **DI-X** as electrophile
Diimine (**DI-X**) (0.010 mmol, 3.20 mg for **DI-C** or 3.24 mg for **DI-O**) was dissolved in 0.50 mL CDCl$_3$. Then benzylamine (**BA**) (0.40 mmol, 44 μL) was added to the solution at room temperature. The mixture was briefly shaken and the conversion of **DI-X** to **BI** (see Figure 4.2B in the Results and Discussion, Section 4.2.1) was followed over time using ^{1}H NMR by integration of the imine signals of the corresponding materials. The imine signal of **DI-C** was typically observed at 8.28 ppm, and the imine signal of **BI** was typically observed

at 8.40–8.41 ppm. The imine signal of **DI-O** was typically observed around 8.26 ppm when both ends were imines, and around 8.30 ppm when one end remained an imine and the other was already transformed back to amine.

<u>Imine metathesis with **DI-X** as nucleophile</u>
(E)-*N*-benzyl-1-(p-tolyl)methanimine (**TI**) (0.010 mmol, 2.2 µL) was dissolved in 0.50 mL CDCl$_3$. Then the diimine (**DI-X**) (0.20 mmol, 64.1 mg for **DI-C** or 64.9 mg for **DI-O**) was added to the solution at room temperature. The mixture was briefly shaken and the conversion of **TI** to **BI** (see Figure 4.2C in the Results and Discussion, Section 4.2.1) was followed over time using ^{1}H NMR by integration of the imine signals of the corresponding materials. The imine signal of **TI** was typically observed around 8.37 ppm and the **BI** imine signal was typically observed around 8.41 ppm.

<u>Imine metathesis with **DI-X** as electrophile</u>
Diimine (**DI-X**) (0.010 mmol, 3.20 mg for **DI-C** or 3.24 mg for **DI-O**) was dissolved in 0.50 mL CDCl$_3$. Then **TI** (0.20 mmol, 43 µL) was added at room temperature. The mixture was briefly shaken and the conversion from **DI-X** to **tol$_2$-DI-X** (see Figure 4.2D in the Results and Discussion, Section 4.2.1) was followed over time using ^{1}H NMR by integration of the imine signals of the corresponding materials. The imine signal of **DI-X** was typically observed around 8.31 ppm, and the imine signal of **tol$_2$-DI-X** was typically observed around 8.27-8.28 ppm. The intermediate **tol-DI-X** (one benzene and one toluene imine) would therefore show one signal at 8.31 ppm and one at 8.27-8.28 ppm. This was included in the integration of the imine signals.

4.5.2   Temperature sweeps
All temperature sweep experiments were measured on polymer discs with a 10 mm diameter and 0.40 mm thickness. A constant strain of 0.1% with a frequency of 1 Hz was introduced while gradually heating the sample with 1 °C per 10 s. Storage (*G'*) and loss (*G''*) moduli were plotted as a function of the temperature. The temperature sweep curves for **PI-C** and **PI-O** are presented in Figure 4.4 in the Results and Discussion (section 4.2.2), and the curves for the **PI-XX** materials are presented in Figure 4.8 below.
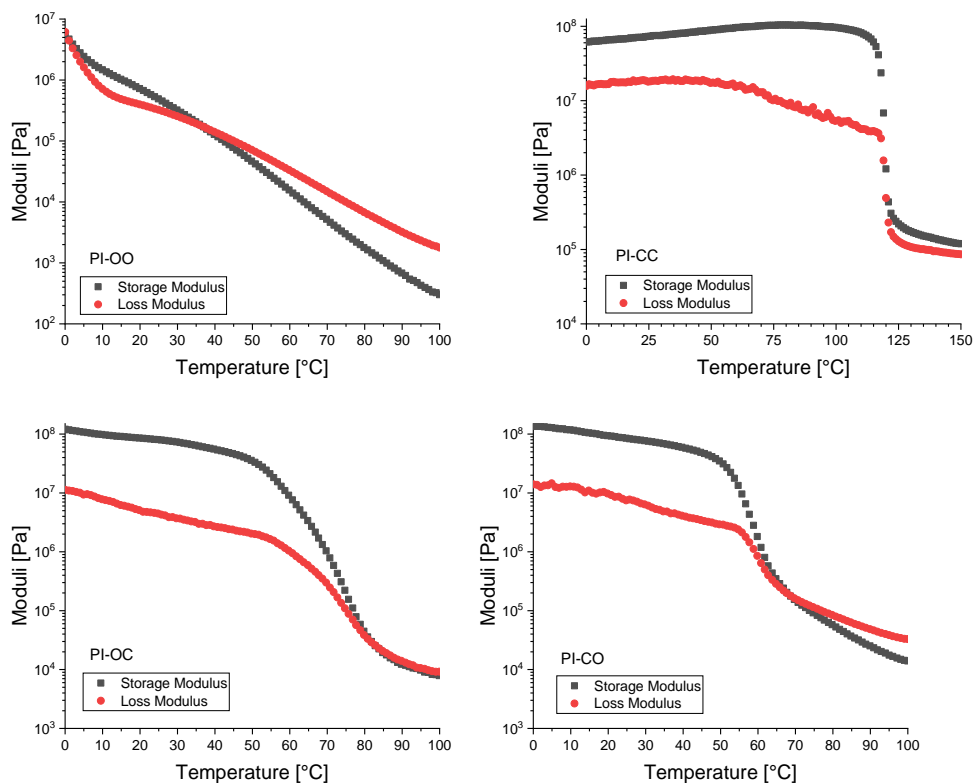
Figure 4.8 Temperature sweep curves of **PI-OO** (top left), **PI-CC** (top right), **PI-OC** (bottom left), and **PI-CO** (bottom right).

4.5.3 Stress relaxation

Stress relaxation experiments were performed on polymer discs with a 0.40 mm thickness and 10 mm diameter. The samples were exposed to a 1% strain and the relaxation modulus ($G(t)$) was measured as a function of the time at several temperatures within the rubbery domain of the material. The data were visualised by plotting the relaxation modulus as a function of the time. The data of the relaxation curves were fitted with a 3-component function of exponential decay:

$$G(t) = A_1 * \exp\left(\frac{-t}{\tau_1}\right) + A_2 * \exp\left(\frac{-t}{\tau_2}\right) + A_3 * \exp\left(\frac{-t}{\tau_3}\right) \qquad \text{(Equation 4.1)}$$

where the first, second and third components were assigned to the network relaxation, imine exchange on local level, and the imine exchange through diffusion, respectively. The relaxation curves for **PI-O**, **PI-O** and **PI-OO** are shown in Figure 4.9.
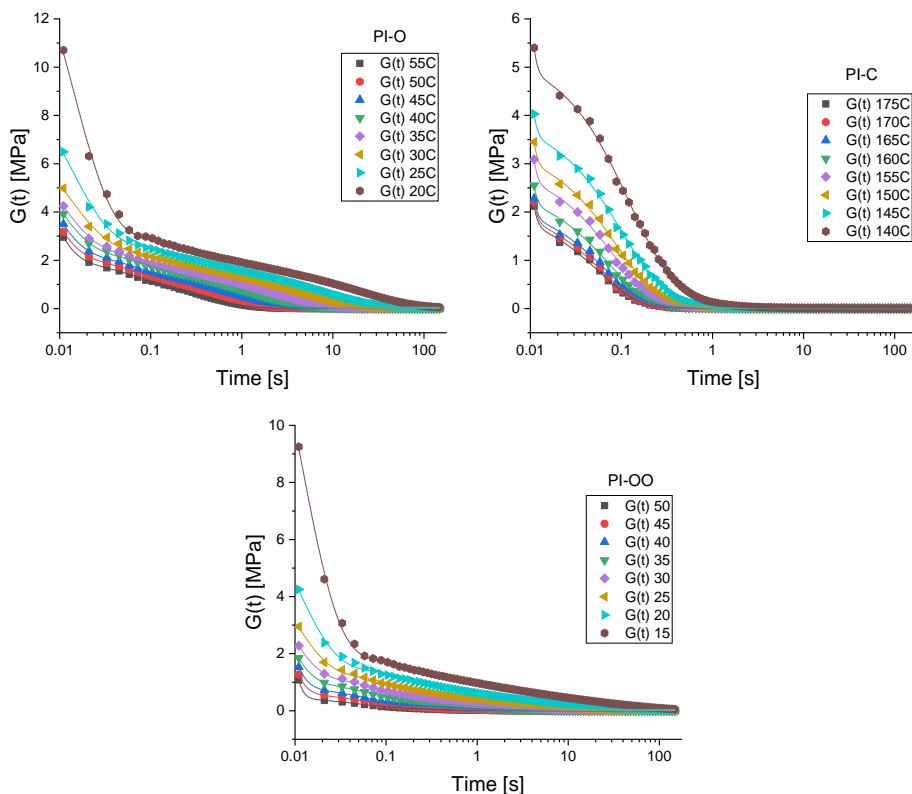

Figure 4.9 Stress relaxation curves of **PI-O** (top left), **PI-C** (top right), and **PI-OO** (bottom). Data points were fitted according to a 3-component exponential decay.

4.5.4   General procedure for polymer synthesis

Tris(2-aminoethyl)amine (30 µL, 0.20 mmol) and diamine (**DA-C**: 534 mg, 3.70 mmol or **DA-O**: 540 µL, 3.70 mmol) were dissolved in 5 mL THF. Then the dialdehyde (**TA**: 537 mg, 4.00 mmol or **AL-C**: 1.42 g, 4.00 mmol or **AL-O**: 1.43 g, 4.00 mmol) was added, and the mixture was shaken until a homogeneous solution was obtained. The solution was poured into a petri dish and left for overnight. To remove remaining solvent and formed water from the polymers, they were further dried in a vacuum oven at 50 °C for another day. FT-IR was

used to check full conversion of the aldehydes (1700 cm^{-1}) to imine (1640 cm^{-1}). In order to further analyse the materials with rheology, they were hot-pressed (max. 40 N and 150 °C, depending on the material) into discs with a 10 mm diameter and 0.4 mm thickness.

4.5.5   Synthetic Procedures
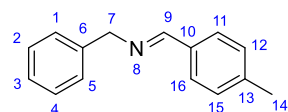
(E)-*N*-benzyl-1-phenylmethanimine (**BI**)
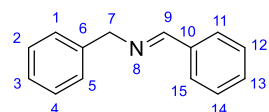
Benzaldehyde (0.52 mL, 5.1 mmol) and benzylamine (0.56 mL, 5.1 mmol) were dissolved in dichloromethane (50 mL). Molecular sieves (3 Å) were added and the mixture was stirred at room temperature for 3 hours. Afterwards, the mixture was filtered over Celite®. The filtrate was concentrated *in vacuo* to obtain the product as a clear yellow liquid with a 99% yield.

R$_f$: 0.55 (EtOAc/heptane 1:9).

^{1}H NMR (400 MHz, CDCl$_3$, δ): 8.41 (s, C9-H, 1H), 7.81-7.78 (m, C11-H + C15-H, 2H), 7.44-7.43 (m, C12-H + C14-H, 2H), 7.42 (m, C13-H, 1H), 7.36-7.35 (m, C1-H + C2-H + C4-H + C5-H, 4H), 7.30-7.25 (m, C3-H, 1H), 4.84 (s, C7-H, 1H).

^{13}C NMR (100 MHz, CDCl$_3$, δ): 162.6 (C9), 138.9 (C6), 136.3 (C10), 131.6 (C12 + C14), 128.7 (C13), 128.6 (C2 + C4), 128.4 (C11 + C15), 128.1 (C1 + C5), 126.2 (C3), 65.2 (C7).

(E)-*N*-benzyl-1-(p-tolyl)methanimine (**TI**)

p-Tolualdehyde (0.59 mL, 5.0 mmol) and benzylamine (0.55 mL, 5.0 mmol) were dissolved in dichloromethane (50 mL). Molecular sieves (3 Å) were added and the mixture was stirred at room temperature for 3 hours. Afterwards, the mixture was filtered over Celite®. The filtrate was concentrated *in vacuo* to obtain the product as a colourless liquid with a 98% yield.

R$_f$: 0.51 (EtOAc/Heptane 1:9).

^{1}H NMR (400 MHz, CDCl$_3$, δ): 8.38 (s, C9-H, 1H), 7.70-7.68 (d, *J* = 8.2 Hz, C11-H + C16-H, 2H), 7.36-7.35 (m, C1-H + C2-H + C4-H + C5-H, 4H), 7.30-7.26 (m, C3-H, 1H), 7.25-7.23 (t, *J* = 8.3 Hz, C12-H + C15-H, 2H), 4.83 (s, C7-H, 2H), 2.40 (s, C14-H, 3H).

^{13}**C NMR** (100 MHz, CDCl$_3$, δ): 162.1 (C9), 141.2 (C13), 139.6 (C6), 133.7 (C10), 129.5 (C12 + C15), 128.6 (C2 + C4), 128.4 (C11 + C16), 128.1 (C1 + C5), 127.1 (C3), 65.2 (C7), 21.6 (C14).

(1E,1'E)-*N*,*N*'-(octane-1,8-diyl)bis(1-phenylmethanimine) (**DI-C**)

Benzaldehyde (0.63 mL, 6.2 mmol) and 1,8-diaminooctane (0.45 g, 3.1 mmol) were dissolved in dichloromethane (50 mL). Molecular sieves (3 Å) were added and the mixture was stirred at room temperature for 3 hours. Afterwards, the mixture was filtered over Celite®. The filtrate was concentrated *in vacuo* to obtain the product as a white crystalline solid with an 84% yield.

R$_f$: 0.45 (EtOAc/Heptane 1:9).

^{1}**H NMR** (400 MHz, CDCl$_3$, δ): 8.27 (s, C7-H + C18-H, 2H), 7.73-7.71 (m, C1-H + C5-H + C20-H + C24-H, 4H), 7.41-7.40 (m, C2-H + C3-H + C4-H + C21-H + C22-H + C23-H, 6H), 3.62-3.58 (t, *J* = 7.2 Hz, C9-H + C16-H, 4H), 1.71-1.68 (m, C10-H + C15-H, 4H) 1.36 (m, C11-H + C12-H + C13-H + C14-H, 8H).

^{13}**C NMR** (100 MHz, CDCl$_3$, δ): 160.9 (C7 + C18), 136.5 (C6 + C19), 130.6 (C3 + C22), 128.7 (C2 + C4 + C21 + C23), 128.2 (C1 + C5 + C20 + C24), 62.0 (C9 + C16), 31.0 (C10 + C15), 29.5 (C12 + C13), 27.5 (C11 + C14).

(1E,1'E)-*N*,*N*'-((ethane-1,2-diylbis(oxy))bis(ethane-2,1-diyl))bis(1-phenylmethanimine) (**DI-O**)

Benzaldehyde (0.63 mL, 6.2 mmol) and 1,2-bis(2-aminoethoxy)ethane (0.45 mL, 3.1 mmol) were dissolved in dichloromethane (50 mL). Molecular sieves (3 Å) were added and the mixture was stirred at room temperature for 3 hours. Afterwards, the mixture was filtered over Celite®. The filtrate was concentrated *in vacuo* to obtain the product as a colourless oil with an 82% yield.
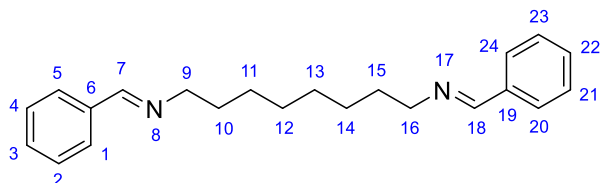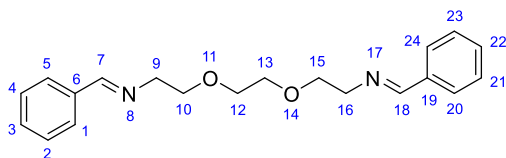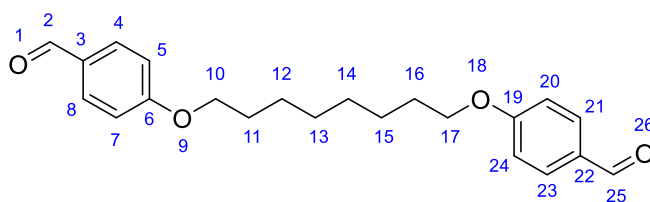
R$_f$: 0.45 (EtOAc/Heptane 1:9).

¹H NMR (400 MHz, CDCl₃, δ): 8.28 (s, C7-H + C18-H, 2H), 7.73-7.71 (m, C1-H + C5-H + C20-H + C24-H, 4H), 7.41-7.39 (m, C2-H + C3-H + C4-H + C21-H + C22-H + C23-H, 6H), 3.77 (s, C10-H + C12-H + C13-H + C15-H, 8H), 3.63 (s, C9-H + C16-H, 4H).

¹³C NMR (400 MHz, CDCl₃, δ): 162.8 (C7 + C18), 136.3 (C6 + C19), 130.8 (C2 + C4 + C21 + C23), 128.7 (C3 + C22), 128.3 (C1 + C5 + C20 + C24), 70.9 (C10 + C15), 70.7 (C12 + C13), 61.3 (C9 + C16).

4,4'-(octane-1,8-diylbis(oxy))dibenzaldehyde (**AL-C**)

4-Hydroxybenzaldehyde (2.44 g, 20.0 mmol) was dissolved in EtOH (25 mL). A solution of NaOH (863 mg, 21.6 mmol) in water (10 mL) was slowly added and the mixture stirred for 15 min at room temperature. 1,8-Dibromooctane (1.88 mL, 10.0 mmol) was added to the reaction mixture, which was then heated to reflux for overnight. The mixture was slowly cooled to room temperature and then placed on an ice bath so that a white solid precipitated from the solution. The solid was captured by filtration and rinsed with cold water. It was then dried *in vacuo* to obtain the product as a white powder with an 83% yield.

R_f: 0.56 (EtOAc/heptane 1:1)

¹H NMR (400 MHz, CDCl₃, δ): 9.88 (s, C2-H + C25-H, 2H), 7.84-7.81 (d, J = 8.75 Hz, C4-H + C8-H + C21-H + C23-H + 4H), 7.00-6.98 (d, J = 8.72, C5-H + C7-H + C20-H + C24-H, 4H), 4.06-4.03 (t, J = 6.47, C10-H + C17-H, 4H), 1.86-1.79 (m, C11-H + C16-H, 4H), 1.53-1.48 (m, C12-H + C15-H, 4H), 1.43-1.39 (m, C13-H + C14-H, 4H).

¹³C NMR (100 MHz, CDCl₃, δ): 190.9 (C2 + C25), 164.4 (C6 + C19) 132.1 (C4 + C8 + C21 + C23), 129.9 (C3 + C22), 114.9 (C5 + C7 + C20 + C24), 68.5 (C10 + C17), 29.4 (C12 + C15), 29.2 (C11 + C16), 26.0 (C13 + C14).

4,4'-(((ethane-1,2-diylbis(oxy))bis(ethane-2,1-diyl))bis(oxy))dibenzaldehyde (**AL-O**)
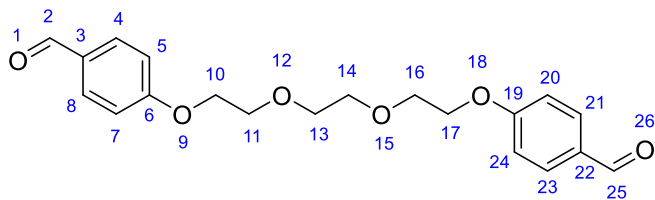
4-Hydroxybenzaldehyde (6.69 g, 54.8 mmol) was dissolved in DMF (100 mL). NaOH (2.67 g, 66.8 mmol) was slowly added to the solution, which then stirred for 15 min at room temperature. Tri(ethylene glycol) dichloride (4.28 mL, 27.4 mmol) was slowly added to the reaction mixture, which was then heated to reflux for overnight. The reaction mixture was cooled to room temperature before pouring onto ice chunks. A white precipitate formed, which was captured by filtration and rinsed with cold water. The material was further dried *in vacuo* to obtain the product as a beige powder with a 28% yield.

R$_f$: 0.41 (EtOAc/heptane 1:1).

¹H NMR (400 MHz, CDCl$_3$, δ): 9.87 (s, C2-H + C25-H, 2H), 7.81 (d, *J*=8.8 Hz, C4-H + C8-H + C21-H + C23-H, 4H), 7.00 (d, *J*=8.7 Hz, C5-H + C7-H + C20-H + C24-H, 4H), 4.20 (t, *J* = 4.8 Hz, C10-H + C17-H, 4H), 3.89 (t, *J*=4.8 Hz, C11-H + C16-H, 4H), 3.76 (s, C13-H + C14-H, 4H).

¹³C NMR (100 MHz, CDCl$_3$, δ): 190.9 (C2 + C25), 163.9 (C6 + C19), 132.1 (C4 + C8 + C21 + C23), 130.2 (C3 + C22), 115.0 (C5 + C7 + C20 + C24), 71.1 (C13 + C14), 69.7 (C11 + C16) 67.9 (C10 + C17)

References

1. D. Montarnal, M. Capelot, F. Tournilhac and L. Leibler, *Science*, 2011, **334**, 965-968.
2. M. Capelot, M. M. Unterlass, F. Tournilhac and L. Leibler, *ACS Macro Lett.*, 2012, **1**, 789-792.
3. W. Denissen, J. M. Winne and F. E. Du Prez, *Chem. Sci.*, 2016, **7**, 30-38.
4. M. Podgórski, B. D. Fairbanks, B. E. Kirkpatrick, M. McBride, A. Martinez, A. Dobson, N. J. Bongiardina and C. N. Bowman, *Adv. Mater.*, 2020, **32**, 1906876.
5. Y. Jin, Z. Lei, P. Taynton, S. Huang and W. Zhang, *Matter*, 2019, **1**, 1456-1493.
6. S. J. Rowan, S. J. Cantrill, G. R. L. Cousins, J. K. M. Sanders and J. F. Stoddart, *Angew. Chem. Int. Ed.*, 2002, **41**, 898-952.
7. Y. Jin, C. Yu, R. J. Denman and W. Zhang, *Chem. Soc. Rev.*, 2013, **42**, 6634-6654.

8. C. J. Kloxin, T. F. Scott, B. J. Adzima and C. N. Bowman, *Macromolecules*, 2010, **43**, 2643-2653.

9. C. J. Kloxin and C. N. Bowman, *Chem. Soc. Rev.*, 2013, **42**, 7161-7173.

10. M. K. McBride, B. T. Worrell, T. Brown, L. M. Cox, N. Sowan, C. Wang, M. Podgorski, A. M. Martinez and C. N. Bowman, *Annu. Rev. Chem. Biomol. Eng.*, 2019, **10**, 175-198.

11. Z. P. Zhang, M. Z. Rong and M. Q. Zhang, *Prog. Polym. Sci.*, 2018, **80**, 39-93.

12. A. Gablier, M. O. Saed and E. M. Terentjev, *Soft Matter*, 2020, **16**, 5195-5202.

13. S. Wu, H. Yang, S. Huang and Q. Chen, *Macromolecules*, 2020, **53**, 1180-1190.

14. O. R. Cromwell, J. Chung and Z. Guan, *J. Am. Chem. Soc.*, 2015, **137**, 6492-6495.

15. M. Röttger, T. Domenech, R. van der Weegen, A. Breuillac, R. Nicolaÿ and L. Leibler, *Science*, 2017, **356**, 62-65.

16. B. Marco-Dufort, R. Iten and M. W. Tibbitt, *J. Am. Chem. Soc.*, 2020, **142**, 15371-15385.

17. A. Jourdain, R. Asbai, O. Anaya, M. M. Chehimi, E. Drockenmuller and D. Montarnal, *Macromolecules*, 2020, **53**, 1884-1900.

18. M. M. Obadia, A. Jourdain, P. Cassagnau, D. Montarnal and E. Drockenmuller, *Adv. Funct. Mater.*, 2017, **27**, 1703258.

19. P. R. Christensen, A. M. Scheuermann, K. E. Loeffler and B. A. Helms, *Nat. Chem.*, 2019, **11**, 442-448.

20. C. He, P. R. Christensen, T. J. Seguin, E. A. Dailing, B. M. Wood, R. K. Walde, K. A. Persson, T. P. Russell and B. A. Helms, *Angew. Chem. Int. Ed.*, 2020, **59**, 735-739.

21. L. Chen, L. Zhang, P. J. Griffin and S. J. Rowan, *Macromol. Chem. Phys.*, 2019, **221**, 1900440.

22. L. Zhang and S. J. Rowan, *Macromolecules*, 2017, **50**, 5051-5060.

23. Z. Wang, S. Gangarapu, J. Escorihuela, G. Fei, H. Zuilhof and H. Xia, *J. Mater. Chem. A*, 2019, **7**, 15933-15943.

24. J. J. Lessard, G. M. Scheutz, S. H. Sung, K. A. Lantz, T. H. Epps and B. S. Sumerlin, *J. Am. Chem. Soc.*, 2020, **142**, 283-289.

25. W. Denissen, I. De Baere, W. Van Paepegem, L. Leibler, J. Winne and F. E. Du Prez, *Macromolecules*, 2018, **51**, 2054-2064.

26. W. Denissen, G. Rivero, R. Nicolaÿ, L. Leibler, J. M. Winne and F. E. Du Prez, *Adv. Funct. Mater.*, 2015, **25**, 2451-2457.

27. W. Denissen, M. Droesbeke, R. Nicolaÿ, L. Leibler, J. M. Winne and F. E. Du Prez, *Nat. Commun.*, 2017, **8**, 14857.

28. J. P. Brutman, D. J. Fortman, G. X. De Hoe, W. R. Dichtel and M. A. Hillmyer, *J. Phys. Chem. B*, 2019, **123**, 1432-1441.

29. N. Van Herck, D. Maes, K. Unal, M. Guerre, J. M. Winne and F. E. Du Prez, *Angew. Chem. Int. Ed.*, 2020, **59**, 3609-3617.

30. B. M. El-Zaatari, J. S. A. Ishibashi and J. A. Kalow, *Polym. Chem.*, 2020, **11**, 5339-5345.

31. F. Van Lijsebetten, Y. Spiesschaert, J. M. Winne and F. E. Du Prez, *J. Am. Chem. Soc.*, 2021, **143**, 15834-15844.

32. Y. Chen, H. Zhang, S. Majumdar, R. A. T. M. van Benthem, J. P. A. Heuts and R. P. Sijbesma, *Macromolecules*, 2021, **54**, 9703-9711.
33. P. Taynton, K. Yu, R. K. Shoemaker, Y. Jin, H. J. Qi and W. Zhang, *Adv. Mater.*, 2014, **26**, 3938-3942.
34. F. García, J. Pelss, H. Zuilhof and M. M. J. Smulders, *Chem. Commun.*, 2016, **52**, 9059-9062.
35. Z. Q. Lei, P. Xie, M. Z. Rong and M. Q. Zhang, *J. Mater. Chem. A*, 2015, **3**, 19662-19668.
36. S. K. Schoustra, J. A. Dijksman, H. Zuilhof and M. M. J. Smulders, *Chem. Sci.*, 2021, **12**, 293-302.
37. F. García and M. M. J. Smulders, *J. Polym. Sci., Part A: Polym. Chem.*, 2016, **54**, 3551-3577.
38. Y. Spiesschaert, C. Taplan, L. Stricker, M. Guerre, J. M. Winne and F. E. Du Prez, *Polym. Chem.*, 2020, **11**, 5377-5385.
39. Y. Liu, Z. Tang, J. Chen, J. Xiong, D. Wang, S. Wang, S. Wu and B. Guo, *Polym. Chem.*, 2020, **11**, 1348-1355.
40. R. Mo, J. Hu, H. Huang, X. Sheng and X. Zhang, *J. Mater. Chem. A*, 2019, **7**, 3031-3038.
41. M. Guerre, C. Taplan, J. M. Winne and F. E. Du Prez, *Chem. Sci.*, 2020, **11**, 4855-4870.
42. R. J. Wojtecki, M. A. Meador and S. J. Rowan, *Nat. Mater.*, 2011, **10**, 14-27.
43. J. M. Winne, L. Leibler and F. E. Du Prez, *Polym. Chem.*, 2019, **10**, 6091-6108.
44. F. Sugiyama, A. T. Kleinschmidt, L. V. Kayser, D. Rodriquez, M. Finn, M. A. Alkhadra, J. M. H. Wan, J. Ramírez, A. S. C. Chiang, S. E. Root, S. Savagatrup and D. J. Lipomi, *Polym. Chem.*, 2018, **9**, 4354-4363.
45. R. L. Snyder, C. A. L. Lidston, G. X. De Hoe, M. J. S. Parvulescu, M. A. Hillmyer and G. W. Coates, *Polym. Chem.*, 2020, **11**, 5346-5355.
46. P. Yan, W. Zhao, X. Fu, Z. Liu, W. Kong, C. Zhou and J. Lei, *RSC Adv.*, 2017, **7**, 26858-26866.
47. N. Zheng, Z. Fang, W. Zou, Q. Zhao and T. Xie, *Angew. Chem. Int. Ed.*, 2016, **55**, 11421-11425.
48. H. Li, J. Bai, Z. Shi and J. Yin, *Polymer*, 2016, **85**, 106-113.
49. D. J. Fortman, D. T. Sheppard and W. R. Dichtel, *Macromolecules*, 2019, **52**, 6330-6335.
50. B. K. Wheatle, N. A. Lynd and V. Ganesan, *ACS Macro Lett.*, 2018, **7**, 1149-1154.
51. Q. Zhao, C. Shen, K. P. Halloran and C. M. Evans, *ACS Macro Lett.*, 2019, **8**, 658-663.
52. L. M. Polgar, E. Hagting, P. Raffa, M. Mauri, R. Simonutti, F. Picchioni and M. van Duin, *Macromolecules*, 2017, **50**, 8955-8964.
53. P. Chakma, C. N. Morley, J. L. Sparks and D. Konkolewicz, *Macromolecules*, 2020, **53**, 1233-1244.
54. M. E. Belowich and J. F. Stoddart, *Chem. Soc. Rev.*, 2012, **41**, 2003-2024.
55. C. D. Meyer, C. S. Joiner and J. F. Stoddart, *Chem. Soc. Rev.*, 2007, **36**, 1705-1723.
56. A. Chao, I. Negulescu and D. Zhang, *Macromolecules*, 2016, **49**, 6277-6284.

57.   C. Zhu, C. Xi, W. Doro, T. Wang, X. Zhang, Y. Jin and W. Zhang, *RSC Adv.*, 2017, **7**, 48303-48307.
58.   P. Taynton, C. Zhu, S. Loob, R. Shoemaker, J. Pritchard, Y. Jin and W. Zhang, *Polym. Chem.*, 2016, **7**, 7052-7056.
59.   M. Ciaccia and S. Di Stefano, *Org. Biomol. Chem.*, 2015, **13**, 646-654.
60.   M. Ciaccia, R. Cacciapaglia, P. Mencarelli, L. Mandolini and S. Di Stefano, *Chem. Sci.*, 2013, **4**, 2253-2261.
61.   M. Ciaccia, S. Pilati, R. Cacciapaglia, L. Mandolini and S. Di Stefano, *Org. Biomol. Chem.*, 2014, **12**, 3282-3287.
62.   H. Zhang, D. Wang, W. Liu, P. Li, J. Liu, C. Liu, J. Zhang, N. Zhao and J. Xu, *J. Polym. Sci., Part A: Polym. Chem.*, 2017, **55**, 2011-2018.
63.   G. M. Scheutz, J. J. Lessard, M. B. Sims and B. S. Sumerlin, *J. Am. Chem. Soc.*, 2019, **141**, 16181-16196.
64.   S. Ciarella, F. Sciortino and W. G. Ellenbroek, *Phys. Rev. Lett.*, 2018, **121**, 058003.
65.   P. E. Rouse, *J. Chem. Phys.*, 1953, **21**, 1272-1280.
66.   R. P. Wool, *Soft Matter*, 2008, **4**, 400-418.
67.   E. B. Stukalin, L. Cai, N. A. Kumar, L. Leibler and M. Rubinstein, *Macromolecules*, 2013, **46**, 7525-7541.
68.   P.-G. de Gennes, *Physics Today*, 1983, **36**, 33-39.
69.   P.-G. de Gennes, *J. Chem. Phys.*, 1971, **55**, 572-579.
70.   M. Doi and S. F. Edwards, *J. Chem. Soc., Faraday Trans. 2*, 1978, **74**, 1789-1801.
71.   P. C. Cai, B. A. Krajina and A. J. Spakowitz, *Phys. Rev. E*, 2020, **102**, 020501.

Chapter 5

Metal Coordination in Polyimine Covalent Adaptable Networks for Tuneable Material Properties and Enhanced Creep Resistance
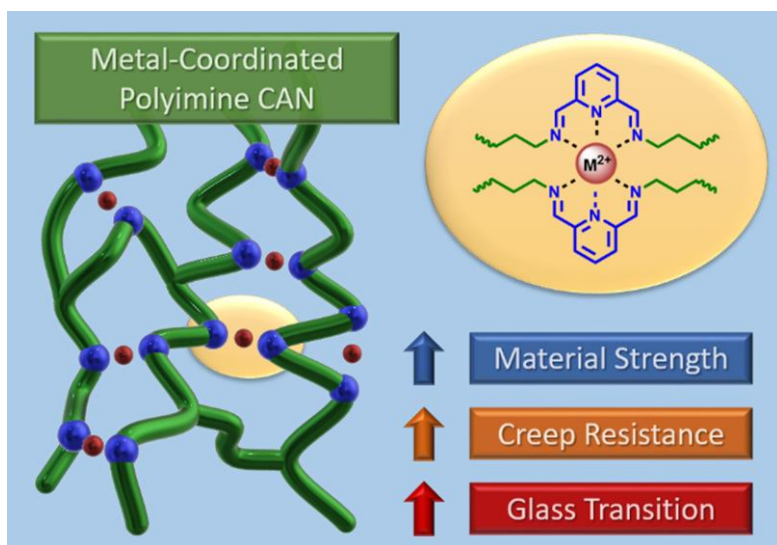
This work was published as:

Abstract

Covalent adaptable networks (CANs) have the potential to replace classical thermosets, as their unique dynamic covalent bonds enable reprocessing and recycling of crosslinked polymers. A challenge for CANs remains their creep susceptibility, which hampers their application. Herein, we demonstrate an efficient strategy to enhance creep resistance of CANs *via* metal coordination to dynamic-covalent imine groups. Crucially, the coordination bonds not only form additional crosslinks inside the network, but also directly affect the imine exchange properties due to metal coordination to the imines. The result of this dual effect is that various material properties, *e.g.*, the glass transition temperature (T_g) and the elastic modulus (G') were enhanced. The robustness of metal coordination was demonstrated by varying metal ion, counter anion, and coordinating imine ligand. All variations in metal or anion significantly enhanced the material properties. The T_g and G' of the CANs could be correlated to the coordination bond strength, offering a tuneable handle by which choice of metal can steer the material properties. Additionally, we observed large differences in T_g and G' for materials with different anions, which were mostly linked to the anion size. This serves as a reminder that for coordination chemistry in the bulk, not only the metal ion is to be considered, but also the accompanying anion. Finally, the reinforcing effect of metal coordination proved largely insensitive to the metal-ligand ratio, which furthers add to the robustness of our approach for tuning material properties.

5.1   Introduction

Covalent adaptable networks (CANs) have gained a tremendous amount of interest in recent years as the incorporation of dynamic covalent bonds in crosslinked polymer networks enables reprocessability of thermosets, and introduces new adaptive features such as stimuli responsiveness or self-healing behaviour.[1-6] An ongoing challenge for CANs, however, is related to their susceptibility towards creep.[7-11] Because of the bond exchange reactions occurring in CANs, the materials can counter an imposed load *via* stress relaxation, leading to permanent material deformation, *i.e.*, creep. Ideally, however, the materials should be mechanically stable at working temperatures, and only become malleable at elevated temperatures.

Efforts to suppress creep and enhance overall material properties cover the combination of dynamic and non-dynamic crosslinks,[7, 12] entrapping reactive groups,[13, 14] or inducing phase separation (as also was discussed in **Chapter 3** for imine-based CANs).[15-19] We envision that the inclusion of metal coordination in CANs could also be used for enhancing material properties. Previously, metal-coordination has been applied in linear or brush polymers,[20, 21] since the metal-ligand (M–L) bonds can be considered as dynamic crosslinks (apart from the permanent, covalent bonds)[22, 23] that not only increase crosslinking density and reduce chain mobility,[24] but also enable self-healing behaviour.[25, 26] Recent work by Bai and co-workers on conductive nanocomposites also reported on the incorporation of dual crosslinks of imine and Zn(II)-amino coordination.[27] They observed that the combination of dynamic covalent bonds and coordination bonds significantly improved material properties of the composites. Similarly, Hoogenboom and co-workers observed that crosslinking of hydrogels with both dynamic covalent bonds and coordination bonds offered superior mechanical properties.[28] These examples, however, showed the inclusion of the two types of dynamic bonds as individual reversible units. In our work we wish to apply the M–L bonds to coordinate the metal ion directly to the dynamic covalent bond. This way, the metal-coordination not only adds additional dynamic crosslinks, but also affects the thermodynamic and kinetic behaviour of the dynamic covalent bond itself. The coordinated metals can then either stabilise the dynamic covalent bonds and slow down bond exchange, or act as internal catalysts to promote bond exchange reactions, independently of the created M–L crosslinks.[29-31]

To study this dual control by metal-coordination in CANs, polyimines are excellent candidates as the dynamic covalent imine groups offer a broad range of tuneable properties (as already presented in previous Chapters),[32-36] and are known to coordinate to various

metals.[37-39] As the kinetics and thermodynamics of M–L interactions are broadly tuneable (*e.g.*, by varying metal, anion, or coordinating ligand),[38, 40] the introduction of metal-coordination in CANs brings a new toolbox for tuneability –and control– of dynamic mechanical properties. Also, inclusion of metal ions in polymers may enable new features: *e.g.*, capacity-based sensing or temperature-dependent luminescence.[41-43]

Herein, we report on the metal-coordination of polyimine CANs (Figure 5.1) to significantly enhance their material properties and creep resistance at working conditions, while maintaining reprocessability at elevated temperatures. Apart from varying the metal-ligand ratio (25, 50, 100, 200%), two different imine pincer ligands were selected: **iso-imine** and **pyr-imine**. As the preferred geometry for M–L coordination is octahedral, we envision that coordination to bidentate **iso-imine** is suboptimal compared to tridentate **pyr-imine**. As such, we expect stronger M–L complexes for the **pyr-imine** materials, with concomitant effect on the macroscopic material properties. Furthermore, we included six different metal ions (Mn^{2+}, Fe^{2+}, Co^{2+}, Ni^{2+}, Cu^{2+}, Zn^{2+}), and six different anions, including a divalent anion (OTf^-, NTf_2^-, BF_4^-, ClO_4^-, NO_3^-, SO_4^{2-}). In particular, we hypothesised that by selection of the appropriate metal ion, we could vary –in a systematic manner– the strength of the crosslinks as well as the effect of the metal ion on the imine bond exchange.
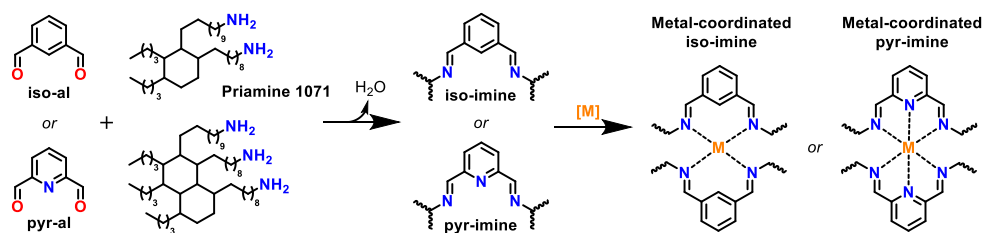

Figure 5.1 Reaction scheme for the synthesis of **iso-imine** and **pyr-imine** networks from reaction of either **iso-al** or **pyr-al** with Priamine 1071 (3:1 mixture of di- and triamine). In a second step, metal coordination to the imine pincers is performed.

5.2   Results and Discussion

5.2.1   Synthesis of polymer networks

First, the non-coordinated polyimine networks were synthesised bearing either the bidentate (**iso-imine**) or tridentate (**pyr-imine**) pincers (Figure 5.1). They were synthesised by reaction of equimolar amounts of either isophthalaldehyde (**iso-al**) or

2,6-pyridinedicarboxaldehyde (**pyr-al**) with Priamine 1071; a 3:1 mixture of biobased flexible aliphatic di- and triamine. In a second step, the metal ions were introduced that coordinate to the imine pincers in a 1:2 fashion. For the synthesis of metal-coordinated polyimines, it is important that the metal-coordination is performed in a second step after the formation of the polyimine network. In attempts to add the metal ions already in the first step, the polymerisation reaction was compromised, resulting in only partial conversions. The probable cause for this is that the metal ions interact with primary amines, preventing initiation of the condensation reaction to form imines. To ensure full conversion towards the imine product in the first step, formation of the polyimine networks was monitored by following the appearance of imine-specific signals, both with ^{1}H NMR (**iso-imine**: H_{imine} = 8.29 ppm, **pyr-imine**: H_{imine} = 8.40 ppm; in CDCl$_3$) and with FT-IR (**iso-imine**: A_{imine} = 1647 cm^{-1}, **pyr-imine**: A_{imine} = 1649 cm^{-1}). All metal-coordinated and non-coordinated materials were then individually characterized using rheology (see Section 5.5 for full details of the synthetic procedures and experimental setups).

5.2.2 Thermal mechanical properties and influence of the metal ion

To study the effects of the metal coordination on the dynamic-mechanical properties of the polymer materials, temperature sweep experiments were first performed to determine the glass transition temperature (T_g) of all polyimine materials (Figure 5.2). Without any metal-coordination, low T_g values below 0 °C were observed for both **iso-imine** and **pyr-imine**. However, upon metal coordination the T_g increased significantly. For **iso-imine** networks T_g values up to 72 °C were obtained (Figure 5.2A), while for **pyr-imine** networks T_g values up to 94 °C were found (Figure 5.2B). **Pyr-imine** materials generally showed higher T_g values than **iso-imine** materials, which is likely the result of the increased number of coordination bonds per pincer. In the temperature sweep experiments, the non-coordinated materials also showed a point at which tan(δ) = 1 (*i.e.*, the crossover point between G' and G''), indicating that a phase transition from a rubbery phase into a viscous phase occurs. This T_{cross} was observed at 119 °C for **iso-imine** and 136 °C for **pyr-imine**. The Fe^{2+}-coordinated **iso-imine** was the only metal-coordinated material for which this was also observed around 135 °C (see Figure 5.11 in Section 5.5.6). None of the other metal-coordinated **iso-imine** or **pyr-imine** materials showed such a phase transition below 150 °C, indicating that a stable rubbery state remained after passing the T_g. In this rubbery state thermomechanical processing is possible, but creep is still limited unless substantial force is applied. As such, hot-pressing the materials at 150 °C and a maximum force of 50 N was used as the default for (re)processing the metal-coordinated materials.
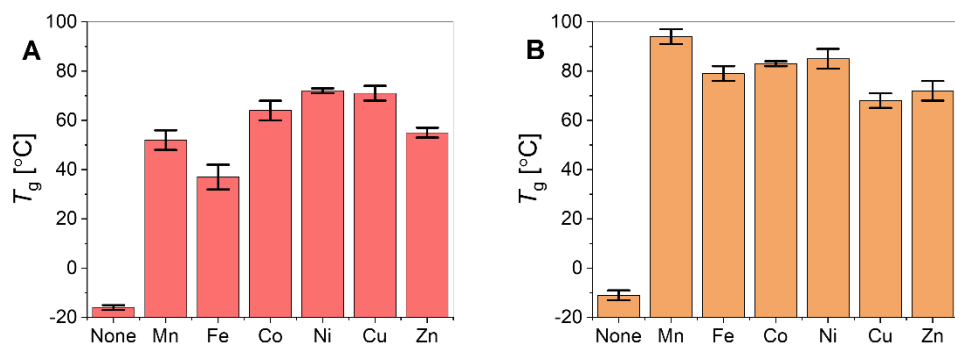
Figure 5.2 Glass transition temperatures (T_g) of different metal-coordinated polyimines: A) **iso-imine** and B) **pyr-imine**. The non-coordinated materials are shown as the leftmost bar for comparison, and the metals are ordered based on their atomic number.

The notable differences in T_g between the different metal-coordinated materials (Figure 5.2) can be attributed to two different factors. First, metal coordination of the imines alters the stability of the imine bonds, and concomitantly the temperature-dependent bond exchange kinetics. Because the binding strength between imine ligand and metal ion is different for each type of metal, the stabilisation of the imine bond because of the newly formed coordination bond is also different per type of metal. As such, the temperature response of the dynamic covalent imine groups varies per metal. Second, the M–L bonds, which form additional crosslinks in the network, also have a reversible character, and the bond strength and dissociation constant (k_d) are unique for each metal ion. For example, Pignanelli *et al*. suggested that shorter or stronger M–L bonds between metal ions and ligands functionalised on the end groups of linear polymer chains cause stronger association, resulting in more brittle materials.[40] The same principle could apply to the temperature response: a shorter or stronger M–L bond requires more energy (*i.e.,* a higher temperature) for dissociation, resulting in a higher T_g of the material.

To relate the T_g of the metal-coordinated polyimines to differences in M–L complex stability we compared the observed T_g values of the differently metal-coordinated polyimines to formation and dissociation constants (k_f and k_d, respectively) and the overall complex stability (K (= k_f / k_d)) of analogous small molecule metal complexes, based on bipyridine and terpyridine, for **iso-imine** and **pyr-imine**, respectively (see Section 5.5.6 in the Supporting Information for all K, k_f and k_d values). From this analysis it followed that the T_g of the metal-coordinated polyimines could be plotted as a function of the log(K) to establish a general trend of increasing T_g of the polymer when the log(K) of the M–L complex increased (Figure 5.3).
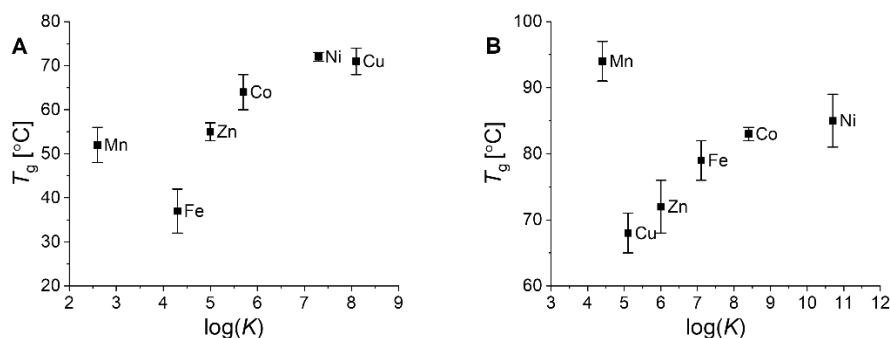
Figure 5.3 T_g of metal-coordinated polyimines plotted as a function of log(K) of analogues small-molecule bidentate and tridentate metal complexes for A) **iso-imine** and B) **pyr-imine**, respectively.

For the **iso-imine** materials (Figure 5.3A), the observed trend in T_g (Fe^{2+} < Mn^{2+} < Zn^{2+} < Co^{2+} < Ni^{2+} ~ Cu^{2+}) correlated relatively well to the log(K) of the corresponding small-molecule (pyridine-based) bidentates,[44, 45] and followed the Irving-Williams series,[46] with the exception that Mn^{2+} and Fe^{2+} appeared to have shifted places. For the **pyr-imine** materials (Figure 5.3B), the trend in T_g (Cu^{2+} < Zn^{2+} < Fe^{2+} < Co^{2+} < Ni^{2+} < Mn^{2+}) was also in good agreement with the small-molecule tridentate analogues,[44] with the exception that Mn^{2+} was again higher than expected.[47] Looking at the k_f and k_d of the **pyr-imine**-based complexes individually, we also observed that an increase in each of the two resulted in a decrease in T_g (see Section 5.5.7 in the Supporting Information). For the **iso-imine** materials, such individual trends in k_f and k_d were not clearly observed, although an overall trend in K was seen. The relatively high T_g for Mn^{2+}-coordinated materials might be related to specific M–L interactions between Mn^{2+} and the selected pincer ligands. Reports in literature have documented on exceptionally high coordination stability between Mn^{2+} and specific ligands with either large or rigid cavities.[48, 49] As such, the imine pincer ligands (potentially in combination with the total polymer network structure) in our CANs could have a preference for coordination to the Mn^{2+} ions. The results depicted in Figure 5.3A (**iso-imine**) and Figure 5.3B (**pyr-imine**) also suggest that such an effect appears to be more prominent for the tridentate **pyr-imine** than for the bidentate **iso-imine**, which could also be related to the more optimal coordination of the metal ion to the imine ligand in the former case.

For the elastic modulus (G'), a significant increase upon metal-coordination was observed as well (Figure 5.4). For both **iso-imine** (Figure 5.4A) and **pyr-imine** (Figure 5.4B) materials the G' could be increased up to two orders of magnitude from the non-coordinated polymers, reaching values around 100 MPa. This large increase is striking, but can be

explained as a result of the increased crosslinking density. Before metal coordination the crosslinking density is relatively low due to the long aliphatic monomers and lower amount of triamine compared to diamine. However, once the metals coordinate to two imine pincers, the formed M–L complexes act as extra crosslinks,[50] which tighten the networks structure and hamper chain mobility.[38] As a result of the stiffer and denser network structure, the modulus of the material increases rapidly.
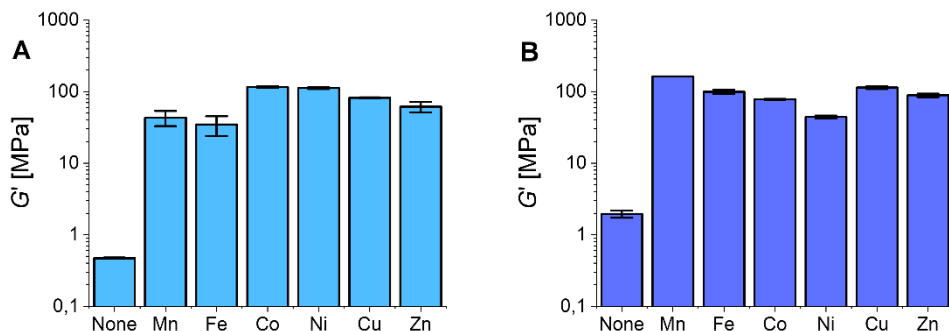

Figure 5.4 Elastic moduli (*G'*) of different metal-coordinated polyimines: A) **iso-imine** and B) **pyr-imine**. The non-coordinated materials are shown as the leftmost bar for comparison, and the metals are ordered by their position in the periodic table. All data were obtained at 20 °C.

By relating the small-molecule metal-complexation parameters to the *G'* of the polymers, we saw again a trend for the **pyr-imine** materials, but this time not for the **iso-imine** materials (see Section 5.5.7 in the Supporting Information). For the **pyr-imine**, we observed that materials derived from metals with a lower log(K) displayed a higher *G'*. At the same time, we observed that both k_f and k_d (as expressed as their log value) increased for networks with a higher *G'*. It was interesting to note that higher *G'* correlated to lower log(K), as we expected that a higher complexation constant would result in tougher polymer networks. To explain the observed opposite trend, it is therefore likely that the coordination of the different metals to the imines also affects the stability and kinetics of the imine bond.

Next, creep experiments were performed in which a constant stress of 10 kPa was applied to the materials, and the strain was followed over time (Figure 5.5). The results showed that the non-coordinated materials have relatively poor creep resistance as strains over 10% were already seen within several minutes. The metal-coordinated materials, however, showed much greater creep resistance. Even after 1000 s most materials still displayed strains below 0.1%, and the differences between the differently metal-coordinated materials were small. Due to these small differences in creep between the different metal ions, no clear correlations could be drawn between the metal-complexation kinetics and

creep of the materials (see Section 5.5.7 in the Supporting Information). However, the observation that all tested variations in metal ion showed such good creep resistance, emphasises the efficiency and robustness of the metal coordination to suppress creep. Similar as for the G', the M–L bonds enhance the stiffness of the materials, and as such their resistance towards deformation. Moreover, the metal coordination seemed to "arrest" the imines and prevent bond exchange reactions between (imine-containing) segments of the polymer network at lower temperatures. However, thermal processing of these networks was still possible: when heated above the T_g the materials started to undergo noticeable stress relaxation (see Section 5.5). The observed stress relaxation at elevated temperatures did however not show single Maxwell-type relaxation that would result in the typical Arrhenius behaviour of vitrimer-like materials.[3, 51] It is likely that multiple relaxation modes (*e.g.*, chain reptation, imine exchange, M–L dissociation) operate simultaneously, which all contribute to the overall relaxation process.[34]
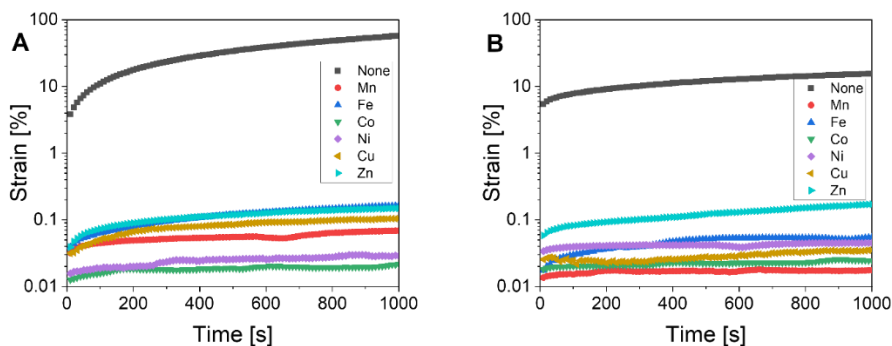

Figure 5.5 Creep curves of different metal-coordinated polyimines: A) **iso-imine** and B) **pyr-imine**. The grey line shows the non-coordinated material. A constant stress of 10 kPa was applied (at 20 °C).

In short, the choice of metal ion can thus serve as a tuneable handle to control the T_g of the polymer over several decades, for which the T_g generally increases with higher log(K) of the corresponding M–L complex. Mn^{2+} was the only exception to the rule, which might be related to specific favourable coordination with the chosen imine ligands. We also observed that the choice of metal ion could be used to tune the G' of the **pyr-imine** materials, by which a lower log(K) resulted in an increase in G'. This opposite trend we attribute to the dual effect of metal coordination in our imine networks: apart from generating additional crosslinks, metal-coordination also affects the kinetics of the imine exchange. The role of the individual metal ions was harder to distinguish in the creep of the materials, as all tested

variations in metal ion resulted in materials with high creep resistance, leaving little room to unravel metal-specific effects. The observation that all tested variations in metal ion resulted in such good creep resistance and other material properties underlines the robustness of this method to enhance materials properties of CANs *via* metal coordination.

5.2.3   Role of the anion

We envisioned that also the anions could contribute to changes in the material properties, as these ions remain in the polymer network as well. Depending on, for example, size or aggregation potential, the anions could affect overall chain mobility. As an example, Cui *et al.* showed that in imidazolium-based poly(ionic liquid)s the size of the counterion had large effects on the T_g.[52] The larger counterions acted as plasticisers and additionally formed loose ionic aggregates, leading to weak crosslinks. Alternatively, anions could potentially facilitate proton transfers, which are known to affect imine exchange.[30] Overall, it is thus likely that different anions in the system could alter the dynamic behaviour of the CAN significantly.

To evaluate the effects of different anions, Zn^{2+}-coordinated **pyr-imine** materials were prepared with either triflate (OTf^-), triflimide (NTf_2^-), tetrafluoroborate (BF_4^-), nitrate (NO_3^-), perchlorate (ClO_4^-) or sulphate (SO_4^{2-}) anions. The same rheological tests as before were performed to determine the material properties (Figure 5.6).
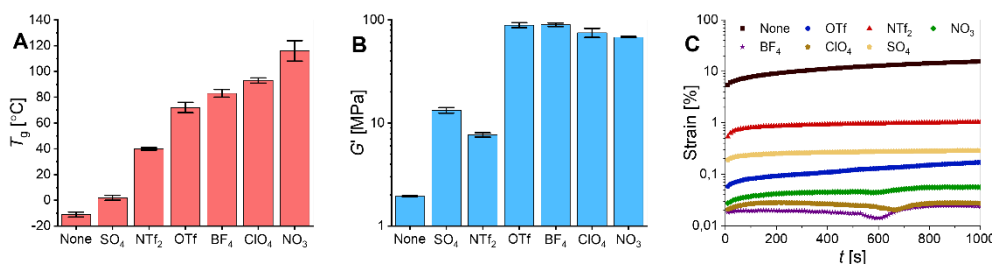

Figure 5.6 Overview of material properties for Zn^{2+}-coordinated **pyr-imine** with different anions. A) glass transition temperature T_g, B) elastic modulus G' at 20 °C, and C) creep curves.

All variations in anions resulted in enhanced material properties when compared to the non-coordinated material. However, we also observed large differences between materials with different anions. First, we observed that the material bearing SO_4^{2-} anions performed relatively poor –in terms of T_g, G' and creep resistance– compared to the other anions. Because the sulphate has a –2 charge, it has a chelating effect and strong binding to the Zn^{2+} ions. As a result, the anions remain closer to the metal centre (*i.e.*, diffusion of anions into

the network is low), and might hamper efficient coordination of Zn^{2+} to the imine ligands. We also observed that the bulky triflimide anion underperformed compared to the other anions, which is likely the result of the large size of the anion causing a plasticising effect, as mentioned by Cui *et al*.[52] The other anions showed similar values of G' (Figure 5.6B), but still noticeable differences in T_g (Figure 5.6A). As the triflate anion is still slightly larger than the other anions, this might explain the lower T_g compared to the three remaining anions. The differences in T_g between BF_4^-, ClO_4^-, and NO_3^- could less easily be accounted for by only differences in size, molar mass, pK_a or base hardness. Instead, a more complex interplay of these factors could account for the observed trend ($BF_4^- < ClO_4^- < NO_3^-$). The observation that the nitrate anions outperformed all other materials might be explained by recent work by Mooibroek *et al*.,[53] who documented that nitrate anions could act as Lewis acids in the solid state. If the anions act as Lewis acids to the imines, the kinetics of the bond exchange reaction will be affected. Such an alteration in imine exchange kinetics could in response also have its consequences for the material properties of the polymer.

5.2.4   Concentration of metal-coordination

Last, we investigated how the stoichiometry between metal ion and imine pincer in the network affected the material properties. Since for all earlier mentioned materials full coordination (100%) was selected, we now also prepared $Zn(OTf)_2$ and $Fe(OTf)_2$ coordinated **pyr-imine** materials with only 25% and 50% of metal ions (in relation to the pincer complex). In addition, materials were synthesised with an excess (200%) of salt. We envisioned that a lower degree of metal coordination would result in mechanically weaker materials due to the lower number of crosslinks.[54] On the other hand, an excess of salt may cause a lubricating effect, or they might (phase) separate out. Alternatively, excess of metal ions might prevent formation of octahedral complexes due to lack of available ligands, and as such, other coordination complexes could potentially be favoured.[55]

Starting from the non-coordinated **pyr-imine**, the material properties seemed to quickly rise when increasing the concentration of metal ions. For materials with different concentrations of $Zn(OTf)_2$ (Figure 5.7), we observed that both T_g and G' increased rapidly when going from 0% to 50%. After 50% of metal-coordination the material properties already appeared robust, as by continuing to 100% and 200% the T_g no longer increased and the G' only increased slightly. Similar trends in T_g and G' were observed for different concentrations of $Fe(OTf)_2$. However, the glass transition of 50% $Fe(OTf)_2$ showed a remarkable result. A long glass transition process was observed in which two distinct stadia were noticed: around 35 °C and 80 °C (see Figure 5.27 in Section 5.5.5). Since the T_g at 100% $Fe(OTf)_2$ was also observed around 80 °C (see Figure 5.28 in Section 5.5.5), we suggest that the flow at 80 °C is likely caused by M–L dissociation. The earlier transition around 35 °C is

then most likely caused by loss of crystallinity in the organic part of the polymer.[34] For the 50% Zn(OTf)$_2$-coordinated material, a similar elongated glass transition was observed (Figure 5.23, Section 5.5.5), although the splitting into two phases was less prominent here. The creep resistance at lower concentrations (25% and 50%) of either Zn(OTf)$_2$ or Fe(OTf)$_2$ was already in the same order as the 100% materials (see Section 5.5), again accentuating the power of the metal coordination to reduce creep. Full coordination of imines would thus not per se be required to gain desired material properties, but depending on specific applications one could consider adjusting the concentration of metal ions.
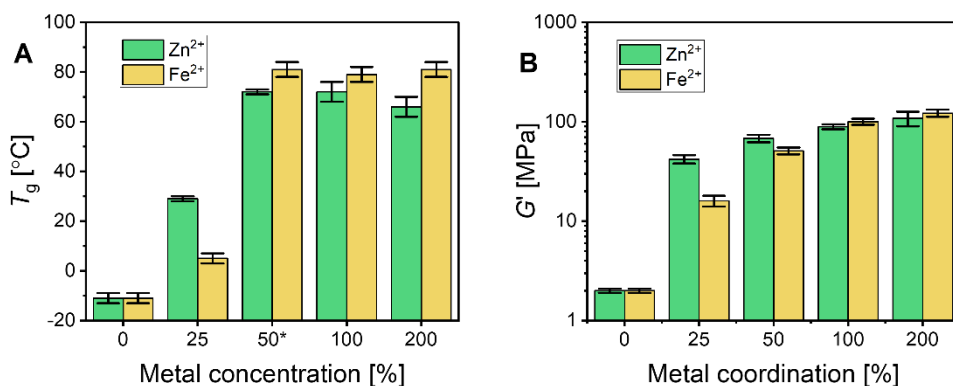

Figure 5.7 Material properties of Zn^{2+} (green) and Fe^{2+} (yellow) coordinated **pyr-imine** materials with different concentrations of metal (relative to the ligand). A metal coordination of 100% corresponds to the optimal 1:2 metal:ligand ratio. A) shows the glass transition temperatures, and B) shows the elastic moduli. *Note that at 50% coordination, it appeared that the glass transition proceeded over two stadia. The temperature represented in this figure is that of the most prominent transition observed from the tan(δ) curves (full temperature sweeps at provided in Section 5.5.5 in the Supporting Information).

When increasing the concentration of salt to 200% for either Fe(OTf)$_2$ or Zn(OTf)$_2$, by simply looking at the T_g and G', the material properties did not appear to change significantly, suggesting that the excess of salt did not drastically affect the material properties. From these observations it is thus not likely that the octahedral coordination of two imine pincers to one metal ion is obstructed, but rather that the excess ions blend within the polymer matrix with little effect on the mechanical properties. However, when looking at the full temperature sweeps of the 200% Zn(OTf)$_2$ material, it was noticed that once the T_g was crossed, the material started to flow more rapidly than was seen at 100% (see Figure 5.25 in Section 5.5.5). This suggests that once the glassy phase is lost, the excess of ions might cause a lubrication effect, but below the T_g the particles are "locked" within the material.

5.3   Conclusion

In conclusion, we found that the material properties and creep resistance of polyimine CANs could be significantly enhanced *via* metal coordination to the dynamic covalent imine groups. We were able to synthesise materials with T_g values over 100 °C, as well as G' values over 100 MPa. More specific material properties were obtained by varying the type and concentration of the metal ion, the corresponding anion, and the nature of imine pincer. We found that the effects of the metal ions correlated relatively well to the stability of analogous small-molecule metal-ligand complexes, and as such could serve as tuneable handles for controlling desired material properties. For example, it was observed that the T_g of the polymer material increased when the $\log(K)$ of analogous small-molecule M–L complexes was higher. We also noticed that changes in anion had a pronounced effect on the material properties. While small anions showed the best material properties, poorer results were observed when the size of the anion was increased. This serves as a reminder that for coordination chemistry in the bulk, not only the metal ion is to be considered, but also the accompanying anion. Finally, the robustness of the approach was further demonstrated by the fact that also outside the preferred 1:2 metal:ligand ratio, the reinforcing effect of metal coordination could be observed.

5.4   Acknowledgements

5.5   Supporting Information

An overview of the most important Supporting Information is provided in the following sections. The full Electronic Supporting Information can be accessed from: https://doi.org/10.1002/marc.202200790.

5.5.1   Synthesis of **iso-imine** and **pyr-imine** networks

Iso-imine and **pyr-imine** networks were prepared by addition of either isophthalaldehyde or 2,6-pyridinedicarboxaldehyde to a solution of Priamine 1071 in THF (Figure S1). The materials were constructed such that an equimolar amount of aldehyde group reacted with amine group. Priamine 1071 consists of a 0.75 to 0.25 ratio of the diamine and triamine, as pictured in Figure S1. As such, the Priamine mixture had an average molecular weight of 601.37 g/mol, while averaging 2.25 mol of amine. And since dialdehydes are used, this translates to 1.125 mol of either isophthalaldehyde or 2,6-pyridinedicarboxaldehyde.

An example of the preparation is then as follows:

Priamine 1071 (601.4 mg, 2.250 mmol amine) was dissolved in 5 mL THF. Then either isophthalaldehyde (150.9 mg, 1.125 mmol) or 2,6-pyridinedicarboxaldehyde (152.0 mg, 1.125 mmol) was added, and the mixture was shaken until all material had fully dissolved. The reaction mixture was poured into a petri dish and left for overnight at room temperature to evaporate most solvent to air. The obtained polymer films were further dried in a vacuum oven at 50 °C for one day. Conversion into the relevant imines was confirmed by ^{1}H NMR (**iso-imine** H_{imine} = 8.29 ppm, **pyr-imine** H_{imine} = 8.40 ppm; in CDCl$_3$) and FT-IR (**iso-imine** A_{imine} = 1647 cm^{-1}, **pyr-imine** A_{imine} = 1649 cm^{-1}).
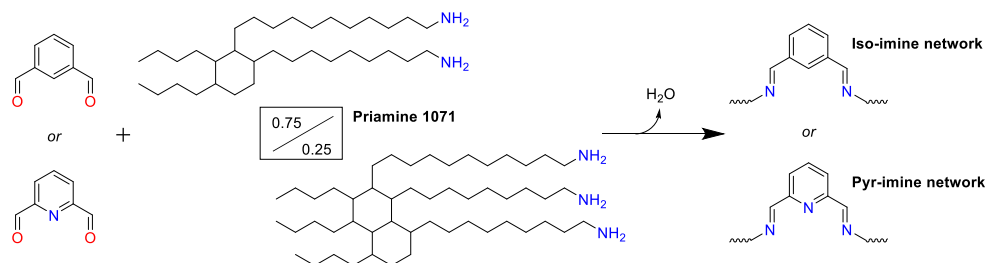

Figure 5.8 Reaction scheme for the formation of **iso-imine** and pyr-imine networks from Priamine 1071 and either isophthalaldehyde or 2,6-pyridinedicarboxaldehyde. The reaction was performed in THF. Water is formed during the reaction, which was removed by drying the polymer films in a vacuum oven.

5.5.2   Metal coordination of polyimine networks

Metal-coordinated polymer networks were synthesised by first dissolving either the **iso-imine** or **pyr-imine** material in chloroform (typically 20 mL solvent per 1 gram polymer). This process is very slow, and may take up to several hours before the material is fully dissolved. The process could be sped up a little by carefully warming up the mixture. Once fully dissolved, the mixture was poured into a petri dish. Then a second solution was prepared of the metal salt in ethanol (typically 1 gram salt per 20 mL). This solution was also poured into the same petri dish and the new mixture was stirred manually with a stirring rod for roughly one minute. Then it was left for overnight to let most of the solvent evaporate to air. The newly obtained polymer film was further dried in a vacuum oven at 50 °C for one day. The dried materials could be hot-pressed at 150 °C into desired shapes for further analysis.

5.5.3   Experimental procedures for rheological measurements

See **Chapter 2**, Section 2.5, for full details on the experimental setup.

Sample preparation

All polymer samples were hot-pressed into disks with a 10 mm radius and 0.5 mm thickness. The temperature at which the hot-pressing was performed varied between 100–150 °C, depending on the specific sample, and a maximum force of 40 N was applied. Hot-pressing generally worked best at least 10 °C above the estimated glass transition temperature.

Temperature sweeps

Temperature sweep experiments were performed on polymer disks with a 10 mm diameter and 0.5 mm thickness. An oscillatory strain of 0.1% was applied at a frequency of 1 Hz, and a temperature ramp was set to heat with 1 °C per 20 s. The storage (G') and loss (G'') moduli were followed over time. The damping factor ($\tan(\delta)$) was determined as G''/G', and also plotted as a function of the temperature in the same plot. The glass transition temperature (T_g) was determined from the top of the $\tan(\delta)$ curve. If observed, the crossover temperature (T_{cross}) was determined at the point for which $\tan(\delta)$ exceeded a value of 1.

Creep

Creep experiments were performed on polymers disks with a 10 mm diameter and 0.5 mm thickness. The films were exposed to a contant stress of 10 kPa, and the strain was followed over time up to 1000 seconds.

Stress relaxation

Stress relaxation experiments were performed with a rheology setup polymer on polymer disks with a 10 mm diameter and 0.5 mm thickness. A strain of 1% was applied to the materials, and the relaxation modulus ($G(t)$) was followed over time at various temperatures.

5.5.4   Overview of rheological data

Rheological data for different metal-coordinated **iso-imine** polymers

Table 5.1 Tabulated rheological data of different metal coordinated **iso-imine** polymers. T_g and T_{cross} are reported in °C. G' is reported in MPa at room temperature. The strain after 1000 s at a stress of 10 kPa (γ) is reported in %, and was also determined at room temperature.

	None	Mn^{2+}	Fe^{2+}	Co^{2+}	Ni^{2+}	Cu^{2+}	Zn^{2+}
T_g	−16 ± 1	52 ± 4	37 ± 5	64 ± 4	72 ± 1	71 ± 3	55 ± 2
T_{cross}	119 ± 1	>150	135 ± 8	>150	>150	>150	>150
G'	0.47 ± 0.01	43 ± 10	35 ± 11	116 ± 3	112 ± 3	82 ± 1	62 ± 10
γ	52 ± 6	0.06 ± 0.01	0.16 ± 0.01	0.03 ± 0.01	0.03 ± 0.01	0.10 ± 0.01	0.15 ± 0.02

Rheological data for different metal-coordinated **pyr-imine** polymers

Table 5.2 Tabulated rheological data of different metal coordinated **pyr-imine** polymers. T_g and T_{cross} are reported in °C. G' is reported in MPa at room temperature. The strain after 1000 s at a stress of 10 kPa (γ) is reported in %, and was also determined at room temperature.

	None	Mn^{2+}	Fe^{2+}	Co^{2+}	Ni^{2+}	Cu^{2+}	Zn^{2+}
T_g	−11 ± 2	94 ± 3	79 ± 3	83 ± 1	85 ± 4	68 ± 3	72 ± 4
T_{cross}	136 ± 3	>150	>150	>150	>150	>150	>150
G'	1.95 ± 0.02	163 ± 1	100 ± 7	78 ± 1	44 ± 2	114 ± 5	89 ± 5
γ	12 ± 3	0.02 ± 0.01	0.04 ± 0.02	0.03 ± 0.01	0.03 ± 0.01	0.03 ± 0.01	0.21 ± 0.04

Rheological data for Zn^{2+}-coordinated **pyr-imine** materials with different anions

Table 5.3 Tabulated rheological data of Zn^{2+}-coordinated **pyr-imine** polymers with different anions. T_g and T_{cross} are reported in °C. G' is reported in MPa at room temperature. The strain after 1000 s at a stress of 10 kPa (γ) is reported in %, and was also determined at room temperature.

	$^-$OTf	$^-$NTf$_2$	$^-$BF$_4$	$^-$NO$_3$	$^-$ClO$_4$	SO$_4^{2-}$
T_g	72 ± 4	40 ± 1	83 ± 3	116 ± 8	93 ± 2	2 ± 2
T_{cross}	>150	>150	>150	>150	>150	>150
G'	89 ± 5	7.7 ± 0.4	90 ± 4	68 ± 1	75 ± 8	13 ± 11
γ	0.21 ± 0.04	1.12 ± 0.08	0.03 ± 0.01	0.05 ± 0.01	0.03 ± 0.01	0.30 ± 0.02

Rheological data for materials with different stoichiometries of metal-coordination

Table 5.4 Tabulated rheological data of Zn^{2+}-coordinated **pyr-imine** polymers with different stoichiometries of metal-coordination. T_g and T_{cross} are reported in °C. G' is reported in MPa at room temperature. The strain after 1000 s at a stress of 10 kPa (γ) is reported in %, and was also determined at room temperature.

	0%	25%	50%	100%	200%
T_g	−11 ± 2	29 ± 1	72 ± 1	72 ± 4	66 ± 4
T_{cross}	136 ± 3	>150	>150	>150	101 ± 4
G'	1.95 ± 0.02	42 ± 1	68 ± 2	89 ± 5	108 ± 18
γ	12 ± 3	0.29 ± 0.02	0.04 ± 0.01	0.21 ± 0.04	0.09 ± 0.04

Table 5.5 Tabulated rheological data of Fe^{2+}-coordinated **pyr-imine** polymers with different stoichiometries of metal-coordination. T_g and T_{cross} are reported in °C. G' is reported in MPa at room temperature. The strain after 1000 s at a stress of 10 kPa (γ) is reported in %, and was also determined at room temperature. *The 50% sample appears to have a two-step glass transition, for which the first transition was observed around 35 °C, and the second was observed around 81 °C (see also the temperature sweeps in Section 5.5.5).

	0%	25%	50%	100%	200%
T_g	−11 ± 2	5 ± 2	35 ± 5 / 81 ± 3 *	79 ± 3	81 ± 3
T_{cross}	136 ± 3	>150	>150	>150	>150
G'	1.95 ± 0.02	16 ± 2	51 ± 4	100 ± 7	122 ± 1
γ	12 ± 3	0.21 ± 0.01	0.05 ± 0.01	0.04 ± 0.02	0.03 ± 0.01

5.5.5   Temperature sweeps
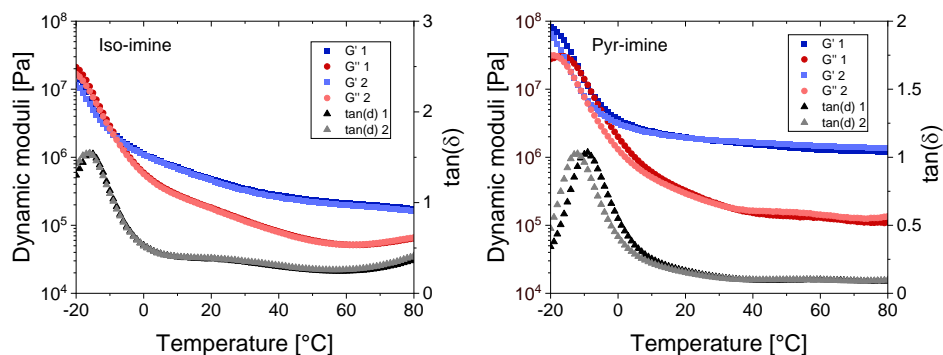
T sweeps of non-coordinated polyimines

Figure 5.9 Temperature sweeps of **iso-imine** (left) and **pyr-imine** (right).

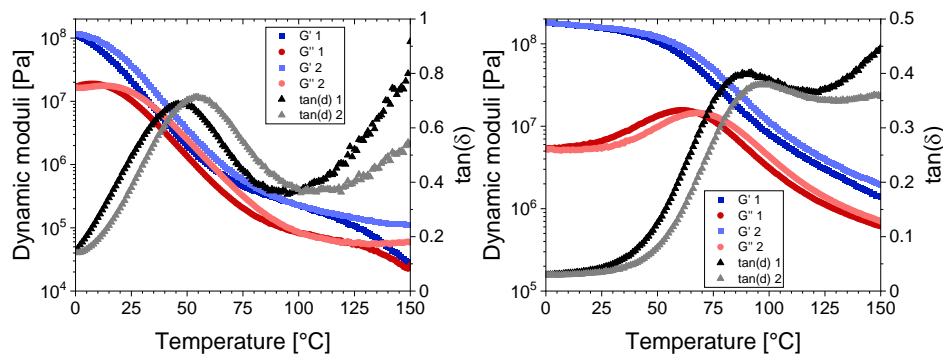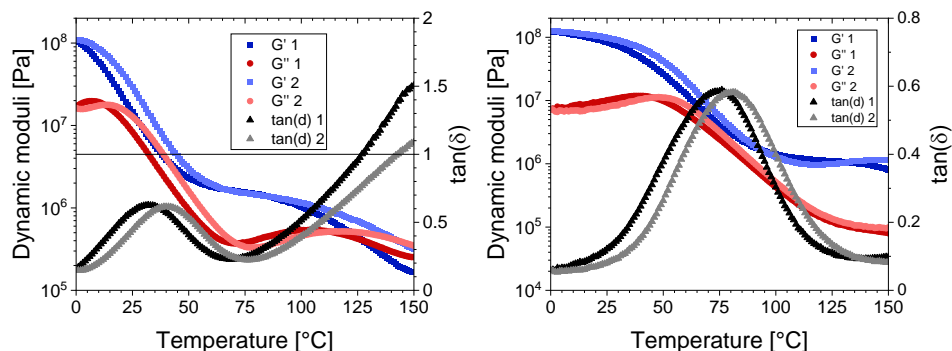### T sweeps of different metal-coordinated polyimines

Figure 5.10 Temperature sweeps of Mn(OTf)$_2$ coordinated **iso-imine** (left) and **pyr-imine** (right).

Figure 5.11 Temperature sweeps of Fe(OTf)$_2$ coordinated **iso-imine** (left) and **pyr-imine** (right).
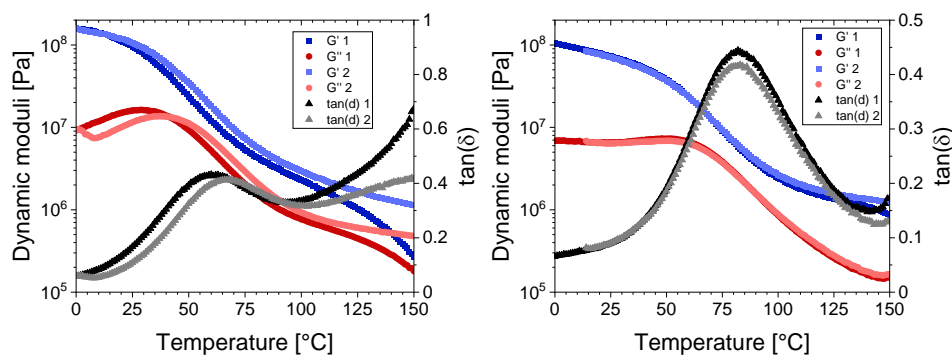

Figure 5.12 Temperature sweeps of Co(OTf)$_2$ coordinated **iso-imine** (left) and **pyr-imine** (right).
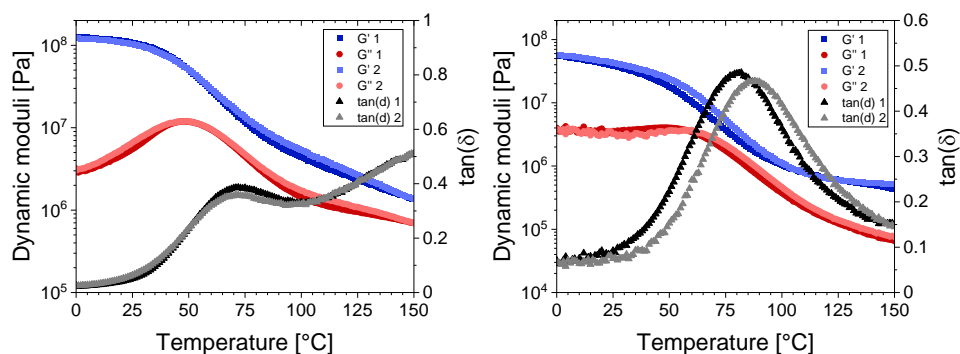

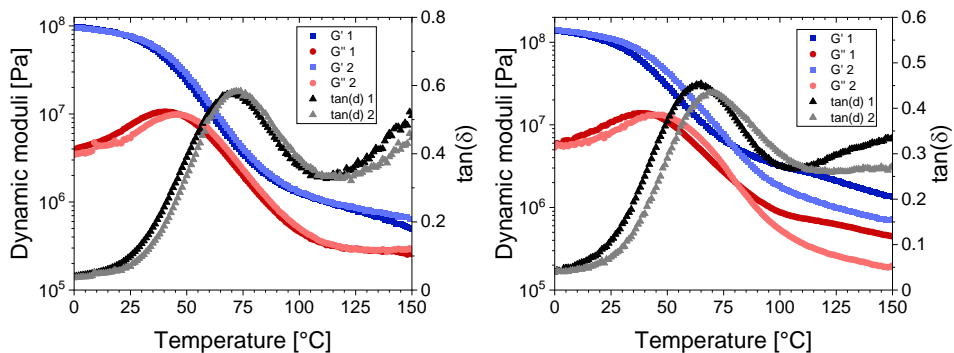**Figure 5.13** Temperature sweeps of Ni(OTf)$_2$ coordinated **iso-imine** (left) and **pyr-imine** (right).

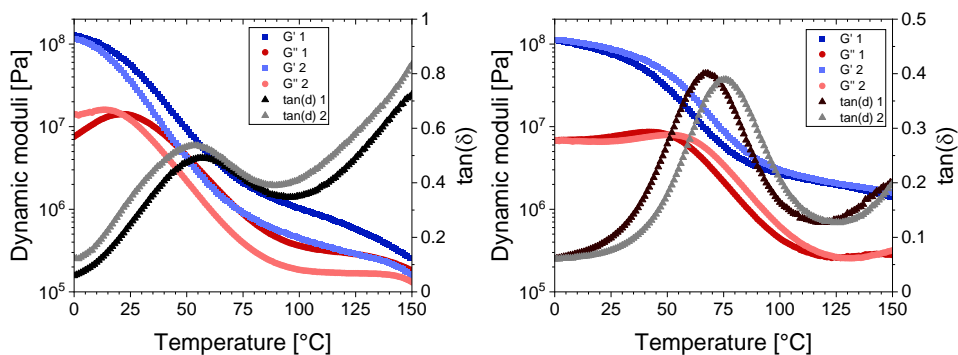**Figure 5.14** Temperature sweeps of Cu(OTf)$_2$ coordinated **iso-imine** (left) and **pyr-imine** (right).

Figure 5.15 Temperature sweeps of Zn(OTf)$_2$ coordinated **iso-imine** (left) and **pyr-imine** (right).

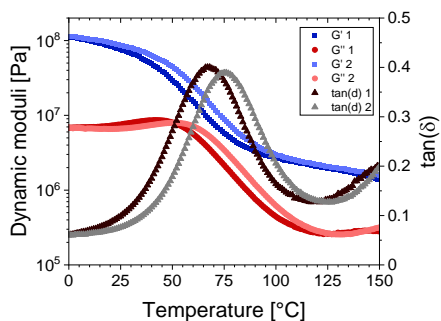## T sweeps of Zn^{2+}-coordinated pyr-imine materials with different anions

Figure 5.16 Temperature sweeps of Zn(OTf)$_2$ coordinated **pyr-imine**.

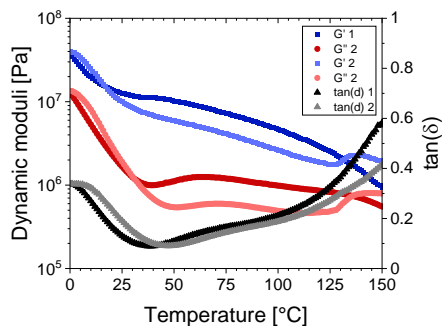**Figure 5.17** Temperature sweeps of ZnSO$_4$ coordinated **pyr-imine**.
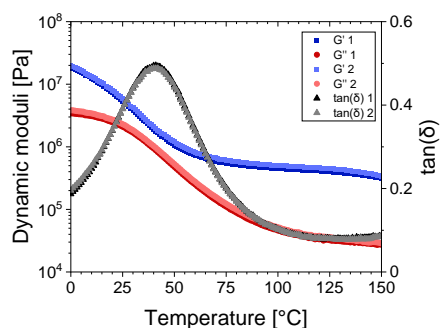
Figure 5.18 Temperature sweeps of Zn(NTf$_2$)$_2$ coordinated **pyr-imine**.
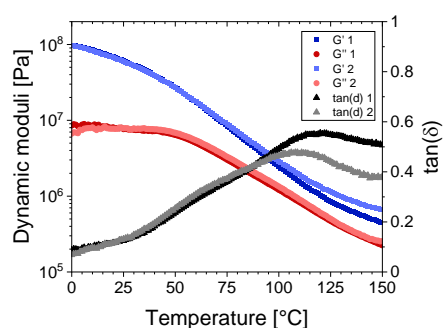
Figure 5.20 Temperature sweeps of Zn(NO$_3$)$_2$ coordinated **pyr-imine**.
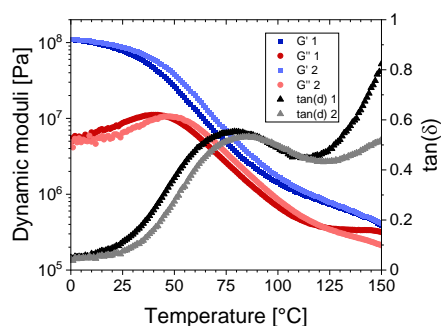
Figure 5.19 Temperature sweeps of Zn(BF$_4$)$_2$ coordinated **pyr-imine**.
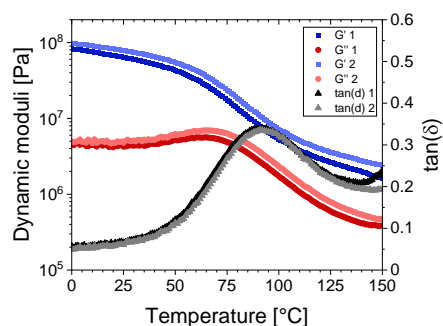
Figure 5.21 Temperature sweeps of Zn(OCl$_4$)$_2$ coordinated **pyr-imine**.

T sweeps for pyr-imine materials with different Zn(OTf)$_2$ concentrations
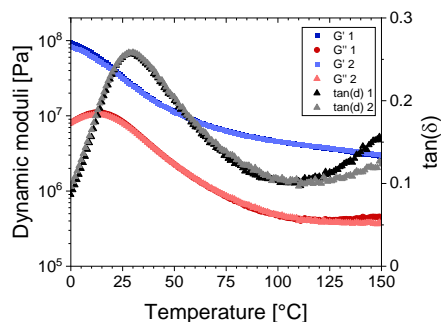
Figure 5.22 Temperature sweeps of **pyr-imine** coordinated to 25% Zn(OTf)$_2$.
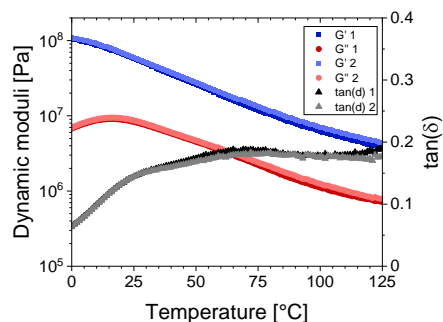
Figure 5.23 Temperature sweeps of **pyr-imine** coordinated to 50% Zn(OTf)$_2$.
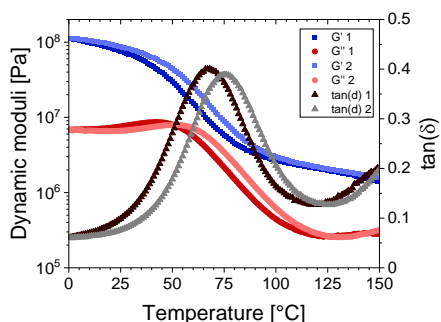
Figure 5.24 Temperature sweeps of **pyr-imine** coordinated to 100% Zn(OTf)$_2$.
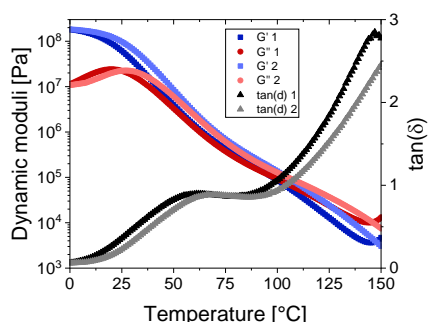
Figure 5.25 Temperature sweeps of **pyr-imine** coordinated to 200% Zn(OTf)$_2$.

T sweeps for pyr-imine materials with different Fe(OTf)$_2$ concentrations
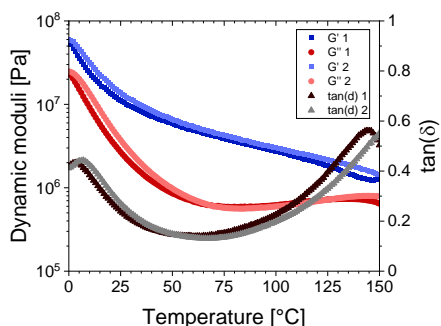
Figure 5.26 Temperature sweeps of **pyr-imine** coordinated to 25% Fe(OTf)$_2$.

Figure 5.28 Temperature sweeps of **pyr-imine** coordinated to 100% Fe(OTf)$_2$.
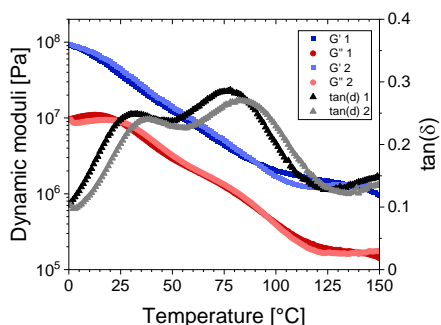
Figure 5.27 Temperature sweeps of **pyr-imine** coordinated to 50% Fe(OTf)$_2$.
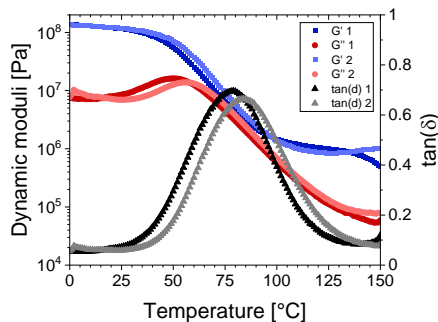
Figure 5.29 Temperature sweeps of **pyr-imine** coordinated to 200% Fe(OTf)$_2$.

5.5.6   Analogous small-molecule metal-ligand complexes

Several examples of the kinetic and thermodynamic stability of metal-coordinated bipyridine and terpyridine can be found in literature.[44, 45, 47, 56] These provided preliminary insights into the behaviour of the imine pincer complexes in o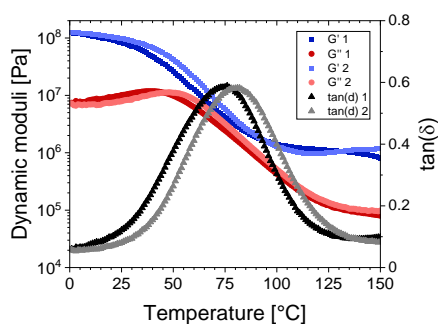ur polyimine materials. To relate the kinetic and thermodynamic details of small-molecules to the data of our metal-coordinated polyimines, we looked at the formation (k_f) and dissociation (k_d) constants of the M–L complexes, as well as the thermodynamic equilibrium constants (K). The kinetic and thermodynamic parameters of bipyridine (Table 5.6) and terpyridine (Table 5.7) complexes are presented below.

Table 5.6 Kinetic and thermodynamic parameters of small-molecule metal-coordinated bipyridine complexes. [a] As documented by Holyer et al.[44] [b] As documented by Irving et al.[45] [c] calculated by combining data from Holyer and Irving, since $K = k_f / k_d$. [d]No kinetic data was presented for Mn^{2+}.

Metal ion	Log(k_f) (M$^{-1} \cdot$ s^{-1})	Log(k_d) (s^{-1})	Log(K) (M^{-1})
Mn^{2+}	_[d]	_[d]	2.6[b]
Fe^{2+}	5.2[a]	0.9[c]	4.3[b]
Co^{2+}	4.8[a]	−0.9[c]	5.7[b]
Ni^{2+}	3.2[a]	−4.3[a]	7.1[b]–7.5[a]
Cu^{2+}	≥7.0[a]	≥−1.1[c]	8.1[b]
Zn^{2+}	6.0[a]	1.2[a]	4.8[a]–5.2[b]

Table 5.7 Kinetic and thermodynamic parameters of small-molecule metal-coordinated terpyridine complexes, documented by Holyer et al.[44] *The k_f for Cu^{2+} was determined at 5 °C, whereas all others were determined at 25 °C. K for Cu^{2+} was documented for 5-methyl-1,10-phenantroline by McBryde et al.[57] The k_d of Cu^{2+} was then calculated by combining data from Holyer and McBryde.

Metal ion	Log(k_f) (M$^{-1} \cdot$ s^{-1})	Log(k_d) (s^{-1})	Log(K) (M^{-1})
Mn^{2+}	5.0	0.6	4.4
Fe^{2+}	4.9	−2.2	7.1
Co^{2+}	4.4	−4.0	8.4
Ni^{2+}	3.1	−7.6	10.7
$Cu^{2+ (*)}$	7.3	1.4	5.1
Zn^{2+}	6.1	0.1	6.0

5.5.7   Comparison of material properties with metal-complex stability

The material properties of metal-coordinated **iso-imine** and **pyr-imine** CANs were compared to the metal-complex stability of small-molecule complexes (Figure 5.30). To do so, the glass transition temperature (T_g), elastic modulus (G') and creep (γ, expressed as the strain at 1000 s and 10 kPa stress) of the polymers were plotted as a function of the $\log(k_f)$, $\log(k_d)$ and $\log(K)$ of analogous small-molecule complexes (see Table 5.6 and Table 5.7 in Section 5.5.6). The individual plots can be found in Figures 5.31–5.36 on the following pages.

bipyridine   *terpyridine*
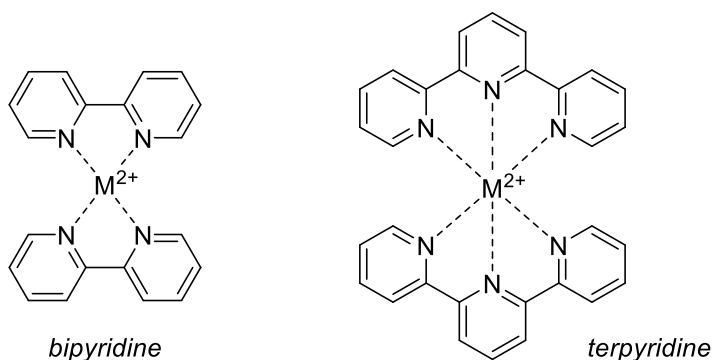
Figure 5.30 Structures of the small-molecule metal-ligand coordination complexes of bipyridine (left) and terpyridine (right) ligands.

T_g of polymers versus $\log(k_f)$, $\log(k_d)$ and $\log(K)$ of small-molecule analogues
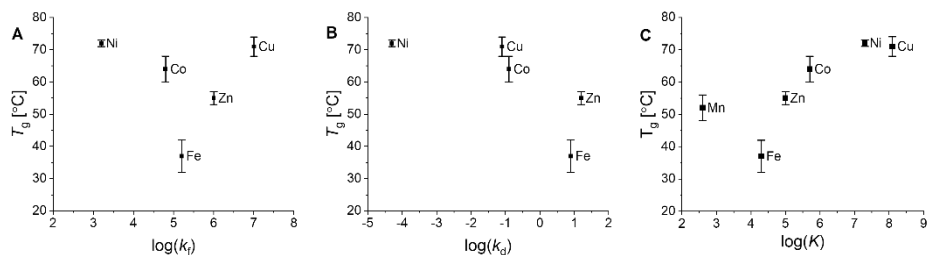
Figure 5.31 T_g of metal-coordinated **iso-imine** materials versus A) $\log(k_f)$, B) $\log(k_d)$, and C) $\log(K)$ of analogous small-molecule complexes.
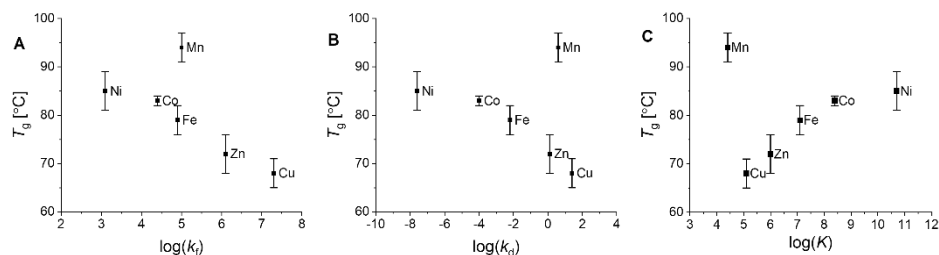
Figure 5.32 T_g of metal-coordinated **pyr-imine** materials versus A) log(k_f), B) log(k_d), and C) log(K) of analogous small-molecule complexes.

G' of polymers versus log(k_f), log(k_d) and log(K) of small-molecule analogues
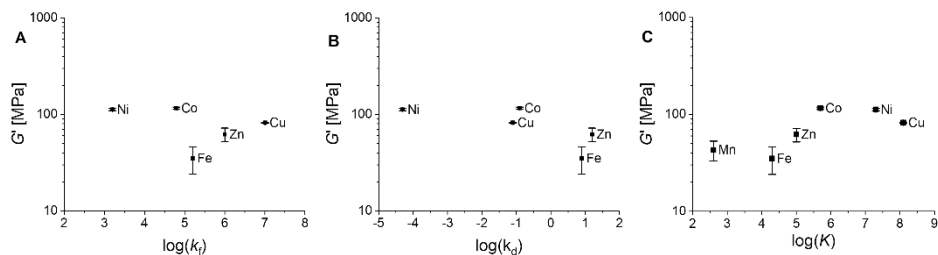
Figure 5.33 G' of metal-coordinated **iso-imine** materials versus A) log(k_f), B) log(k_d), and C) log(K) of analogous small-molecule complexes.
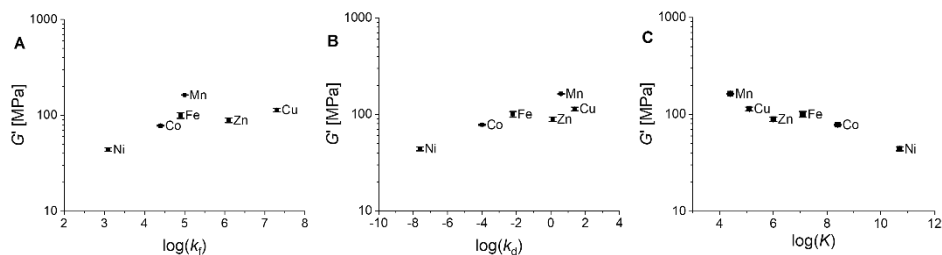
Figure 5.34 G' of metal-coordinated **pyr-imine** materials versus A) log(k_f), B) log(k_d), and C) log(K) of analogous small-molecule complexes.

Creep of polymers versus log(k_f), log(k_d) and log(K) of small-molecule analogues

Figure 5.35 Creep of metal-coordinated **iso-imine** versus A) log(k_f), B) log(k_d), and C) log(K) of analogous small-molecule complexes. The creep is expressed as the strain after exposure to a constant force of 10 kPa for 1000 s.

Figure 5.36 Creep of metal-coordinated **pyr-imine** versus A) log(k_f), B) log(k_d), and C) log(K) of analogous small-molecule complexes. The creep is expressed as the strain after exposure to a constant force of 10 kPa for 1000 s.

References

1. C. J. Kloxin, T. F. Scott, B. J. Adzima and C. N. Bowman, *Macromolecules*, 2010, **43**, 2643-2653.
2. C. J. Kloxin and C. N. Bowman, *Chem. Soc. Rev.*, 2013, **42**, 7161-7173.
3. D. Montarnal, M. Capelot, F. Tournilhac and L. Leibler, *Science*, 2011, **334**, 965-968.
4. N. De Alwis Watuthanthrige, P. Chakma and D. Konkolewicz, *Trends Chem.*, 2021, **3**, 231-247.
5. N. J. Van Zee and R. Nicolaÿ, *Prog. Polym. Sci.*, 2020, **104**, 101233.
6. L. D. Dugas, W. D. Walker, R. Shankar, K. S. Hoppmeyer, T. L. Thornell, S. E. Morgan, R. F. Storey, D. L. Patton and Y. C. Simon, *Macromol. Rapid Commun.*, 2022, **n/a**, 2200249.
7. L. Li, X. Chen, K. Jin and J. M. Torkelson, *Macromolecules*, 2018, **51**, 5537-5546.
8. W. Denissen, J. M. Winne and F. E. Du Prez, *Chem. Sci.*, 2016, **7**, 30-38.

9. M. A. Bin Rusayyis and J. M. Torkelson, *Polym. Chem.*, 2021, **12**, 2760-2771.
10. A. Perego and F. Khabaz, *Macromol. Rapid Commun.*, 2022, **n/a**, 2200313.
11. F. Van Lijsebetten, T. Debsharma, J. M. Winne and F. E. Du Prez, *Angew. Chem. Int. Ed.*, 2022, **n/a**, e202210405.
12. A. Breuillac, A. Kassalias and R. Nicolaÿ, *Macromolecules*, 2019, **52**, 7102-7113.
13. F. Van Lijsebetten, K. De Bruycker, Y. Spiesschaert, J. M. Winne and F. E. Du Prez, *Angew. Chem. Int. Ed.*, 2022, **61**, e202113872.
14. X. Zhang, S. Wang, Z. Jiang, Y. Li and X. Jing, *J. Am. Chem. Soc.*, 2020, **142**, 21852-21860.
15. R. G. Ricarte, F. Tournilhac and L. Leibler, *Macromolecules*, 2019, **52**, 432-443.
16. J. J. Lessard, G. M. Scheutz, S. H. Sung, K. A. Lantz, T. H. Epps and B. S. Sumerlin, *J. Am. Chem. Soc.*, 2020, **142**, 283-289.
17. R. W. Clarke, M. L. McGraw, B. S. Newell and E. Y. X. Chen, *Cell Rep. Phys. Sci.*, 2021, **2**, 100483.
18. K. M. Herbert, P. T. Getty, N. D. Dolinski, J. E. Hertzog, D. de Jong, J. H. Lettow, J. Romulus, J. W. Onorato, E. M. Foster and S. J. Rowan, *Chem. Sci.*, 2020, **11**, 5028-5036.
19. S. Weerathaworn and V. Abetz, *Macromol. Chem. Phys.*, 2022, **n/a**, 2200248.
20. D. Mozhdehi, S. Ayala, O. R. Cromwell and Z. Guan, *J. Am. Chem. Soc.*, 2014, **136**, 16128-16131.
21. C.-H. Li and J.-L. Zuo, *Adv. Mater.*, 2020, **32**, 1903762.
22. M. Murali, D. Berne, C. Joly-Duhamel, S. Caillol, E. Leclerc, E. Manoury, V. Ladmiral and R. Poli, *Chem. Eur. J.*, 2022, **n/a**, e202202058.
23. Y. Xue, C. Li, W. Wang, Z. Liu, Z. Guo, J. Tan and Q. Zhang, *Macromol. Rapid Commun.*, 2021, **43**, 2100510.
24. Y. Liu, Z. Tang, D. Wang, S. Wu and B. Guo, *J. Mater. Chem. A*, 2019, **7**, 26867-26876.
25. D.-P. Wang, J.-C. Lai, H.-Y. Lai, S.-R. Mo, K.-Y. Zeng, C.-H. Li and J.-L. Zuo, *Inorg. Chem.*, 2018, **57**, 3232-3242.
26. M. Burnworth, L. Tang, J. R. Kumpfer, A. J. Duncan, F. L. Beyer, G. L. Fiore, S. J. Rowan and C. Weder, *Nature*, 2011, **472**, 334-337.
27. L. Bai, X. Yan, B. Feng and J. Zheng, *Compos. B. Eng.*, 2021, **223**, 109123.
28. X. Xu, F. A. Jerca, V. V. Jerca and R. Hoogenboom, *Adv. Funct. Mater.*, 2019, **29**, 1904886.
29. M. Yang, X. Lu, Z. Wang, G. Fei and H. Xia, *J. Mater. Chem. A*, 2021, **9**, 16759-16768.
30. M. Ciaccia and S. Di Stefano, *Org. Biomol. Chem.*, 2015, **13**, 646-654.
31. L. Zhang, Z. Liu, X. Wu, Q. Guan, S. Chen, L. Sun, Y. Guo, S. Wang, J. Song, E. M. Jeffries, C. He, F.-L. Qing, X. Bao and Z. You, *Adv. Mater.*, 2019, **31**, 1901402.
32. S. K. Schoustra, J. A. Dijksman, H. Zuilhof and M. M. J. Smulders, *Chem. Sci.*, 2021, **12**, 293-302.
33. P. Taynton, C. Zhu, S. Loob, R. Shoemaker, J. Pritchard, Y. Jin and W. Zhang, *Polym. Chem.*, 2016, **7**, 7052-7056.

34. S. K. Schoustra, T. Groeneveld and M. M. J. Smulders, *Polym. Chem.*, 2021, **12**, 1635-1642.

35. A. Liguori and M. Hakkarainen, *Macromol. Rapid Commun.*, 2022, **43**, 2100816.

36. Y. Wang, A. Xu, L. Zhang, Z. chen, R. Qin, Y. Liu, X. Jiang, D. Ye and Z. Liu, *Macromol. Mater. Eng.*, 2022, 2100893.

37. F. García, J. Pelss, H. Zuilhof and M. M. J. Smulders, *Chem. Commun.*, 2016, **52**, 9059-9062.

38. G. Nasr, T. Macron, A. Gilles, Z. Mouline and M. Barboiu, *Chem. Commun.*, 2012, **48**, 6827-6829.

39. S. Wang, S. Ma, Q. Li, X. Xu, B. Wang, K. Huang, Y. liu and J. Zhu, *Macromolecules*, 2020, **53**, 2919-2931.

40. J. Pignanelli, Z. Qian, X. Gu, M. J. Ahamed and S. Rondeau-Gagné, *New J. Chem.*, 2020, **44**, 8977-8985.

41. J. Pignanelli, B. Billet, M. Straeten, M. Prado, K. Schlingman, M. J. Ahamed and S. Rondeau-Gagné, *Soft Matter*, 2019, **15**, 7654-7662.

42. D. Asil, J. A. Foster, A. Patra, X. de Hatten, J. del Barrio, O. A. Scherman, J. R. Nitschke and R. H. Friend, *Angew. Chem. Int. Ed.*, 2014, **53**, 8388-8391.

43. X. de Hatten, N. Bell, N. Yufa, G. Christmann and J. R. Nitschke, *J. Am. Chem. Soc.*, 2011, **133**, 3158-3164.

44. R. H. Holyer, C. D. Hubbard, S. F. A. Kettle and R. G. Wilkins, *Inorg. Chem.*, 1966, **5**, 622-625.

45. H. Irving and D. H. Mellor, *J. Chem. Soc.*, 1962, **0**, 5222-5237.

46. H. Irving and R. J. P. Williams, *Nature*, 1948, **162**, 746-747.

47. M. A. R. Meier, B. G. G. Lohmeijer and U. S. Schubert, *J. Mass Spectrom.*, 2003, **38**, 510-516.

48. P. Cieslik, P. Comba, B. Dittmar, D. Ndiaye, É. Tóth, G. Velmurugan and H. Wadepohl, *Angew. Chem. Int. Ed.*, 2022, **61**, e202115580.

49. K. Born, P. Comba, R. Ferrari, G. A. Lawrance and H. Wadepohl, *Inorg. Chem.*, 2007, **46**, 458-464.

50. G. Nasr, T. Macron, A. Gilles, C. Charmette, J. Sanchez and M. Barboiu, *Chem. Commun.*, 2012, **48**, 11546-11548.

51. M. Capelot, M. M. Unterlass, F. Tournilhac and L. Leibler, *ACS Macro Lett.*, 2012, **1**, 789-792.

52. J. Cui, F.-M. Nie, J.-X. Yang, L. Pan, Z. Ma and Y.-S. Li, *J. Mater. Chem. A*, 2017, **5**, 25220-25229.

53. A. Bauzá, A. Frontera and T. J. Mooibroek, *Nat. Commun.*, 2017, **8**, 14522.

54. P. Zhao, L. Wang, L. Xie, W. Wang, L. Wang, C. Zhang, L. Li and S. Feng, *Macromol. Rapid Commun.*, 2021, **42**, 2100519.

55. D. Venkataraman, Y. Du, S. R. Wilson, K. A. Hirsch, P. Zhang and J. S. Moore, *J. Chem. Educ.*, 1997, **74**, 915.

56. G. Anderegg, *Helv. Chim. Acta*, 1963, **46**, 2397-2410.

57. W. A. E. McBryde, D. A. Brisbin and H. Irving, *J. Chem. Soc.*, 1962, **0**, 5245-5253.

Metal Coordination in Polyimine Covalent Adaptable Networks
for Tuneable Material Properties and Enhanced Creep Resistance

Chapter 6

Internal Hydrogen Bonding of Imines to Control and Enhance the Dynamic Mechanical Properties of Covalent Adaptable Networks

165
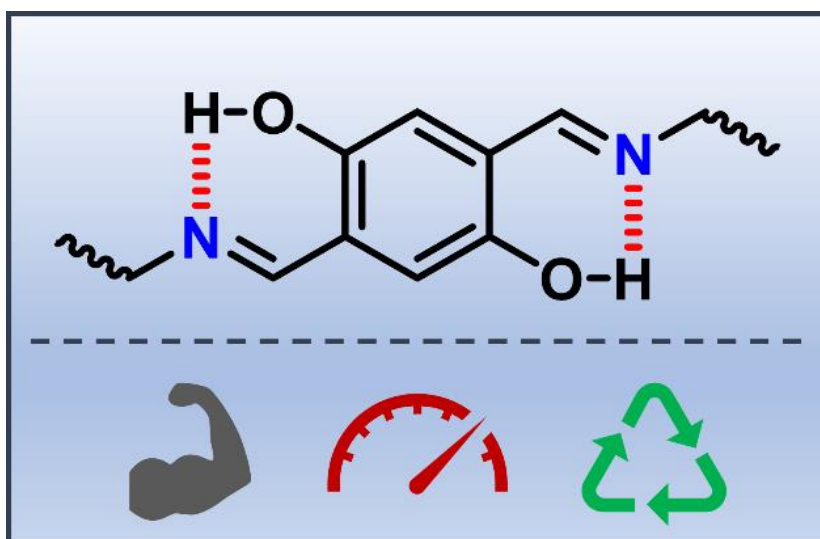
Abstract

Covalent Adaptable Networks (CANs) have the potential to replace current thermoset materials, as the dynamic covalent bonds in CANs enable reprocessability and recycling of crosslinked polymer networks. A current limitation of CANs is, however, that they are generally susceptible towards creep, as the bond exchange reactions facilitate stress relaxation. As such, CANs would benefit from developments in creep reduction at operating temperatures, while still enabling malleability at elevated temperatures, by means of shielding or deactivation of the dynamic covalent bonds. In this Chapter, we propose the use of internal hydrogen bonding in polyimine CANs as an efficient tool to enhance creep resistance and further control the dynamic mechanical properties of the material. We were able to show on a small-molecule level that *ortho*-substituted hydroxy groups stabilise the dynamic covalent imine bonds as a result of the internal hydrogen bond that is formed between the hydroxy and imine group. Furthermore, we show that polyimine CANs with incorporated *ortho* hydroxy groups have significantly enhanced material properties, as was seen in the glass transition temperature (T_g), elastic modulus (G') and creep resistance. While we also considered additional and steric effects that might have arisen due to installation of the hydroxy groups, we found that the stabilising effect of the internal hydrogen bond was primarily dictating the material performance. In short, we show that the internal hydrogen bond between *ortho* hydroxy and imine demonstrates the concept of shielding the dynamic covalent bond in order to suppress creep and enhance material properties of CANs.

6.1   Introduction

Covalent adaptable networks (CANs) have shown in recent years that they are capable of replacing traditional poorly-recyclable thermosets and elastomers for the development of more sustainable polymer materials.[1-5] Many studies have elaborated on the development, enhancement and tuneability of material properties of CANs,[6-9] but a major challenge still lies in their susceptibility towards creep.[10-12] CANs contain dynamic covalent bonds, which enable the materials to release stress via bond exchange reactions to rearrange the polymer network.[13] This feature enables reprocessability of the materials. However, this is also what facilitates creep when a material is exposed to a (large) loading force at the working temperature.[14] It is thus key to develop a CAN that resists strongly to deformation at low temperatures, but still enables reprocessability at elevated temperatures.

Different strategies to control and enhance the material properties of CANs have been documented recently. This was, for example, achieved by inducing phase separation (see also **Chapter 3**),[15] which was seen for block-copolymer vitrimers,[16-18] or by grafting functional groups that are incompatible with the polymer backbone.[19, 20] Other means to enhance material properties as a result of the network structure are to build in (a small degree of) static crosslinks within the dynamic network,[21, 22] or a secondary reversible bond.[23-27] Alternative ways to control the dynamic mechanical properties are by targeting the dynamic covalent bonds specifically, for example, *via* neighbouring group participation or internal catalysis.[8, 28-32]

In this chapter, we describe an efficient method to control and enhance material properties of polyimine CANs by stabilising the dynamic covalent imine bonds *via* internal hydrogen bonding. First, the internal hydrogen bond between an imine and 2-hydroxy group on the same aromatic ring (Figure 6.1) is expected to suppress the nucleophilicity of the nitrogen end of the imine bond, increasing the energetic barrier to initiate bond exchange (provided the installed 2-hydroxy group does not prevent imine formation due to additional stabilisation of the corresponding aldehyde starting material). Furthermore, the 2-hydroxy group enables imine-enamine tautomerisation,[33] which will result in loss of the double bond character of the imine bond. Finally, the internal hydrogen bond prevents rotation of the C–C bond between the imine and benzene ring to hold it in one plane,[34] and as such may enable π-π stacking interactions that can further stabilise the material.[35]
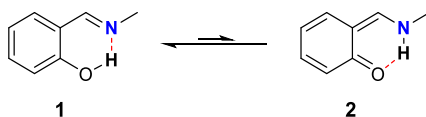
Figure 6.1 The 2-hydroxy group on the aromatic ring facilitates a strong internal hydrogen bond between the imine and hydroxy group (shown as a red dotted line). Additionally, imine-enamine tautomerisation is possible.

Internal hydrogen bonding of imines has been studied well for small molecules,[36, 37] covalent organic frameworks (COFs),[34] and enzymatic derivatives,[38] but to the best of our knowledge, has not been applied for CANs. Some examples of hydrogen bonding in CANs have been documented,[39-41] but these generally refer to intermolecular hydrogen bonding between polymer chains,[42-45] rather than intramolecular hydrogen bonding to stabilise or entrap the dynamic covalent bonds.

To study the effects of internal hydrogen bonding in imine-based CANs, polyimine networks were synthesised from substituted terephthalaldehyde monomers (Figure 6.2). The aldehydes (**TA-R**) were reacted to imines using a flexible **TOTDDA** diamine monomer and **TREN** as a triamine crosslinker, using a similar synthetic procedure as reported in previous Chapters.[46] First, we compared the results for non-substituted materials (**PI-H**) with the hydroxy-substituted materials (**PI-OH**). Second, we also compared the hydroxy-substituted materials to materials with different substituents to rule out underlying effects of the hydroxy substitution, such as electronic[46-48] or steric[49] effects. The methoxy-substituted material (**PI-OMe**) was included in our studies since the OMe group has a similar electronic effect as the OH group,[50] but is not able to provide the internal H-bond.
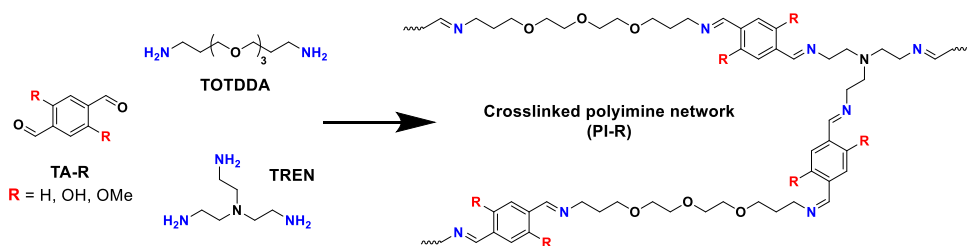
Figure 6.2 Reaction scheme for the preparation of polyimine networks (**PI-R**) from dialdehyde (**TA-R**), diamine (**TOTDDA**), and triamine crosslinker (**TREN**). Dialdehydes and polyimines are named correspondingly to the respective R group being either H, OH, or OMe.

6.2 Results and Discussion

6.2.1 Small-molecule studies

Before analysis of the polymer materials, the effects of internal hydrogen bonding on the stability and dynamics of the imine bonds were first analysed on small-molecule analogues. First, the structure of the *ortho*-OH imine was evaluated computationally for three potential structures: **1**) as imine with hydrogen bonding, the conformation that we hypothesised to be most stable, **2**) as keto-enamine with hydrogen bonding, **3**) as imine without hydrogen bonding (Figure 6.3). The calculations showed that structure **1** had the lowest free energy (see Section 6.5.5 for further details on the calculations). Tautomerisation to structure **2** showed a relative ΔG of +2.35 kcal/mol, whereas rotation of the C–O bond to point the OH group away from the imine (*i.e.*, breaking the hydrogen bond) to structure **3** showed a relative ΔG of +9.83 kcal/mol, making formation of this structure unlikely. Also note that structure **1** and **2** should be fully flat, which might give rise to additional π-π stacking stabilisation.
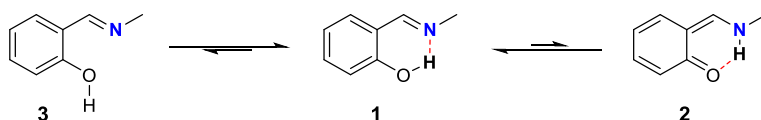
Figure 6.3 Structures of (2-hydroxyphenyl)imine with hydrogen bond (**1**), keto-enamine tautomer with hydrogen bond (**2**), and 2-hydroxyphenyl)imine without hydrogen bond (**3**).

To further evaluate the effects of the internal hydrogen bonding, a competition experiment was performed, in which one equivalent of benzaldehyde and one equivalent of either 2-hydroxybenzaldehyde, 3-hydroxybenzaldehyde or 4-hydroxybenzaldehyde were dissolved together in CDCl$_3$. Then, one equivalent of propylamine was added, which immediately reacted with half of the available aldehydes. As only half of the total amount of aldehyde groups is able to form imines, an equilibrium is formed (Figure 6.4). *Via* integration of the imine and aldehyde signals in the NMR spectra, the equilibrium constant *K* could be determined (see Section 6.5 for full experimental details).
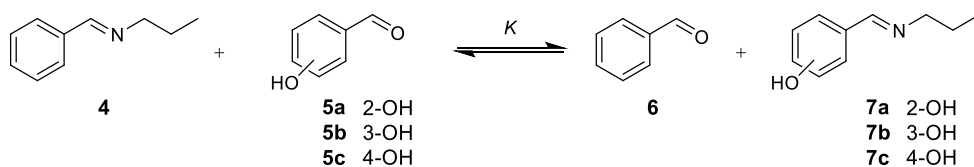
Figure 6.4 Equilibrium reaction of aldehyde *versus* imine formation for benzaldehyde and hydroxybenzaldehydes with their corresponding imines.

First, the reaction with 2-hydroxybenzaldehyde (**5a**) was evaluated, and a *K* value of 6.31 ± 0.61 was found. This means that the equilibrium is pushed in favour of formation of (2-hydroxyphenyl)imine (**7**), although the *K* is lower than expected for a stabilisation of 2.35 kcal/mol. The reason for the observed *K* value can, however, be best explained based on differential H-bond strengths, as we compare the H-bond strengths between the *ortho* hydroxy group and either the aldehyde of **5** or the imine of **7**. We calculated that the difference in H-bond strength was 1.91 kcal/mol, whereas a ∆*G* of −1.98 kcal/mol was calculated for the overall reaction (see Section 6.5.5 for further details on the calculations). This thus shows that the difference in H-bond strength nearly fully drives this reaction: *i.e.*, the 2-hydroxy group more strongly stabilises the imine than the corresponding aldehyde.

Next, also the *meta* and *para*-substituted hydroxybenzaldehyde –that are unable to form internal H-bonds– were evaluated. For the reactions with 3-hydroxybenzaldehyde (**2b**) and 4-hydroxybenzaldehyde (**2c**) *K* values of 0.281 ± 0.001 and 0.247 ± 0.002 were determined, respectively. This means that the equilibrium actually disfavours the formation of the hydroxy-substituted imine (**7**). As the 2-hydroxy group is the only one that facilitates internal hydrogen bonding, the large difference in *K* between the 2-hydroxy with the other two thus supports our hypothesis that the internal hydrogen bonding promotes formation of the imine.

6.2.2 Synthesis of polyimine CANs

To study the effects of internal hydrogen bonding of imines on the material properties of CANs, polyimines were synthesised as pictured in Figure 6.2. Either of the substituted dialdehydes was added to a solution of **TOTDDA** and **TREN** in dichloromethane (DCM), such that the total amount of aldehyde to imine groups were on an equimolar amount. The solution was then poured into a petri dish, and left for overnight at room temperature. Most of the solvent was able to evaporate to air, but to fully dry the materials and remove water that forms during the reaction, the obtained polymer films were further dried in a vacuum oven at 50 °C for at least one day. Conversion of all aldehydes into imines was confirmed by NMR and FT-IR spectroscopy. In addition, for the **PI-OH** material, the IR spectrum revealed

that no "free" OH signals (~3600 cm^{-1}) or intermolecularly hydrogen bonded OH signals (3200–3600 cm^{-1}) were observed,[51] but it did show an OH signal that is typical to intramolecular hydrogen bonding (~2800 cm^{-1}),[51] which confirmed that indeed the internal hydrogen bonding is present in the polymer. Before further analysis with rheology, the materials were hot-pressed at 150 °C into the desired shape. Further experimental details are provided in the Supporting Information (Section 6.5).

6.2.3 Thermal mechanical properties of the polyimine CANs

The polyimine materials were first analysed for their material properties by performance of a temperature sweep experiment from 0–150 °C (the same procedures as mentioned in **Chapter 2** were used). The storage modulus (G'), loss modulus (G'') and damping factor (tan(δ) = G''/G') were plotted as a function of the temperature (Figure 6.5). From the obtained curves, we could derive the moduli of the glass and rubbery phases of the material, as well as find the glass transition temperature (T_g). As the T_g of the **PI-H** material was very close to 0 °C, an additional temperature sweep was performed from −20 to +20 °C to determine the T_g more accurately (Figure 6.5B).
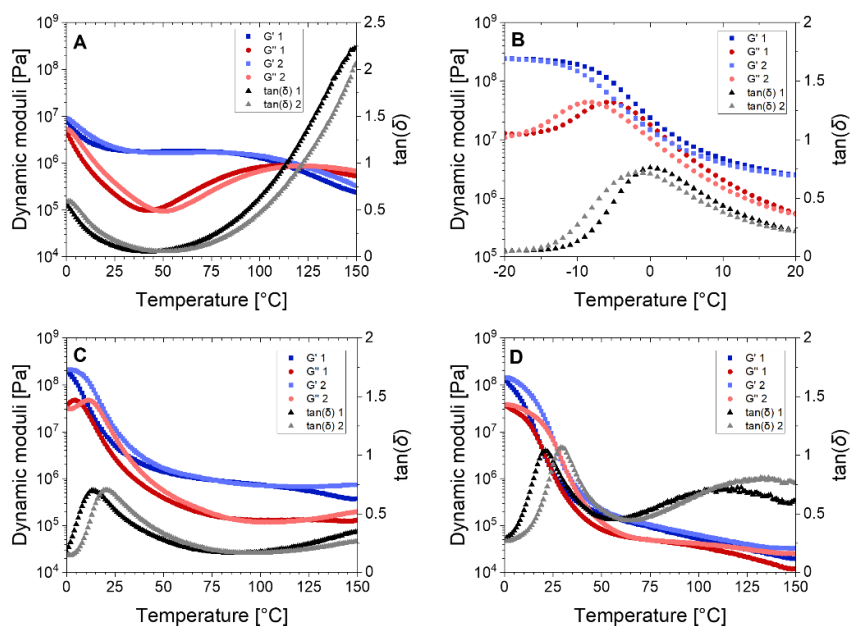
Figure 6.5 Temperature sweeps of polyimine materials (all shown *in duplo*). Storage modulus (G', blue), loss modulus (G'', red), and damping factor (tan(d), grey) are plotted as a function of the temperature. A) shows the temperature sweep results of **PI-H** from 0 to 150 °C, and B) shows an additional T sweep from −20 to +20 °C to more accurately determine the T_g at the top of the tan(d) peak. C) and D) show the T sweep results from 0 to 150 °C for **PI-OH** and **PI-OMe**, respectively.

From the temperature sweeps we first compared the T_g values, which were derived from the top of the peak from the tan(δ) curves. It was found that the T_g for **PI-H** was only −1 ± 1 °C, but for **PI-OH** and **PI-OMe** the T_g increased to 17 ± 3 °C and 25 ± 4 °C, respectively. As the T_g increased for both the hydroxy- and methoxy-substituted materials, we could not yet establish what the effect of the internal hydrogen bond was. Since the OH and OMe groups typically have similar electronic effects,[50, 52] which are known to affect the material properties of CANs (as presented also in **Chapter 2**),[46] the observed increase in T_g for both materials might thus be related to electronic effects of the substituents. For non-substituted **PI-H** also a crossover point (T_{cross}), where G' = G'' (*i.e.*, tan(δ) = 1) was observed at 118 ± 4 °C, Indicating that the material transitions from a viscoelastic solid to a viscoelastic liquid (*i.e.*, the material starts to flow).[53, 54] For neither **PI-OH** or **PI-OMe** this was observed below 150 °C, reaching the limits of our setup.

From the temperature sweeps we also noticed that in the glassy phase all materials had a similar G' around roughly 200 MPa, indicating that in this frozen state of the network the materials behave similar. The G' of the rubbery phase was, however, not the same for all materials. Where for **PI-H** and **PI-OH** a G' was observed in the range of 1 MPa, for **PI-OMe** the G' was roughly an order of magnitude lower at 100 kPa. The size of the substituents might be the cause for the drop in G', as the methoxy group was the largest of the three. Sun *et al*. also observed that larger steric groups in CANs cause looser arrangements, making molecular chains move easier along the stretching directions under external force.[42] As a result, the tensile strength decreased when the size of the steric bulk increased. For **PI-OH**, the small steric effect of the hydroxy group might either not be sufficient to affect the material properties, or potential steric effects might be compensated for by the internal hydrogen bonding.

6.2.4   Creep experiments

To get a better understanding of the effects of the internal hydrogen bonding on the material properties of our polyimine CANs, we performed several creep experiments. The same materials as before were now exposed to a constant stress of 10 kPa, and the creep of the material was followed over time. We performed the experiment at different temperatures (20, 60 and 100 °C) to see if the materials would be able to resist creep at higher working temperatures, which is especially important in the rubbery phase of the material in light of potential applications. All creep experiments were performed *in triplo*, and are presented in Figure 6.6.
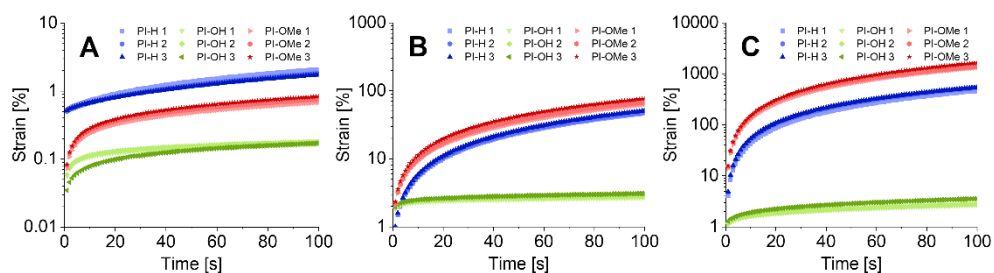
Figure 6.6 Creep curves of **PI-H** (blue), **PI-OH** (green), and **PI-OMe** (blue), at A) 20 °C, B) 60 °C, and C) 100 °C. Note the different scales used in A, B and C. All measurements were performed *in triplo*.

At 20 °C (which is around the T_g value for **PI-OH** and **PI-OMe**), we already see clearly that **PI-OH** showed very good creep resistance, as over time the observed strain hardly goes beyond 0.1%. For **PI-H** and **PI-OMe** we see a creep at roughly one order of magnitude greater than was observed for **PI-OH**. This already gives a good indication that the internal hydrogen bonding supresses the susceptibility towards creep. However, an even greater result was observed at elevated temperatures. When increasing the temperature to 60 °C and even 100 °C (for above the T_g of all materials), the creep resistance of **PI-OH** remained rather good, as at both temperatures the creep was similar and remained below 3% in the given time interval. For **PI-H** and **PI-OMe** a much higher creep was observed at the elevated temperatures. Where the creep of **PI-OH** only slightly increased at 60 °C, for **PI-H** and **PI-OMe** the increase was almost two orders of magnitude, nearing 100% strain after 100 s. When increasing the temperature even further to 100 °C, we observed that no notable difference was observed for **PI-OH**, but the creep for **PI-H** and **PI-OMe** became highly problematic. These results thus clearly indicate that the internal hydrogen bond in the **PI-OH** materials significantly suppress the susceptibility towards creep, even at elevated temperatures where analogous materials without internal hydrogen bonding will flow drastically.

6.2.5 Stress relaxation and kinetic activation energy

Stress relaxation experiments were performed at several different temperatures to construct Arrhenius plots (see Figure 6.7), in order to calculate the kinetic activation energy (E_a) and gain more insights in the dynamics of the bond exchange reactions for the differently substituted materials (see the Supporting Information, Section 6.5, for full experimental details).
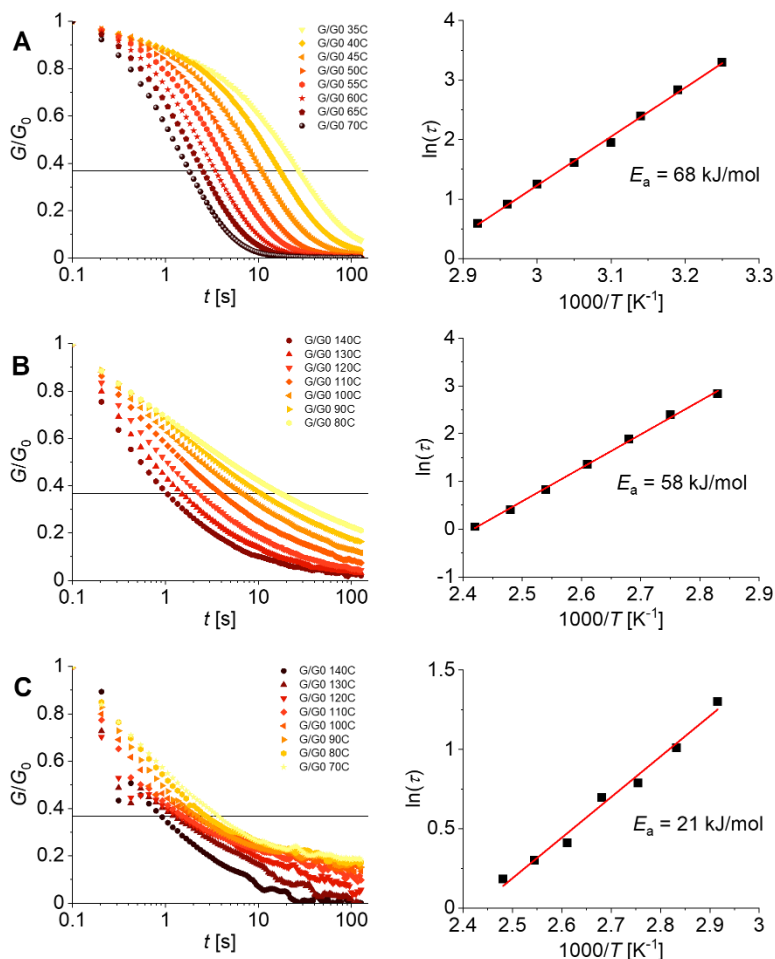
Figure 6.7 Normalised stress relaxation curves (left) and Arrhenius plots (right) of A) **PI-H**, B) **PI-OH**, and C) **PI-OMe**. The horizontal line pictures the value of 1/e. The point at which each of the relaxation curves reaches this point represents the corresponding relaxation time (τ), which is used to derive the Arrhenius plots. In the corresponding the Arrhenius plot a linear trendline was fit to derive the E_a. See Section 6.5.4 in the Supporting Information for the non-normalised relaxation curves.

From the three polyimine materials, **PI-H** had the highest E_a of 68 kJ/mol. The E_a of **PI-OH** was only slightly lower (58 kJ/mol), but the E_a for **PI-OMe** was much lower (21 kJ/mol). The decrease in E_a for **PI-OH** and **PI-OMe** can be explained by the electronic effect of the functional groups, as expressed by the Hammett parameter (σ). In **Chapter 2** we showed that an increase in σ (*i.e.*, more electron-withdrawing substituent) resulted in a decrease

in E_a.[46] Given that hydrogen has a Hammett parameter of 0.00, whereas OH and OMe both have Hammett parameters for *meta* substitution (σ_m) of 0.12,[50] it was in line with earlier work that the **PI-OH** and **PI-OMe** materials showed a lower E_a. Note, however, that in the previous work in **Chapter 2**, the substituents were positioned on the aniline monomer instead of the aldehyde monomer, and that we now used the value for *meta*substitution (σ_m), whereas in our earlier work we used the *para*substitution (σ_p), corresponding to the position of the substituents on the aromatic ring. In the current work, technically, the functional groups are present at both *ortho* and *meta* position with respect to either of the two aldehyde groups on the aromatic ring, given the symmetrical appearance of the dialdehyde monomers. However, Hammett parameters are only available for *meta* and *para* substitution.[55] This is for reasons that at the *ortho* position, it is experimentally impossible to determine the electronic effect of a particular substituent without any interfering effect of the steric bulk imposed by that substituent.[56] It is, however, noted that the OMe has a larger steric bulk than the OH group, and that at the *ortho* position OH and OMe would have a more electron donating character compared to an electron withdrawing character at the *meta* position.

With this in mind, the relatively large difference in E_a between **PI-OH** and **PI-OMe** was thus quite striking as OH and OMe have similar Hammett parameters for the *meta* substitution (σ_m = 0.12 for both).[50] It would, however, fit the hypothesis of internal hydrogen bonding in **PI-OH**. As the internal hydrogen bond stabilises the imine bond, the required energy to activate bond exchange increases, expressing the observed increase in E_a when comparing **PI-OH** to **PI-OMe**.

6.2.6 Solvent resistance

The solvent resistance of the polyimine CANs was tested for THF, water and MeOH. A small piece of polymer materials was soaked in the respective solvent for 48 h at room temperature. Then, the liquid and remaining solid were separated, and the dissolved and non-dissolved fractions were determined (see Section 6.5 for further experimental details). The solvent resistance, expressed as remaining fraction, for each of the materials in every solvent is pictured in Figure 6.8.

From the results in Figure 6.8 can be concluded firstly that the solvent resistance towards THF and MeOH is far greater for **PI-OH** compared to **PI-H** and **PI-OMe**, indicating that the internal hydrogen bonding in the **PI-OH** also enhances solvent resistance. Especially the solvent resistance of **PI-OH** towards MeOH (~90%) was striking, as MeOH can form hydrogen bonds with the polymer material as well. The good resistance against MeOH of **PI-OH** can be seen as evidence that intermolecular hydrogen bonding of **PI-OH** with

methanol cannot compete with the intramolecular hydrogen bonds within the polyimine structure. We also, importantly, observed that all materials resist relatively well to water (~90%), which shows that the imines do not easily hydrolyse in aqueous environments.
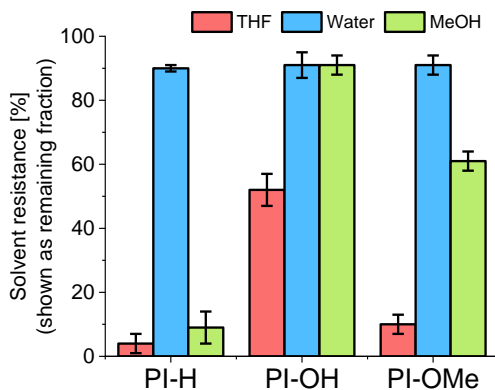
Figure 6.8 Solvent resistance of polyimines, showing the remaining fraction (%) of polymer after soaking for 48 h at room temperature in the respective solvent.

6.3 Conclusion

The introduction of hydroxy groups on the *ortho* position of the aromatic imines enables an internal hydrogen bond between the hydroxy and imine groups. The increased stability of the imine as a result of the internal hydrogen bond was first shown in small-molecule experiments. Next, polymer materials were synthesised with either hydrogen, hydroxy or methoxy groups on the *ortho* position of the aromatic rings. These results showed that the hydroxy groups, facilitating the internal hydrogen bonds, could significantly reduce creep of the materials, especially at elevated temperatures. Furthermore, we showed that the glass transition temperature (T_g), elastic modulus (G'), kinetic activation energy (E_a) and solvent resistance of the polyimine CANs were also positively affected by the internal hydrogen bonding. We foresee that intramolecular stabilisation or deactivation of dynamic covalent groups in CANs, such as the described internal hydrogen bond between 2-hydroxy and imine groups, may form a promising basis for the further development of tuneable, high performance, and creep-resistant CANs.

6.4   Acknowledgement

6.5   Supporting Information

An overview of the most important supporting information is given in the following section. The full supporting information can be found online at: shorturl.at/eNWX6.

See **Chapter 2**, Section 2.6, for the experimental setups of rheology, NMR and FT-IR.

6.5.1   Small molecule studies

To investigate the effect of the internal hydrogen bond on the stability of the imine bond, a small-molecule competition experiment using NMR was performed. In this experiment, 1 equivalent of benzaldehyde (0.50 mmol) and 1 equivalent of a hydroxybenzaldehyde (either **5a**, **5b** or **5c**; 0.50 mmol) were dissolved together in CDCl$_3$ (0.5 mL) in and NMR tube. To the solution, 1 equivalent of propylamine (0.50 mmol) was added, and the mixture was shaken briefly. As the two different aldehydes compete for the available amine, an equilibrium is formed (see Figure 6.4 in the Result and Discussion, Section 6.2.1). This equilibrium was generally reached within several minutes. After 30 minutes, the equilibrium constant (*K*) was then determined *via* integration of the NMR signals of relevant aldehydes and imines as:

$$K = \frac{[aldehyde\ \mathbf{6}][imine\ \mathbf{7}]}{[imine\ \mathbf{4}][aldehyde\ \mathbf{5}]}$$

An overview of the used NMR signals is given in Table S6.1.

Table 6.1 Overview of NMR signals of aldehyde and imine groups, used for integration to determine *K* values of the equilibrium reaction shown in Figure 6.3. All signals are noted in ppm using CDCl₃ as the solvent.

	Aldehyde (ppm)	Imine (ppm)
Benzaldehyde	10.02	8.29
2-OH	9.90	8.33
3-OH	9.89	8.19
4-OH	9.81	8.14

6.5.2   Synthesis of 2,5-dihydroxyterephthalaldehyde (**TA-OH**)

Dimethoxyterephthalaldehyde (0.987 g, 5.06 mmol) was dissolved in 200 mL dry DCM, and cooled to 0 °C. Under N_2 atmosphere, BBr₃ (3.9 mL, 41 mmol) was added dropwise while keeping the temperature at 0 °C. Afterwards, stirring was continued for 16 hours. The reaction was quenched by slowly adding 50 mL water to the mixture. Then another 100 mL water was added, and the mixture was extracted 4× with 50 mL DCM and 1× with 100 mL EtOAc. The combined organic phase was washed with brine, dried over $MgSO_4$, filtered, and dried *in vacuo*. The product (0.480 g, 2.89 mmol) was obtained as a beige powder with a 57% yield.

¹H NMR (400 MHz, DMSO-d₆, δ): 10.31 (s, 2H), 10.27 (s, 2H), 7.23 (s, 2H).

¹³C NMR (100 MHz, DMSO-d₆, δ): 190.7, 153.3, 128.1, 115.6.

6.5.3   Synthesis of polyimine networks

4,7,10-trioxa-1,13-tridecanediamine (**TOTDDA**) (0.15 mL, 0.70 mmol) and tris(2-aminoethyl) amine (**TREN**) (0.030 mL, 0.20 mmol) were dissolved in 2 mL DCM. A second solution was prepared of the corresponding aldehyde (1.00 mmol) in 5 mL DCM. Then, the two solutions were mixed and poured into a petri dish. The petri dish was left open to air for overnight so that the solvent was able to evaporate. The obtained polymer films were further dried in a vacuum oven at 50 °C for overnight. ¹H NMR and FT-IR were used to confirm the transformation from aldehyde to imine (Table 6.2). Typical conversion rates varied between 95-100%, as could be determined from ¹H NMR analysis. Before analysis with rheology, the polyimines were hot-pressed at 150 °C into disks with a 10 mm diameter and 1.0 mm thickness.

Table 6.2 Characteristic ^{1}H NMR and FT-IR signals of aldehyde and imine groups.

R	Aldehyde (ppm)	Imine (ppm)	Aldehyde (cm^{-1})	Imine (cm^{-1})
H	10.0	8.3	1686	1641
OH	9.9	8.3	1660	1627
OMe	10.4	8.7	1670	1630

6.5.4   Stress relaxation curves

For the stress relaxation experiments, a strain of 1% was applied to the materials, and the relaxation modulus (G(t)) was followed over time (see **Chapter 2**, Section 2.5, for extensive details on the experimental setup). The experiments were performed at several different temperatures within the rubbery domain of the material. From the stress relaxation curves, the relaxation times (τ) were determined at the point where the normalised relaxation modulus (G/G_0) was 1/e ($\approx$0.37). Plotting the relaxation time as a function of the inverse temperature revealed that the stress relaxation nicely followed the Arrhenius law, which is typical for vitrimer-like materials.[6, 57] As such, we could derive kinetic activation energies (E_a) from the Arrhenius plots. The normalised stress relaxation curves and Arrhenius plots of **PI-H**, **PI-OH** and **PI-OMe** are presented in Figure 6.7 in the Results and Discussion (Section 6.2.4), and the non-normalised stress relaxation curves are shown below in Figure 6.9.
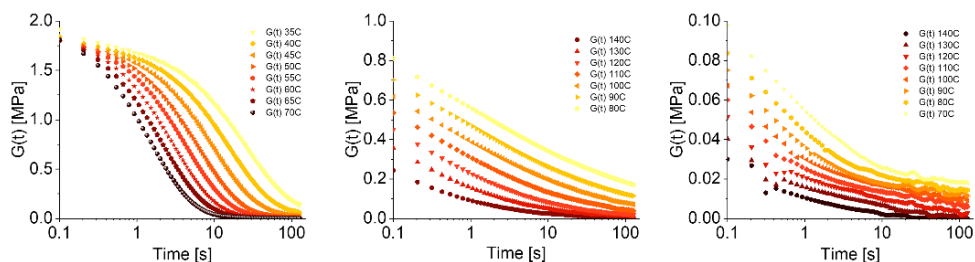
Figure 6.9 Stress relaxation curves of **PI-H** (left), **PI-OH** (middle), and **PI-OMe** (right).

6.5.5   Computational calculations

All structures were first optimised in Gaussian16 using ωB97XD/6-311+G(d,p) calculations (*in vacuo*), and subsequently optimised using the (large) QZVPP basis set, using an SMD solvent model representing chloroform. Once the optimised geometry vibrational frequency calculations were performed, the free energy was determined using internal free energy corrections.

References

1.   C. J. Kloxin and C. N. Bowman, *Chem. Soc. Rev.*, 2013, **42**, 7161-7173.
2.   C. J. Kloxin, T. F. Scott, B. J. Adzima and C. N. Bowman, *Macromolecules*, 2010, **43**, 2643-2653.
3.   Y. Jin, Z. Lei, P. Taynton, S. Huang and W. Zhang, *Matter*, 2019, **1**, 1456-1493.
4.   G. M. Scheutz, J. J. Lessard, M. B. Sims and B. S. Sumerlin, *J. Am. Chem. Soc.*, 2019, **141**, 16181-16196.
5.   F. García and M. M. J. Smulders, *J. Polym. Sci., Part A: Polym. Chem.*, 2016, **54**, 3551-3577.
6.   M. Capelot, M. M. Unterlass, F. Tournilhac and L. Leibler, *ACS Macro Lett.*, 2012, **1**, 789-792.
7.   J. M. Winne, L. Leibler and F. E. Du Prez, *Polym. Chem.*, 2019, **10**, 6091-6108.
8.   M. Guerre, C. Taplan, J. M. Winne and F. E. Du Prez, *Chem. Sci.*, 2020, **11**, 4855-4870.
9.   V. Zhang, B. Kang, J. V. Accardo and J. A. Kalow, *J. Am. Chem. Soc.*, 2022, DOI: 10.1021/jacs.2c08104.
10.   L. Li, X. Chen, K. Jin and J. M. Torkelson, *Macromolecules*, 2018, **51**, 5537-5546.
11.   A. Perego and F. Khabaz, *Macromol. Rapid Commun.*, 2022, **n/a**, 2200313.
12.   F. Van Lijsebetten, T. Debsharma, J. M. Winne and F. E. Du Prez, *Angew. Chem. Int. Ed.*, 2022, **n/a**, e202210405.
13.   W. Denissen, J. M. Winne and F. E. Du Prez, *Chem. Sci.*, 2016, **7**, 30-38.
14.   A. M. Hubbard, Y. Ren, C. R. Picu, A. Sarvestani, D. Konkolewicz, A. K. Roy, V. Varshney and D. Nepal, *ACS Appl. Polym. Mater.*, 2022, **4**, 4254-4263.
15.   S. K. Schoustra, M. H. P. de Heer Kloots, J. Posthuma, D. van Doorn, J. A. Dijksman and M. M. J. Smulders, *Macromolecules*, 2022, DOI: 10.1021/acs.macromol.2c01595, DOI: 10.1021/acs.macromol.1022c01595.
16.   J. J. Lessard, G. M. Scheutz, S. H. Sung, K. A. Lantz, T. H. Epps and B. S. Sumerlin, *J. Am. Chem. Soc.*, 2020, **142**, 283-289.
17.   J. S. A. Ishibashi, I. C. Pierce, A. B. Chang, A. Zografos, B. M. El-Zaatari, Y. Fang, S. J. Weigand, F. S. Bates and J. A. Kalow, *Macromolecules*, 2021, **54**, 3972-3986.
18.   R. W. Clarke, M. L. McGraw, B. S. Newell and E. Y. X. Chen, *Cell Rep. Phys. Sci.*, 2021, **2**, 100483.
19.   R. G. Ricarte, F. Tournilhac, M. Cloître and L. Leibler, *Macromolecules*, 2020, **53**, 1852-1866.
20.   R. G. Ricarte, F. Tournilhac and L. Leibler, *Macromolecules*, 2019, **52**, 432-443.
21.   A. Breuillac, A. Kassalias and R. Nicolaÿ, *Macromolecules*, 2019, **52**, 7102-7113.
22.   S. Kato, D. Aoki and H. Otsuka, *Polym. Chem.*, 2019, **10**, 2636-2640.
23.   X. Xu, S. Ma, S. Wang, B. Wang, H. Feng, P. Li, Y. Liu, Z. Yu and J. Zhu, *Macromol. Rapid Commun.*, 2022, **n/a**, 2100777.
24.   Z. Liu, Y. Ma, Z. Zhang, Z. Shi and J. Gao, *Langmuir*, 2022, **38**, 4812-4819.

25. X. Xu, S. Ma, H. Feng, J. Qiu, S. Wang, Z. Yu and J. Zhu, *Polym. Chem.*, 2021, **12**, 5217-5228.
26. C. Lv, J. Wang, Z. Li, K. Zhao and J. Zheng, *Compos. B. Eng.*, 2019, **177**, 107270.
27. Y. Lei, A. Zhang and Y. Lin, *Polym. Chem.*, 2021, **12**, 4052-4062.
28. F. Cuminet, D. Berne, S. Lemouzy, É. Dantras, C. Joly-Duhamel, S. Caillol, É. Leclerc and V. Ladmiral, *Polym. Chem.*, 2022, **13**, 2651-2658.
29. D. Berne, B. Quienne, S. Caillol, E. Leclerc and V. Ladmiral, *J. Mater. Chem. A*, 2022, DOI: 10.1039/D2TA05067F.
30. O. R. Cromwell, J. Chung and Z. Guan, *J. Am. Chem. Soc.*, 2015, **137**, 6492-6495.
31. F. Van Lijsebetten, J. O. Holloway, J. M. Winne and F. E. Du Prez, *Chem. Soc. Rev.*, 2020, **49**, 8425-8438.
32. M. Delahaye, J. M. Winne and F. E. Du Prez, *J. Am. Chem. Soc.*, 2019, **141**, 15277-15287.
33. C. M. Metzler, A. Cahill and D. E. Metzler, *J. Am. Chem. Soc.*, 1980, **102**, 6075-6082.
34. S. Kandambeth, D. B. Shinde, M. K. Panda, B. Lukose, T. Heine and R. Banerjee, *Angew. Chem. Int. Ed.*, 2013, **52**, 13052-13056.
35. B. P. Benke, T. Kirschbaum, J. Graf, J. H. Gross and M. Mastalerz, *Nat. Chem.*, 2022, DOI: 10.1038/s41557-022-01094-w.
36. A. Grabowska, K. Kownacki, J. Karpiuk, S. Dobrin and Ł. Kaczmarek, *Chem. Phys. Lett.*, 1997, **267**, 132-140.
37. Z. Feng, S. Jia, H. Chen and L. You, *Tetrahedron*, 2020, **76**, 131128.
38. J. Crugeiras, A. Rios, E. Riveiros and J. P. Richard, *J. Am. Chem. Soc.*, 2009, **131**, 15815-15824.
39. F. Song, Z. Li, P. Jia, M. Zhang, C. Bo, G. Feng, L. Hu and Y. Zhou, *J. Mater. Chem. A*, 2019, **7**, 13400-13410.
40. Y. Liu, Z. Yu, G. Lu, W. Chen, Z. Ye, Y. He, Z. Tang and J. Zhu, *Chem. Eng. J.*, 2023, **451**, 139053.
41. Y. Liu, Z. Tang, S. Wu and B. Guo, *ACS Macro Lett.*, 2019, **8**, 193-199.
42. S. Sun, G. Fei, X. Wang, M. Xie, Q. Guo, D. Fu, Z. Wang, H. Wang, G. Luo and H. Xia, *Chem. Eng. J.*, 2021, **412**, 128675.
43. L. Wang, Y. Liu, Y. Qiao, Y. Wang, Z. Cui, S. Zhu, F. Dong, S. Fang and A. Du, *Polym. Chem.*, 2022, **13**, 4144-4153.
44. J. Zhang, C. Zhang, F. Song, Q. Shang, Y. Hu, P. Jia, C. Liu, L. Hu, G. Zhu, J. Huang and Y. Zhou, *Chem. Eng. J.*, 2022, **429**, 131848.
45. J. Xie, L. Fan, D. Yao, F. Su, Z. Mu and Y. Zheng, *Mater. Today Chem.*, 2022, **23**, 100708.
46. S. K. Schoustra, J. A. Dijksman, H. Zuilhof and M. M. J. Smulders, *Chem. Sci.*, 2021, **12**, 293-302.
47. N. Van Herck, D. Maes, K. Unal, M. Guerre, J. M. Winne and F. E. Du Prez, *Angew. Chem. Int. Ed.*, 2020, **59**, 3609-3617.
48. B. M. El-Zaatari, J. S. A. Ishibashi and J. A. Kalow, *Polym. Chem.*, 2020, **11**, 5339-5345.

49.   L. Zhang and S. J. Rowan, *Macromolecules*, 2017, **50**, 5051-5060.
50.   C. Hansch, A. Leo and R. W. Taft, *Chem. Rev.*, 1991, **91**, 165-195.
51.   M. Hesse, H. Meier and B. Zeeh, *Spektroskopische Methoden in der organischen Chemie*, George Thieme Verlag Stuttgart, New York, 1987.
52.   C. Hansch, A. Leo, S. H. Unger, K. H. Kim, D. Nikaitani and E. J. Lien, *J. Med. Chem.*, 1973, **16**, 1207-1216.
53.   Z. Q. Lei, P. Xie, M. Z. Rong and M. Q. Zhang, *J. Mater. Chem. A*, 2015, **3**, 19662-19668.
54.   H. Zhang, D. Wang, W. Liu, P. Li, J. Liu, C. Liu, J. Zhang, N. Zhao and J. Xu, *J. Polym. Sci., Part A: Polym. Chem.*, 2017, **55**, 2011-2018.
55.   L. P. Hammett, *J. Am. Chem. Soc.*, 1937, **59**, 96-103.
56.   L. P. Hammett, *Chem. Rev.*, 1935, **17**, 125-136.
57.   D. Montarnal, M. Capelot, F. Tournilhac and L. Leibler, *Science*, 2011, **334**, 965-968.

Chapter 7

Probing the Solubility of Imine-based Covalent Adaptable Networks

Abstract

The solubility of covalent adaptable networks (CANs) has been a topic of discussion ever since their first developments. CANs are polymer materials that are covalently crosslinked *via* dynamic covalent bonds. As such, the crosslinked polymer network is not expected to show solubility, as can be seen for traditional thermosets. However, in recent years, it has become apparent that –under certain conditions– both dissociative and associative CANs can be dissolved in a good solvent. For some applications, solubility of CANs can be problematic, but (selective) solubility of CANs can also be used advantageously. For example, in recycling or post-synthetic modification of the materials. In this chapter, we provide results and insights related to the solubility of imine-based CANs. We observed that selected CANs could be fully dissolved in a good solvent without observing any dissociation of the imine bonds. For the polyimines, only in an acidic environment (partial) dissociation of imines was observed, which could be reverted to the associated state when the acid was neutralised *via* addition of base. By adjusting the network composition, we were able to either facilitate or hamper solubility of the CANs in specific solvents. We furthermore studied the size of dissolved CAN particles, and found that higher diluted states (*i.e.*, lower concentration of polymer in the solvent) resulted in a decrease in size of the dissolved particles. We also observed that decreasing the crosslinking density resulted in smaller dissolved particles. Last, we showed that we could use the solubility of the CANs as a means for chemical recycling. The CANs could be fully dissolved, without observing dissociation of imines bonds, and the solution could be cast into a new mould. By evaporation of the solvent, a newly recycled polymer film was formed that showed similar material properties as the pristine material. Based on our results, we further comment on the wider implications of our work in relation to the question of solubility of CANs.

7.1   Introduction

Thermosets are widely applied materials because their covalently crosslinked polymer structure enables superior strength and toughness when compared to linear or branched thermoplastics. The permanent covalent network structure of thermosets, however, comes with certain drawbacks. Probably the most prominent drawback is that recycling and reprocessing are no longer possible once the material is made. Once the polymer network is set, it is permanent. A solution to this problem was presented by the development of covalent adaptable networks (CANs).[1, 2] CANs are thermoset polymers by nature, as they have the same covalently crosslinked network structure, although with the exception that dynamic covalent bonds are incorporated in the network. These dynamic covalent bonds can perform bond exchange reactions,[3] which effectively means that polymer chains within the network can be exchanged to create a molecular flow within the material.[4, 5] In order to activate this flow in the material, the bond exchange requires some sort of activation or stimulus. This can, for example, be achieved by heating and/or with a catalyst,[6] which can even be internal.[7-9] A break-through for these dynamic polymer systems was when Leibler and co-workers (2011) documented on polymer networks that exchange bonds *via* transesterification reactions, showing Arrhenius type behaviour in their temperature dependence of the viscosity, similar to vitreous silica, and therefore coining the term *vitrimer*.[4] Since then, many researchers have expanded the field, and different types of dynamic covalent bonds have been studied for their inclusion in CANs and vitrimer-like materials. Some promising chemistries include dioxaborolane exchange,[10-13] transesterifications,[4, 6, 14-16] 1,2,3-triazolium[17, 18] or anilinium salts,[19, 20] sulphur-based exchange such as from disulphides and thioesters,[21-27] or amine-based exchange such as from guanidines,[28] vinylogous urethanes,[29-32] diketoenamines,[33, 34] and imines.[35-39]

7.1.1   Solvent resistance *versus* solubility

The covalently crosslinked network structure of thermosets is what generally protects these materials against the influence of solvents. Many thermosets are still able to swell in good solvents, but fully dissolving them is inherently not possible. Current efforts have, however, been made regarding controlled degradation of thermosets by means of solvolysis.[40] For CANs, the effects of solvent resistance, swelling and solubility are not as trivial. First, CANs tend to swell more than classical thermosets as bond exchange reactions and cleavage can take place during swelling.[41-43] Here, the mechanism of the bond exchange reaction is crucial. In general, we can distinguish each exchange reaction to be either dissociative or associative.[44, 45] For the dissociative exchange mechanism (elimination/addition), a bond is first broken before a new bond is formed, leading to a temporary decrease in crosslinking

density. For the associative mechanism (addition/elimination) a new bond is formed before the old bond breaks, leading to a temporary increase in crosslinking. From this perspective it could be postulated that the dissociative mechanism would increase the possibility to dissolve respective CANs (when heated),[46] as the network could be broken down back to soluble monomers or oligomers. Meanwhile, this would not be the case for CANs relying on associative bond exchange as the network would never break down.[45] As such, associative networks (vitrimers) were initially expected to never fully dissolve in any solvent.[47] However, there has recently been debate on the solubility of both dissociative and associative CANs,[48] which will be addressed below.

Normally, initial exposure of a freshly made thermosetting material – or vitrimer for that matter – to a good solvent would always result in a small soluble fraction containing either unreacted monomers and/or small fragments or chains that were not connected to the rest of the network structure (*e.g.*, small loops or terminated oligomers). However, the main polymer network would not dissolve and only swell to some degree. With a so-called theoretical "patchy particle model", Smallenburg, Leibler and Sciortino (2013) were able to further characterise this swelling behaviour for vitrimer materials.[49] Their model suggested that addition of a good solvent to a vitrimer system would favour the formation of a dilute phase consisting of small clusters. However, their calculations demonstrated that the vitrimer would never fully dissolve, as was initially proposed on the basis of experimental results.[4] Instead they noted that only monomers and smaller clusters escape into the solvent, while the majority of the bulk network remains as a whole, emphasising that separation into dissolved or non-dissolved state is driven purely by entropy. Here, it is important to note that bond exchange reactions enable that both small clusters can separate from a bigger whole, while also small clusters may assemble and recombine *via* bond exchange reactions to other clusters (Figure 7.1). In theory, this can be seen as an equilibrium reaction.
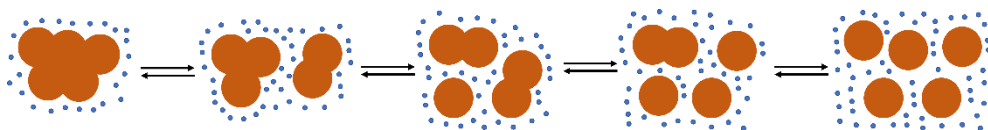
Figure 7.1 Schematic representation of the continues merging and separation/splitting of dynamic polymer clusters (pictured in orange) facilitated by solvent (pictures as blue dots). Note that both merging and separation progress *via* dynamic covalent bond exchange reactions.

Simulations from the patchy particle model, however, showed that assembly of smaller particles to a bigger aggregate is thermodynamically favourable,[49] which is in favour of the postulate against full solubility of vitrimers. However, although the theoretical model shows

good coherence to the description of vitrimer-like behaviour,[4, 6, 14] some questions regarding the full extent of swelling and solubility remain. Some understudied parameters are, for example, the type of solvent (*e.g.*, polar/apolar, protic/aprotic), the crosslinking density of the polymer network, the concentration of dynamic covalent bonds, or kinetics of the dynamic covalent bonds.

First, different solvents may have different interactions to the materials, which could apply to both the chemical nature of the network, and to the dynamics of the bond exchange reactions. Second, by addition of large amounts of solvents, one could prevent the likeliness of small cluster to meet and reassemble into bigger clusters (Figure 1). As a consequence, this would result in a shift in the equilibrium from non-soluble bulk to soluble small particles. This could, in theory, be extended to the point at which even the largest remaining mass would be considered as a dissolved particle. Based on the size (distribution) of the particles in the solvent one could, however, still question whether to call the solvent-polymer mixture either a solution, colloid or suspension. It is also important to note that transparency of the mixture does not always mean full dissolution.[50, 51] Typically, a mixture is considered a solution when the dissolved particles are smaller than 1 nm, a colloid when particle sizes are in between 1–1000 nm, and a suspension when particle sizes are bigger than 1000 nm.[52] For this reason, true solutions do not scatter light as the particles are too small, whereas colloids do scatter light. The scattering of visible light by colloidal particles is also known as the Tyndall effect.

Since CANs combine properties of both classical thermosets and thermoplastics, it is always good to compare the dynamics of both systems when describing the behaviour of a CAN. As such, the principle of solvent diffusion, chain disentanglement and diffusion of disentangled chains in linear polymers,[53] may apply similarly to CANs. For example, the splitting off of smaller particles as a result of bond exchange in CANs shows similarities to disentanglement or unfolding processes in linear polymers in which weaker bonds (*e.g.*, hydrogen bonds or Van der Waals forces) are broken.[53]

The influence of temperature on the solubility of vitrimers (associative CANs) is generally not considered to be of mayor concern. Even though higher temperature increases the bond exchange kinetics, the vitrimer network would never dissociate and remains intact.[54] However, as a result of more efficient topological rearrangements at higher temperatures, higher swelling ratios can be expected.[47] On the other hand, CANs relying on dissociative bond exchange are expected to show a better solubility at elevated temperatures as a result of full network dissociation, driven by entropy and dilution.[20] A recent study by Kalow and co-workers did, however, also show a temperature-dependent solubility of block copolymer

vitrimers relying on associative vinylogous urethane exchange.[55] Their results showed that the vitrimers remained largely intact at lower temperatures, but when heated to 110 °C in a sealed vessel swelling and fragmentation was observed in THF. No quantitative degradation occurred, but rather nanoscale particles in the sol were observed with DLS. This observation of dissolution at higher temperatures thus suggests that stimulating faster bond exchange could realise the dissolution of vitrimers.

Other factors affecting solubility apply to the chemical nature and composition of the materials. For example, Tellers and co-workers noticed a trend of poorer solubility at increasing crosslinking densities for vinylogous urethane CANs.[56] Where highly crosslinked materials showed to be only partially soluble, leaving few gel-like residues, the lower crosslinked materials were able to fully dissolve within several hours. This result was expected as the lower crosslinking density of the material facilitates easier penetration of the solvent into the network.[42, 57] Since the vinylogous urethane is considered an associative dynamic bond,[31, 45] the results of both Tellers' and Kalow's studies thus show that associative CANs can be dissolved.

7.1.2   Solvent-assisted dissolution

An existing technique to fully dissolve both associative and dissociative based CANs is by solvent-assisted dissolution, which has been applied in several studies as a means of chemical recycling.[58-63] The solvent-assisted dissolution works somewhat different than simple dissolution, as here the polymer network is essentially depolymerised into small molecules or oligomers. A schematic image in the case of an ester-based CANs is pictured in Figure 7.2 below. A specific solvent is chosen (here ethylene glycol) that can perform bond exchange with the dynamic bonds in the polymer.[48] As a result, the polymer network is broken down into smaller end-capped pieces. To reverse this depolymerisation (repolymerisation) the volatile solvent can be evaporated again, and as a consequence the network structure will be reformed. Such solvent-assisted dissolution has already been applied for various types of CANs. For example, ester-based CANs could be dissolved using alcohols as solvent,[64-66] disulphide-based CANs could be dissolved by using thiols as the solvent,[67, 68] and imine-based CANs could be dissolved using primary amines as the solvent.[37, 69, 70] As mentioned before though, this technique of solvent-assisted dissolution does, by definition, not dissolve the actual polymer, but rather cuts it into small soluble end-capped pieces or monomers. It could therefore perhaps better be described as a practise of degradation or depolymerisation.[71]
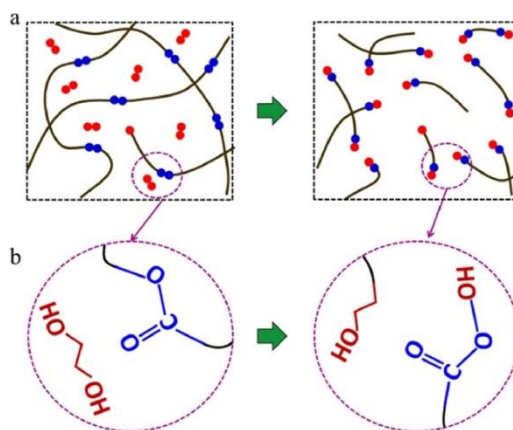
Figure 7.2 Schematic representation of solvent assisted dissolution of ester-based CANs. The solvent (ethylene glycol) gradually breaks down the polymer network in smaller soluble parts. Image adapted from Yu *et al*. **2017**.[48]

7.1.3   Dissolution of polyimine CANs

In this thesis, research has focussed on imine-based CANs. An interesting feature of imines is that they can perform both associative and dissociative bond exchange.[72-74] Three ways of imine exchange are considered: hydrolysis, transimination, and metathesis (Figure 7.3). The hydrolysis (and reformation *via* condensation) has a dissociative mechanism (Figure 7.3A), whereas the transimination (Figure 7.3B) and metathesis (Figure 7.3C) are considered associative. The underlying mechanisms of the imine exchange have been studied thoroughly for a long time,[75-80] however, a full understanding, especially regarding the metathesis reaction,[81, 82] is still a topic of discussion and requires further investigations.[73]
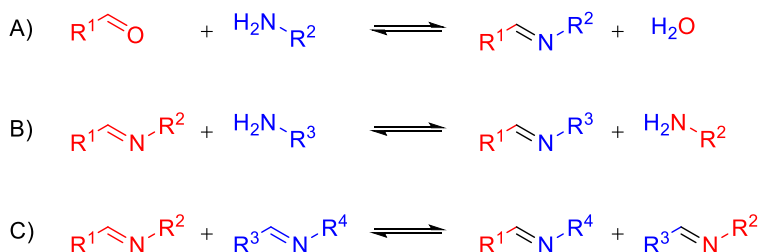
Figure 7.3 Overview of bond exchange mechanisms of imines: A) condensation and hydrolysis of aldehyde and amine, B) transimination of imine and amine, and C) imine metathesis of different imines.

Even though imines are able to perform bond exchange *via* both dissociative and associative mechanisms, methods have been developed to push the exchange to either one of the two. For example, by increasing the stability of the imine bond (*e.g.*, *via* aromatic conjugation) the dissociative hydrolysis reaction can be suppressed (see **Chapter 2**).[35] Conversely, the availability of acidic protons can stimulate the dissociative exchange mechanism *via* hydrolysis and condensation.

The mode of bond exchange of imines is important for the consideration of solubility of polyimine CANs. Imines networks can be dissolved by all three exchange pathways. First, aqueous acidic environments are known to promote the hydrolysis of imines, leading to depolymerisation into soluble particles or monomers.[83] Second, *via* means of solvent-assisted solubility (see Figure 7.2), primary amines can be added that would perform transimination.[37, 69, 70] Third, small imine-containing molecules can be added that could perform metathesis in order to break the network down into smaller end-capped pieces, although this method is not commonly used.

More importantly, however, recent work pointed out that polyimine CANs can be dissolved in good solvents without the addition of acid, primary amines or imines.[84, 85] For example, Liu and co-workers noticed good solubility of polyimines in either THF or DMSO, depending on the network structure of the polyimines.[84] Similarly, Fang and co-workers observed solubility of polyimine CANs in chloroform, for which a Tyndall effect was noticed when exposed to red laser light.[85] Potential hydrolysis of imines could easily be ruled out *via* NMR analysis as imine signals remained and aldehyde signals were not observed, indicating that no net dissociation occurred. Dynamic light scattering (DLS) was applied to reveal that dissolved nanoparticles with sizes of 2.0 and 11.7 nm were formed, for which the sizes were related to the different types of used monomers. They speculated that the fast imine exchange enables efficient rearrangement from polymer network into soluble nanoparticles.

In this work, we will further address the solubility of imine-based CANs. We will look further into what factors determine the solubility, and try to gain insight in what happens when the CANs are being dissolved. We will look into the nature of the polymer network to study whether specific linkers could cause either enhanced or decreased solubility in specific solvents. Furthermore, we address what effects the network composition has on the size of the soluble polymer particles. Last, we test the potential of chemical recycling of the CANs *via* dissolution.

7.2   Results and discussion

To study the solubility of polyimine CANs, we started with the preparation of a polymer network from terephthalaldehyde (**TA**), 4,7,10-trioxa-1,13-tridecanediamine (**TOTDDA**) and tris(2-aminoethyl)amine (**TREN**) (Figure 7.5). A stoichiometric amount of aldehyde to amine groups was used, where 30% of amines were from **TREN** and 70% from **TOTDDA**, hence the abbreviation **PI-30** was used. The synthesis was performed according to the methods described in **Chapter 2**.
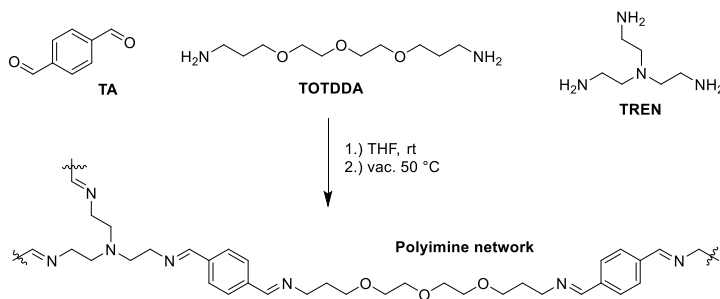
Figure 7.5 Reaction scheme for the polymerisation of polyimine networks from **TA**, **TOTDDA** and **TREN**.

7.2.1   Solubility of polyimines

The solubility of the polyimine material was studied for several solvents that are commonly used to dissolve organic molecules (see Figure 7.6). The solubility was determined by dispersing 100 mg of polymer in 10 mL solvent and leaving it for 10 days at room temperature in a closed vial. Then, the liquid and solid phases were separated and dried to determine the dissolved and non-dissolved fractions. The dissolved fractions in each solvent are shown in Figure 7.6, and are ordered from most polar (left) to most apolar (right) solvent. Most solvents offered relatively poor solubility towards the polyimine material, and few showed reasonable solubility. Chloroform was the only solvent that was able to fully dissolve all material. MeOH, THF and EtOAc still had a reasonably high solubility (>50%). Interestingly, the solubility did not seem to be polarity dependent, nor was there a clear trend between protic and aprotic solvents. This was rather unexpected, as other studies have highlighted correlations between imine exchange and solvent polarity,[86] as well as network polarity (see **Chapter 3**).[36] The dynamics of the bond exchange might therefore not directly correlate to better solubility, but instead the network structure may play a larger part here, as the nature of the polymer network may affect the penetration of specific solvents.[87] Also note that long soaking times were required to dissolve all material. Even in

chloroform, several hours were required before full solubility was observed. This indicates that the penetration of solvent molecules into the polymer network is a slow process. It was observed that material first underwent swelling, and only afterwards the actual dissolution process started, rather than the material being broken down from the outside inwards.
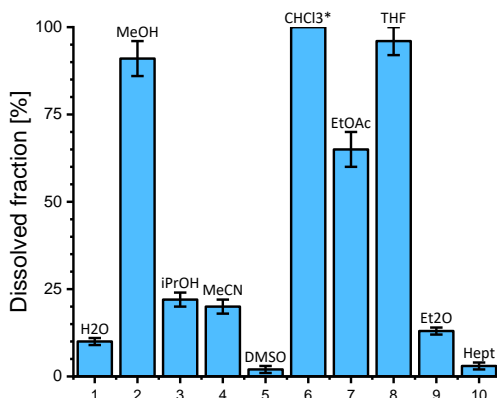
Figure 7.6 Dissolved fractions of **PI-30** in several common solvents, determined by the addition of 100 mg of polymer material to 10 mL of the respective solvent (performed *in triplo*). Only for CHCl₃ full solubility (100%) was observed. As such, it does not contain an error margin (indicated by the *). Solvents were ordered from most polar (left) to apolar (right).

Next up, five additional polyimine networks were prepared with diamines of similar length, but different chemical nature (Figure 7.7A). The aldehyde (**TA**) and triamine (**TREN**) monomers were held constant for all materials. We hypothesised that chemical differences in the chains of the network structure would affect the solubility of the polyimine materials, and with the chosen variations we envisioned to gain a better understand of which chemical groups would facility better solubility or solvent resistance. We expected the effects of the different diamine linkers to be mostly minimal, as their chemical structures were relatively similar. Only the diethylenetriamine (**DETA**) is expected to potentially affect the imine kinetics, as a result of the polarity of the chain or the potential to form hydrogen bonds with the imines.[36, 39] A similar solubility test as before was performed for all five polyimine materials, using chloroform, methanol, THF and EtOAc as solvents. From the results (Figure 7.7B) some clear conclusions could be drawn by relating solubility to the chemical structure of the diamine chains. First was observed that the xylylene (**Xyl**) groups showed significantly higher solvent resistance than any of the other materials for each of the tested solvent. This can be expected, as xylylene groups have been applied in other materials to create though networks.[70, 88] Next, by comparing the **Cad** and **MeP** materials, we observed

that branching of the diamine structure significantly improved solubility of the materials for all tested solvents. This observation could be explained as branching of polymer chains generally results in a more flexible network and loss of crystallinity,[89] which could facilitate better penetration of solvent molecules within the polymer. A similar effect was also observed for the **Cy** material, as the cyclohexane structure would result in more amorphous materials compared to the **Cad** material. Last, we noticed significantly improved solubility of **DETA** in methanol, which is likely related to the hydrogen-bonding potential of the secondary amine groups with the solvent,[39] although we cannot rule out the effect of the secondary amine on the imine exchange kinetics.[36]
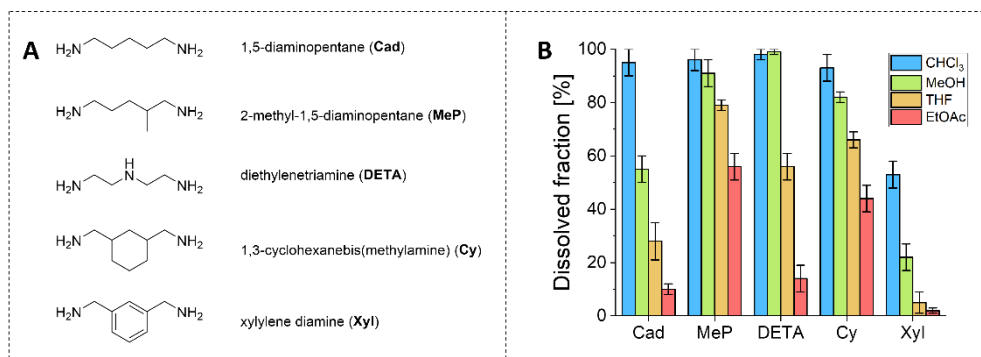
Figure 7.7 A) Chemical structures of the different diamine monomers, including full name and abbreviation. B) dissolved fractions of the polyimine materials synthesised from each of the pictured diamines (together with **TA** and **TREN**, with a crosslinking of 30%).

Given the observations from the solubility tests (see Figure 7.7), some speculations can be made regarding the mechanisms involved in the dissolution. We observed that penetration of solvent molecules into the network is essential for the dissolution. However, it remains challenging to study what happens once the material is in its swollen state. We hypothesised that when solvent molecules penetrate the network structure, the network is being stretched outwards, firstly resulting in a swollen state. In order to compensate this outwards force, bond exchange reactions could cause the network to rearrange, similar to stress relaxation mechanisms. These rearrangements could, in turn, cause rupture of (small) parts of the network. Once these small parts are released from the network, they can diffuse into the solvent. Over time, when more of these small particles separate from the bulk into the solvent, the material is essentially being dissolved. The exchange of polymer chains can, in theory, proceed via associative exchange. However, in a (very) short frame in time, the imines could potentially also dissociate into aldehyde and amine (given that water is present

in the system), and immediately react again on a different location. This was, however, not observable with *e.g.* NMR, as the time interval in which this mechanism occurs would be extremely short.

7.2.2   Solubility of V-Ureas

To transfer the observations made for our polyimine CANs to other CANs, a similar solubility experiment was performed for vinylogous urea (V-Urea) networks. V-Urea networks have a similar synthetic design as imines, but during the synthesis the aldehyde is replaced by an acetoamide. The V-Urea networks perform bond exchange *via* transamination, which occurs *via* an associative mechanism.[90] Note, however, that for V-Ureas an excess of amine is required to facilitate the transimination reaction, which is not the case for imines, as they are generally synthesised from stoichiometric amounts of aldehyde and amine. For our synthesis of V-Urea networks, the same amine monomers were used as for the imine networks. They were then reacted with ethylenediamine-*N*-*N'*-bis(acetamide) (**EDABA**) to construct V-Urea networks (Figure 7.8A). The synthetic procedure was similar as to the polyimines, except DMF was used as the solvent, and a temperature of 80 °C was required (see Section 2.5 for further experimental details).
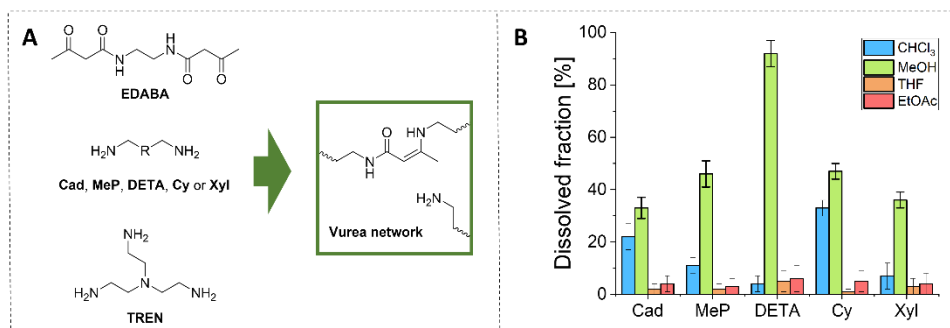
Figure 7.8 A) Synthetic overview for the preparation of V-Urea networks from **EDABA**, **TREN** and a variable diamine monomer. B) Dissolved fractions for the different V-Urea networks in several common organic solvents.

After successful synthesis of the V-Urea networks, they were soaked in either chloroform, MeOH, THF or EtOAc using the same procedure as before for the imine CANs. The dissolved fractions were again determined (Figure 7.8B). We observed that generally the V-Urea networks showed greater solvent resistance than the imines. We do, however, clearly see that dissolution is observed in MeOH. Particularly the V-Urea networks with **DETA** as diamine showed very good solubility (~90% dissolved fraction). By adding more solvent, all

material eventually dissolved. In chloroform, we also observed some solubility for **Cad** and **Cy** V-Ureas, but all other tested solvents and materials showed high solvent resistance (<10% dissolved fractions). Likely, the hydrogen bonding potential of MeOH might thus facilitate better solubility of the V-Urea networks, whereas for the other, non-protic solvents this is lacking. Specifically for **DETA**, the extra secondary amine in the chain facilitates even more hydrogen bonding potential with the solvent, resulting in enhanced solubility as was also seen for the polyimines. Apart from the network effects, the hydrogen bonding potential of MeOH with the V-Ureas might also cause enhanced bond exchange, resulting in better solubility of the V-Ureas in MeOH.

In short, although we do observe generally good solvent resistance of the associative V-Urea networks, when choosing a specific solvent (this time MeOH), we can facilitate solubility of the material. As such, when a CAN exchanges *via* an associative mechanism, this does not automatically imply that the CAN is insoluble. And although the mechanism of the bond exchange may play an important role in the possibility to dissolve a CAN, the nature of the polymer network also significantly affects the solubility.

7.2.3   NMR analysis of dissolved polyimine CANs

When dissolving the polyimine CANs, it was necessary to make sure that we indeed dissolved polymers, and not dissociate the polymers back to monomers. To check if indeed the polymers stay intact and do not dissociate, NMR analysis was used. First, we examined the **PI-30** material discussed before (see Figure 7.5). To check if imines would hydrolyse upon dissolution, a small amount of **PI-30** was allowed to dissolve in CDCl$_3$ in an NMR tube, and ^{1}H NMR spectra were recorded. The ^{1}H NMR spectra of the dissolved polymer were then analysed and compared to all individual starting materials (Figure 7.9). The NMR spectra showed that the imines (8.1–8.4 ppm) stayed intact and no dissociation back to aldehydes (10.1 ppm) and amines (1.0-1.5 ppm) was observed. This observation, in combination with the fact that the network does dissolve, implies that the polymer network reorganises into small soluble particles such as loops or vesicles,[91] rather than dissociating back to monomers. This is an important result, as it shows that soluble polymeric structures can be formed *via* bond exchange of the CANs without degrading the material back to monomers. ^{1}H NMR spectra of the **Cad**, **MeP**, **DETA**, **Cy** and **Xyl** imines were also measured, which all showed that imine groups stayed intact, and no dissociation back to aldehyde had occurred during the dissolution (see Section 7.5.4).
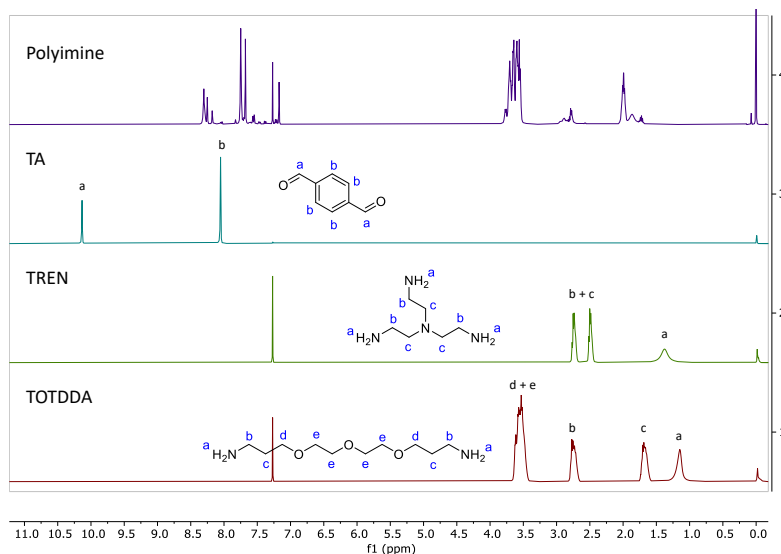
Figure 7.9 From top to bottom: stacked ^{1}H NMR spectra of the dissolved **PI-30** (after immersion for 24 hours in CDCl$_3$) (purple), **TA** (blue), **TREN** (green), and **TOTDDA** (red). All spectra were measured in CDCl$_3$ (solvent signal at 7.26 ppm) with TMS as a reference (signal at 0.00 ppm).

Dissociation of imines can, however, be achieved by addition of acid. To test this for **PI-30**, acetic acid was added to a solution of the dissolved polymer in CDCl$_3$. We observed that after the addition of acid, a partial dissociation of imines was noticed (see Section 7.5.5). An equilibrium between imine and aldehyde was observed, which shifted more towards the dissociated products when the concentration of acid was increased. Neutralising the solution by addition of triethylamine, however, showed to fully push the equilibrium back towards the imine formation (see Section 7.5.5).

7.2.4   Size of dissolved particles

To further study how the dissolved polyimines behaved in solution, dynamic light scattering (DLS) was used to determine the size of the dissolved polyimine particles. Three solutions of **PI30** were prepared with concentrations of 0.1, 1.0 and 10 g/L in chloroform. In addition, a new polyimine material was synthesised, for which the **TOTDDA** monomer was replaced with a longer poly(ethylene glycol) chain with an M$_w$ ~ 1500 g/mol. This material was named **PEGI30**. The same synthetic procedure as for **PI-30** was used (see Section 7.5) As a result of the much longer PEG chain, the crosslinking density of the material is much lower. After the synthesis of this material, also three solutions were prepared with concentrations of 0.1,

1.0 and 10 g/L in chloroform. All solutions were kept at room temperature for 4 days before they were analysed with DLS to make sure that a stable size distribution was obtained. The sizes of dissolved particles for **PI30** (Figure 7.10) showed a clear trend for which a lower concentration result in smaller particles sizes. For the **PEGI30** material, the difference between 10 and 1 g/L solutions was relatively small, but at the lowest concentration of 0.1 g/L the size of the dissolved particles decreased more clearly. The results of smaller particle sizes at lower concentrations are in favour of the hypothesis that when diluting (*i.e.*, ratio of polymer to solvent decreases) the chance of dissolved particles meeting and reassociating is smaller. As such, the equilibrium shown in Figure 1 in the introduction is pushed to the right. From the DLS results it was also observed that **PEGI30** showed smaller particles sizes compared to **PI30**, which implies that a lower crosslinking density results in smaller particles sizes. The most probable cause for this event is that a lower crosslinking density facilitates easier penetration of solvent molecules into the polymer,[56] and as such facilitates easier dissociation of large polymer particles into smaller ones. It should however also be noted that by using the longer PEG chains compared to the shorter chains, that the relative amount of dynamic covalent imine groups in the material decreases. As such, fewer bond exchange reactions might take place, affecting the overall dynamic behaviour.
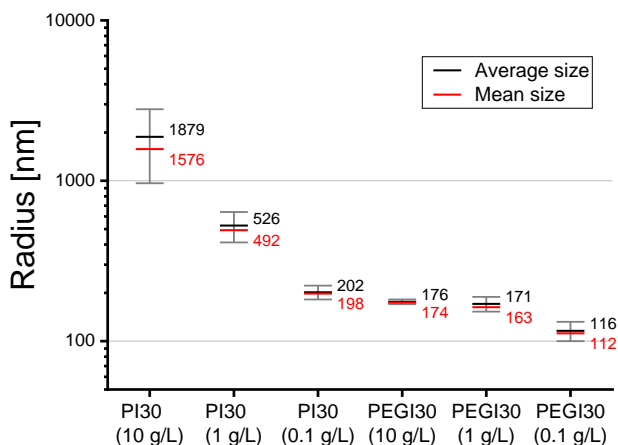
Figure 7.10 Size of dissolved polyimine particles for **PI30** and **PEGI30** for concentration of 10, 1 and 0.1 g/L in chloroform. The average hydrodynamic radius is given in black, and the mean is given in red.

The same DLS experiment was then also performed for the polyimines synthesised from different pentane diamine structures, as presented in Figure 7.7A, with a concentration of 1 g/L. These results showed that the dissolved particles of **Cad**, **MeP** and **DETA** had similar

sizes with a hydrodynamic radius around 50 μm (Figure 7.11). Larger particles were observed for **Cy** (67 μm) and **Xyl** (104 μm). It is likely that the bulkiness of the diamine chain has an effect here, as the chain lengths are relatively similar, but the bulkiness is not: **Cad**, **MeP** and **DETA** have similar bulkiness of the chains, but **Cy** and **Xyl** contain larger cyclohexane and benzene rings, respectively. The variations in size of the dissolved particles might thus not per se be related to the difference in solubility for these specific cases, but rather in terms of size of the monomeric units within the polymer. Together with the previously observed results from **PI30** and **PEGI30** (Figure 7.10), we thus expect that concentration, crosslinking density and bulkiness of the monomer units are the most important factors that determine the size of the dissolved particles.
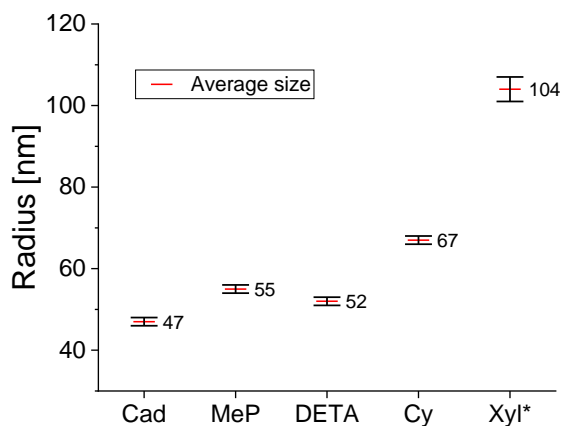
Figure 7.11 Hydrodynamic radius of dissolved polyimines synthesised from different pentane diamines. All measurements were performed in chloroform at a concentration of 1 g/L. *Since the **Xyl** material did not fully dissolve and the remaining mass remained on the bottom of the flask, only the dissolved particles were observed.

7.2.5 Recycling *via* dissolution

An important application for the solubility of CANs can be found in chemical recycling. As such, recycling of **PI30** materials *via* dissolution was investigated. First, pristine materials were synthesised and analysed. The materials were then cut into pieces and fully dissolved in THF. Evaporation of the solvent then resulted in the formation of a new recycled polymer film. The newly obtained film was analysed and compared to the pristine material (see Section 7.5.6 for further experimental details). From temperature sweep experiments (see Figure 7.19 in Section 7.5.6), we concluded that the elastic (G') and viscous (G'') moduli of pristine and recycled materials showed comparable values over a temperature range from 20–100 °C. In addition, the crossover temperature (T_{cross}), where G' and G'' cross,[92, 93] was

comparable for pristine (78 ± 2 °C) and recycled (74 ± 2 °C) materials. Frequency sweep experiments (see Figure 7.19 in Section 7.5.6) also showed that both pristine and recycled materials reached a constant plateau in G', indicating that both materials showed a constant crosslinking density at elevated temperatures, even above the T_{cross}.

The results from the dissolution-based recycling show that the materials do not significantly suffer from the dissolution. However, thermomechanical reprocessing of CANs is in most cases still preferred, as it generally requires less effort and prevents the use of (large amounts of) solvent. In cases where the requirement of high temperatures causes problems to the materials, however, recycling *via* dissolution can offer a way out.[9] Alternatively, "wetting" of the materials can be applied to increase the efficiency of vitrimeric welding.[94] This wetting can serve as an energy efficient method to lower the amount of required energy for thermal reprocessing, and can be a more sustainable alternative, especially when low-toxicity and greener solvents (*e.g.*, bio-ethanol) can be used. The varying solubility of specific CANs can also prove useful in solubility-based separation processes of different plastics and other contaminants in waste streams.

Last, we would also like to discuss the potential to perform post-synthetic modifications to the CANs while in either the dissolved or swollen state. In previous work, we observed that phase separation of polyimine CANs could be reverted by swelling the phase-separated materials in solvent, to which additional monomers were added (see **Chapter 3**). The new monomers were able to penetrate the dynamic network, by which the overall chemical nature of the network could be altered. In another example, metal-coordination of the dynamic covalent imines was performed *via* dissolution of polyimine networks, to which metal salts were then added to significantly enhance the material properties of the CANs (see **Chapter 5**). From the perspective of durability, it can also be more feasible to enhance the material properties of old, weak or damaged materials *via* this dissolution and addition of new components, rather than simply making an entirely new material while discarding the old one. However, since many applications still require materials with high solvent-resistance, tuning CANs to only (selectively) dissolve in a specific solvent while keeping high resistance towards other solvents may be required.

7.3   Conclusions

As CANs are crosslinked polymer structures, they were initially not expected to be soluble in organic solvents. However, bond exchange reactions within the CAN enable the material to swell and rupture to eventually rearrange into smaller soluble particles. Depending on

the chemical composition of the polymer network and the dynamics of the bond exchange reaction, the penetration of solvent molecules into the polymer network and splitting off soluble parts can be either suppressed or stimulated. In addition, adjustments to the network structure may affect how the dissolved CAN particles behave in solution. We observed that higher crosslinked materials formed larger (but still soluble) particles when dissolved in a good solvent. We also observed that the size of the dissolved particles decreased when the concentration of dissolved CAN particles was reduced (*i.e.*, a higher solvent/polymer ratio). Although good solvent resistance might be required for some applications, the (selective) solubility of CANs can also be used advantageously. For example, in chemical recycling or post-synthetic functionalisation of the materials.

7.4   Acknowledgements

7.5   Supporting Information

For the used materials and methods, see also **Chapter 2**, Section 2.5.

7.5.1   Synthesis of polyimine networks

All polyimine networks were prepared by dissolving terephthalaldehyde (**TA**, 4.00 mmol), tris(2-aminoethyl)amine (**TREN**, 0.80 mmol) and either of the specified diamines (2.80 mmol) in a small amount of THF (typically ~5 mL per gram material). The solution was briefly mixed until a homogenous mixture was obtained. It was then poured into a glass petri dish, which was left for overnight. Most of the solvent evaporated to air, and a wet polymer film resulted. The film was further dried in a vacuum oven at 50 °C for at least one day.

7.5.2   Synthesis of V-Urea networks

Ethylenediamine-*N*-*N'*-bis(acetamide) (**EDABA**, 4.00 mmol), **TREN** (0.80 mmol) and either of the specified diamines (2.80 mol) were mixed together in 10 mL DMF. The mixture was carefully heated with a heat gun, while swirling the flask, to dissolve all material. Then, the

mixture was poured into a petri dish, which was placed in an oven at 80 °C for at least 24 hours. The obtained polymers were further dried in a vacuum oven at 50 °C for overnight.

7.5.3   NMR analysis of acidic solution of **PI-30**

Solutions of **PI-30** were prepared by dissolving **PI-30** (5 mg) in 0.5 mL CDCl$_3$. When the polymer was fully dissolved 2.9 µL (0.050 mmol; for 0.1 M solution) or 29 µL (0.50 mmol; for 1.0 M solution) acetic acid was added to the mixture. The solutions were briefly shaken and several ^{1}H NMR spectra were recorded up to 30 min after addition to check whether equilibrium had been reached. The imine (8.2–8.5 ppm) and aldehyde (10.0–10.2 ppm) regions were integrated to determine the ratio of imine : aldehyde.

Next, to neutralise the 1.0M acetic acid solution an equimolar amount of triethylamine (70 µL, 0.50 mmol) was added. The mixture was briefly shaken and ^{1}H NMR spectra were recorded every 10 minutes. After 30 mins only trace (<1%) signal of aldehyde was observed, which indicated that the equilibrium was again fully pushed towards the imines.

7.5.4   NMR spectra of dissolved polyimines

The ^{1}H NMR spectra of polyimines networks with different diamine structures are presented below.
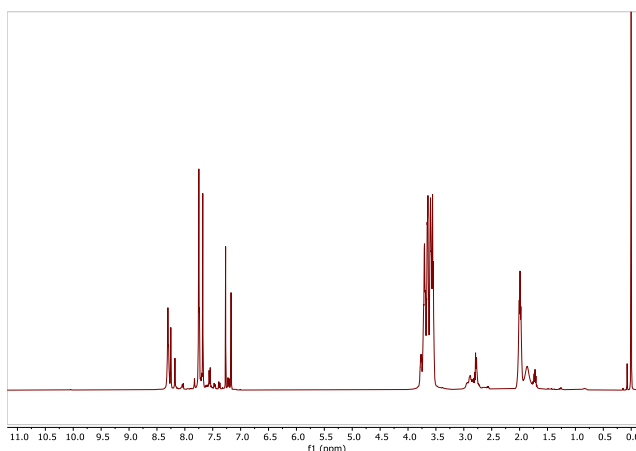
Figure 7.12 Full ^{1}H NMR spectrum of **PI-30** in CDCl$_3$. A close inspection of the imine region of the spectrum (8.1-8.4 ppm) revealed 4 different imine signals (that to some degree overlap). This can be explained as the **TA** monomer can form an imine on both aldehyde ends, which can either be formed with two molecules of **TOTDDA** or **TREN**, or with one of each. In the last case, both ends have a different chemical nature, bringing the total to 4 different imine signals. A similar splitting of signals was also noticed for the hydrogens on the benzene ring. The assigned chemicals shifts of imines from the formation of **TA** with either amines were as follows: **TREN** on both ends (8.18 ppm), **TREN** and **TOTDDA** each once (8.25 and 8.29 ppm), and **TOTDDA** on both ends (8.30 ppm).

Figure 7.13 ^{1}H NMR spectrum of **Cad30** in CDCl$_3$.
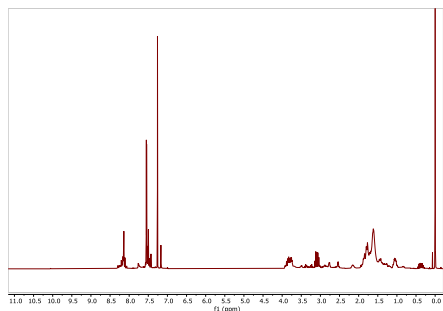
Figure 7.16 ^{1}H NMR spectrum of **Cy30** in CDCl$_3$.

Figure 7.14 ^{1}H NMR spectrum of **MeP30** in CDCl$_3$.
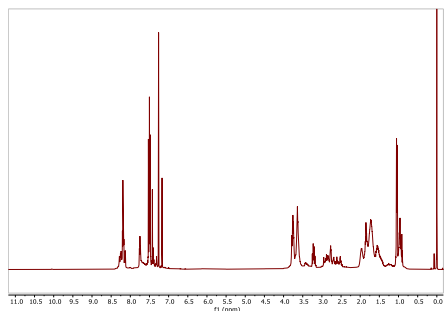
Figure 7.17 ^{1}H NMR spectrum of **Xyl30** in CDCl$_3$. Note the poor signal intensity due to the very low solubility. Signals originating from traces of water (1.56 ppm) and THF (3.76 ppm, 1.85 ppm) are therefore also overexpressed in the spectrum.
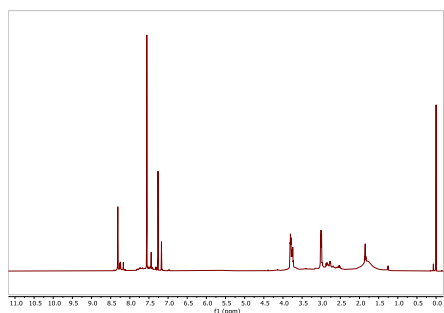
Figure 7.15 ^{1}H NMR spectrum of **DETA30** in CDCl$_3$.

7.5.5   Reversible dissociation of dissolved polyimines by addition of acid

The dissociation of imines is known to be catalysed by acid, and as such we investigated if the polyimines would hydrolyse in more acidic environments. When decreasing the pH to stronger acidic environments we noticed that the imines started to partially dissociate to form a new equilibrium between imine and aldehyde and amine (Figure 7.18). Solutions were prepared of 0.1 M and 1.0 M acetic acid in CDCl$_3$, to which the polyimine material was added (see Section 7.5.3). ^{1}H NMR analysis showed that an equilibrium between imines and hydrolysed products formed instantly, where a higher concentration of acid resulted in the equilibrium being shifted more towards the dissociated products. These results show that in acidic conditions the imines do not fully dissociate, but instead the equilibrium between dissociation and formation of imines is shifted. We then also investigated if we could push the equilibrium back towards formation of the imines. For this, an equimolar amount of the base triethylamine was added (see Section 7.5.3), and indeed the equilibrium was pushed back towards formation of the imines, as only trace amounts (<1%) of aldehyde remained.
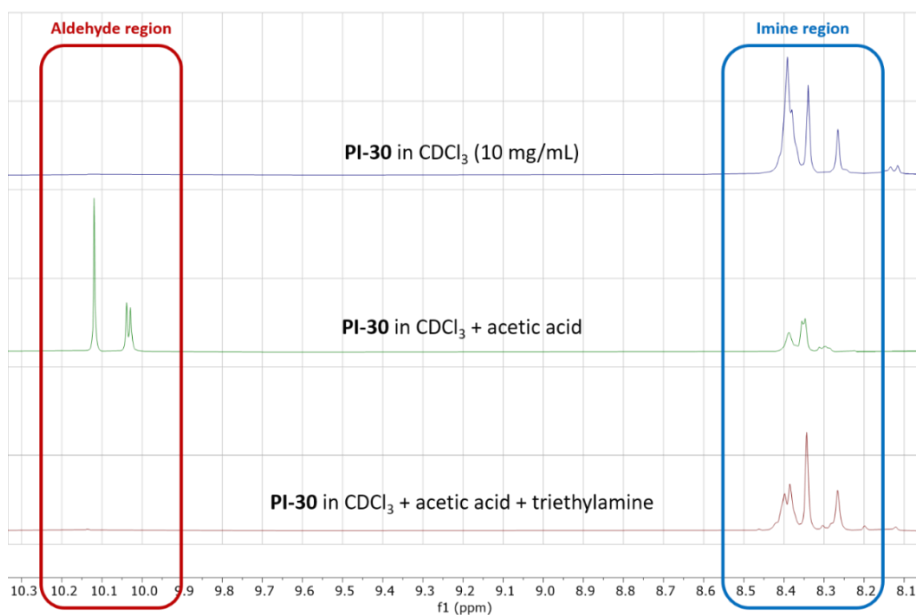
Figure 7.18 ^{1}H NMR spectra of **PI-30** in CDCl$_3$ (top), after addition of acetic acid (middle) and when neutralised with triethylamine (bottom). The spectra indicate that after addition of the acid the imines partially dissociate back to aldehyde, but after neutralisation with triethylamine the equilibrium is again pushed fully towards imine formation.

7.5.6   Recycling *via* dissolution of **PI-30**

For the recycling experiment, a pristine **PI-30** material was first synthesised. A temperature sweep experiment was performed to determine the T_{cross} (where tan(δ) = 1),[92] giving the temperature at which the material transitions from a rubbery to a viscous (malleable) state.[93] Next, frequency sweep experiments at several temperatures were performed to check for a constant plateau of the storage modulus (G'), indicating that the crosslinking density remains constant at elevated temperatures.[4, 6, 14] Next, the pristine material was fully dissolved in THF. The solution was then poured into a petri and the solvent was slowly evaporated to air overnight. The newly obtained polymer film was further dried in a vacuum oven at 50 °C for one day. The same rheology tests as for the pristine materials were performed to compare the material properties of the pristine material to the recycled material (Figure 10).
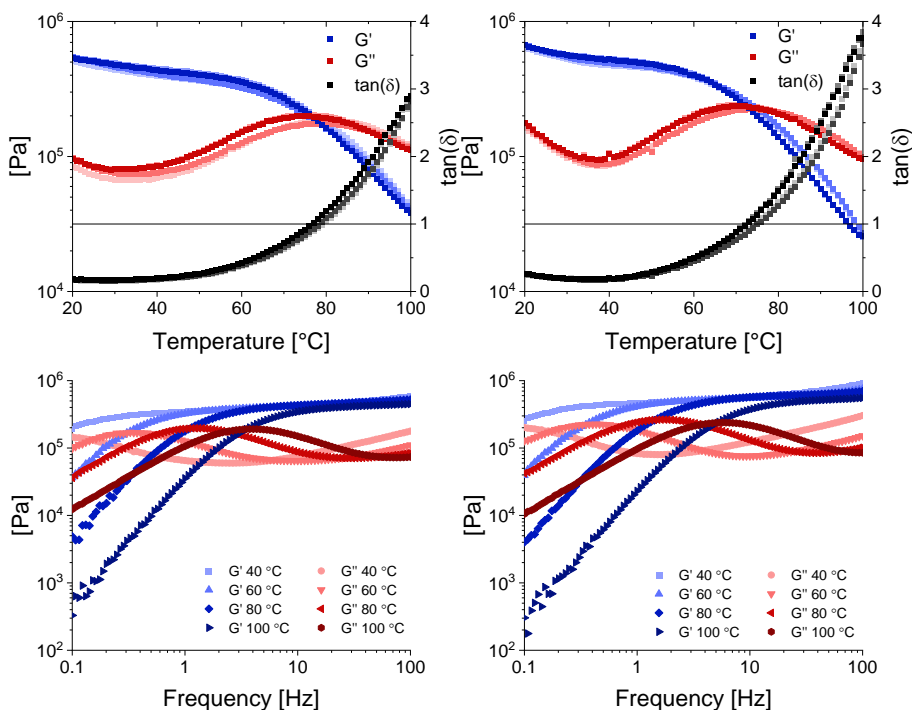
Figure 7.19 Top: temperature sweeps of pristine (left) and recycled (right) polyimine material. In blue the storage modulus (G'), in red the loss modulus (G''), and in grey the tan(δ). The T_{cross} was determined at tan(δ) = 1. Bottom: frequency sweeps of pristine (left) and recycled (right) polyimine material. In blue the storage modulus (G') and in red the loss modulus (G''), where a darker shade of the colour indicated a higher temperature.

References

1. C. J. Kloxin and C. N. Bowman, *Chem. Soc. Rev.*, 2013, **42**, 7161-7173.
2. C. J. Kloxin, T. F. Scott, B. J. Adzima and C. N. Bowman, *Macromolecules*, 2010, **43**, 2643-2653.
3. S. J. Rowan, S. J. Cantrill, G. R. L. Cousins, J. K. M. Sanders and J. F. Stoddart, *Angew. Chem. Int. Ed.*, 2002, **41**, 898-952.
4. D. Montarnal, M. Capelot, F. Tournilhac and L. Leibler, *Science*, 2011, **334**, 965-968.
5. R. J. Wojtecki, M. A. Meador and S. J. Rowan, *Nat. Mater.*, 2011, **10**, 14-27.
6. M. Capelot, M. M. Unterlass, F. Tournilhac and L. Leibler, *ACS Macro Lett.*, 2012, **1**, 789-792.
7. F. Van Lijsebetten, J. O. Holloway, J. M. Winne and F. E. Du Prez, *Chem. Soc. Rev.*, 2020, **49**, 8425-8438.
8. F. Cuminet, S. Caillol, É. Dantras, É. Leclerc and V. Ladmiral, *Macromolecules*, 2021, **54**, 3927-3961.
9. M. Delahaye, J. M. Winne and F. E. Du Prez, *J. Am. Chem. Soc.*, 2019, **141**, 15277-15287.
10. M. Maaz, A. Riba-Bremerch, C. Guibert, N. J. Van Zee and R. Nicolaÿ, *Macromolecules*, 2021, **54**, 2213-2225.
11. M. Röttger, T. Domenech, R. van der Weegen, A. Breuillac, R. Nicolaÿ and L. Leibler, *Science*, 2017, **356**, 62-65.
12. R. G. Ricarte, F. Tournilhac, M. Cloître and L. Leibler, *Macromolecules*, 2020, **53**, 1852-1866.
13. R. G. Ricarte, F. Tournilhac and L. Leibler, *Macromolecules*, 2019, **52**, 432-443.
14. M. Capelot, D. Montarnal, F. Tournilhac and L. Leibler, *J. Am. Chem. Soc.*, 2012, **134**, 7664-7667.
15. A. Demongeot, S. J. Mougnier, S. Okada, C. Soulié-Ziakovic and F. Tournilhac, *Polym. Chem.*, 2016, **7**, 4486-4493.
16. H. Zhang, S. Majumdar, R. A. T. M. van Benthem, R. P. Sijbesma and J. P. A. Heuts, *ACS Macro Lett.*, 2020, **9**, 272-277.
17. A. Jourdain, R. Asbai, O. Anaya, M. M. Chehimi, E. Drockenmuller and D. Montarnal, *Macromolecules*, 2020, **53**, 1884-1900.
18. M. M. Obadia, A. Jourdain, P. Cassagnau, D. Montarnal and E. Drockenmuller, *Adv. Funct. Mater.*, 2017, **27**, 1703258.
19. P. Chakma, Z. A. Digby, M. P. Shulman, L. R. Kuhn, C. N. Morley, J. L. Sparks and D. Konkolewicz, *ACS Macro Lett.*, 2019, **8**, 95-100.
20. P. Chakma, C. N. Morley, J. L. Sparks and D. Konkolewicz, *Macromolecules*, 2020, **53**, 1233-1244.
21. B. M. El-Zaatari, J. S. A. Ishibashi and J. A. Kalow, *Polym. Chem.*, 2020, **11**, 5339-5345.
22. D. J. Fortman, R. L. Snyder, D. T. Sheppard and W. R. Dichtel, *ACS Macro Lett.*, 2018, **7**, 1226-1231.

23. B. Hendriks, J. Waelkens, J. M. Winne and F. E. Du Prez, *ACS Macro Lett.*, 2017, **6**, 930-934.

24. N. Van Herck, D. Maes, K. Unal, M. Guerre, J. M. Winne and F. E. Du Prez, *Angew. Chem. Int. Ed.*, 2020, **59**, 3609-3617.

25. M. A. Bin Rusayyis and J. M. Torkelson, *Polym. Chem.*, 2021, **12**, 2760-2771.

26. M. Podgórski, S. Huang and C. N. Bowman, *ACS Appl. Mater. Interfaces*, 2021, **13**, 12789-12796.

27. A. Trejo-Machin, L. Puchot and P. Verge, *Polym. Chem.*, 2020, **11**, 7026-7034.

28. A. J. Melchor Bañales and M. B. Larsen, *ACS Macro Lett.*, 2020, **9**, 937-943.

29. J. J. Lessard, G. M. Scheutz, R. W. Hughes and B. S. Sumerlin, *ACS Appl. Polym. Mater.*, 2020, **2**, 3044-3048.

30. W. Denissen, M. Droesbeke, R. Nicolaÿ, L. Leibler, J. M. Winne and F. E. Du Prez, *Nat. Commun.*, 2017, **8**, 14857.

31. W. Denissen, G. Rivero, R. Nicolaÿ, L. Leibler, J. M. Winne and F. E. Du Prez, *Adv. Funct. Mater.*, 2015, **25**, 2451-2457.

32. J. P. Brutman, D. J. Fortman, G. X. De Hoe, W. R. Dichtel and M. A. Hillmyer, *J. Phys. Chem. B*, 2019, **123**, 1432-1441.

33. P. R. Christensen, A. M. Scheuermann, K. E. Loeffler and B. A. Helms, *Nat. Chem.*, 2019, **11**, 442-448.

34. C. He, P. R. Christensen, T. J. Seguin, E. A. Dailing, B. M. Wood, R. K. Walde, K. A. Persson, T. P. Russell and B. A. Helms, *Angew. Chem. Int. Ed.*, 2020, **59**, 735-739.

35. S. K. Schoustra, J. A. Dijksman, H. Zuilhof and M. M. J. Smulders, *Chem. Sci.*, 2021, **12**, 293-302.

36. S. K. Schoustra, T. Groeneveld and M. M. J. Smulders, *Polym. Chem.*, 2021, **12**, 1635-1642.

37. P. Taynton, H. Ni, C. Zhu, K. Yu, S. Loob, Y. Jin, H. J. Qi and W. Zhang, *Adv. Mater.*, 2016, **28**, 2904-2909.

38. P. Taynton, K. Yu, R. K. Shoemaker, Y. Jin, H. J. Qi and W. Zhang, *Adv. Mater.*, 2014, **26**, 3938-3942.

39. P. Taynton, C. Zhu, S. Loob, R. Shoemaker, J. Pritchard, Y. Jin and W. Zhang, *Polym. Chem.*, 2016, **7**, 7052-7056.

40. W. An, X.-L. Wang, X. Liu, G. Wu, S. Xu and Y.-Z. Wang, *Green Chem.*, 2022, **24**, 701-712.

41. A. Breuillac, A. Kassalias and R. Nicolaÿ, *Macromolecules*, 2019, **52**, 7102-7113.

42. R. Hajj, A. Duval, S. Dhers and L. Avérous, *Macromolecules*, 2020, **53**, 3796-3805.

43. R. Nicolaÿ, J. Kamada, A. Van Wassen and K. Matyjaszewski, *Macromolecules*, 2010, **43**, 4355-4361.

44. G. M. Scheutz, J. J. Lessard, M. B. Sims and B. S. Sumerlin, *J. Am. Chem. Soc.*, 2019, **141**, 16181-16196.

45. J. M. Winne, L. Leibler and F. E. Du Prez, *Polym. Chem.*, 2019, **10**, 6091-6108.

46. Y. Jin, Z. Lei, P. Taynton, S. Huang and W. Zhang, *Matter*, 2019, **1**, 1456-1493.

47. W. Denissen, J. M. Winne and F. E. Du Prez, *Chem. Sci.*, 2016, **7**, 30-38.

48. K. Yu, H. Yang, B. H. Dao, Q. Shi and C. M. Yakacki, *J. Mech. Phys. Solids*, 2017, **109**, 78-94.

49. F. Smallenburg, L. Leibler and F. Sciortino, *Phys. Rev. Lett.*, 2013, **111**, 188002.

50. S. Schmitz, A. C. Dona, P. Castignolles, R. G. Gilbert and M. Gaborieau, *Macromol. Biosci.*, 2009, **9**, 506-514.

51. J. J. Thevarajah, J. C. Bulanadi, M. Wagner, M. Gaborieau and P. Castignolles, *Anal. Chim. Acta*, 2016, **935**, 258-268.

52. R. G. Jones, J. Kahovec, R. Stepto, E. S. Wilks, M. Hess, T. Kitayama and W. V. Metanomski, *Compendium of Polymer Terminology and Nomenclature*, RSC Publishing, 2008.

53. B. A. Miller-Chou and J. L. Koenig, *Prog. Polym. Sci.*, 2003, **28**, 1223-1270.

54. A. Perego and F. Khabaz, *Macromolecules*, 2020, **53**, 8406-8416.

55. J. S. A. Ishibashi, I. C. Pierce, A. B. Chang, A. Zografos, B. M. El-Zaatari, Y. Fang, S. J. Weigand, F. S. Bates and J. A. Kalow, *Macromolecules*, 2021, **54**, 3972-3986.

56. J. Tellers, R. Pinalli, M. Soliman, J. Vachon and E. Dalcanale, *Polym. Chem.*, 2019, **10**, 5534-5542.

57. P. J. Flory and J. R. Jr., *J. Chem. Phys.*, 1943, **11**, 521-526.

58. A. Takahashi, T. Ohishi, R. Goseki and H. Otsuka, *Polymer*, 2016, **82**, 319-326.

59. J. S. A. Ishibashi and J. A. Kalow, *ACS Macro Lett.*, 2018, **7**, 482-486.

60. L. Yu, Z. Lei, X. Sun, P. Ding, A. Wesche, Y. Jin, W. Zhang and R. Long, *ACS Appl. Polym. Mater.*, 2021, DOI: 10.1021/acsapm.1c01027.

61. M. Hayashi, Y. Oba, T. Kimura and A. Takasu, *Polymer Journal*, 2021, **53**, 835-840.

62. J. Zhao, Z. Zhang, L. Cheng, R. Bai, D. Zhao, Y. Wang, W. Yu and X. Yan, *J. Am. Chem. Soc.*, 2022, **144**, 872-882.

63. Q. Mu, L. An, Z. Hu and X. Kuang, *Polym. Degrad. Stab.*, 2022, **199**, 109895.

64. Q. Shi, K. Yu, M. L. Dunn, T. Wang and H. J. Qi, *Macromolecules*, 2016, **49**, 5527-5537.

65. K. Yu, Q. Shi, M. L. Dunn, T. Wang and H. J. Qi, *Adv. Funct. Mater.*, 2016, **26**, 6098-6106.

66. Q. Shi, K. Yu, X. Kuang, X. Mu, C. K. Dunn, M. L. Dunn, T. Wang and H. Jerry Qi, *Mater. Horiz.*, 2017, **4**, 598-607.

67. A. Ruiz de Luzuriaga, R. Martin, N. Markaide, A. Rekondo, G. Cabañero, J. Rodríguez and I. Odriozola, *Mater. Horiz.*, 2016, **3**, 241-247.

68. L. M. Johnson, E. Ledet, N. D. Huffman, S. L. Swarner, S. D. Shepherd, P. G. Durham and G. D. Rothrock, *Polymer*, 2015, **64**, 84-92.

69. X. He, Z. P. Lei, W. Zhang and K. Yu, *3d Print. Addit. Manuf.*, 2019, **6**, 31-39.

70. H. Zheng, Q. Liu, X. Lei, Y. Chen, B. Zhang and Q. Zhang, *J. Polym. Sci., Part A: Polym. Chem.*, 2018, **56**, 2531-2538.

71. X. Zhao, X. Liu, K. Feng, W.-L. An, F. Tian, R. Du, S. Xu, L. Chen, G. Wu and Y.-Z. Wang, *ChemSusChem*, 2021, e202101607.

72. M. Ciaccia, R. Cacciapaglia, P. Mencarelli, L. Mandolini and S. Di Stefano, *Chem. Sci.*, 2013, **4**, 2253-2261.

73. M. Ciaccia and S. Di Stefano, *Org. Biomol. Chem.*, 2015, **13**, 646-654.

74. M. Ciaccia, S. Pilati, R. Cacciapaglia, L. Mandolini and S. Di Stefano, *Org. Biomol. Chem.*, 2014, **12**, 3282-3287.
75. G. M. Santerre, C. J. Hansrote and T. I. Crowell, *J. Am. Chem. Soc.*, 1958, **80**, 1254-1257.
76. R. B. Martin, *J. Phys. Chem.*, 1964, **68**, 1369-1377.
77. W. P. Jencks, in *Prog. Phys. Org. Chem.*, 1964, vol. 2, pp. 63-128.
78. E. H. Cordes and W. P. Jencks, *J. Am. Chem. Soc.*, 1962, **84**, 832-837.
79. W. P. Jencks, *Acc. Chem. Res.*, 1976, **9**, 425-432.
80. M. J. Mäkelä and T. K. Korpela, *Chem. Soc. Rev.*, 1983, **12**, 309-329.
81. Z. Q. Lei, P. Xie, M. Z. Rong and M. Q. Zhang, *J. Mater. Chem. A*, 2015, **3**, 19662-19668.
82. M. C. Burland, T. Y. Meyer and M.-H. Baik, *J. Org. Chem.*, 2004, **69**, 6173-6184.
83. K. Saito, F. Eisenreich, T. Türel and Ž. Tomović, *Angew. Chem. Int. Ed.*, 2022, **n/a**, e202211806.
84. Y. Wang, A. Xu, L. Zhang, Z. chen, R. Qin, Y. Liu, X. Jiang, D. Ye and Z. Liu, *Macromol. Mater. Eng.*, 2022, 2100893.
85. Y. Tao, L. Fang, J. Zhou, C. Wang, J. Sun and Q. Fang, *ACS Appl. Polym. Mater.*, 2020, **2**, 295-303.
86. A. Chao, I. Negulescu and D. Zhang, *Macromolecules*, 2016, **49**, 6277-6284.
87. X. Shi, X. He, C. Luo, C. Chung, Y. Ding and K. Yu, *Polymer*, 2022, **252**, 124964.
88. H. Zheng, Q. Liu, X. Lei, Y. Chen, B. Zhang and Q. Zhang, *J. Mater. Sci.*, 2019, **54**, 2690-2698.
89. J.-L. Wietor, D. J. M. van Beek, G. W. Peters, E. Mendes and R. P. Sijbesma, *Macromolecules*, 2011, **44**, 1211-1219.
90. W. Denissen, I. De Baere, W. Van Paepegem, L. Leibler, J. Winne and F. E. Du Prez, *Macromolecules*, 2018, **51**, 2054-2064.
91. H. Sun, C. P. Kabb, M. B. Sims and B. S. Sumerlin, *Prog. Polym. Sci.*, 2019, **89**, 61-75.
92. B. J. Adzima, H. A. Aguirre, C. J. Kloxin, T. F. Scott and C. N. Bowman, *Macromolecules*, 2008, **41**, 9112-9117.
93. W. Liu, S. Yang, L. Huang, J. Xu and N. Zhao, *Chem. Commun.*, 2022, **58**, 12399-12417.
94. L. An and W. Zhao, *Materials*, 2022, **15**, 4488.

Chapter 8

General Discussion and Future Prospects
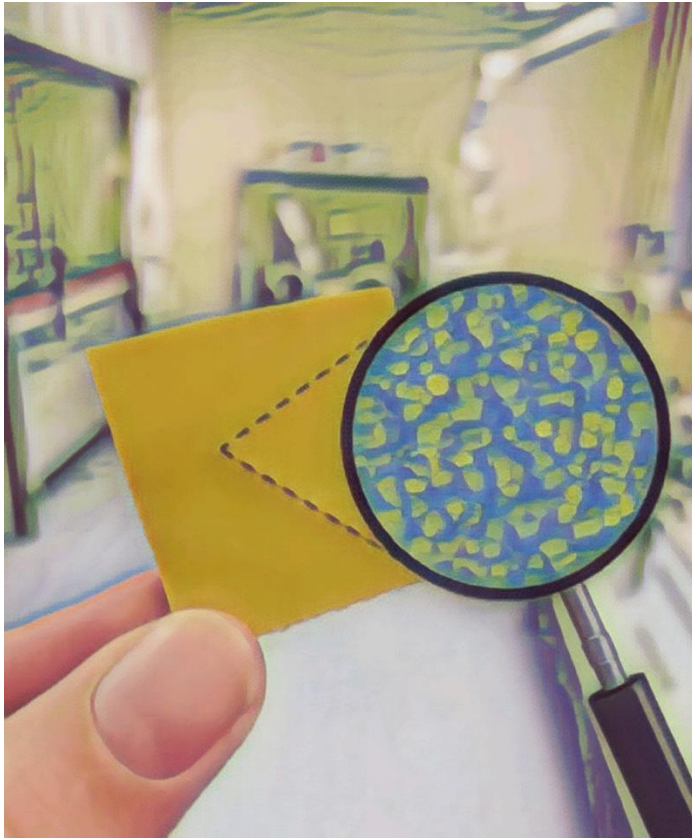
8.1 Introduction

The general subject of this thesis was to develop imine-based CANs, in which was focussed on molecular tuneability of the materials. Each individual chapter described a different approach to gain control over the material properties, and to enhance the material's performance, or steer it into a desired direction for specific applications. To summarise, we have discussed tuneability of material properties *via* electronic effects (**Chapter 2**), phase separation (**Chapter 3**), polarity (**Chapter 4**), metal coordination (**Chapter 5**), and internal hydrogen bonding (**Chapter 6**). Additionally, in **Chapter 7** the solubility of CANs was discussed, which was also linked to the molecular composition of the materials. For every study, a relation was observed between the molecular behaviour of the monomeric building blocks and the material properties on the macroscopic level.

The results of the different studies mentioned in this thesis were promising for the development of tuneable CANs with high-end material properties. However, many different strategies can be thought of and are being developed. Numerous reports in literature document on alternative strategies to gain control over the material properties of CANs or reduce potential downsides that are common to certain polymers.[1-6] Additionally, other (smart) features of CANs are being discovered and further developed,[7-9] of which some promising prospects will be discussed in this Chapter.

8.2 Control over the bond exchange

In this thesis, several approaches have been proposed on how to target dynamic covalent groups within CANs in order to tune and enhance material properties. It was also shown that this could be achieved either intramolecularly (*e.g.*, steric or electronic effects)[10-12] or intermolecularly (*e.g.*, by changing the content and nature of catalyst).[13] Various works have shown that control over the kinetics of the bond exchange prove to be an efficient method to tune the material properties of the CAN.[5] As such, it is highly expected that future work on CANs will focus further on different approaches to target and control the bond exchange reactions within the materials.

As an example, a strategy that has not yet been discussed before, is based on imine-halogen bonding. In a recent study, Schmidt and co-workers described the synthesis of supramolecular networks based on imine-halogen bonding,[14] which stimulated the proposal to introduce imine-halogen bonds into our polyimine networks. The imine-halogen bond would both act as an additional reversible crosslink, as well as alter the kinetics of the

imine bond, similarly to the metal coordination described in **Chapter 5** of this thesis. In order to include the imine-halogen bonding, first a polyimine network should be synthesised, to which then a halogen bond donor molecule should be added. In Figure 8.1, this idea is schematically presented, in which a known 1,4-diiodotetrafluorobenzene halogen bond donor molecule[15] is used to form the imine-halogen bonding crosslinks. It is, however, known that the imine-halogen bond is a relatively weak bond compared to, for example, metal-ligand bonding or hydrogen bonding.[16] As such, the effect of the imine-halogen bond is expected to be more subtle than was, for example, seen in the metal-coordinated CANs in **Chapter 5**.
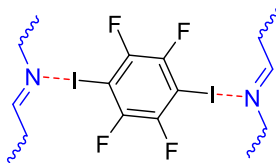
Figure 8.1 Concept of imine-halogen bonding in polyimine CANs using 1,4-diiodotetrafluorobenzene to bind two imine groups and create an additional dynamic crosslink, as well as alter the imine stability.

8.3   Stimuli-responsive materials

Adding responsive features to CANs can be very useful in the development of functional materials. As such, different studies focus on the incorporation of different responsive units.[3, 17, 18] A current hot topic is the development of light-responsive materials.[19, 20] Zheng and co-workers showed that polyimine CANs could be developed that respond to near-infrared (NIR) light by building in photo-responsive aniline trimer (ACAT) units.[21] When irradiated by NIR light, the ACAT units convert light into heat. As a result, the bond exchange kinetics are enhanced, leading to accelerated healing and more efficient welding. In addition, the NIR trigger enabled photoinduced shape memory properties. Other works on the inclusion of ACAT in ester-based CANs also showed that the ACAT enables responsiveness to redox reagents and electrical fields,[22] which highlight the potentials to further develop multi-responsive CANs for future applications, such as sensors or actuators.[23, 24]

An example of polyimine-based sensors was presented by Kathan and co-workers, who developed a photo-programmable amine sensing device.[20] They made use of a photo-switchable aldehyde monomer, which enabled reversible imprinting of custom-designed patterns on the surface of the material with (sun)light. This way, information could be

stored in a non-invasive way. When amine vapours were present, however, penetration of these amines into the material occurred, leading to liquification of the polymer. This caused the imprinted pattern to be lost over time. *Via* this methodology it was therefore possible to use these materials as amine sensor devices, as loss of the patterns clearly indicated when amines vapours are present in the environment.

In our own attempts to construct light-responsive polyimine materials, we proposed to build diazobenzene structures into our polyimine networks. Diazobenzenes are known to switch between *cis* and *trans* configuration when light of certain wavelength is applied (see Figure 8.2).[25, 26] Upon radiation with UV light, the *cis* configuration is formed. Under visible light or *via* thermal relaxation, the configuration is switched back to *trans*. Our hypothesis was that by including these diazobenzene structures within our polyimine CANs, that a physical response to light of different wavelengths would result. To this end, we started from the **P-XDA** polymers, described in **Chapter 2** of this thesis, and used an azodianiline as the **XDA** monomers (Figure 8.2).
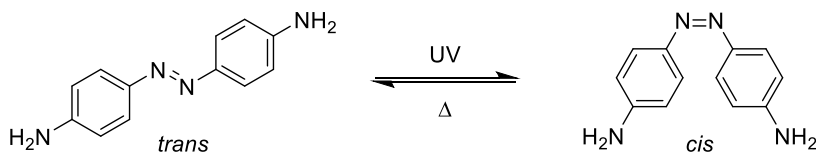
Figure 8.2 *Cis-trans* configuration switch of azodianiline. Under UV light, the *cis* configuration is formed, and after thermal relaxation (under visible light) the *trans* configuration is reformed.

In our first attempts, we synthesised **P-XDA** materials with 20% of the azodianiline monomer, similar to the procedures described in **Chapter 2**.[27] We then tried to look for a physical response of the material when they were exposed to UV light. Unfortunately, no physical response was observed, either by eye or under the rheometer. We then hypothesised that because of the turbid appearance, the UV light was not able to penetrate well into the material. Another attempt was made by incorporating the azodianiline into a PDMS network, but here miscibility problems arose. From there on, no further attempts were made.

However, since we now have more knowledge of the phase separation of the dianilines in the **P-XDA** materials (as discussed in **Chapter 3**), this study can be picked up again. By varying the concentration of the azodianiline, new polymers can be synthesised that either phase separate or not. As a result, we can design the material in such a manner that the

azodianilines pack together in phase-separated domains, or randomly distribute in a non-phase-separated polymer matrix. As was discussed in **Chapter 3**, phase-separated materials appeared turbid and non-phase separated materials were transparent. As such, **p**revention of phase-separation might be required as (UV) light might not be able to efficiently penetrate through the turbid phase-separated materials. Lowering the concentration of the azodianiline might thus be required to prevent phase separation. However, if the concentration becomes too low, this might result in too little of the light-responsive units to see any noticeable physical change. Another possibility might then be to add sterically bulked groups to the azodianiline monomers to prevent phase separation. This way, a higher concentration of the azodianiline can be built into the polymer material, resulting in a more efficient light response.

8.4 Materials with a dual dynamic response from the combination of dynamic chemistries

In the introduction of this thesis, the combination of different dynamic (covalent) chemistries has already been shortly introduced, and several examples have been documented in literature.[18, 28-30] Among these is the combination of imines with disulfides.[31-34] In our **P-XDA** polyimine systems (see **Chapter 2**), we have also made our first attempts to combine reversible imine and disulfide chemistries. For this, a 4,4'-dithiodianiline monomer (Figure 8.3) was included as the **XDA** monomer in the **P-XDA** polymer systems described in **Chapter 2**. The 4,4'-dithiodianiline monomer already includes the disulfide group in its structure, while the imines are formed during the polymerisation reaction with aldehydes.
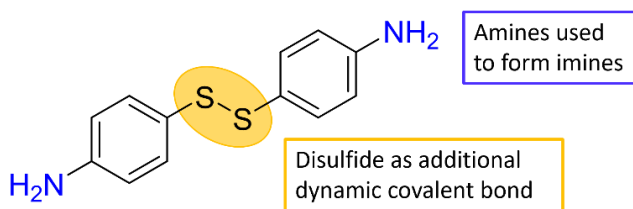

Figure 8.3 Monomer structure of 4,4'-dithiodianiline, used for constructing dual dynamic disulphide-imine CANs. The monomer was incorporated into a **P-XDA** network, as described in **Chapter 2**.

From initial rheological experiments we could observe that both the kinetic activation (E_a) and crossover temperature (T_{cross}) were significantly lower when compared to a similar material using 4,4-thiodianiline (**TDA**, with only a singular sulfur atom as the bridge between the anilines). This indicates that the addition of the disulfides into the system enhanced the overall bond exchange. It is possible that the combination of imines and disulfides might add up in the total amount of bond exchange reactions in the material. In addition, a synergistic mechanism between imine and disulfide exchange may be present as well. To further speculate on this, more investigations into the exact mechanisms of bond exchange are however still required.

In addition to the above, the proposed dual dynamic systems also appeared to phase separate. As such, there is also an interest in locking of the different dynamic chemistries within the different phases. Since the disulfides are only present in the dianiline parts, it is very possible that the disulfide exchange is limited to the phase-separated domains where the dianilines stack (see also **Chapter 3**). Further investigations of the effects of different dynamic domains within the same material are therefore recommended.

8.5   Phase separation

The phase separation behaviour of our polyimines (see **Chapter 3**), in addition to other works and phase separation in dynamic polymer networks (see also Section 1.6.7 in **Chapter 1**), has really intrigued us to look further into the underlying dynamics that cause the phase separation. We also envision to extend our work with the previously discussed dianilines in our polyimine networks to other structures and networks as well.

8.5.1   Use of different aniline(-like) monomers

As an example that is currently being investigated, we seek to include the use of different aromatic moieties to trigger the phase separation to see how stacking or organisation of the aromatic moieties proceeds within the matrix. In **Chapter 3** was discussed how aromatic dianiline moieties are the probable cause to induce phase separation. Therefore, in future work we proposed several similar structures (see Figure 8.4) that could induce phase separation *via* similar mechanisms. In **Chapter 3**, we mainly focussed on the use of different dianiline (**XDA**) monomers, in which either the aniline bridge moiety (**X**) was adjusted, or steric bulk (**R**) was introduced on the aniline rings (see the **XDA** structure in Figure 8.4). Our results suggested that phase separation was only observed when the steric bulk was minimal. Additionally, when the length of the bridging moiety (**X**) was increased from a methylene to an ethylene group, the phase separation did still occur, but to a lesser degree.

From these initial results, we propose to extend the research towards additional structures, like the benzidine and fluorene diamine (see Figure 8.3), to gain a better understanding into the mechanism of stacking of these moieties to induce phase separation. With the given structures we could, for example, deduce the preferred shape of the aromatic monomers for efficient stacking.
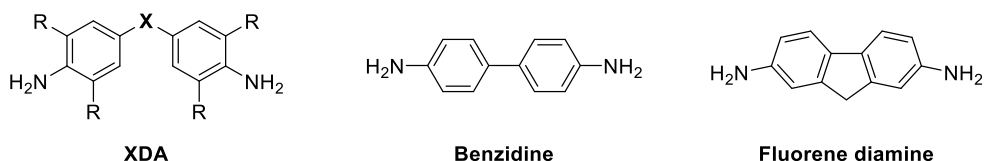
Figure 8.4 Structure of **XDA** monomers, as described in **Chapter 2** and **Chapter 3**, and different related structures (benzidine and fluorene diamine), to use in future studies on the origin and mechanism is phase separation in polyimine CANs.

8.5.2   Other mechanisms for phase separation

In addition to the work on phase separation in **P-XDA** CANs, we also wish to study different supramolecular interactions that could cause phase separation. These include, for example, fluorophobic effects[35] and intermolecular hydrogen bonding.[36, 37] Such investigations are particularly interesting for studying the relations between different length scales of chemistry and physics that operate within the same polymeric system. To study fluorophobic effects, our current plans consist of making use of fluorinated aldehydes (Figure 8.5), which can be built into polyimine networks. By varying the ratio between fluorinated and non-fluorinated components, we hypothesise to find a trigger point at which phase separation is induced, much like the studies into the threshold concentration of dianilines (as seen in **Chapter 3**). If such phase separation can be concluded, the next steps will involve further studies into the mechanism of phase separation and the effect on material properties of the CANs.
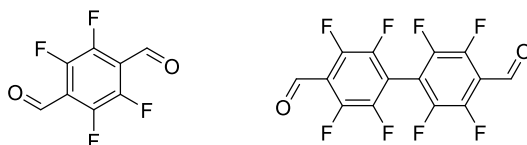
Figure 8.5 Molecular structure of proposed fluorinated dialdehyde monomers to induce phase separation *via* fluorophobic effects.

8.6   Bio-based materials

We have seen that CANs are excellent candidates for the development of more durable and sustainable thermosets and elastomers due to their efficient recycling methods. However, if we wish to fully close the cycle of sustainability, we would also prefer to build our polymers out of materials from sustainable sources.[38-40] Currently, most materials are still gathered or produced on a petrochemical basis, which means that they come from fossil sources such as oil. In recent years, there have luckily been more examples of bio-inspired sources, from which monomers can be gathered or produced.[41]

Specifically for polyimines, some very promising process has been made in the application of bio-sourced materials.[42-46] In a recent review by Liguori and Hakkarainen, they highlight some of the most promising polyimine materials that have been synthesised from bio-based monomers.[47] Among these bio-based polyimine materials, vanillin is commonly applied.[48-52] Vanillin is well known for its use as a flavouring ingredient, causing the typical vanilla flavour and odour. It can be gathered from different plant-based sources, but on an industrial level, it can nowadays be produced from breaking down of lignin.[53-55] Vanillin is especially interesting for the production of polyimines due to its aldehyde functionality, which is used to form the imine. Furthermore, the alcohol group can also be used to link either two or more vanillin molecules together to create a monomer, or for addition of other functionalities. Another great example of a bio-based aldehyde was presented by Avérous and co-workers, who derived furan dialdehyde monomers from naturally occurring sugars.[56, 57] Apart from the aldehydes, nature also provides numerous sources of amines. Some simple examples of naturally occurring diamines are putrescine, cadaverine or spermidine-like compounds. Alternatively, amine monomers can also be synthesised from amino acids or fatty acids. As an example, the Priamine 1071 monomer mix, used in **Chapter 5** of this thesis, is also derived from conversion of fatty acids.

Apart from these examples, more developments in bio-based materials are currently being investigated or upscaled for industrial applications. We envision that in the foreseeable future more bio-sourced materials will be studied and produced. Especially the use of lignin as a biological source for polymer building blocks has been highlighted frequently,[53, 58-60] due to the large availability of the material and increasingly better methods to derive useful materials from this otherwise commonly seen waste product.[55, 61, 62] Other current investigation document on the application of various biologically available oils, such as castor oil,[63-65] sunflower oil,[66] soybean oil,[67] or other vegetable oils,[68] which show promising prospects for the future development of bio-based products.

8.7   Application in safe materials and electronics

8.7.1   Flame-retardant materials

Flammability is a major problem for many existing thermosets, which hampers their application in many fields that are prone to fire hazards, such as in electronic devices or the automotive industry.[69] Therefore, flame retardants are often added to the thermosets to reduce their susceptibility towards inflammation. Previously, halogenated fire retardants were commonly utilised, however, these were recently banned by the European Union due to their toxicity. A safer and more environmental friendly alternative for these materials was found to be in phosphorus-containing materials instead.[70-72] A good example of such a phosphorus-containing monomer is tris(4-formyl-2-methoxyphenyl)phosphate (**TFMP**), which can be synthesised from a reaction of vanillin and phosphorus oxychloride (Figure 8.6). Wang *et al.* used this **TFMP** trialdehyde, in combination with several diamines, to synthesise high-performance polyimine materials with excellent flame resistance.[73] Furthermore, the materials showed a high malleability, were reprocessable within several minutes, and were able to be broken down again to the **TFMP** monomer when immersed in an acidic solution. Recovery rates up to 70% of the initial **TFMP** content could be achieved under relatively mild conditions. A drawback of the materials was mentioned, however, as side reactions during the remoulding process occurred. Additionally, the rapid relaxation of the materials is in favour of fast recovery, although it limits the application at high temperatures.
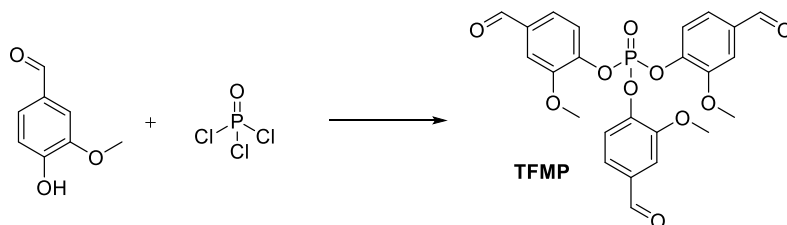
Figure 8.6 Synthetic pathway of the **TFMP** monomer for flame-retardant polyimine CANs.

Although the phosphorus in the structure was hypothesised to be the main flame-retardant part of the polymer, the imines may also contribute to the flame resistance. The radical scavenging properties of the dynamic imine bond is one reason that supports this hypothesis.[74] Secondly, with the use of aromatically linked imine structures, excellent thermal stability can be achieved due to resonance of the imine bond with the conjoining

aromatic rings.[75] This hypothesis was consistent to the results obtained by Wang *et al.* from comparing the materials that included aromatically linked imines (similar to the **MDA** materials discussed in **Chapter 3** of this thesis) with those that had aliphatically linked imines (Figure 8.7A).[73] Similarly, in a study by Fang *et al.*,[76] three imine-containing flame retardant copolymers were synthesised (Figure 8.7B), of which the aromatically linked imine structures showed best flame-retardance results compared to their aliphatic counterparts.
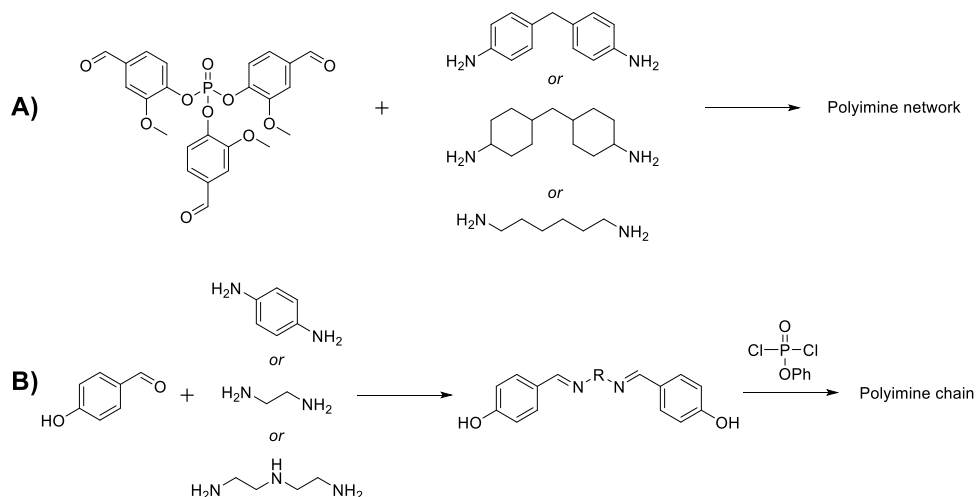
Figure 8.7 Overview of the tested monomers for flame retardant polyimines A) by Wang *et al.*,[73] and B) by Fang *et al.*[76] In both cases, materials with added aromatic amines showed improved flame resistance.

Further developments and highlights on flame-retardant CANs were also recently discussed in a review by Rashid *et al.*,[77] that pointed out the need for recyclable flame-retardant thermosets. Especially applications in the automotive-, railway- and aircraft industries, as well as electronics and batteries, in general, are in need of good flame-resistant materials. We envision that polyimine CANs are excellent materials for this, thanks to their tuneable material properties, good recyclability and self-healing behaviour (as seen throughout this thesis), as well as the potential to synthesise them from bio-based components (see Section 8.6). In terms of applications for our own developed polyimine CANs, for future work, it would thus be interesting to include flame-retardant structures, such as the discussed phosphates (*e.g.*, by replacing the commonly used terephthalaldehyde (**TA**) by a phosphate-linked aldehyde monomer), into the polymer network.

8.7.2 Safer self-repairing batteries and electronics

A specific application of (flame-retardant) CANS lays in the production of safer and more durable batteries. Batteries (in particular lithium-ion batteries) have an important role in current society to store and transport energy. Inside these batteries liquid electrolytes are commonly included, which pose potential fire hazards, especially in the event of a short circuit or mechanical damage to the battery. A way to overcome the use these hazardous liquid electrolytes is to use solid polymer electrolytes (SPEs).[78] When CANs are applied as these SPE polymers, it is however also possible to include many other advantageous features to the batteries. Not only can CANs be used to construct light-weight and highly conductive systems, but the dynamic covalent bonds also provide self-repairing properties.[79-81] As such, cracks or other damages in the battery, which could otherwise cause potential safety hazards, are easily recovered.[44] In addition, such vitrimeric electrolytes can be more easily recycled compared to traditional SPEs.[82] Combining all the advantageous features of CANs, their application can thus enhance lifetime durability and safety of the batteries. Further development of our polyimine systems into the direction of SPEs is therefore an interesting future prospect. Some important parameters which need to be discussed and tested beforehand include the conductivity of polyimines or other electronic properties.

The use of (polyimine) CANs in electronical devices has already been partially addressed in literature.[83] The versatility of such applications for polyimine CANs was nicely shown by Zou and co-workers, who developed an electronic skin (e-skin) using a polyimine network as the key material, which was doped with conductive silver nanoparticles.[84] Their designs resulted in the production of e-skin that was able to be fully recycled, but also showed self-healing behaviour, enabling the material to self-repair damages. Furthermore, the e-skin was able to sense pressure, flow, temperature and humidity. These features essentially mimic that of biological human/mammalian skin. The prospects of the developed e-skin are envisioned to stimulate durable, economical and eco-friendly technologies in applications such as (soft) robotics, prosthetics, or other human-computer related healthcare products.[84] In important note for further application of polyimine CANs, especially in healthcare, regards the toxicity of the materials. Although many (polyimine) CANs are generally considered safe to use, not much is known about their long-term toxicity. As such, before widespread applications, more extensive toxicity testing may be required.

8.8   3D printing

A nice feature of the tuneable heat-induced malleability of CANs also includes its use in 3D printing.[85-88] 3D printing is becoming more relevant for current industrial applications, as it enables on-demand in-house manufacturing of a wide range of customisable products. In addition, the amounts of generated waste are generally lower than for other moulding methods.[89] The use of CANs for 3D printing is very desirable for two reasons. First, CANs generally show better material properties than other thermoplastic filaments. Second, they can easily be recycled once used. It is thus possible to print an object, which can later be recycled into new filament, enabling it to be printed again into a new product.[87] As such, it would be interesting to study if our tuneable imine-based CANs are suitable for application in 3D printing. In order to test the suitability, we may first need to extend the synthetic procedure towards production of filaments, rather than films (as has mostly been the case up till now). Next, a setup is required that enables "melting" of the polyimine filaments, by which they can be printed. Last, it is probably also of importance to study the cooling mechanism of the materials, as they are printed when hot, and may creep once printed if the cooling proceeds too slow. We do, however, envision that the broad tuneability of polyimine CANs, as discussed in this thesis, would provide plenty of space to develop materials that are suitable for applications in 3D printing.

References

1.   N. J. Van Zee and R. Nicolaÿ, *Prog. Polym. Sci.*, 2020, **104**, 101233.
2.   F. Van Lijsebetten, J. O. Holloway, J. M. Winne and F. E. Du Prez, *Chem. Soc. Rev.*, 2020, **49**, 8425-8438.
3.   M. Podgórski, B. D. Fairbanks, B. E. Kirkpatrick, M. McBride, A. Martinez, A. Dobson, N. J. Bongiardina and C. N. Bowman, *Adv. Mater.*, 2020, **32**, 1906876.
4.   B. Krishnakumar, R. V. S. P. Sanka, W. H. Binder, V. Parthasarthy, S. Rana and N. Karak, *Chem. Eng. J.*, 2020, **385**, 123820.
5.   M. Guerre, C. Taplan, J. M. Winne and F. E. Du Prez, *Chem. Sci.*, 2020, **11**, 4855-4870.
6.   F. Van Lijsebetten, T. Debsharma, J. M. Winne and F. E. Du Prez, *Angew. Chem. Int. Ed.*, 2022, **n/a**, e202210405.
7.   N. Zheng, Y. Xu, Q. Zhao and T. Xie, *Chem. Rev.*, 2021, **121**, 1716-1745.
8.   Y. Wu, Y. Wei and Y. Ji, *Polym. Chem.*, 2020, **11**, 5297-5320.
9.   Z. P. Zhang, M. Z. Rong and M. Q. Zhang, *Prog. Polym. Sci.*, 2018, **80**, 39-93.
10.   L. Zhang and S. J. Rowan, *Macromolecules*, 2017, **50**, 5051-5060.

11. B. M. El-Zaatari, J. S. A. Ishibashi and J. A. Kalow, *Polym. Chem.*, 2020, **11**, 5339-5345.
12. N. Van Herck, D. Maes, K. Unal, M. Guerre, J. M. Winne and F. E. Du Prez, *Angew. Chem. Int. Ed.*, 2020, **59**, 3609-3617.
13. M. Capelot, M. M. Unterlass, F. Tournilhac and L. Leibler, *ACS Macro Lett.*, 2012, **1**, 789-792.
14. E. Nieland, D. Komisarek, S. Hohloch, K. Wurst, V. Vasylyeva, O. Weingart and B. M. Schmidt, *Chem. Commun.*, 2022, **58**, 5233-5236.
15. M. Zbačnik, M. Vitković, V. Vulić, I. Nogalo and D. Cinčić, *Cryst. Growth Des.*, 2016, **16**, 6381-6389.
16. H. Guo, R. Puttreddy, T. Salminen, A. Lends, K. Jaudzems, H. Zeng and A. Priimagi, *Nat. Commun.*, 2022, **13**, 7436.
17. S. Shahi, H. Roghani-Mamaqani, R. Hoogenboom, S. Talebi and H. Mardani, *Chem. Mater.*, 2022, **34**, 468-498.
18. Z. Liu, Y. Ma, Z. Zhang, Z. Shi and J. Gao, *Langmuir*, 2022, **38**, 4812-4819.
19. D. Tang, L. Zhang, X. Zhang, L. Xu, K. Li and A. Zhang, *ACS Appl. Mater. Interfaces*, 2022, **14**, 1929-1939.
20. M. Kathan, C. Jurissek, P. Kovaříček and S. Hecht, *J. Polym. Sci., Part A: Polym. Chem.*, 2019, **57**, 2378-2382.
21. H. Zheng, S. Wang, C. Lu, Y. Ren, Z. Liu, D. Ding, Z. Wu, X. Wang, Y. Chen and Q. Zhang, *Ind. Eng. Chem. Res.*, 2020, **59**, 21768-21778.
22. Q. Chen, X. Yu, Z. Pei, Y. Yang, Y. Wei and Y. Ji, *Chem. Sci.*, 2017, **8**, 724-733.
23. G.-H. Zhang, L. Zhang, Q.-H. Zhu, H. Chen, W.-L. Yuan, J. Fu, S.-L. Wang, L. He and G.-H. Tao, *ACS Mater. Lett.*, 2022, **4**, 136-144.
24. J. Pignanelli, B. Billet, M. Straeten, M. Prado, K. Schlingman, M. J. Ahamed and S. Rondeau-Gagné, *Soft Matter*, 2019, **15**, 7654-7662.
25. Y. Li, O. Rios, J. K. Keum, J. Chen and M. R. Kessler, *ACS Appl. Mater. Interfaces*, 2016, **8**, 15750-15757.
26. K. Wang, L. Yin, T. Miu, M. Liu, Y. Zhao, Y. Chen, N. Zhou, W. Zhang and X. Zhu, *Mater. Chem. Front.*, 2018, **2**, 1112-1118.
27. S. K. Schoustra, J. A. Dijksman, H. Zuilhof and M. M. J. Smulders, *Chem. Sci.*, 2021, **12**, 293-302.
28. X. Xu, S. Ma, S. Wang, B. Wang, H. Feng, P. Li, Y. Liu, Z. Yu and J. Zhu, *Macromol. Rapid Commun.*, 2022, **n/a**, 2100777.
29. Y. Lei, A. Zhang and Y. Lin, *Polym. Chem.*, 2021, **12**, 4052-4062.
30. B. Zhang, N. De Alwis Watuthanthrige, S. V. Wanasinghe, S. Averick and D. Konkolewicz, *Adv. Funct. Mater.*, 2021, 2108431.
31. C. Lv, J. Wang, Z. Li, K. Zhao and J. Zheng, *Compos. B. Eng.*, 2019, **177**, 107270.
32. S. Yu, G. Zhang, S. Wu, Z. Tang, B. Guo and L. Zhang, *J. Mater. Chem. A*, 2020, **8**, 20503-20512.
33. Y. Yang, L. Huang, R. Wu, Z. Niu, W. Fan, Q. Dai, L. Cui, J. He and C. Bai, *ACS Appl. Mater. Interfaces*, 2022, **14**, 3344-3355.

34. X. Xu, S. Ma, H. Feng, J. Qiu, S. Wang, Z. Yu and J. Zhu, *Polym. Chem.*, 2021, **12**, 5217-5228.
35. Y. Miwa, T. Udagawa and S. Kutsumizu, *Sci. Rep.*, 2022, **12**, 12009.
36. L. Wang, Y. Liu, Y. Qiao, Y. Wang, Z. Cui, S. Zhu, F. Dong, S. Fang and A. Du, *Polym. Chem.*, 2022, **13**, 4144-4153.
37. W.-X. Liu, Z. Yang, Z. Qiao, L. Zhang, N. Zhao, S. Luo and J. Xu, *Nat. Commun.*, 2019, **10**, 4753.
38. M. A. Lucherelli, A. Duval and L. Avérous, *Prog. Polym. Sci.*, 2022, **127**, 101515.
39. S. Engelen, A. A. Wróblewska, K. De Bruycker, R. Aksakal, V. Ladmiral, S. Caillol and F. E. Du Prez, *Polym. Chem.*, 2022, **13**, 2665-2673.
40. L. Stricker, C. Taplan and F. E. Du Prez, *ACS Sustainable Chem. Eng.*, 2022, **10**, 14045-14052.
41. X.-L. Zhao, Y.-D. Li and J.-B. Zeng, *Polym. Chem.*, 2022, DOI: 10.1039/D2PY01167K.
42. H. Zhang, Z. Su and X. Wang, *ACS Sustainable Chem. Eng.*, 2022, **10**, 8650-8657.
43. J. Li, Z. Weng, Q. Cao, Y. Qi, B. Lu, S. Zhang, J. Wang and X. Jian, *Chem. Eng. J.*, 2022, **433**, 134512.
44. W. Gu, F. Li, T. Liu, S. Gong, Q. Gao, J. Li and Z. Fang, *Adv. Sci.*, 2022, **n/a**, 2103623.
45. Y. Sun, D. Sheng, H. Wu, X. Tian, H. Xie, B. Shi, X. Liu and Y. Yang, *Polymer*, 2021, **233**, 124208.
46. Y.-H. Chen, Y.-C. Cheng and S.-P. Rwei, *ACS Sustainable Chem. Eng.*, 2022, **10**, 14794-14805.
47. A. Liguori and M. Hakkarainen, *Macromol. Rapid Commun.*, 2022, **43**, 2100816.
48. H. Geng, Y. Wang, Q. Yu, S. Gu, Y. Zhou, W. Xu, X. Zhang and D. Ye, *ACS Sustainable Chem. Eng.*, 2018, **6**, 15463-15470.
49. Q. Yu, X. Peng, Y. Wang, H. Geng, A. Xu, X. Zhang, W. Xu and D. Ye, *Eur. Polym. J.*, 2019, **117**, 55-63.
50. H. Memon, H. Liu, M. A. Rashid, L. Chen, Q. Jiang, L. Zhang, Y. Wei, W. Liu and Y. Qiu, *Macromolecules*, 2020, **53**, 621-630.
51. Y. Tao, L. Fang, J. Zhou, C. Wang, J. Sun and Q. Fang, *ACS Appl. Polym. Mater.*, 2020, **2**, 295-303.
52. Z. Zhou, X. Su, J. Liu and R. Liu, *ACS Appl. Polym. Mater.*, 2020, **2**, 5716-5725.
53. M. Fache, B. Boutevin and S. Caillol, *ACS Sustainable Chem. Eng.*, 2016, **4**, 35-46.
54. M. Fache, E. Darroman, V. Besse, R. Auvergne, S. Caillol and B. Boutevin, *Green Chem.*, 2014, **16**, 1987-1998.
55. B. M. Upton and A. M. Kasko, *Chem. Rev.*, 2016, **116**, 2275-2306.
56. S. Dhers, G. Vantomme and L. Avérous, *Green Chem.*, 2019, **21**, 1596-1601.
57. R. Hajj, A. Duval, S. Dhers and L. Avérous, *Macromolecules*, 2020, **53**, 3796-3805.
58. G. Foyer, B. H. Chanfi, B. Boutevin, S. Caillol and G. David, *Eur. Polym. J.*, 2016, **74**, 296-309.
59. G. F. Bass and T. H. Epps, *Polym. Chem.*, 2021, **12**, 4130-4158.
60. A. Moreno, M. Morsali and M. H. Sipponen, *ACS Appl. Mater. Interfaces*, 2021, **13**, 57952-57961.

61.   A. J. Ragauskas, G. T. Beckham, M. J. Biddy, R. Chandra, F. Chen, M. F. Davis, B. H. Davison, R. A. Dixon, P. Gilna, M. Keller, P. Langan, A. K. Naskar, J. N. Saddler, T. J. Tschaplinski, G. A. Tuskan and C. E. Wyman, *Science*, 2014, **344**, 1246843.

62.   R. Tang, B. Xue, J. Tan, Y. Guan, J. Wen, X. Li and W. Zhao, *ACS Appl. Polym. Mater.*, 2022, **4**, 1117-1125.

63.   J. Zhang, C. Zhang, F. Song, Q. Shang, Y. Hu, P. Jia, C. Liu, L. Hu, G. Zhu, J. Huang and Y. Zhou, *Chem. Eng. J.*, 2022, **429**, 131848.

64.   Y. Zhu, F. Gao, J. Zhong, L. Shen and Y. Lin, *Eur. Polym. J.*, 2020, **135**, 109865.

65.   D.-M. Xie, D.-X. Lu, X.-L. Zhao, Y.-D. Li and J.-B. Zeng, *Ind. Crops Prod.*, 2021, **174**, 114198.

66.   S. Nicolas, T. Richard, J. Dourdan, L. Lemiègre and J.-L. Audic, *J. Appl. Polym. Sci.*, 2021, **n/a**, 50904.

67.   F. Zhao, W.-Q. Lian, Y.-D. Li, Y. Weng and J.-B. Zeng, *Ind. Crops Prod.*, 2022, **187**, 115499.

68.   K.-K. Tremblay-Parrado, C. García-Astrain and L. Avérous, *Green Chem.*, 2021, **23**, 4296-4327.

69.   S. Wang, S. Ma, C. Xu, Y. Liu, J. Dai, Z. Wang, X. Liu, J. Chen, X. Shen, J. Wei and J. Zhu, *Macromolecules*, 2017, **50**, 1892-1901.

70.   L. Qian, Y. Qiu, N. Sun, M. Xu, G. Xu, F. Xin and Y. Chen, *Polym. Degrad. Stab.*, 2014, **107**.

71.   X. Zhang, Y. Eichen, Z. Miao, S. Zhang, Q. Cai, W. Liu, J. Zhao and Z. Wu, *Chem. Eng. J.*, 2022, **440**, 135806.

72.   W. Yang, H. Ding, W. Zhou, T. Liu, P. Xu, D. Puglia, J. M. Kenny and P. Ma, *Compos. Sci. Technol.*, 2022, **230**, 109776.

73.   S. Wang, S. Ma, Q. Li, W. Yuan, B. Wang and J. Zhu, *Macromolecules*, 2018, **51**, 8001-8012.

74.   Z. Q. Lei, P. Xie, M. Z. Rong and M. Q. Zhang, *J. Mater. Chem. A*, 2015, **3**, 19662-19668.

75.   İ. Kaya, M. Yıldırım, M. Kamacı and A. Avcı, *J. Appl. Polym. Sci.*, 2011, **120**, 3027-3035.

76.   Y. Liu, Y. Zhang, Z. Cao and Z. Fang, *Ind. Eng. Chem. Res.*, 2012, **51**, 11059-11065.

77.   M. A. Rashid, W. Liu, Y. Wei and Q. Jiang, *J. Appl. Polym. Sci.*, 2022, **139**, e52493.

78.   M. Y. Tan, D. Safanama, S. S. Goh, J. Y. C. Lim, C.-H. Lee, J. C. C. Yeo, W. Thitsartarn, M. Srinivasan and D. W. H. Fam, *Chem. Asian J.*, 2022, **n/a**, e202200784.

79.   J. M. Whiteley, P. Taynton, W. Zhang and S.-H. Lee, *Adv. Mater.*, 2015, **27**, 6922-6927.

80.   B. B. Jing and C. M. Evans, *J. Am. Chem. Soc.*, 2019, **141**, 18932-18937.

81.   Y. H. Jo, S. Li, C. Zuo, Y. Zhang, H. Gan, S. Li, L. Yu, D. He, X. Xie and Z. Xue, *Macromolecules*, 2020, **53**, 1024-1032.

82.   Y. Lin, Y. Chen, Z. Yu, Z. Huang, J.-C. Lai, J. B. H. Tok, Y. Cui and Z. Bao, *Chem. Mater.*, 2022, **34**, 2393-2399.

83.   W. Alabiso and S. Schlögl, *Polymers*, 2020, **12**, 1660.

84.   Z. Zou, C. Zhu, Y. Li, X. Lei, W. Zhang and J. Xiao, *Sci. Adv.*, 2018, **4**, eaaq0508.

85.   Q. Shi, K. Yu, X. Kuang, X. Mu, C. K. Dunn, M. L. Dunn, T. Wang and H. Jerry Qi, *Mater. Horiz.*, 2017, **4**, 598-607.
86.   X. He, Z. P. Lei, W. Zhang and K. Yu, *3d Print. Addit. Manuf.*, 2019, **6**, 31-39.
87.   K. P. Cortés-Guzmán, A. R. Parikh, M. L. Sparacin, A. K. Remy, L. Adegoke, C. Chitrakar, M. Ecker, W. E. Voit and R. A. Smaldone, *ACS Sustainable Chem. Eng.*, 2022, **10**, 13091-13099.
88.   S. Sun, G. Fei, X. Wang, M. Xie, Q. Guo, D. Fu, Z. Wang, H. Wang, G. Luo and H. Xia, *Chem. Eng. J.*, 2021, **412**, 128675.
89.   D. R. Berry, K. P. Cortés-Guzmán, A. Durand-Silva, S. D. Perera, A. K. Remy, Q. Yan and R. A. Smaldone, *MRS Commun.*, 2021, **11**, 146-156.

Summary

Plastics are among the most applied materials in current society. They come in many forms, and can have very different properties. Traditionally, plastics are classified into two different categories: *thermoplastics* (soft plastics) and *thermosets* (hard plastics). The main difference between the two is that thermoplastics flow when heated (they melt), while thermoset stay set when heating (their structure is permanent). The permanent structure of a thermoset is favourable for many applications, as it gives the material high strength. A downside of thermosets is, however, that they cannot be recycled or repurposed once they have been made. As current society more and more demands the use of recyclable products, we thus need to find a solution to overcome the recyclability issues of thermosets.

One of the most promising current methods to solve this issue is by incorporating dynamic covalent bonds within the polymeric structure of a thermoset. Dynamic covalent bonds are by definition just as strong as classical covalent bonds, which means that if these bonds are included in a polymer material, the material remains robust. However, the dynamic covalent bonds have an additional special feature: they can perform bond exchange reactions. This means, that even if the material appears solid, on the molecular level there is still exchange of polymer chains, with bonds between polymer chains continuously being broken en formed. Such materials are generally referred to as covalent adaptable networks (**CANs**).

In general, the dynamic covalent bonds respond to heat, which means that at low temperatures they do not easily perform their bond exchange. This results in the material to be static at lower temperatures. Only when heated up, the bond exchange becomes more efficient and prominent, resulting in the material to become malleable. In this heated malleable state, the material can be reshaped into a new product.

In this thesis, we focus on the development of CANs that rely on dynamic covalent imine bonds. Imines are well-known chemical structures in the (bio)chemical world, and their applications cover a wide range of possibilities. The main reasons why we chose to work with imines are: **1**) they are easy to make from commercially available molecules, and **2**) they offer a broad range of tuneability.

For industrial purposes the ease in the synthesis of polyimine CANs is very advantageous, but from a fundamental (scientific) point of view, the tuneability that is offered from imine structures is more interesting.

The main objective of this thesis was to use the high degree of tuneability of imine bonds and use them in tuneable CANs. Every chapter discusses a different approach or strategy that enabled tuneability of material properties in order to produce high-performance materials with on-demand specialty properties.

In **Chapter 2**, it was discussed how molecular tuneability was achieved *via* electronics effects, as expressed by the Hammett parameter. Here, we developed a model in which we could predict material properties based on the electron withdrawing or donating effects in one of the monomers that make up the network (*i.e.*, the dianiline monomer).

In **Chapter 3**, continued studies were presented on the polymeric structures of the materials discussed in **Chapter 2**. More specifically, phase separation within the material on the micrometre scale was studied. It was observed that, based on the structure and concentration of aromatic dianiline monomers, we could either suppress or induce phase separation. As a result of the phase separation, the materials showed enhanced material properties. As such, we could use this principle of phase separation to further tune desired properties of our materials. Furthermore, we introduced imaging based in Raman spectroscopy as a new and efficient tool to visualise and analyse the phase separation.

In **Chapter 4** a different technique to tune material properties based on network effects was discussed with a specific focus on the polarity of the polymer network. By studying the kinetics of the imine exchange on both molecular and macroscopic level, we could conclude that the presence of polar groups in the polymeric structure enhanced imine exchange. As a result, the materials became more dynamic and malleable. On the other hand, when apolar chains were used the imine exchange was suppressed and the polymer network become more rigid. This resulted in stiffer and harder materials. We also observed that we could distinguish the overall network dynamics into three different domains: **1**) movement of polymer chains (reptation), **2**) local imine exchange of imines that are within close range, and **3**) diffusion of imine groups through the network.

In **Chapter 5**, the fields or organic and inorganic chemistry were combined by applying metal coordination to polyimine CANs. The metal coordination of the dynamic covalent imine

groups was initially used to enhance the stability of the imines, and as such suppress the bond exchange at lower temperatures to prevent creep. This methodology proved efficient as superior material properties were obtained once the metal-coordination was applied. In addition, different metal ions were tested for coordination, which showed that a correlation was present between the stability of the metal-ligand complex and the material properties of the metal-coordinated CAN. Also, by testing different anions that remained in the polymer network, we observed that inclusion of smaller anions resulted in better performing materials when compared to those with large anions.

In **Chapter 6**, another approach to reduce the high dynamicity of imines was presented by using internal hydrogen bonding. The internal hydrogen bond between imine and a hydroxy on the *ortho* position on an aromatic ring enhances the stability of the imine bond, making it less prone to initiate bond exchange. This way, a higher energy barrier is required to activate the imine. As a result, the materials are less prone creep. We observed that the creep reduction at room temperature was already enhanced significantly compared to materials without his internal hydrogen bond. Moreover, even at elevated temperatures (up till 100 °C) the hydrogen-bonded material still showed good creep resistance, whereas other similar materials without internal hydrogen bonding started to flow rapidly.

In **Chapter 7**, a perspective was provided on the solubility of polyimine CANs. For the application of CANs as thermosets, it is often required to have materials with high resistance to (organic) solvents. However, we discussed that (selective) solubility of CANs can also be desirable. For example, when CANs can be redissolved in a good solvent, this offers new approaches towards recyclability or recovery of raw materials. In addition, having a material that is resoluble in a good solvent enables easier post-synthetic functionalisation. This effectively means that a material can always be adjusted at a later stage.

In **Chapter 8** the results from the previous chapters were addressed in a broader context. In addition, an outlook was provided for future and ongoing research on (imine-based) CANs. Several new and potential applications of CANs will also be discussed, which emphasise the great potential of CANs.

Samenvatting

Plastics behoren tot de meest toegepaste materialen in onze huidige maatschappij. Ze komen in vele vormen en kunnen hierom ook erg verschillende eigenschappen hebben. Dit maakt ze interessant voor allerlei verschillende toepassingen. Oorspronkelijk kunnen plastics worden onderverdeeld in twee categorieën: de *thermoplasten* (zachte plastics) en *thermoharders* (harde plastics). Het grootste verschil tussen de twee is dat thermoplasten kunnen vloeien wanneer zij worden verhit (ze smelten), terwijl thermoharders hard blijven bij verhitting (hun structuur is permanent). Deze permanente structuur is voordelig voor verschillende toepassingen omdat het extra sterkte verschaft aan de materialen. Een groot nadeel is echter dat ze hierdoor niet gerecycled kunnen worden. Omdat onze huidige maatschappij steeds meer verlangt naar recyclebare materialen moeten we dus een oplossing vinden voor het probleem van niet-recyclebare thermoharders.

Een veelbelovende methode om recyclebare thermoharders te produceren is door dynamisch covalente bindingen in te bouwen in de structuur van de thermoharder. Dynamisch covalente bindingen zijn per definitie net zo sterk als andere covalente bindingen, wat betekent dat de sterkte van het materiaal behouden blijft. De dynamisch covalente bindingen hebben echter een extra speciale eigenschap: ze kunnen uitwisselingsreacties ondergaan. Dit betekent dat hoewel het materiaal zijn vaste vorm behoudt, er op moleculair niveau continu uitwisseling plaatsvindt tussen de polymeerketens. Dit soort dynamische materialen worden *covalent adaptable networks* (**CANs**) genoemd.

De meeste dynamisch covalente bindingen reageren op hitte, wat betekent dat ze bij lage temperaturen significant minder actief zijn (minder uitwisselingsreacties). Hierdoor zijn CANs bij lage temperaturen vaak hard en statisch. Alleen wanneer zij verhit worden, worden de dynamische bindingen geactiveerd, waardoor uitwisselingsreacties plaatsvinden en het materiaal zachter en vervormbaar wordt. In deze geactiveerde, zachtere staat kan het materiaal opnieuw gevormd – en dus gerecycled – worden. Wanneer het materiaal weer afgekoeld wordt, heb je een nieuw gerecycled product.

In dit proefschrift ligt de voornaamste focus op het ontwikkelen van CANs die gebruik maken van dynamisch covalente imine groepen. Imines zijn bekende chemische structuren in de (bio)chemische wereld, en ze worden breed toegepast. De voornaamste redenen

waarom wij hebben gekozen om te werken met imines zijn: **1**) ze zijn gemakkelijk te maken vanuit commercieel verkrijgbare materialen, en **2**) ze bieden grote ruimte en mogelijkheden voor design en ontwerpbaarheid.

Voor industriële toepassingen het is met name interessant dat de materialen snel, makkelijk en goedkoop geproduceerd worden, maar vanuit fundamenteel wetenschappelijk oogpunt zijn juist de eigenschappen met betrekking tot (moleculair) ontwerp interessanter.

Door dit proefschrift heen loopt er een rode draad met betrekking tot deze moleculaire ontwerpbaarheid. Ieder hoofdstuk gaat in op een specifieke manier waarop de materiaaleigenschappen van CANs kunnen worden gecorreleerd aan de moleculaire samenstelling van het materiaal. Hierdoor hebben we vele verschillende materialen kunnen maken met specifieke eigenschappen. Verder kunnen we onze kennis gebruiken om te voorspellen hoe een materiaal zich zal gedragen als we weten wat de moleculaire samenstelling is. Daarnaast kunnen we via de omgekeerde weg zelf een formulering maken van welke moleculaire bouwstenen nodig zijn om een materiaal te produceren met de gewenste eigenschappen voor een specifieke toepassing.

In **Hoofdstuk 2** is er gekeken naar hoe materiaaleigenschappen van imine netwerken kunnen worden beïnvloed en gecontroleerd aan de hand van elektronische effecten in de moleculaire structuur. Dit is gedaan met behulp van de Hammett vergelijking, die aangeeft of een chemische groep elektronen aanzuigt of juist duwt. Door dianiline monomeren te gebruiken, waarin chemische groepen verschillende waarden hebben waarin zij elektronen duwen of trekken, kon de imine uitwisseling beïnvloed worden. Als resultaat veranderen hiermee de fysische eigenschappen van het materiaal.

In **Hoofdstuk 3** is er dieper ingegaan op de micro- en macroscopische structuur van deze materialen. Met behulp van Raman spectroscopie hebben we kunnen kijken naar de structuur van het materiaal op de micrometer schaal, en hieruit zagen we dat sommige materialen fase-scheiden in domeinen van enkele micrometers groot. Vervolgens werd geobserveerd dat materialen die dit soort fasescheiding vertoonden, significant sterker en stabieler waren. Daarnaast is er gekeken naar hoe het komt dat sommige materialen wel- of niet fase-scheiden. Hierin kwamen we tot de conclusie dat dit voornamelijk te maken had met interacties tussen de aromatische dianiline bouwstenen die we in het netwerk inbouwen en hoe deze zich "stapelen" in de netwerkstructuur.

In **Hoofdstuk 4** is er gekeken naar aan andere aanpak om de materiaaleigenschappen te beïnvloeden, waarbij de focus lag op de samenstelling van het polymeernetwerk zelf. We hebben hier voornamelijk gekeken naar de rol van polariteit in het netwerk. Door de kinetiek van de imines te bestuderen op zowel moleculair als macroscopisch niveau hebben we kunnen concluderen dat polaire groepen de imine uitwisseling bevorderen. Als gevolg daarvan worden de materialen dynamischer en zachter. Apolaire ketens zorgen juist voor een verminderde imine uitwisseling en een stug netwerk, waardoor het materiaal harder wordt. Daarnaast werd geobserveerd dat de dynamiek in deze CANs kon worden onderverdeeld in drie domeinen: **1**) beweging van polymeerketens (reptatie), **2**) lokale imine uitwisseling tussen imines die dicht bij elkaar liggen, en **3**) diffusie van de imine groepen door het netwerk heen. Deze kennis kan vervolgens worden gebruikt om te voorspellen hoe aanpassingen aan het polymeernetwerk zullen resulteren in veranderingen in materiaaleigenschappen.

In **Hoofdstuk 5** zijn wetenschapsgebieden van de organische en anorganische chemie gecombineerd door metaal coördinatie toe te passen in onze polyimine CANs. De metaal coördinatie met de dynamisch covalente imine groepen was in eerste instantie bedoeld om de stabiliteit van de imines te verhogen en hiermee hun hoog dynamische karakter iets te verlagen. Hierdoor kunnen we het kruipgedrag (vervorming) bij lage temperaturen voorkomen. Onze initiële resultaten lieten zien dat de metaal coördinatie inderdaad een efficiënte methode was om dit te realiseren. Daarna hebben we verder gekeken naar de toepassing van verschillende metalen, en kwamen tot de conclusie dat de materiaaleigenschappen van de CANs grotendeels konden worden gerelateerd aan de stabiliteit van de metaal-imine coördinatiebindingen. Verder is er ook nog gekeken naar de rol van anionen omdat de metaalionen altijd samen komen met corresponderende anionen, die ook in het polymeernetwerk achterblijven. Hierin kwamen wij tot de conclusie dat toepassing van kleinere anionen resulteerde in betere materiaaleigenschappen. Wanneer grotere anionen werden gebruikt zagen we daarentegen dat de sterkte van het materiaal afnam.

In **Hoofdstuk 6** is een andere methode gebruikt om de hoge dynamiciteit van de imines te controleren: het gebruik van interne waterstofbruggen. De aanwezigheid van een interne waterstofbrug tussen een imine en een in nabijheid aanwezige hydroxyl groep (op de *ortho* positie van de aromatische ring) stabiliseert de imine groep. Hierdoor is het imine minder gevoelig om uitwisselingsreacties te ondergaan, en is er een hogere energiebarrière om de

uitwisseling te activeren. Als gevolg zagen we dat deze materialen beter weerstand boden tegen vervormbaarheid. We zagen dat bij zowel lage temperaturen (20 °C) als hogere temperaturen (tot 100 °C), de weerstand tegen vervormbaarheid significant hoger was dan vergelijkbare materialen zonder deze interne waterstofbruggen.

In **Hoofdstuk 7** is een nieuw perspectief besproken over de oplosbaarheid, dan wel oplosmiddel-resistentie, van CANs. Voor de meeste toepassingen van CANs vereist men materialen die een goede weerstand bieden tegen (organische) oplosmiddelen. We beargumenteerden hier echter dat oplosbaarheid van CANs ook juist voordelig kan zijn. Wanneer een materiaal her-oplosbaar is, dan kan dit bijvoorbeeld gebruikt worden voor efficiëntere recycling, of om de gebruikte bouwstenen terug te winnen uit afval. Daarnaast kan het her-oplossen van materialen worden gebruikt om op een later punt aanpassingen aan het materiaal te maken door bijvoorbeeld nieuwe componenten in te bouwen. Dit kan erg nuttig zijn, omdat een oud materiaal opnieuw gebruikt kan worden om een verbeterd product te maken, in plaats van het oude materiaal weg te moeten gooien.

In **Hoofdstuk 8** zijn gezamenlijk de resultaten van de voorgaande hoofdstukken besproken en in een breder perspectief geplaatst. Er is bijvoorbeeld in gegaan op hoe we de kennis die we hebben, kunnen gebruiken om nieuwe ontwikkelingen te stimuleren. Ook is besproken wat voor (nieuwe) toepassingen voor CANs er nog staan te wachten in de toekomst.

About the Author

Sybren Klaas Schoustra was born on 10 December 1993 in Heeze, The Netherlands. His first scientific encounter took place in 2012, when during secondary school he enrolled in a masterclass on organic solar cells at the Eindhoven University of Technology. A year later, in 2013, he graduated from secondary school at the Cambreur College, and started his studies in Chemistry at the Radboud University in Nijmegen. In 2016, he received his BSc degree here and performed his graduation internship in the group of Synthetic Organic Chemistry (supervised by dr. Paloma Engel García, dr. Daniel Blanco Ania and prof. Floris Rutjes). He then continued his stay at the Radboud University for his MSc degree with a specialisation in Molecular Chemistry, and performed internships at the departments of Synthetic Organic Chemistry (supervised by dr. Ivan Bernar, dr. Dani Blanco and prof. Floris Rutjes) and Systems Chemistry (supervised by dr. Sjoerd Rijpkema and prof. Daniela Wilson). During this time he also participated in the Radboud Honours Programme for Masters. In 2018, he received his MSc degree in Chemistry from the Radboud University. Soon after, he started his PhD at the Wageningen University in the group of Organic Chemistry (supervised by prof. Han Zuilhof and dr. Maarten Smulders) on the topic of tuneable imine-based covalent adaptable networks, for which he defends this thesis.

List of Publications

1. S. K. Schoustra, M. M. J. Smulders, "Internal hydrogen bonding of imines to control and enhance the dynamic mechanical properties of covalent adaptable networks", *Manuscript submitted*.

2. M. H. P. De Heer Kloots, S. K. Schoustra, J. A. Dijksman, M. M. J. Smulders, "Phase separation in dynamic polymer networks", *Manuscript submitted*. *Shared first author*

3. S. K. Schoustra, M. M. J. Smulders, "Metal coordination in polyimine covalent adaptable networks for tunable material properties and enhanced creep resistance", *Macromol. Rapid Commun.* **2023**, 2200790, Accepted Article.

4. S. K. Schoustra, M. H. P. De Heer Kloots, J. Posthuma, D. Van Doorn, J. A. Dijksman, M. M. J. Smulders, "Raman spectroscopy reveals phase separation in imine-based covalent adaptable networks", *Macromolecules* **2022**, *55*, 10341-10355.

5. S. K. Schoustra, T. Groeneveld, M. M. J. Smulders, "The effect of polarity on the molecular exchange dynamics in imine-based covalent adaptable networks", *Polym. Chem.* **2021,** *12*, 1635-1642.

6. S. K. Schoustra, J. A. Dijksman, H. Zuilhof, M. M. J. Smulders, "Molecular control over vitrimer-like mechanics – tuneable dynamic motifs based on the Hammett equation in polyimine materials", *Chem. Sci.* **2021,** *12*, 293-302.

7. S. Bressers, H v. d. Elzen, C. Gräwe, D. v. d. Oetelaar, P. H. A. Postma, S. K. Schoustra, "Policy driven changes in animal research practices: mapping researchers' attitudes towards animal-free innovations using the Netherlands as an example", *Res. Integr. Peer Rev.* **2019,** *4*, 8. *All authors contributed equally to this work.*

Overview of Completed Training Activities

Discipline specific activities	Organising institute	Year
ACS Spring	ACS	2021[a]
Advanced Organic Chemistry	VLAG	2019-2022
Bordeaux Polymer Conference	LCPO	2022[a,b]
Brightlands Polymer Days	BPG, KNCV, PTN, DPD, BRPC	2021[a]
Chains	NWO	2018, 2019,[b] 2020,[a,b] 2021,[b] 2022[b]
Dutch Polymer Days	PTN	2019[b]
EPF Summer School on Dynamic and Reversible Polymers	EPF	2019
Rheology Dos and Donts	VLAG	2019[a]
RSC Twitter Conference	RSC	2021,[b] 2022[b]
Symposium Plastic Fantastic	VCMW Sigma	2019
Wageningen MLS seminars	ORC	2018-2022

[a] Oral presentation, [b] Poster presentation

General courses	Organising institute	Year
BCF career event BeNeLux	BCF	2022
BCF career event NL	BCF	2022
Career perspectives	WGS	2022
Online presenting skills for materials science	4TU.HTM	2021
PhD workshop carousel	VLAG	2022
Scientific writing	WGS	2020
Scientific artwork	WGS	2020
Scientific publishing	WGS	2021
VLAG PhD week	VLAG	2019

Other activities	Organising institute	Year
Research proposal	ORC	2018
PhD study tour to Israel	ORC	2019
Weekly group meetings and discussions	ORC	2018-2022
ORC/Surfix trip	ORC, Surfix	2019

Teaching activities	Year
Bio-organic chemistry	2019, 2020, 2021
Bio-organic chemistry for life sciences	2020
Internal reviewer for RMC proposal	2022
Organic chemistry 1	2021
Organic chemistry 2	2020
Proctor at student exams	2022
Research methods for organic chemistry	2021, 2022
Supervising BSc/MSc thesis students	2019-2022
Thesis compendium	2019

Acknowledgements

The last four years of my life as a PhD candidate have been life changing. I have learned so many new things and have developed myself in many other ways as well. All progress and achievements that were made during this time is thanked to the many good people that have sticked together with me and have helped me in numerous different ways. Friends, colleagues and family have supported, guided and shaped the success of my PhD journey. As such, I will forever be grateful to all people in my life that have brought me to where I am today.

First of all, *Maarten*, I would like to sincerely thank you for all your help, supervision and guidance throughout the last four years. You have been an amazing mentor to me. I am grateful for your trust in me to work in your team. Together we have made many great discoveries and gained many more insights in the fascinating field of covalent adaptable networks. This is largely thanked to our many useful discussions and shared interests to make and understand new and innovative materials. Furthermore, your door was always open to discuss either work- or non-work related things, and I have always felt welcome and supported. For this, I will forever be grateful, and thank you again for guiding me towards this amazing milestone in my life.

Han, I am grateful to have you as my promotor and as a guide through my journey as a PhD candidate. I would like to thank you for the talks and discussions we had on our work, science in general, but also life outside of the lab. In addition, I would once more like to emphasise my appreciation for doing everything in your power to keep the labs of ORC running during the Corona pandemic. It has been a privilege that we were able to continue most of our work under suitable conditions during these tricky times.

Joshua, you have basically been the "unofficial" third supervisor of my PhD, as you more-or-less adopted me in the group of PCC. You were the one that taught me most of the basics of rheology, and showed me how to analyse materials from the perspective of a physicist, rather than a chemist. Your contributions have been highly valuable to our research and my development into a better scientist.

To my paranymphs, *Ellen* and *Andriy*, you have not only been great colleagues, but more importantly, have been amazing friends. We have had many "gezellige" lunches, drinks,

dinners or just chillings in- or outside the office in the last couple of years. I hope there will be many more in future, even when we separate our ways after our work in Wageningen is done. In many ways, the three of us have been in the same boat, although we have had our own individual shares as well. I am glad I always had your backs when needed, and have you to share our joy and happiness together.

To all members of the thesis committee, *prof. Filip Du Prez*, *prof. Katja Loos*, *dr. Hans Heuts*, and *prof. Jasper van der Gucht*, a big thanks for reading and validating my thesis, and your presence at my defence.

In the four years of my PhD, I spend a lot of time in what some refer to as the "party office", but which officially known as room 8056 on the 8th floor of the Helix building. During this time I shared many good times in the office with *Alice*, *Annemieke, Bas*, *Dongdong*, *Ellen*, *Esther*, *Namitharan* and *Simon*. Officially, *Andriy*'s desk was never officially in our office, but yet he probably may have spent as much time here as the rest of us.

The great atmosphere at work was also mainly thanks to all other amazing people within the department. As such I would like to thank each and every one that was a part of the many lunches, coffee breaks, (random) discussions, (last-Friday-of-the-month) drinks, and other activities. Some of the people in particular include *Alice, Andriy, Anouk, Ariadni, Bas, Daniele, Dongdong, Ellen, Esther, Hamit, Jasper, Jay, Jordi, Jorick, Julian, Lucas, Marieke, Martijn, Michel, Pepijn Tjerk, Sevil*, *Sjoerd* and *Yuri*.

From the start, all the way to the end of my PhD, I had a lot of help from a great number of people that have guided and helped me in my studies. Especially the technicians and other supporting staff members prove of great value. Some important people within the laboratory of Organic Chemistry (ORC) that were of great importance (not only to me but also to many others and the department in general) include: *Aleida, Barend, Dieuwertje, Elly, Esther, Frank, Hans, Henny, Judith, Maurice, Sidhu* and *Tjerk*. From the department of Physical Chemistry and Soft Matter (PCC) I would also like to thank *Joshua* and *Raoul* for their great help with the rheology, *Remco* for his help with DSC and *Anbu* for his help on the DMA. Last, I would also like to thank *Arjen* from the laboratory of Biophysics for his help with the Raman confocal microscopy and *Herman* from Wageningen Food & Biobased Research (WFBR) for his assistance with the TGA and DSC measurements.

During my PhD I had the honour to guide and supervise a great selection of BSc and MSc students that have helped me in many different ways; either in ways to support our scientific research, but also to help me grow as a person, a tutor and a scientist. In (more-or-less) chronological order from their starting dates I would like to thank *Reint Alberda van Ekenstein* for his investigations in thiol-ene networks, *Timo Groeneveld* for his help in the studies of network polarity, *Luuk Lanters* for his work on bio-based polyimines, *Daphne van Doorn* for her work on steric effects, *Martijn de Heer Kloots* for his great contribution to the studies on phase separation and Raman imaging, *Joris Posthuma* for further development of Raman imaging to study the phase separation, *Martijn Ekhart* for the more thorough analysis of the imaging, and *Robin van Krieken* for his studies on the molecular composition that lays on the origin of the phase separation.

Before I arrived in Wageningen for my PhD candidacy, my academic career started at the Radboud University in Nijmegen, where I graduated for my BSc and MSc degrees in Chemistry. During my studies, and especially the internships, some very important people have helped me become the person and scientist that I am today, for which I would like to share my gratitude. In particular, I would like to thank *dr. Sjoerd Rijpkema* and *prof. Daniela Wilson* from the department of Systems Chemistry, and *dr. Paloma Engel García*, *dr. Ivan Bernar*, *dr. Dani Blanco* and *prof. Floris Rutjes* from the department of Synthetic Organic Chemistry.

Many of the friends that I made in Nijmegen have stayed close, even when I (temporarily) moved out of the city and the whole corona thing happened. Of all the people from Nijmegen there are some specific friends I like to mention. First, I would like to thank *Sverre* and *Marieke*, as they have been very close and good friends to me, and to whom I could always come in times of need. I would also like to thank my friends from the "Nimma crew" (*Baranca, Ellen, George, Heleen, Henjo, Jasper, Lara, Laura, Lotte, Luuk, Ralf, Remco, Sanne, Sverre* and *Xian*), the Nanda crew (*Bas, Florian, Fronk, Jeroen, Jules, Mitchell* and *Sjoerd*), the ParTNT (former Explosief) crew (*Clara, Coen, Dries, Emmy, Harmke, Justus, Marieke, Ralf, Sander* and *Sverre*), my old housemates (*Huub, Jelle* and *Luc)*, and many more along the way. I would also like to thank *Kim* for all the support and good times we had together.

I would like to thank my life-long friends from Rijen (Brabant): *Björn, Bram, Daan, Maarten, Maxime, Mike, Olaf, Roy* and *Tim*. They have showed me that true friendship has no limitations regarding *e.g.* time or distance. I love the fact that we all came from similar roots

as youngsters, but each went our individual ways. Yet, we never lost contact and still remain good friends until this day.

I am very grateful to my loving family. In particular, *Mama* and *Heiti*, thank you for always loving and supporting me since the day I was born. I would also like to thank *Esther*, who was there for a large part in my life as well. I am also grateful to my loving brothers *Arjen* and *Bauke*, and their partners *Simone* and *Evy*, respectively. I would also like to thank my "in laws" *Berry* and *Bea* for their love and care. Last, for mental support and lots of love, I am grateful of our amazing pets *Pico* and *Pluis*.

Harmke, these last few lines are specifically for you. I already apologise for the cheesiness of this paragraphs, but I cannot describe in words how happy I am to have you in my life. Who would have thought that when we met so many years ago, and (jokingly) discussed we would have a golden retriever someday in the future, that since little over a year now we would actually become a couple. In this time, I have always had your fullest love and support. We have shared many good times together, but also in the more stressful times you have always had my back and were there for me. As such, I am very grateful that we could always share and rely on each other in whatever we went through. I am beyond happy to have you by my side. I love you!

Acknowledgements